Curtin Medical School

Quantitative Measurements of Breast Density Using Magnetic Resonance Imaging

Rooa Sindi

0000-0002-9813-9611

This thesis is presented for the Degree of

Doctor of Philosophy of

Curtin University

April 2021

Declaration

To the best of my knowledge and belief this thesis contains no material previously published by any other person except where due acknowledgment has been made.

This thesis contains no material which has been accepted for the award of any other degree or diploma in any university.

The research presented and reported in this thesis was conducted in accordance with the National Health and Medical Research Council National Statement on Ethical Conduct in Human Research (2007) – updated March 2014. The proposed research study received human research ethics approval from the Curtin University Human Research Ethics Committee (EC00262), Approval Number HRE2019-0466.

[redacted]

Rooa Sindi

April 2021

Abstract

Breast density, a measure of dense fibroglandular tissue relative to non-dense fatty tissue, has been determined as an independent risk factor for developing breast cancer. Previous studies have reported that the potential risk of breast cancer in women with dense breasts is three- to five-fold higher than in women with fatty breasts. Numerous MR breast-imaging protocols have been applied to the screening and/or the assessment of breast density, ranging from contrast- to non-contrast-enhanced imaging with or without the implementation of fat-suppression techniques. However, there has been little consensus on the optimal MR breast-imaging protocol and measurement method for breast density screening and/or assessment, especially in the context of women with dense breast tissues. The main aim of this study was to determine the most appropriate technical/operational MRI protocols for the quantitative assessment of breast density.

A systematic review and meta-analysis study was first conducted to review the existing measurement methods and breast-imaging protocols for the quantitative assessment of breast density using MRI over the previous decade of publications. Following this, a patient-specific breast model was developed using 3D-printing techniques and tissue mimicking materials to identify the most appropriate materials for simulating the MRI related-characteristics of fibroglandular and adipose breast tissues. Anthropomorphic shapes of skin and fibroglandular tissues were constructed using 3D-printing techniques based on the segmentations of breast MR images from a selected healthy patient's data. All the 3D skin and fibroglandular region shells were designed as hollow structures using polylactic acid (PLA) and photopolymer resin.

Then, using a personalized 3D-printed breast model and an objective comparison of the non-fat-suppressed and fat-suppressed sequences, an analysis was conducted to determine the most suitable MR breast-imaging protocols for the quantitative assessment of breast density. Finally, in a cohort of 11 high-risk women, a study was performed to investigate the difference between the quantitative measurements of breast volume, fibroglandular tissue volume, and percentage of breast density of two MR techniques, the non-fat-suppressed versus the fat-suppressed T2-weighted imaging sequences.

The following are some of the study's findings:

Results for the quantitative measurement of breast density using MRI: A systematic review and meta-analysis:

- The review of 38 studies confirmed high levels of heterogeneity within the breast density studies, mainly due to the applications of MR breast-imaging protocols and the use of different breast density segmentation/measurement methods.
- The analysis confirmed that the non-contrast-enhanced T1-weighted acquisition was commonly utilized among all MR breast-imaging protocols and the fuzzy C-mean clustering (FCM) is the most frequently used algorithm amongst the breast density segmentation/measurement methods.

Results for the development of patient-specific 3D-printed breast model using silicone and peanut oils for MRI:

- A patient-specific 3D-printed breast phantom was successfully designed and constructed using silicone and peanut oils to simulate the MR imaging characteristics of fibroglandular and adipose tissues.
- The silicone and peanut oils were found to closely resemble the T1 relaxation times and imaging characteristics of these two tissues, which are 1,515.8±105.5 and 405.4±15.1 ms, respectively.
- The agarose gel with different concentrations, ranging from 0.5 to 2.5 wt%, was found to have the longest T1 relaxation times.

Results for the quantitative measurement of breast density using personalized 3D-printed breast model for MRI:

- The volume of fibroglandular tissue and the percentage of breast density were significantly higher in the fat-suppressed sequences than in the non-fat-suppressed sequences ($p < 0.05$); however, the difference in breast volume was not statistically significant ($p = 0.529$).
- A fat-suppressed T2-weighted with turbo inversion recovery magnitude (TIRM) imaging sequence was superior to the non-fat- and fat-suppressed T1- and T2-weighted sequences for the quantitative measurement of breast density due to its ability to represent the exact breast tissue compositions.
- This study shows that the fat-suppressed sequences tended to be more useful than the non-fat-suppressed sequences for the quantitative measurements of the volume of fibroglandular tissue and the percentage of breast density.

Results for the quantitative measurement of breast density in a high-risk group using fat-suppressed and non-fat-suppressed T2-weighted MRI sequences:

- The results revealed no indication of measurement bias between the non-fat-suppressed and fat-suppressed T2-weighted imaging sequences with respect to breast density parameters, and no evidence to reject the presumption that the differences were normally distributed.
- Although the breast volume measured in the fat-suppressed T2-weighted sequence was slightly higher than that in the non-fat-suppressed T2-weighted sequence and the difference was close to significant ($p = 0.078$), the findings showed no significant difference in the breast density parameters analyzed from the two imaging techniques.
- This study showed no substantial differences between the non-fat-suppressed and fat-suppressed sequences in the quantitative measurement of breast density parameters; however, further studies with inclusion of a larger sample size are required to validate the complementary role of T2-weighted imaging in this regard.

In conclusion, this research has intensified the need for a standardized imaging protocol and/or measurement method for the evaluation of breast density predominantly for women at an elevated risk of developing breast cancer, such as those with high breast density. Using 3D-printing techniques and tissue mimicking materials, this study has suggested that silicone and peanut oils can be used to efficiently simulate the MR imaging characteristics of breast structures and produce further models. The proposed methodologies can be used as a preliminary work for breast structure simulations and the construction of further patient models using MRI dataset.

Acknowledgements

First and foremost, I would like to express my heartfelt gratitude to “God” for lavishing me with much more than I deserve.

I am deeply thankful to my supervisor Professor Zhonghua Sun for his patience, encouragement, enthusiasm, tremendous knowledge, and invaluable guidance during the research journey and writing of this thesis. He has been a fantastic mentor in helping me plan out my PhD journey, providing research advice, connecting me with resources, being available and responding to my emails and questions. Professor Sun is a pioneer in the field of Medical Radiation Science, and his extensive expertise in research and publication has been instrumental in my success.

I would like to thank Dr. Chai Hong Yeong and Dr. Yin How Wong from Taylor’s University in Malaysia for their assistance with the breast phantom construction and the use of the 3D printing facilities.

I appreciate Mr. Gil Stevenson, who, although no longer with us, for his unwavering support and assistance with the statistical analysis used in this project. He is one of the smartest people I have ever had the privilege of working with; he challenged me to think deeper, work harder, and seek out new opportunities.

I would also like to express my deepest appreciation to the Saudi Armed Forces Medical Service Division, the King Fahd Armed Forces Hospital, and the Saudi Arabian Cultural Mission for their financial support.

Last but not least, I owe a debt of gratitude to my family, brothers and sisters for their continued encouragement. Mrs. Rania Sindi, my soulmate, for her unwavering support, love, prayers, and devotion, without which I would not have made it through this project.

3. List of publications included as part of the thesis

- Sindi R, Sá Dos Reis C, Bennett C, Stevenson G, Sun Z. Quantitative measurements of breast density using magnetic resonance imaging: a systematic review and meta-analysis. Journal of Clinical Medicine. 2019; 8(5): 745.
- Sindi R, Sun Z. Optimal protocols for quantitative assessment of breast density using magnetic resonance imaging. Australas Med J. 2019; 12(6): 186-188.
- Sindi R, Wong YH, Yeong CH, Sun Z. Development of patient-specific 3D-printed breast phantom using silicone and peanut oils for magnetic resonance imaging. Quant Imaging Med Surg. 2020; 10(6): 1237-1248.
- Sindi R, Sun Z. Personalized three-dimensional printed breast model for quantitative assessment of breast density using magnetic resonance imaging. Australas Med J. 2020; 13(7): 234-238.
- Sindi R, Wong YH, Yeong CH, Sun Z. Quantitative Measurement of Breast Density Using Personalized 3D-Printed Breast Model for Magnetic Resonance Imaging. Diagnostics. 2020; 10(10): 793.

Statements of contributions of others

Rooa Sindi input into this study and the associated papers as well as the dominant contribution to the intellectual property involved in the project. As is almost always the case in conducting research studies with assistance by collaborators, other researchers made contributions to the work that were significant enough to warrant co-authorship on the resulting journal articles.

Rooa Sindi

Professor Zhonghua Sun

5. List of conference presentations

- 19th Asian Oceanian Congress of Radiology, July 2021, Kuala Lumpur, Malaysia (Development of patient-specific 3D-printed breast phantom using silicone and peanut oils for magnetic resonance imaging - abstract accepted).
- Saudi Arabian Cultural Mission, Saudi Research IDOL 2021, January 2021, Canberra, Australia (Quantitative Measurement of Breast Density Using Personalized 3D-Printed Breast Model for Magnetic Resonance Imaging).
- MLS HDR Science Symposium 2020, Curtin University, Perth, Australia, December 2020 (Quantitative Measurement of Breast Density Using Magnetic Resonance Imaging).
- Australian Institute of Physics 2020 WA Student Conference, University of Western Australia, Perth, Australia, November 2020 (Development of patient-specific 3D-printed breast phantom using silicone and peanut oils for magnetic resonance imaging).
- Saudi Arabian Cultural Mission Virtual Scientific Seminar 2020, May 2020, Canberra, Australia (Quantitative Measurement of Breast Density Using Magnetic Resonance Imaging).

6. Introduction to Thesis

Breast density, a measure of dense fibroglandular tissue relative to non-dense fatty tissue, has been determined as an independent risk factor for developing breast cancer. To date different MR breast imaging protocols have been applied to the screening and/or the assessment of breast density, ranging from non-contrast-enhanced T1-weighted to contrast-enhanced T1-weighted and diffusion-weighted acquisitions. Along with this growth in the quantitative assessment of breast density using MR imaging, however, there has been no general agreement about the optimal technical approach in this aspect.

The applications of 3D printing in breast tissue are limited, therefore, a patient-specific 3D printed breast model could be used to examine different MR breast-imaging protocols. This can make a substantial contribution to the quantitative assessment of breast density by exploring the optimal protocol with this regard. An important implication of this is the possibility that breast density is assessed, thus, the risk factor of breast cancer can be identified to some extent.

The purpose of this study is to identify the optimal MR breast-imaging protocol and measurement method for the quantitative assessment of breast density. In more detail, this study aims to achieve the following objectives:

- Development of patient-specific breast model using 3D-printing techniques and tissue mimicking materials for MRI. This endeavours to identify the most appropriate materials for simulating the MR imaging characteristics of fibroglandular and adipose tissues, demonstrates the feasibility of creating a

realistic 3D-printed breast model for breast density assessment and further study.

- Quantitative measurement of breast density using a patient-specific 3D-printed breast model for MRI. This attempts to determine the optimal MR breast-imaging protocol for assessing breast density quantitatively, taking into account a variety of imaging techniques, acquisition modes, and fat-suppression methods. This entails a review of the usefulness, applicability, ease of use, and outcomes of a semi-automated approach for segmenting and measuring breast density parameters.
- Quantitative measurement of breast density in participants' clinical breast MRI datasets. This aims to investigate the difference between the quantitative measurements of breast volume, fibroglandular tissue volume, and percentage of breast density of two MR techniques, the non-fat-suppressed versus the fat-suppressed T2-weighted imaging sequences.

7. Thesis Outline

The thesis is divided into six chapters in its overall structure. Chapter 1 is the introductory background for this study. It includes a summary of the importance role of MRI in breast density screening and evaluation, as well as a literature review of current MRI protocols and segmentation/measurement for breast density assessment. This chapter concludes with a discussion of existing 3D printing technologies and MRI breast phantoms. Chapter 2 is the chronologically first publication and is entitled "Quantitative Measurements of breast density using magnetic resonance imaging: A

systematic review and meta-analysis". Chapter 3 is the chronologically third publication and is entitled "Development of patient-specific 3D-printed breast phantom using silicone and peanut oils for magnetic resonance imaging". Chapter 4 is the chronologically fifth publication and is entitled "Quantitative measurement of breast density using personalized 3D-printed breast model for magnetic resonance imaging". Chapter 5 is the "Quantitative measurement of breast density in a high-risk group using fat-suppressed and non-fat-suppressed T2-weighted magnetic resonance imaging sequences". Finally, Chapter 6 is a list of observations, which includes a concise summary and critique of the findings as well as potential future directions.

8. Statistical Analysis

In chapter 2, a single arm meta-analysis was conducted to determine the quantitative values of MRI in breast density assessments. Combined means with their 95% confidence interval (CI) were calculated using a fixed- effect model. A forest plot was generated, displaying the individual study (% breast density) means with 95% confidence interval (CI) limits, inverse variance study weights, and the pooled mean and confidence limits. The data was analyzed by the "metamean" function in the "meta" package in the R system, Version 3.4.1 (http://www.r- project.org/). Heterogeneity of study means was assessed using Cochran's Q-test, and heterogeneity of study variances was assessed with Bartlett's test. A conclusion to pool studies requires both heterogeneity tests to be non-significant at the 5% level

Furthermore, alternative groupings based on statistical similarities were identified via a cluster analysis employing study means and standard deviations in a Nearest Neighbor/Single Linkage. The International Business Machines Statistical Package for the Social Sciences (IBM SPSS) Statistics software Version 25.0 was used for cluster analysis.

In chapter 4, the repeated-measures analysis of variance (ANOVA) was performed to examine the difference between the quantitative measurements of breast volume, fibroglandular tissue volume, and percentage of breast density with regard to the non-fat-suppressed and fat-suppressed MRI sequences. This variance model was employed to account for the variation both between sequences (i.e., between subjects) and within repeated measurements (i.e., within subjects). Significance levels were set at the 5% level. Descriptive data and box plots were also produced for all variables, demonstrating the distribution and median of breast volume, fibroglandular tissue volume, and percentage of breast density measured in the non-fat-suppressed and fat-suppressed imaging groups. Statistical analyses were conducted using NCSS V 19.0.5 (NCSS, LLC., Kaysville, UT, USA).

In chapter 5, averages of repeated-measures observations through the Bland-Altman comparison of measurements were conducted to examine the difference between the non-fat-suppressed T2-weighted TSE and the fat-suppressed T2-weighted STIR MRI sequences with regard to the quantitative measurements of breast volume, fibroglandular tissue volume, and percentage of breast density. The Bland-Altman scatter plots were produced for the two MRI sequences, demonstrating the difference against the average, which illustrates a system with zero bias of one method relative to the other with respect to breast volume, fibroglandular tissue volume, and

percentage of breast density. The normality assumptions of the datasets distributed were also examined using the Shapiro-Wilk, Skewness, Kurtosis, and Omnibus tests. Statistical significance was evaluated using the one-sample t-test as appropriate and set at the 5% level.

Statistical analyses for chapters 4 and 5 were conducted using NCSS V 19.0.5 (NCSS, LLC. Kaysville, UT, USA).

Table of Contents

9. Abbreviations

ACR – American college of radiology

BIRADS – breast imaging-reporting and data system

2D FFDM – two dimensional full-field digital mammography

DBT – digital breast tomosynthesis

3D – three dimensional

FDA – food and drug administration

US – ultrasound

HHUS – hand-held ultrasound

ABUS – automated breast ultrasound

ABVS – automated breast volumetric scanning

FGT – fibroglandular tissue

MRI – magnetic resonance imaging

EUSOBI – European society of breast imaging

BRCA – breast cancer gene

DCE – dynamic contrast-enhanced

DWI – diffusion-weighted imaging

ADC – apparent diffusion coefficient

SE – spin echo

GRE – gradient echo

SNR – signal-to-noise ratio

T1WI – T1-weighted imaging

T2WI – T2-weighted imaging

B_0 – magnetic field

EPI – echo-planar imaging

CHESS – chemical shift spectral-selective saturation

IR – inversion recovery

TE – echo time

Fat Sat – fat saturation

B_1 – radio frequency field

TR – repetition time

STIR – short TI inversion recovery

TI – inversion time

SAR – specific absorption rate

SPIR – spectral pre-saturation with inversion recovery

SPAIR – spectral pre-saturation attenuated with inversion recovery

FCM – fuzzy C-means

N3 – non-parametric non-uniformity normalization

CT – computed tomography

CAD – computer-aided design

STL – standard tessellation language

SLS – selective laser sintering

SLA – stereolithography

UV – ultraviolet

DLP – digital light projection

FDM – fused deposition modelling

FFF – fused filament fabrication

3DP – three-dimensional printing

CJP – colour jet printing

TMM – tissue-mimicking material

Gd-DTPA – gadolinium-diethylenetriamine penta-acetic acid

PVC – polyvinyl chloride

PVCP – polyvinyl chloride plastisol

PRISMA – preferred reporting items for systematic reviews and meta-analysis

IQR – interquartile range

BV – breast volume

BD – breast density

FV – fibroglandular volume

DBV – dense breast volume

CI – confidence interval

SD – standard deviation

SE – standard error

CV – coefficient variation

PLA – polylactic acid

DICOM – digital imaging and communications in medicine

NA-MIC – national alliance for medical image computing

mm – millimetre

cm^3 – cubic centimetre

μm – micrometre

% – percentage

sec – second

ms – millisecond

mm/s – square meter per second

°C – centigrade

L – litter

wt – weight

TSE – turbo spin echo

FSE – fast spin echo

ANOVA – analysis of variance

TIRM – turbo inversion recovery magnitude

SPACE – sampling perfection with application optimized contrasts using different flip angle evaluation

FOV – field-of-view

NSA – number of signal averages

NEX – number of excitations

PFP – partial fourier phase

10. List of Figures and Figure Legends

List of Tables and Table Legends

Chapter 1

Background and Literature Review

1.1 Breast Density and Classification

Breast density, a measure of fibroglandular, dense tissue relative to fatty, non-dense tissue, is an independent risk factor of breast cancer.[1-3] Consistent with this risk relationship, women who have dense breasts have a likelihood of developing breast cancer that is fourfold higher than those with fatty breasts.[4, 5]

The evaluation of fibroglandular tissue is based on a subjective assessment recommended by the American College of Radiology (ACR) Breast Imaging-Reporting and Data System (BI-RADS), which is commonly used for mammography but also for magnetic resonance imaging (MRI). The BI-RADS Atlas can be described as a classification system that characterises breast density on the basis of the amount of fibroglandular tissue into four categories: 1) almost entirely fat, 2) scattered fibroglandular tissue, 3) heterogeneous fibroglandular tissue, and 4) extreme fibroglandular tissue.[6, 7]

1.2 Imaging Modalities for Breast Density Assessment

Most information about breast density estimation and screening for breast cancer is obtained through full-field digital mammography (FFDM), a two-dimensional (2D) imaging technique. FFDM is considered an effective screening modality that can contribute to the reduction of breast cancer mortality, particularly at an early stage of the disease.[8, 9] However, the evaluation of breast density based on mammograms is limited due to tissue overlapping, variations in breast compression, and inappropriate positioning, which can lead to artefacts (skin folds) and insufficient imaging of breast tissue.[10, 11] Another problem with this modality is its low sensitivity in detecting breast cancer when the breast tissue is dense, which is the case for 40% to 50% of women

under the age of 50 years.[12] Kolb et al[13] found that as breast density increases, the sensitivity in detecting breast cancer is decreased from 89% in fatty breasts to 42% in women with over 75% mammographic density. These factors can limit mammography's precision and reliability for the detection of small changes in breast density over brief timespans.[14, 15]

1.2.1 Digital Breast Tomosynthesis

To address the limitations of conventional mammography, digital breast tomosynthesis (DBT) has been developed, which enables three-dimensional (3D) reconstructions of the breast volume and has become one of the most widely imaging tools in breast centres worldwide.[16, 17] Recent research has shown a dramatic improvement in screening outcomes of breast density assessments with this technique.[16-19] It provides high-resolution imaging, higher diagnostic accuracy, and better detection rates compared to conventional digital mammography.[20, 21] DBT differs from conventional two-dimensional mammography in several respects. In FFDM, the planar information is obtained from multiple projection images. As each scan can create only one image plane, multiple scans are required to reconstruct the whole breast.[22, 23]

In contrast, in DBT, the planar information is obtained using only one set of X-ray projections at various angles; therefore, one scan can produce a 3D reconstruction of all planes, creating a full breast volume.[20-22] However, despite differences of opinion, there appears to be some agreement that 2D images are still essential, as some microcalcification clusters are not easily detectable in 3D images.[8] The US Food and Drug Administration (FDA) has recommended that DBT be used in combination with FFDM to enhance the diagnostic reliability and screening performance of standard

mammography.[22, 23] However, a major problem with this recommendation is the exposure of patients to a double radiation dose, as the radiation exposure of DBT is comparable to that of FFDM.[8, 22, 23] Therefore, there seems to be a need for wider acceptance of DBT in breast screening to limit radiation exposure.

1.2.2 Breast Ultrasonography

Breast ultrasonography (US), a non-ionizing technology, is an important imaging modality for breast cancer detection. It has played a key role in image-guided biopsy and lymph node diagnosis for a long time, as it is inexpensive and widely available.[25, 26, 30] A variety of ultrasound imaging techniques have been used for breast cancer detection, which can be classified into five main categories: ultrasound-based elastography, contrast-enhanced ultrasound, 3D ultrasound, automated breast sonography, and computer-aided detection of breast lesions.[25-30]

For breast density assessments, two types of automatic breast volume scanning have been used as a tool complementary to mammography, each with its advantages and disadvantages: hand-held ultrasound (HHUS) and automated breast ultrasound (ABUS).[25, 29, 30] HHUS is a novel technique for breast tissue characterization that uses a conventional US system and a passive reflector, which is placed at the opposite side of the US probe. The purpose of the passive reflector is to measure the speed of sound in tissue and reflect it back to the US probe.[29, 30] However, due to practical constraints, HHUS cannot yield reproducible results or image and/or store 3D volumes of the breast. Other major drawbacks of this approach are that it cannot reconstruct the whole breast and that it largely relies on the operator's skills.[29, 30]

ABUS, also known as automated breast volumetric scanning (ABVS), was approved by the US FDA in September 2012 and has been used in various studies for 3D ultrasonographic depictions of the whole-breast structure to assess breast density.[25, 26] The ABUS technique is one of the more practical methods of breast density analysis, as it can provide true volumetric imaging data. The concept of this modality is based on combining breast echoic reflex images to produce multiplanar whole-breast reconstructions.[25, 27] Most of the breast structure, such as the skin, subcutaneous fat, fibroglandular tissue (FGT), mamilla, retromammary fat, muscle fascia, and ribs, can be clearly visible in ABUS images.[26] Several studies have shown that the echogenicity and speed of sound tend to be higher in FGT than in subcutaneous and retromammary fat.[26, 28, 29] This provides the ability to differentiate between FGT and other breast structures in surrounding tissue, thus enabling more accurate breast density measurements. ABUS can mainly be applied in women with high breast density, no previous invasive procedures, and a BI-RADS score of 1, which indicates negative cancer results on X-ray mammography.[25-28, 30] However, despite its increasing popularity for breast density assessments, ABUS has certain limitations, such as its reliance on a dedicated ultrasound system and custom add-on software.[28, 29] Therefore, further studies should be conducted to determine the exact utility of this novel technique for breast density assessments and as a biomarker for breast cancer.

1.2.3 Magnetic Resonance Imaging

Magnetic resonance imaging (MRI) is one of the most widely used methods for breast cancer detection, in conjunction with mammography, US, and image-guided needle biopsy. It has been extensively applied for the screening of women at high risk of breast cancer, preoperative staging of newly diagnosed breast cancer (ipsilateral and

contralateral), evaluation of women with breast implants, and breast cancer treatment follow-ups.[31-33] The European Society of Breast Imaging (EUSOBI) has recommended that breast MRI be used as an adjuvant modality in women at high risk of developing breast cancer, such as those with breast cancer susceptibility gene (BRCA)-positive genetic mutation carriers, a family history of breast cancer, and/or high breast density.[33, 34] Previous studies have reported that the sensitivity of MRI for breast cancer is up to 98% for invasive and 60–80% for ductal in situ breast carcinomas.[32, 33] Several studies have also shown that MRI can detect enhancing invisible in mammography and US, 50% of which are cancerous.[32, 33]

1.3 MRI Protocols for Breast Density Assessment

1.3.1 Dynamic Contrast-Enhanced Imaging

To date, various breast MRI protocols have been developed. The dynamic contrast-enhanced (DCE)-MRI technique is the most frequently used for the screening of women at high risk of breast cancer and has been included in standard clinical breast MRI protocols.[35, 36] The sensitivity of this technique for breast characterization tends to be very high, in the range of 94–100 %, whereas its specificity is relatively low, ranging between 40 % and 80%.[37] Despite its long clinical success, DCE-MRI has certain disadvantages, such as long scanning time, high cost, and potential harm caused by the contrast agent.[37] Although contradictory findings have been reported in the literature about the precipitation and accumulation of gadolinium contrast–based agents in the brain, there is no general agreement regarding the risk of repeated gadolinium administration.[36] Nevertheless, questions have been raised about the safety of prolonged use of DCE-MRI as a primary screening method for breast cancer. On the other hand, despite considerable new knowledge about the role of MRI in breast

screening, many studies have reported the role of MRI in breast density analysis.[36] It has been used for qualitative and/or quantitative evaluations of breast density because it provides a three-dimensional volume image of breast tissue with excellent soft tissue contrast, which assists in the differentiation between fibroglandular and fatty, or adipose, tissue.[12, 38-40]

1.3.2 Diffusion-Weighted Imaging

Diffusion-weighted imaging (DWI) is a non-contrast-enhanced MRI technique that measures Brownian motion, that is, random movements of free water molecules in all directions.[35, 41, 42] Evidence suggests that the diffusion of water molecules is greatly affected by the tissue's cellularity.[35, 41, 42] Restricted diffusion generally occurs in tissue with higher cellular density, as water molecules cannot diffuse easily within the tissue, bouncing back towards the impermeable cell walls.[35, 41, 42] This phenomenon is observed in most cancers and is associated with high intensity on DWI.[35, 41, 42] Apparent diffusion coefficients (ADCs), also known as estimated diffusion rates, calculated from DWI, play an important role in the differentiation between benign and malignant breast lesions.[35] Several studies exploring DWI as a screening tool supplemental to mammography have reported its advantages for breast cancer detection, predominantly in high-risk women with dense breasts.[35, 43, 44] As an unenhanced MRI technique, DWI has been proposed as an alternative to DCE-MRI in terms of safety and cost related to the exposure to gadolinium contrast– based agents.[35, 41, 42] However, breast DWI technique has not been standardized yet, and more research is required to determine its value as an adjunct screening tool in women at high risk of breast cancer.

1.3.3 Non- and Fat-Suppression T1-Weighted Imaging

Non-fat-suppressed and fat-suppressed T1-weighted images are frequently used either with 2D spin echo (SE) or 3D gradient echo (GRE) in standard clinical breast MRI protocols.[36, 45] However, there is no consensus about the optimal protocol in this regard. The American College of Radiology (ACR) has recommended that fat-suppressed images with high spatial resolution be used in clinical breast MRI protocols, as the evaluation of fat-suppressed sequences based on the acquisition of post-contrast images without subtraction can eliminate misregistration, which mainly occurs when a patient moves during the acquisition of pre- and post-contrast images.[36, 45] However, this recommendation is at odds with that of the EUSOBI, which considers non-fat-suppressed sequences based on the acquisition of subtraction images more useful.[45, 46] In fact, non-fat-suppressed images tend to have a higher signal-to-noise ratio (SNR) and stronger tissue contrast than fat-suppressed images.[45, 46]

Although non-fat-suppressed T1-weighted acquisition is commonly included in standard clinical MRI protocols to better visualize the breast's anatomy and fat distribution, there appears to be some agreement that other breast MRI techniques, including T2-weighted images, DCE, and DWI, tend to benefit from its combination with fat-suppression techniques for several reasons.[1, 36, 45, 47] First, fat tends to appear bright in T2-weighted images due to its long T2 relaxation time. Therefore, if the fat signal is not completely eliminated, it can obfuscate the features of interest and interfere with the assessment of benign lesions.[1, 36, 45, 47] Second, an unsuppressed fat signal can induce a chemical shift artefact caused by signal variations due to the inherent differences in resonant frequency between fat and water, usually observed on fat and soft tissue boundaries.[45, 47, 48] Third, fat appears hyperintense on DCE-MRI

because of its comparatively short T1 relaxation time. If the fat signal is not completely suppressed, it can obfuscate the enhancing lesions and interfere with the variations of signal intensity caused by the contrast agent.[45, 47, 49] It can thus be suggested that fat suppression is a very important technique to better visualize the enhancing lesions on DCE-MRI.[49] Furthermore, breast MRI is more susceptible to the inherent magnetic field (B_0) inhomogeneity caused by the difference in magnetic susceptibility between breast tissue and the surrounding air.[48, 50] Therefore, the fat-suppression technique could be a reasonable approach to tolerate the B_0 inhomogeneity.[48, 50] Finally, fat suppression has received considerable critical attention in breast DWI, which is largely based upon an echo-planar imaging (EPI) sequence.[50, 53, 54] In a single-shot EPI, all the spatial-encoding data of an image can be obtained after a single radio frequency excitation in a few seconds. However, a main issue with this application is that chemical shift artefacts can lead to a significant displacement of the fat signal in the phase-encoding direction of EPI.[50, 53, 54] Therefore, since the breast consists of a considerable amount of fat, fat suppression is necessary to eliminate its signal in breast DWI.[50, 53, 54] Fat suppression has proven to be an essential component of DWI for different parts in the body, as it assists to overcome the limitations associated with fatty tissue.[50, 53]

1.3.4 Fat-Suppression Imaging

Fat suppression is used in breast MRI to improve the visibility of pathology, contrast enhancement, and image quality, thus allowing a better differentiation between fatty non-glandular and glandular tissue.[45, 47] It has been combined with other techniques because of the difficulty of eliminating the high signal intensity associated with fatty tissue.[45, 47] Over the years, several methods have been proposed for fat suppression in

breast MRI, including chemical shift spectral-selective saturation (CHESS), which relies on the chemical shift variation between fat and water, inversion recovery (IR), which relies on the variation of T1 relaxation time, hybrid CHESS–inversion recovery methods, and Dixon fat-water separation, which relies on the phase variation between fat and water signals at different echo times (TEs).[3, 41, 42, 45, 47, 55]

In CHESS, also known as fat saturation (Fat Sat), a 90^{o} frequency-selective excitation pulse followed by a homogeneity spoiler gradient is applied to saturate/dephase the fat protons only, thus suppressing the fat signal while leaving the water signal relatively unaffected.[47, 56-59] Although the CHESS technique has been successfully used in breast MRI, it has certain limitations related to its higher sensitivity to the inhomogeneity of the magnetic (B_0) and radio frequency (B_1) fields, which can cause significant heterogeneity in fat suppression.[47, 56-59] Another limitation of this approach is that it cannot be implemented at each pulse repetition time (TR) on a repeated series of pulses and echoes in a fast GRE acquisition. Consequently, the steady-state signal and the quality of fat suppression can be affected even if the B_0 is completely homogeneous across the entire field of view.[56, 59] Fat suppression based on CHESS or other chemical shift selective excitation techniques can be improved by using a high-field MRI system (≥3T), especially with the acquisition of a GRE pulse sequence.[47, 56, 60] This is because the chemical shift difference between fat and water at higher magnetic field strengths is increased, achieving B_0 and B_1 homogeneity. Nevertheless, field heterogeneity is more prominent in 3T MRI systems, which inevitably affects the fat suppression performance and image quality.[47, 56, 60]

In an inversion-based technique known as short TI inversion recovery (STIR), a 180° non-spectral-selective inversion pulse is applied, followed by either a single 90° pulse or a pair of 90° and 180° pulses for the IR and SE imaging, respectively.[47, 56, 58, 61, 62] The time between the 180° inversion pulse and the subsequent 90° pulse is referred to as inversion time (TI), which for fatty tissue is assumed to be 180 and 215 ms for 1.5T and 3T MR systems, respectively.[47, 56, 58, 61, 62] During the TI interval, the T1 relaxation time of fat is shorter than that of water, and thus fat is recovered faster. Subsequently, at the 90° excitation pulse, the fat signal is nulled out, and a fat-free signal is produced.[47, 56, 58, 61, 62] Because of the expected longer T1 relaxation time of water, more time is required for the signal to reach the null point; consequently, it is attenuated and/or reduced.[47, 56, 58, 61, 62] STIR sequences are among the most widely used fat-suppression techniques in breast imaging due to their insensitivity to B_0 and B_1 heterogeneity.[47, 62] However, STIR suffers from major drawbacks, including its long imaging time, low SNR, and high specific absorption rate (SAR) of the radio frequency energy.[41, 47, 56, 58, 61, 62] Another considerable disadvantage is that, because STIR is not a fat-specific suppression technique and relies on the variation of T1 relaxation times, during the TI interval, it can also suppress all other tissues and substances with a short T1 relaxation time along with fat tissue.[47, 56, 58, 61, 62]

Regarding hybrid approaches, two fat-suppression techniques have commonly been used: spectral pre-saturation with inversion recovery (SPIR) and spectral pre-saturation attenuated with inversion recovery (SPAIR).[41,47,62] In SPIR, an 180° spectral-selective inversion pulse is applied for fat only, followed by a single 90° excitation pulse after a certain TI.[41, 47, 62] Clear benefits of SPIR are that it has a higher SNR than purely inversion-based techniques and that it does not suppress other tissues with short T1 relaxation times, as the latter do.[41, 47, 62] Despite its advantageous fat-

suppression approach, SPIR still suffers from B_1 inhomogeneity due to the expected variation of the radio frequency amplitude across the entire field of view.[41, 47, 56, 58, 61, 62] On the other hand, in SPAIR, an 180° spectral-selective adiabatic inversion pulse is applied for fat only, followed by a single 90° excitation pulse after a certain TI.[41, 47, 62] The purpose of the adiabatic radio frequency pulse is to reduce the radio frequency amplitude variations, thus mitigating the B1 inhomogeneity and providing more uniform fat suppression than CHESS and STIR, particularly in high-field MRI systems.[41, 47, 56, 58, 61, 62] Overall, perhaps the most obvious advantage of using hybrid methods for fat suppression in breast MRI is their higher SNR, since SPIR and SPAIR are fat-selective techniques.[41, 47]

In the Dixon technique, also known as fat-water separation, two separate images can be produced based on the resonant frequency difference between fat and water, by combining an in-phase and an opposed-phase GRE image at different TEs.[41, 47, 55, 57] As fat and water can be specifically constructed, the sum of the fat and water signals generates a water-only image, while the difference between them generates a fat-only image.[41, 47, 55-60] A significant advantage of the Dixon technique is its lower sensitivity to the B_0 and B_1 inhomogeneity – especially in high-field MRI systems, where the heterogeneity is more pronounced – which enables more uniform fat suppression.[41, 47, 55, 57] In addition, it can be implemented with various pulse sequences in breast imaging.[59] In view of its advantages, fat-water separation is a highly recommended sequence among fat-suppression methods for breast imaging, as it can be used to specifically image the water that corresponds to the FGT, thus allowing an optimal assessment of breast density.[41, 47, 55-60]

1.4 MR Breast Density Segmentation/Measurement Methods

Conventionally, breast density assessment is based on a qualitative approach using the ACR BI-RADS Atlas, which classifies density into four categories based on the amount of FGT.[6, 7] Despite its long clinical success, BI-RADS scores are subjective, resulting in inter- and even intra-reader variability.[63-65] To overcome this issue, several methods and algorithms have been proposed for quantitative breast density assessments.[66-72]

While various definitions of the term "breast density" have been proposed, in this context, the term "fibroglandular tissue" (FGT) is used to refer to breast density. Indeed, breast density is measured as the percentage of FGT volume to the total breast volume.[1-3] Two steps are required to quantify the FGT volume from MRI data: breast segmentation and FGT segmentation.[38, 72] Breast segmentation distinguishes the breast's body from the surrounding tissue, including the pectoral muscle, heart, lungs, and thorax. FGT segmentation distinguishes parenchymal from adipose tissue.[38, 66, 72] Several methods have been developed to segment the FGT in breast MRIs, which can be categorized into four conceptual models: a clustering algorithm, an interactive thresholding algorithm to segment glandular and fatty tissue, a logistic function approach, and a curve-fitting algorithm.[36, 66-72]

Clustering algorithms classify breast regions into clusters/groups displayed in a histogram using a code based on greyscale intensity. As an unsupervised algorithm, each voxel is assigned to a cluster. In other words, all voxels in the segmented breast are assigned a code representing the FGT content with different greyscale tones.[12, 38] An updated version of this algorithm, the fuzzy C-means (FCM) clustering algorithm, is one of the most common methods used to separate FGT from fatty tissue in breast

MRI.[36] It has also been combined with the non-parametric non-uniformity normalization (N3) algorithm for image inhomogeneity and/or bias field correction .[67, 68] The N3 algorithm is used for non-parametric non-uniform intensity normalization to adjust the signal intensity variations within the same structure.[67, 68]

Interactive thresholding algorithms categorize the breast voxels according to a threshold value usually specified by the radiologist. The breast voxels are classified into two groups: voxel values above the threshold correspond to dense tissue, while voxel values below the threshold correspond to fat tissue. Breast density is calculated as the number of voxels in the dense area divided by the total number of voxels across the whole breast region.[70] The logistic function approach, or Bayesian probability, estimates the highest-probability combination of materials within each voxel-sized region. Then, the possible tissue types within each voxel are identified, and continuous ‘‘basis’’ functions are assumed to represent the probability that a particular voxel contains a specific type of tissue.[71]

The curve-fitting algorithm technique compares breast tissue to a mixture model known as the 3D volume-rendered breast model, whereby all MR voxel signal intensities are extracted from the 3D model to generate a signal intensity histogram. On that basis, a two-compartment model of breast tissue compositions can be constructed. The histogram of the MRI signal intensities usually contains two major peaks: one corresponds to adipose tissue, and the other to non-adipose tissue. The sum of voxels represents the FGT.[70]

Each of the aforementioned semi-automatic thresholding and segmentation approaches has its own advantages and limitations in the quantitative assessment of breast density.[66-72] No consensus has been reached about the best method to date.[36]

1.5 3D Printing Technology

The last decade has seen significant advances in 3D printing technology, also known as additive manufacturing, rapid prototyping, or solid freeform fabrication.[73-78] It is used in various medical applications, including cardiovascular disease treatment, orthopaedic surgery, prosthetics, and neurosurgery.[73-78] Prosthetics was the first biomedical field to take advantage of 3D printing, with considerable achievements in terms of improved visualization and surgical outcomes.[79, 80] Patient-specific guides and 3D-printed anatomical models and prostheses derived from either computed tomography (CT) or MRI data have assisted in developing surgical implants, practising procedures, teaching students, and improving the individual's understanding with precise reproductions of complex anatomical structures and pathologies.[73-78, 81, 82] The technology's main advantages are shorter surgical times, reduced radiation exposure, and improved diagnosis and outcomes.[73, 81]

Additive manufacturing can be generally described as the construction of an object's components by placing a material on a certain kind of building platform.[79-82] It starts with a meshed 3D computer model that can be generated through the acquisition of image data and/or structures, mostly designed using computer-aided design (CAD) software.[80-83] Standard Tessellation Language (STL) is the standard file format for storing 3D models.[80-83] The mesh data is further divided into a 2D-layered build file and fed into the 3D printer.[80-83] Various additive manufacturing techniques have been extensively used for fabricating polymer composites and other composite materials, each with its own advantages and disadvantages.[80-83] Multiple factors determine the appropriate additive manufacturing technique, such as raw materials, processing

speed, resolution requirements, costs, and performance specifications of the final product.[80-83]

Additive manufacturing techniques can be classified into three categories: selective binding, selective solidification, and selective deposition.[79, 80, 82] Selective binding technologies render a 3D-printed object from a powder (thermoplastic powders are the most common) using binding agents or heat to bind the powder's particles together.[79, 80] An example is selective laser sintering (SLS), whereby constructive layers of powdered material are fused by a laser.[79-83] The first layer is melted to a base; then, another thin layer is deposited on top of it. The process is repeated until the model construction is complete[79-83]. The powder serves as a print support medium; therefore, highly complex and precise prints can be produced.[79-83] However, fine powders can be difficult to handle, and printers based on the SLS technique are often expensive.[79-83] The resolution of SLS 3D-printing technology is mainly determined by the material's particle size, laser strength, scan spacing, and scanning speed.[80-83]

Selective solidification technologies render a solid object of a liquid vat under a light source (photopolymer resins are the most commonly used materials), where constructive layers of liquid photopolymer resin are solidified using selective energy.[79, 80] The first layer is usually constructed on a kind of building platform that is elevated onto a resin tank, a light source, and galvanometers.[79-86] Examples are stereolithography (SLA), which uses a laser to solidify the resin with ultraviolet (UV) light, and a digital light projection (DLP) imager used to stiffen each layer[79-86]. In both approaches, the mould needs to be cured thereafter, and the resin can be challenging to handle.[79-83] The main benefit of SLA 3D printing is its capability of producing models with high resolution and/or quality.[80-83] Furthermore, as a nozzle-free

technique, it eliminates nozzle clogging.[80-83] Nevertheless, the main disadvantages are its high cost, which can be a significant concern for industrial and medical applications, and its potential cytotoxicity of the uncured resin and the residual photoinitiator.[80-84]

In selective deposition technologies, a layer-by-layer deposition of a molten polymeric material on a building platform is the working concept, whereby a heated nozzle moves at the xyz axis, where layers are fused and then solidified into the final object.[79-85] Thermoplastic filaments are the most commonly used materials owing to their melting temperature.[79-83,85] An example is fused deposition modelling (FDM), also known as fused filament fabrication (FFF).[79, 80] Filament-based printers melt a filament into a semi-liquid and deposit it precisely to create an object [80-83]. Other 3D printers use liquid resin with inkjet, which is then cured with UV light.[83] Some printers combine the selective binding and selective deposition techniques using a powder mixed with a binder.[79-83]

FDM/FFF is one of the most used approaches for rapid prototyping, primarily due to the wide availability of cheap printers with high speed, simplicity, and low operation costs.[80, 81, 84] An important drawback is that the composite materials need to be in a filament shape to facilitate the extrusion process and are limited to thermoplastic polymers with melt viscosity high enough for structural support and low enough to allow extrusion.[80-84] It can thus be difficult to remove the supporting structures when the printing process is completed.[80-84] Comparison of different types of 3D-printing techniques, including their advantages and disadvantages are summarized in Table 1.1.

Table 1.1. Comparison of different types of 3D-printing technologies.[79-86]

Technology	Approach	Principle	Materials	Layer Thickness	Advantages	Disadvantages
SLS	Laser and heat induced sintering.	Localized powder melting.	Thermoplastic powder: Nylon (e.g., PA), steel, titanium, alloys, and ceramic powders.	25-92 µm.	-No requirement of pre-designed support structure. -Good strength of produced parts. -Low UV radiation. -Less post-processing.	-Parts may suffer shrinkage and warpage due to sintering and cooling. -Powder can get into vulnerable areas, inducing health problems. -High cost.
SLA	Laser and UV induced curing.	Localized co-polymerization.	Photopolymer resins (e.g., epoxy or acrylate-based resin), with high-temperature resistant resins.	< 10 µm.	-High resolution. -Nozzle-free technology.	-Cytotoxicity of residual photoinitiator and uncured resin. -Misuse of liquid resins constitutes a risk, and ingestion is hazardous. -Post-processing is required to remove support materials. -High UV radiation. -High cost.
FDM/FFF	Extrusion and deposition.	Liquified polymers using nozzles.	Thermoplastic filament: ABS, PLA, PVA, PC, HIPS, PETG, and Nylon (e.g., PA).	100-250 µm.	-Low cost. -Good strength of produced parts. -Deposition of different materials. -Printed parts are multi-purpose. -No use of UV radiation.	-Low resolution on the z axis relative to other 3D printing technologies. -It may require days to produce through, complicated pieces for a slow operation. -Should be in a filament format. -Homogeneity lack for the disperse material. -A limitation with nozzle clogging. -Post-processing is required to remove support materials.

Abbreviations: SLS: selective laser sintering; SLA: stereolithography; FDM: fused deposition modelling; FFT: fused filament fabrication; PA: polyamide; ABS: acrylonitrile butadiene styrene; PLA: polylactic acid; PVA: polyvinyl alcohol; PC: polycarbonate; HIPS: high impact polystyrene; PETG: polyethylene terephthalate (glycol).

Table 1.1. Continued.[74,80, 82]

Technology	Approach	Principle	Materials	Layer Thickness	Advantages	Disadvantages
PolyJet	Laser and UV induced curing.	Polymerization of deposited droplets of photopolymer ink.	Photopolymer resins.	25-50 µm.	-High resolution. -Good surface finish and smoothness.	-Post-processing is required to remove support materials. -High cost. -Slow speed.
3DP/CJP	Powders and binders.	Drop-on-demand binder printing.	Powder.	100-400 µm.	-Low cost. -Multi-material capability. -Supporting material can be easily removed.	-Clogging of binder jet. -Binder contamination. -Printing resolution is limited.

Abbreviations: 3DP: three-dimensional printing; CJP: colour jet printing.

1.6 MRI Breast Phantom

A breast phantom comparable to the anatomical structures of human tissues can be a valuable tool for examining different breast MRI protocols, test the radio frequency coils, and evaluate system performance.[87-94] Such a phantom should resemble the MR-related characteristics of T1 and T2 relaxation times that are analogous to those of the simulated tissue and load the radio frequency coils electrically as real tissue.[87-94] Further, it should be made from appropriate materials to produce precise shapes and/or sizes of such complex anatomical structures.[87-94] These materials should ideally be affordable, readily accessible, and easy to process.[87-94] More broadly, the phantom should also maintain its chemical and physical characteristics over an extended period.[87-94]

Although several studies have produced anthropomorphic breast phantoms for X-ray imaging, the data available for MR imaging is still insufficient.[88-95] Carton et al[88] used a computational model and a rapid prototyping technique to generate 3D breast phantoms with different compositions, sizes, and shapes made from tissue-equivalent materials for quality assessments of 2D and 3D breast X-ray imaging systems. The epoxy resins used in their study can simulate 100% of the characteristics of adipose tissue, while the FC-270 photopolymer simulates 50% of the properties of fibroglandular tissue.[88] Although this phantom effectively demonstrated a heterogeneous distribution of fibroglandular and adipose tissue that can be analogous to clinical breast images, it has certain limitations in terms of its fabrication method and applications: it is printed in slab form, which is overly complicated and time-consuming to manufacture on its actual format.[88]

Mazzara et al[89] used the polysaccharide material TX-151 with water, sodium chloride (NaCl), and aluminium (Al) powder to create a tissue-mimicking material (TMM) in the form of a gel for constructing a realistic, inexpensive, easily mouldable, and temporally stable tissue-equivalent MRI breast phantom. The Al powder was used to decrease the T2 relaxation time, allowing the adaptation of the phantom to a wide range of relaxation times to simulate various human tissues and organs.[89] In addition, gadolinium-diethylenetriamine penta-acetic acid (Gd-DTPA), a paramagnetic metal complex, was used to adjust the T1 (and T2) relaxation times.[89]

Liney et al[90] designed a simple and an inexpensive tissue-equivalent MRI breast phantom consisting of a layer of lard (a commercially available fat product) simulating adipose tissue, surrounded by a commercial jelly with varying concentrations simulating normal glandular tissue. Both of these phantoms can be used to conduct multipurpose quality assurance tests of such parameters as SNR, uniformity, and resolution, test the radio frequency coils, or examine various MRI diagnostic protocols.[89, 90] Freed et al[91] developed a tissue-equivalent phantom for quantitative assessments of breast MRI protocols using a combination of lard and egg whites to simulate adipose and glandular tissue, respectively. Although the materials successfully simulated the MR-related characteristics of T1 and T2 relaxation times of the tissues, they lack a heterogeneous structure and thus have minimal applicability for quantitative breast density assessment studies.[91]

Although some research has been conducted on the use of 3D printing techniques to develop breast phantoms for MRI, few studies have attempted to generate a personalized 3D-printed phantom based on breast MR images that can be similar to the anatomical structures of human tissues.[88-95] Burfeindt et al[92] reported a convenient

synthetic procedure to develop an MRI-derived 3D-printed phantom for preclinical use in microwave breast imaging experiments. Although it successfully simulated the dielectric properties of biological breast tissues, it was designed for microwave breast imaging rather than for MRI systems.[92]

The importance of realistic phantom structures simulating the acoustic and optical breast tissue properties for the assessment of photoacoustic breast imaging systems was demonstrated by Dantuma et al.[93] In this study, a semi-anthropomorphic 3D-printed mould derived from an MRI segmented numerical breast model was developed using polyvinyl chloride plastisol (PVCP) to imitate real breast morphology.[93] However, there are limits to the extent to which a phantom designed for ultrasound and photoacoustic imaging can be used to simulate the MRI characteristics of breast tissues.[93] He et al[94] developed a 3D-printed breast phantom for machine calibration and image optimization in multi-modality imaging using a mixture of PVC powder and softener (dioctyl terephthalate) as a TMM. Although breast structures were successfully simulated, they lacked the appearance, variability, and heterogeneity of physiological tissue constructions.[94] Another potential limitation is that the materials' T1 and T2 relaxation times were found to be shorter than those reported in human breast tissues.[94, 95]

1.7 References

1. Chen JH, Chang YC, Chang D, Wang YT, Nie K, Chang RF, Nalcioglu O, Huang CS, Su MY. Reduction of breast density following tamoxifen treatment evaluated by 3-D MRI: Preliminary study. Magn Reson Imaging. 2011; 29(1):91–98.
2. Wang J, Azziz A, Fan B, Malkov S, Klifa C, Newitt D, Yitta S, Hylton N, Kerlikowske K, Shepherd JA. Agreement of mammographic measures of volumetric breast density to MRI. PloS ONE. 2013; 8(12):e81653.
3. Tagliafico A, Bignotti B, Tagliafico G, Astengo D, Martino L, Airaldi S, Signori A, Sormani MP, Houssami N, Calabrese M. Breast density assessment using a 3T MRI system: Comparison among different sequences. PLoS ONE. 2014; 9(6):e99027.
4. Lienart V, Carly B, Kang X, Guzy L, Sajovitz AM, Liebens F. Effect of preventive hormonal therapy on breast density: A systematic qualitative review. Sci World J. 2014; 2014.
5. Tagliafico A, Tagliafico G, Astengo D, Airaldi S, Calabrese M, Houssami N. Comparative estimation of percentage breast tissue density for digital mammography, digital breast tomosynthesis, and magnetic resonance imaging. Breast Cancer Res Treat. 2013; 138(1):311–317.
6. American College of Radiology. ACR BI-RADS® Atlas: Breast Imaging Reporting and Data System; American College of Radiology: Reston, VA, USA, 2013.
7. Mainiero MB, Lourenco A, Mahoney MC, Newell MS, Bailey L, Barke LD, D'Orsi C, Harvey JA, Hayes MK, Huynh PT, Jokich PM. ACR appropriateness criteria breast cancer screening. J Am Coll Radiol. 2016; 13(11):45-49.

8. Choi G, Woo OH, Shin HS, Jang S, Cho KR, Seo BK. Comparison of two-dimensional synthesized mammogram (2DSM) and conventional full-field digital mammogram (FFDM) for evaluation of breast cancer. Clin Imaging. 2017; 43:170-174.
9. Park JM, Franken Jr EA, Garg M, Fajardo LL, Niklason LT. Breast tomosynthesis: present considerations and future applications. Radiographics. 2007; 27:S231-S240.
10. Li H, Weiss WA, Medved M, Abe H, Newstead GM, Karczmar GS, Giger ML. Breast density estimation from high spectral and spatial resolution MRI. J Med Imaging. 2016; 3(4):044507.
11. Wu S, Weinstein SP, Conant EF, Kontos D. Automated fibroglandular tissue segmentation and volumetric density estimation in breast MRI using an atlas-aided fuzzy C-means method. Med Phys. 2013; 40(12):122302.
12. Klifa C, Carballido-Gamio J, Wilmes L, Laprie A, Shepherd J, Gibbs J, Fan B, Noworolski S, Hylton N. Magnetic resonance imaging for secondary assessment of breast density in a high-risk cohort. Magn Reson Imaging. 2010; 28(1):8–15.
13. Kolb TM, Lichy J, Newhouse JH. Comparison of the performance of screening, mammography, physical examination and breast US and evaluation of factors that influence them: An analysis of 27,825 patient evaluations. Radiology. 2002; 225(1):165–175.
14. Ding J, Stopeck AT, Gao Y, Marron MT, Wertheim BC, Altbach MI, Galons JP, Roe DJ, Wang F, Maskarinec G, Thomson CA. Reproducible automated breast density measure with no ionizing radiation using fat-water decomposition MRI. Magn Reson Imaging. 2018; 48(4):971–981.

15. Sak MA, Littrup PJ, Duric N, Mullooly M, Sherman ME, Gierach GL. Current and future methods for measuring breast density: A brief comparative review. Breast Cancer Manag. 2015; 4(4):209–221.
16. Pertuz S, McDonald ES, Weinstein SP, Conant EF, Kontos D. Fully automated quantitative estimation of volumetric breast density from digital breast tomosynthesis images: Preliminary results and comparison with digital mammography and MR imaging. Radiology. 2016; 279(1):65-74.
17. Skaane P, Bandos AI, Eben EB, Jebsen IN, Krager M, Haakenaasen U, Ekseth U, Izadi M, Hofvind S, Gullien R. Two-view digital breast tomosynthesis screening with synthetically reconstructed projection images: Comparison with digital breast tomosynthesis with full-field digital mammographic images. Radiology. 2014; 271(3): 655-663.
18. Friedewald SM, Rafferty EA, Rose SL, Durand MA, Plecha DM, Greenberg JS, Hayes MK, Copit DS, Carlson KL, Cink TM, Barke LD. Breast cancer screening using tomosynthesis in combination with digital mammography. JAMA. 2014; 311(24):2499-2507.
19. McCarthy AM, Kontos D, Synnestvedt M, Tan KS, Heitjan DF, Schnall M, Conant EF. Screening outcomes following implementation of digital breast tomosynthesis in a general-population screening program. JNCI. 2014; 106(11):1-7.
20. Zuley ML, Guo B, Catullo VJ, Chough DM, Kelly AE, Lu AH, Rathfon GY, Lee Spangler M, Sumkin JH, Wallace LP, Bandos AI. Comparison of two-dimensional synthesized mammograms versus original digital mammograms alone and in combination with tomosynthesis images. Radiology. 2014; 271(3):664-671.

21. Lång K, Andersson I, Zackrisson S. Breast cancer detection in digital breast tomosynthesis and digital mammography—a side-by-side review of discrepant cases. Br J Radiol. 2014; 87(1040):20140080.
22. Moon WK, Chang JF, Lo CM, Chang JM, Lee SH, Shin SU, Huang CS, Chang RF. Quantitative breast density analysis using tomosynthesis and comparison with MRI and digital mammography. Comput Meth Prog Bio. 2018; 154:99-107.
23. Skaane P, Bandos AI, Gullien R, Eben EB, Ekseth U, Haakenaasen U, Izadi M, Jebsen IN, Jahr G, Krager M, Niklason LT. Comparison of digital mammography alone and digital mammography plus tomosynthesis in a population-based screening program. Radiology. 2013; 267(1):47-56.
24. Jing H, Yang Y, Wernick MN, Yarusso LM, Nishikawa RM. A comparison study of image features between FFDM and film mammogram images. Med Phys. 2012; 39(7Part1):4386-4394.
25. Zanotel M, Bednarova I, Londero V, Linda A, Lorenzon M, Girometti R, Zuiani C. Automated breast ultrasound: Basic principles and emerging clinical applications. Radiol Med. 2018; 123(1):1-12.
26. Moon WK, Shen YW, Huang CS, Luo SC, Kuzucan A, Chen JH, Chang RF. Comparative study of density analysis using automated whole breast ultrasound and MRI. Med Phys. 2011; 38(1):382–389.
27. Chen JH, Lee YW, Chan SW, Yeh DC, Chang RF. Breast density analysis with automated whole-breast ultrasound: Comparison with 3-D magnetic resonance imaging. Ultrasound Med Biol. 2016; 42(5):1211-1220.
28. Giger ML, Inciardi MF, Edwards A, Papaioannou J, Drukker K, Jiang Y, Brem R, Brown JB. Automated breast ultrasound in breast cancer screening of

women with dense breasts: Reader study of mammography-negative and mammography-positive cancers. Am J Roentgenol. 2016; 206(6):1341-1350.

29. Sanabria SJ, Goksel O, Martini K, Forte S, Frauenfelder T, Kubik-Huch RA, Rominger MB. Breast-density assessment with hand-held ultrasound: A novel biomarker to assess breast cancer risk and to tailor screening? Eur Radiol. 2018; 28(8):3165-3175.
30. Guo R, Lu G, Qin B, Fei B. Ultrasound imaging technologies for breast cancer detection and management: A review. Ultrasound Med Biol. 2018; 44(1):37-70.
31. Sardanelli F, Boetes C, Borisch B, Decker T, Federico M, Gilbert FJ, Helbich T, Heywang-Köbrunner SH, Kaiser WA, Kerin MJ, Mansel RE. Magnetic resonance imaging of the breast: Recommendations from the EUSOMA working group. Eur J Cancer. 2010; 46(8):1296–1316.
32. Londero V, Zuiani C, Linda A, Girometti R, Bazzocchi M, Sardanelli F. High-risk breast lesions at imaging-guided needle biopsy: Usefulness of MRI for treatment decision. Am J Roentgenol. 2012; 199(2):W240–W250.
33. Mann RM, Balleyguier C, Baltzer PA, Bick U, Colin C, Cornford E, Evans A, Fallenberg E, Forrai G, Fuchsjäger MH, Gilbert FJ. Breast MRI: EUSOBI recommendations for women's information. Eur Radiol. 2105; 25(12):3669-3678.
34. Heller SL, Yeong Lin LL, Melsaether AN, Moy L, Gao Y. Hormonal Effects on Breast Density, Fibroglandular Tissue, and Background Parenchymal Enhancement. Radiographics. 2018; 38(4):983-996.
35. Bu Y, Xia J, Joseph B, Zhao X, Xu M, Yu Y, Qi S, Shah KA, Wang S, Hu J. Non-contrast MRI for breast screening: Preliminary study on detectability of

benign and malignant lesions in women with dense breasts. Breast Cancer Res Treat. 2019; 177(3):629-639.

36. Sindi R, Sá Dos Reis C, Bennett C, Stevenson G, Sun Z. Quantitative measurements of breast density using magnetic resonance imaging: A systematic review and meta-analysis. J Clin Med. 2019; 8(5):745.
37. An YY, Kim SH, Kang BJ. Differentiation of malignant and benign breast lesions: Added value of the qualitative analysis of breast lesions on diffusion-weighted imaging (DWI) using readout-segmented echo-planar imaging at 3.0 T. PloS ONE. 2017; 12(3):e0174681.
38. Niukkanen A, Arponen O, Nykänen A, Masarwah A, Sutela A, Liimatainen T, Vanninen R, Sudah M. Quantitative volumetric K-means cluster segmentation of fibroglandular tissue and skin in breast MRI. J Digit Imaging. 2018; 31(4):425-434.
39. Ertas G, Doran SJ, Leach MO. A computerized volumetric segmentation method applicable to multi-centre MRI data to support computer-aided breast tissue analysis, density assessment and lesion localization. Med Biol Eng Comput. 2017; 55(1):57-68.
40. Petridou E, Kibiro M, Gladwell C, Malcolm P, Toms A, Juette A, Borga M, Leinhard OD, Romu T, Kasmai B, Denton E. Breast fat volume measurement using wide-bore 3 T MRI: Comparison of traditional mammographic density evaluation with MRI density measurements using automatic segmentation. Clin Radiol. 2017; 72(7):565-572.
41. McRobbie DW, Moore EA, Graves MJ, Prince MR. MRI from Picture to Proton. Cambridge University Press; 2017.

42. Brown MA, Semelka RC, Dale BM. MRI: Basic principles and applications. John Wiley & Sons, Inc; 2015.
43. McDonald ES, Hammersley JA, Chou SH, Rahbar H, Scheel JR, Lee CI, Liu CL, Lehman CD, Partridge SC. Performance of DWI as a rapid unenhanced technique for detecting mammographically occult breast cancer in elevated-risk women with dense breasts. Am J Roentgenol. 2016; 207(1):205-216.
44. Kazama T, Kuroki Y, Kikuchi M, Sato Y, Nagashima T, Miyazawa Y, Sakakibara M, Kaneoya K, Makimoto Y, Hashimoto H, Motoori K. Diffusion-weighted MRI as an adjunct to mammography in women under 50 years of age: An initial study. J Magn Reson Imaging. 2012; 36(1):139-144.
45. Chang DH, Chen JH, Lin M, Bahri S, Yu HJ, Mehta RS, Nie K, Hsiang DJ, Nalcioglu O, Su MY. Comparison of breast density measured on MR images acquired using fat-suppressed versus nonfat-suppressed sequences. Med Phys. 2011; 38(11):5961-5968.
46. Mann RM, Kuhl CK, Kinkel K, Boetes C. Breast MRI: Guidelines from the European society of breast imaging. Eur Radiol. 2008; 18(7):1307-1318.
47. Del Grande F, Santini F, Herzka DA, Aro MR, Dean CW, Gold GE, Carrino JA. Fat-suppression techniques for 3-T MR imaging of the musculoskeletal system. Radiographics. 2014; 34(1):217-233.
48. Harvey JA, Hendrick RE, Coll JM, Nicholson BT, Burkholder BT, Cohen MA. Breast MR imaging artifacts: How to recognize and fix them. Radiographics. 2007; 27:S131-S145.
49. Warren RM, Pointon L, Thompson D, Hoff R, Gilbert FJ, Padhani A, Easton D, Lakhani SR, Leach MO. Reading protocol for dynamic contrast-enhanced

MR images of the breast: Sensitivity and specificity analysis. Radiology. 2005; 236(3):779-788.

50. Mürtz P, Tsesarskiy M, Kowal A, Träber F, Gieseke J, Willinek WA, Leutner CC, Schmiedel A, Schild HH. Diffusion-weighted magnetic resonance imaging of breast lesions: The influence of different fat-suppression techniques on quantitative measurements and their reproducibility. Eur Radiol. 2014; 24(10):2540-2551.
51. Kazama T, Nasu K, Kuroki Y, Nawano S, Ito H. Comparison of diffusion-weighted images using short inversion time inversion recovery or chemical shift selective pulse as fat suppression in patients with breast cancer. Japanese J Radiol. 2009; 27(4):163-167.
52. Baron P, Dorrius MD, Kappert P, Oudkerk M, Sijens PE. Diffusion-weighted imaging of normal fibroglandular breast tissue: Influence of microperfusion and fat suppression technique on the apparent diffusion coefficient. NMR BIOMED. 2010; 23(4):399-405.
53. Poustchi-Amin M, Mirowitz SA, Brown JJ, McKinstry RC, Li T. Principles and applications of echo-planar imaging: A review for the general radiologist. Radiographics. 2001; 21(3):767-779.
54. An YY, Kim SH, Kang BJ. Differentiation of malignant and benign breast lesions: Added value of the qualitative analysis of breast lesions on diffusion-weighted imaging (DWI) using readout-segmented echo-planar imaging at 3.0 T. PloS ONE. 2017; 12(3):e0174681.
55. Ledger AE, Scurr ED, Hughes J, Macdonald A, Wallace T, Thomas K, Wilson R, Leach MO, Schmidt MA. Comparison of Dixon sequences for estimation of percent breast fibroglandular tissue. PLoS ONE. 2016; 11(3):e0152152.

56. Miyazaki M, Wheaton A, Kitane S. Enhanced fat suppression technique for breast imaging. J Magn Reson Imaging. 2013; 38(4):981-986.
57. Kalovidouri A, Firmenich N, Delattre BM, Picarra M, Becker CD, Montet X, Botsikas D. Fat suppression techniques for breast MRI: Dixon versus spectral fat saturation for 3D T1-weighted at 3 T. Radiol Med. 2017; 122(10):731-742.
58. Le-Petross H, Kundra V, Szklaruk J, Wei W, Hortobagyi GN, Ma J. Fast three-dimensional dual echo Dixon technique improves fat suppression in breast MRI. J Magn Reson Inaging. 2010; 31(4):889-894.
59. Dogan BE, Ma J, Hwang K, Liu P, Yang WT. T1-weighted 3D dynamic contrast-enhanced MRI of the breast using a dual-echo Dixon technique at 3 T. J Magn Reson Imaging. 2011; 34(4):842-851.
60. Clauser P, Pinker K, Helbich TH, Kapetas P, Bernathova M, Baltzer PA. Fat saturation in dynamic breast MRI at 3 Tesla: is the Dixon technique superior to spectral fat saturation? A visual grading characteristics study. Eur Radiol. 2014; 24(9):2213-2219.
61. Hendrick RE. Breast MRI: fundamentals and technical aspects. Springer Science & Business Media; 2007.
62. Mamourian AC. Practical MR Physics: And Case File of MR Artefacts and Pitfalls. Oxford University Press; 2010.
63. Timmers JM, van Doorne-Nagtegaal HJ, Verbeek AL, Den Heeten GJ, Broeders MJ. A dedicated BI-RADS training programme: Effect on the inter-observer variation among screening radiologists. Eur Radiol. 2012; 81(9):2184-2188.

64. Lazarus E, Mainiero MB, Schepps B, Koelliker SL, Livingston LS. BI-RADS lexicon for US and mammography: Interobserver variability and positive predictive value. Radiology. 2006; 239(2):385-391.

65. Ciatto S, Houssami N, Apruzzese A, Bassetti E, Brancato B, Carozzi F, Catarzi S, Lamberini MP, Marcelli G, Pellizzoni R, Pesce B. Categorizing breast mammographic density: Intra-and interobserver reproducibility of BI-RADS density categories. The Breast. 2005; 14(4):269-275.

66. Nayeem F, Ju H, Brunder DG, Nagamani M, Anderson KE, Khamapirad T, Lu LJ. Similarity of fibroglandular breast tissue content measured from magnetic resonance and mammographic images and by a mathematical algorithm. Int J Breast Cancer. 2014; 2014:961679.

67. Lin M, Chan S, Chen JH, Chang D, Nie K, Chen ST, Lin CJ, Shih TC, Nalcioglu O, Su MY. A new bias field correction method combining N3 and FCM for improved segmentation of breast density on MRI. Med Phys. 2011; 38(1):5-14.

68. Doran SJ, Hipwell JH, Denholm R, Eiben B, Busana M, Hawkes DJ, Leach MO, Silva ID. Breast MRI segmentation for density estimation: Do different methods give the same results and how much do differences matter? Med Phys. 2017; 44(9):4573-4592.

69. Tagliafico A, Tagliafico G, Tosto S, Chiesa F, Martinoli C, Derchi LE, Calabrese M. Mammographic density estimation: Comparison among BI-RADS categories, a semi-automated software and a fully automated one. The Breast. 2009; 18(1):35-40.

70. Boston RC, Schnall MD, Englander SA, Landis JR, Moate PJ. Estimation of the content of fat and parenchyma in breast tissue using MRI T1 histograms and phantoms. J Magn Reson Imaging. 2005; 23(1):591-599.
71. Lu LJ, Nishino TK, Johnson RF, Nayeem F, Brunder DG, Ju H, Leonard Jr MH, Grady JJ, Khamapirad T. Comparison of breast tissue measurements using magnetic resonance imaging, digital mammography and a mathematical algorithm. Phys Med Biol. 2012; 57(21):6903.
72. Nie K, Chen JH, Chan S, Chau MK, Yu HJ, Bahri S, Tseng T, Nalcioglu O, Su MY. Development of a quantitative method for analysis of breast density based on three-dimensional breast MRI. Med Phys. 2008; 35(12):5253-5262.
73. Matsumoto JS, Morris JM, Foley TA, Williamson EE, Leng S, McGee KP, Kuhlmann JL, Nesberg LE, Vrtiska TJ. Three-dimensional physical modeling: Applications and experience at Mayo Clinic. Radiographics. 2015; 35(7):1989-2006.
74. Sun Z, Lau I, Wong YH, Yeong CH. Personalized three-dimensional printed models in congenital heart disease. J Clin Med. 2019; 8(4):522.
75. Perica E, Sun Z. A systematic review of three-dimensional printing in liver disease. J Digit Imaging. 2018; 31(5):692-701.
76. Sun Z, Liu D. A systematic review of clinical value of three-dimensional printing in renal disease. Quant Imaging Med Surg. 2018; 8(3):311-325.
77. Sun Z. Insights into 3D printing in medical applications. Quant Imaging Med Surg. 2019; 9(1):1-5.
78. Ratinam R, Quayle M, Crock J, Lazarus M, Fogg Q, McMenamin P. Challenges in creating dissectible anatomical 3D prints for surgical teaching. J Anat. 2019; 234(4):419-437.

79. Horvath J. A brief history of 3D printing. In Mastering 3D printing. Apress, Berkeley, CA. 2014; 2014:3-10.
80. Gardan J. Additive manufacturing technologies: State of the art and trends. Int J Prod Res. 2016; 54(10):3118-3132.
81. Tack P, Victor J, Gemmel P, Annemans L. 3D-printing techniques in a medical setting: A systematic literature review. Biom Eng Online. 2016; 15(1):1-21.
82. Wang X, Jiang M, Zhou Z, Gou J, Hui D. 3D printing of polymer matrix composites: A review and prospective. Composites Part B: Engineering. 2017; 110:442-458.
83. Gardan J, Makke A, Recho N. A method to improve the fracture toughness using 3D printing by extrusion deposition. Procedia Structural Integrity. 2016; 2:144-151.
84. Sandeep DC, Chhabra D. Comparison and analysis of different 3D printing techniques. IJLTET. 2017; 8(4-1):264-272.
85. Jasveer S, Jianbin X. Comparison of different types of 3D printing technologies. IJSRP. 2018; 8(4):1-9.
86. Macdonald E, Salas R, Espalin D, Perez M, Aguilera E, Muse D, Wicker RB. 3D printing for the rapid prototyping of structural electronics. IEEE. 2014; 2:234-242.
87. Freed M, Badal A, Jennings RJ, de las Heras H, Myers KJ, Badano A. X-ray properties of an anthropomorphic breast phantom for MRI and x-ray imaging. Phys Med Biol. 2011; 56(12):3513-3533.
88. Carton AK, Bakic P, Ullberg C, Derand H, Maidment AD. Development of a physical 3D anthropomorphic breast phantom. Med Phys. 2011; 38(2):891-896.

89. Mazzara GP, Briggs RW, Wu Z, Steinbach BG. Use of a modified polysaccharide gel in developing a realistic breast phantom for MRI. Magn Reson Imaging. 1996; 14(6):639-648.
90. Liney GP, Tozer DJ, Turnbull LW. A simple and realistic tissue-equivalent breast phantom for MRI. J Magn Reson Imaging. 1999;10(6):968-971.
91. Freed M, de Zwart JA, Loud JT, El Khouli RH, Myers KJ, Greene MH, Duyn JH, Badano A. An anthropomorphic phantom for quantitative evaluation of breast MRI. Med Phys. 2011; 38(2):743-753.
92. Burfeindt MJ, Colgan TJ, Mays RO, Shea JD, Behdad N, Van Veen BD, Hagness SC. MRI-derived 3-D-printed breast phantom for microwave breast imaging validation. IEEE ANTENN WIREL PR. 2012; 11:1610-1613.
93. Dantuma M, van Dommelen R, Manohar S. Semi-anthropomorphic photoacoustic breast phantom. Biomed Opt Express. 2019; 10(11):5921-5939.
94. He Y, Liu Y, Dyer BA, Boone JM, Liu S, Chen T, Zheng F, Zhu Y, Sun Y, Rong Y, Qiu J. 3D printed breast phantom for multi-purpose and multi-modality imaging. Quant Imaging Med Surg. 2019; 9(1):63-74.
95. He Y, Qin S, Dyer BA, Zhang H, Zhao L, Chen T, Zheng F, Sun Y, Shi L, Rong Y, Qiu J. Characterizing mechanical and medical imaging properties of polyvinyl chloride-based tissue-mimicking materials. J Appl Clin Med Phys. 2019; 20(7):176-183.

2. Chapter 2

Quantitative Measurements of Breast Density Using Magnetic Resonance Imaging: A Systematic Review and Meta-Analysis

2.1 Abstract

Breast density, a measure of dense fibroglandular tissue relative to non-dense fatty tissue, is confirmed as an independent risk factor of breast cancer. Although there has been an increasing interest in the quantitative assessment of breast density, no research has investigated the optimal technical approach of breast MRI in this aspect. Therefore, we performed a systematic review and meta-analysis to analyze the current studies on quantitative assessment of breast density using MRI and to determine the most appropriate technical/operational protocol. Databases (PubMed, EMBASE, ScienceDirect, and Web of Science) were searched systematically for eligible studies. Single arm meta-analysis was conducted to determine quantitative values of MRI in breast density assessments. Combined means with their 95% confidence interval (CI) were calculated using a fixed- effect model. In addition, subgroup meta-analyses were performed with stratification by breast density segmentation/measurement method. Furthermore, alternative groupings based on statistical similarities were identified via a cluster analysis employing study means and standard deviations in a Nearest Neighbor/Single Linkage. A total of 38 studies matched the inclusion criteria for this systematic review. Twenty-one of these studies were judged to be eligible for meta-analysis. The results indicated, generally, high levels of heterogeneity between study means within groups and high levels of heterogeneity between study variances within groups. The studies in two main clusters identified by the cluster analysis were also subjected to meta-analyses. The review confirmed high levels of heterogeneity within the breast density studies, considered to be due mainly to the applications of MR breast-imaging protocols and the use of breast density segmentation/measurement methods. Further research should be performed to determine the most appropriate protocol and method for quantifying breast density using MRI.

Keywords Magnetic resonance imaging; breast density; fibroglandular-tissue; systematic review and meta-analysis; cluster analysis; segmentation; FCM; breast-imaging protocol; non-contrast- enhanced T1-weighted

2.2 Introduction

Breast density, a measure of dense fibroglandular tissue relative to non-dense fatty tissue, is an independent risk factor for breast cancer.[1–3] Consistent with this risk relationship, women who have dense breasts have a likelihood of developing breast cancer that is fourfold higher than those with fatty breasts.[4,5] Most of the information regarding breast density has been acquired with two- dimensional imaging, which is mammography. However, the evaluation of breast density based on mammograms is limited due to the overlapping of tissues, variations in breast compression, and inappropriate positioning that lead to artefacts (skin folder) and inclusion of insufficient breast tissue.[6,7] These factors could affect mammography's performance for precise, reliable measurements of small changes in breast density over brief timespans.[8,9]

Magnetic resonance imaging (MRI), an alternative imaging modality in breast imaging can estimate the actual breast density value because it provides a three-dimensional volume assessment of breast tissue, with excellent contrast resolution in the differentiation between fibroglandular and fatty tissues.[10–13] Conventionally, breast density is assessed qualitatively using the American College of Radiology (ACR) Breast Imaging-Reporting and Data System (BI-RADS) atlas, which is a classification system commonly used for mammography, according to which density has four categories based on the amount of fibroglandular tissue: "(1) almost entirely fat, (2) scattered fibroglandular tissue, (3) heterogeneous fibroglandular dense and (4)

extreme fibroglandular tissue".[14,15] The interpretations of these four categories are also applied for MRI. Despite its long clinical success, the BI-RADS scoring atlas is subjective and varies between readers, even within the same reader.[16] To overcome a subjective assessment of breast density and to reduce inter- and intra- reader variability, different methods for quantitative breast density have been proposed, with a range of algorithms or methods reported in the literature.[17–22] Each of these methods were shown to have advantages and limitations through the use of semi-automatic thresholding and segmentation approaches for quantitative assessment of breast density.

There is no doubt that MRI is one of the most useful modalities for breast imaging and that the analysis of breast density in quantitative synthesis is a well-established approach. In spite of the fact that extensive research has been carried out on breast density measurements, no consensus has been reached about the optimal approach to quantify breast density using MRI. Therefore, the purpose of this review is to analyze the current methods for the quantitative assessment of breast density using MRI over the past decade of publications. Due to the expected heterogeneity of MRI scanning protocols, both systematic review and meta-analysis were performed to analyze the available studies.

2.3 Materials and Methods

This systematic review and meta-analysis were performed according to the Preferred Reporting Items for Systematic Reviews and Meta-Analysis (PRISMA) criteria.[23,24] No ethics committee approval was required.

2.3.1 Search Strategy and Eligibility Criteria

A systematic literature review was conducted of studies that analyzed breast density in a quantitative pattern using MRI. Briefly, a search for studies published between 1 January 2009 and 31 December 2018 was conducted in different databases: PubMed (MEDLINE, U.S. National Library of Medicine and National Institutes of Health, Bethesda, MD, USA), EMBASE (Elsevier, Amsterdam, The Netherlands), ScienceDirect (Elsevier, Amsterdam, The Netherlands), and Web of Science (Clarivate Analytics, Philadelphia, PA, USA) using the search terms detailed below.

Systematic search expressions were employed using MeSH (medical subject headings) in PubMed and the thesaurus in EMBASE, ScienceDirect, and Web of Science. A search structure was based on combining three main terms as follows: "breast density," "quantitative analysis," and "MRI." The exact search expressions were "Breast Density" (MeSH term) OR "fibroglandular tissue" (Text word) OR "breast densit*" (Text word) OR "FGT" (Text word) OR "FT" (Text word) OR "fibroglandular densit*" (Text word) AND "Quantitative analysis" (Subject heading) AND "Magnetic Resonance Imaging" (MeSH term) OR "nuclear magnetic resonance imaging" (Text word) OR "MRI" (Text word) OR "magnetic resonance imaging" (Text word). The criteria for selecting the studies for eligibility were based on their title, abstract, and subsequently the full text, this was performed independently by two reviewers (R.S. and Z.S.). Studies addressing the quantitative analysis of breast density using MRI were considered eligible for inclusion and also studies on human subjects since 2009 had to be published in peer-reviewed journals and written in English. For study inclusion, the subjects must have undergone breast MRI studies and the breast density measurement method is known. Eligible studies were retrieved, and full manuscripts

were read. No restricted conditions have been applied in terms of study characteristics, the purpose of study, and the results. Publications were only included in the analysis if the measurement of breast density had been performed in a quantitative manner regardless of the MRI technique or breast density segmentation/measurement method.

2.3.2 Data Extraction

On completing the eligibility screening, the process of data extraction from the included studies was carried out manually by the same two reviewers. Descriptive data were extracted for all variables as follows: the first author's surname; year of publication; journal of publication; study type; total number of participants/patients; mean age; age range of participants/patients; MRI technique (pulse sequence/breast-imaging protocol and static magnetic field strength); and breast segmentation/measurement method. For each study analyzed, estimates of breast volume, fibroglandular-tissue volume and percentage breast density were recorded using descriptive statistics, arithmetic means and standard deviations, whenever appropriate. Due to the heterogeneous nature of this analysis, some of the included studies produced their results in a median and interquartile range (IQR). Accordingly, the researchers decided to stratify results and excluded them from the meta-analysis only.

2.3.3 Data Synthesis

The combinations of MRI techniques and the applied breast segmentation/measurement methods encountered in the studies were considered to be technologically heterogeneous. To address this issue and acquire more reasonable estimates, the analyses were stratified by breast segmentation method into three

discrete groups (fuzzy c-mean clustering (FCM), FCM and nonparametric nonuniformity normalization (N3), and signal intensity thresholding). In each sub meta-analysis, the number of the included studies were selected on the basis of a degree of homogeneity of their breast density segmentation/measurement results.

2.3.4 Statistical Analysis

The measurement of breast density as ascertained by MRI using semi- or fully-automated segmentation method was assessed. The primary outcome was the percentage breast density (%BD). Data input for each study within a group consisted of the study size (N), the 'raw' study mean (i.e., with no re-scaling or standardization), and the study standard deviation. The data was analyzed by the "metamean" function in the "meta" package in the R system, Version 3.4.1 (http://www.r- project.org/). This facilitates the meta-analysis of a single arm trial, as opposed to the traditional two arm trial with a control group and a treatment group, equivalent to a one-way analysis of variance. A forest plot was generated, displaying the individual study (%BD) means with 95% confidence interval (CI) limits, inverse variance study weights, and the pooled mean and confidence limits. Heterogeneity of study means was assessed using Cochran's Q-test, and heterogeneity of study variances was assessed with Bartlett's test. A conclusion to pool studies requires both heterogeneity tests to be non-significant at the 5% level.

As an alternative to grouping the studies on a technological basis, a cluster analysis was run to investigate any similarities between studies with respect to two attributes, namely study mean and study standard deviation. The International Business Machines Statistical Package for the Social Sciences (IBM SPSS) Statistics software Version 25.0 was used for cluster analysis. The procedure provides for a wide selection

of combinations of distance measures and clustering methods, but for the current application, the simplest of these was chosen, namely Euclidean distance and nearest neighbor agglomeration. This algorithm calculates a proximity matrix of distances between all possible pairs of studies and allocates the closest pair into a cluster, then examines the remaining clusters to identify which is the next nearest or whether there is a pair that are closer to one another, and so on.

2.4 Results

2.4.1 Literature Search

Figure 2.1 presents an overview of the systematic search of the literature through different databases. The complete search yielded 941 studies. After removing duplicates (n = 70), 871 were screened, based on their titles, which resulted in 765 being excluded, followed by 27 of the remaining studies being excluded on the basis of their abstracts. Of the remaining 79 studies, the full manuscript was retrieved and reviewed. Forty-one studies did not meet the selection inclusion criteria: no adequate breast density data (n = 20), qualitative analysis (n = 12), editorials (n = 4), conference abstracts (n = 3), post-mortem study (n = 1), and phantom study (n = 1). Finally, 38 studies attained the inclusion criteria[1–3,5,11,25–57] and were included in the analysis as shown in Table 2.1.

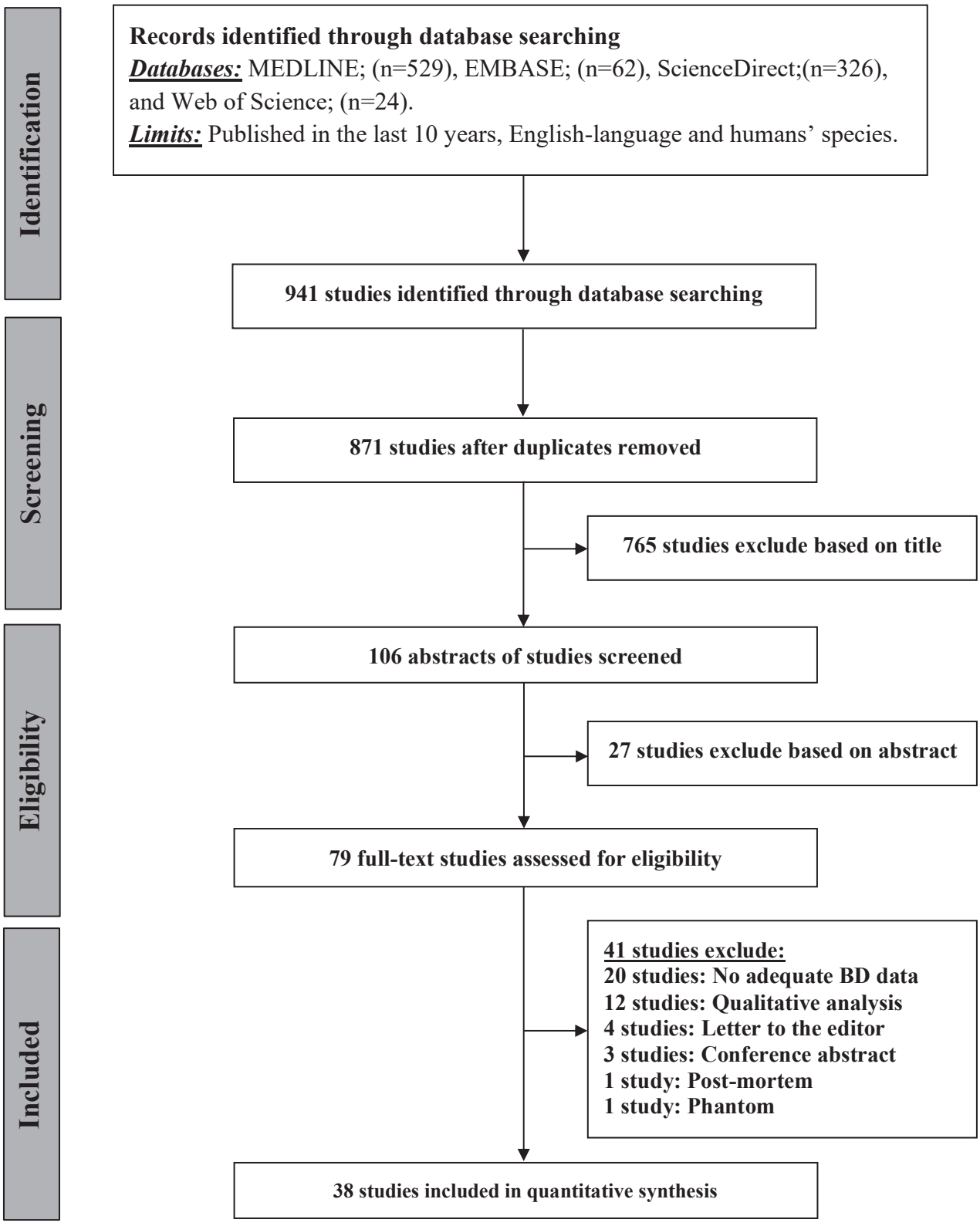

Figure 2.1. Preferred reporting items for systematic review and meta-analysis (PRISMA) flowchart of systematic review and meta-analysis of the excluded and included studies.

2.4.2 Systematic Search

Table 2.1 demonstrates some of the main characteristics of the 38 included studies, while Figure 2.2 shows details of the study design and MRI system used in these studies. Several MRI sequences were used to enable the precise differentiation between adipose and fibroglandular tissues; of these, non- contrast-enhanced T1-weighted was widely used either with 2D spin echo or 3D gradient echo. In fact, 16 studies (41.03%) used non-contrast-enhanced T1-weighted,[1,2,26–29,31,33,35,44,45,48–51,53] while in 12 studies (30.77%) non-contrast-enhanced images were integrated with contrast-enhanced images.[25,36–44,47,49] In terms of breast density segmentation/measurement, the majority of the studies (20 studies; 51.28%) used FCM clustering algorithm,[1,2,11,25–29,31–42] while 7 studies (17.95%) used FCM and N3 algorithm,[45–51] 4 studies (10.26%) interactive thresholding algorithm,[3,5,52,53] 4 studies (10.26%) in-house customized software,[29,53–55] one study (2.56%) manual software;[57] however, two studies did not provide the information.[43,44]

Among the thirty-eight studies included in the systematic review and meta-analysis, 21 studies qualified for meta-analysis since they reported the percent breast density using an identical expression of measurement and dispersion (Table 2.1).[1,3,11,25–32,36–38,45,48–50,53–55] However, for the remaining 17 studies, the percent breast density was reported in different format: in eight of these studies, it was defined as a median and interquartile range (IQR),[2,39–44,47] and in the other nine, it was reported either in different measurement unit or the subject's sets were not independent, due to multiple usage.[5,33–35,46,51,52,56,57] To perform the meta-analysis precisely, all the measured quantities should be reported in an identical expression of measurement and dispersion, thus we decided to exclude them from the meta-analysis.

Table 2.1. Characteristics of the included studies in the systematic review and meta-analysis.

Author, year of publication [Reference]	Study design	Study participants	Age range, average (Years) or Mean ± SD	MR Scanner Manufacturer, Field Strength (Tesla, T)	MRI Sequence	Orientation, Slice #	TR/TE (ms)	FOV (cm)	Slice Thickness (mm)	Matrix size	Flip angle (°)	Breast coil	Segmentation method
Chang, 2011 [25]	NA	38	(28-82), 48	Philips, 3.0	Fat-suppressed 3D SPAIR	Axial, 160	6.20/1.26	(3.01-38.0)	1.0	480×480	12	NA	FCM
					Non-fat-suppressed 2D TSE	Axial, 84	800/8.6	(31.0-38.0)	2.0	480×480	90	NA	
Nie, 2010 [26]	NA	230	50±11.0	Philips, 1.5	Non-fat-suppressed 3D SGRE (T1W)	Axial, 32	8.1/4.0	(31.0-38.0)	4.0	256×256	20	NA	FCM
Pertuz, 2016 [27]	Retro.	68	(24-82), 52	Siemens, 1.5	Non-fat-suppressed (T1W)	NA	NA	NA	(2.4-3.5)	512×512	NA	NA	FCM
Moon, 2018 [28]	Retro.	89	51.81±11.08	GE, 1.5	Non-fat-suppressed (T1W)	Axial	6.2/2.1	20.0	1.0	512×217	NA	NA	FCM
Chen, 2010 [29]	Retro.	35	(30-74), 47	Philips, 1.5	Non-fat-suppressed 3D SGRE (T1W)	Axial, 32	8.1/4.0	38.0	(3.0-4.0)	256×128	20	Dedicated 4-channel phased array	FCM
Chen, 2016 [31]	NA	23	40.5±8.2	Philips, 3.0	Non-fat-suppressed 2D TSE (T1W)	Axial, 90	654/9.0	33.0	2.0	328×384	NA	NA	FCM
Moon, 2011 [32]	Retro.	40	50.9±9.4	GE, 1.5	Fat-suppressed 3D VIBRANT (T1W)	Sagittal, 144-192	6.1/2.5	19.0	1.5	512×512	NA	NA	FCM

Table 2.1. Continued.

Author, Year [Reference]	Study design	Subject number	Age range, average (Years) or Mean ± SD	MR Scanner Manufacturer, Field Strength (Tesla, T)	MRI Sequence	Orientation, Slice #	TR/TE (ms)	FOV (cm)	Slice Thickness (mm)	Matrix size	Flip angle (°)	Breast coil	Segmentation method
Klifa, 2010 [11]	Retro.	35	(28-59), 43	GE, 1.5	Fat-suppressed 3D Fast GRE (T1W)	Axial, 60	8.0/4.2	NA	2.0	NA	20	Dedicated bilateral phased array	FCM
Chen, 2011 [1]	Retro.	16	(33-51), 43	GE, 1.5	Non-fat-suppressed 3D (T1W)	Axial, 56	7.4/3.3	30	2.0	512×512	NA	Dedicated 8-channel bilateral	FCM
Nie, 2010 [33]	NA	50	NA	Philips, 1.5	Non-fat-suppressed 3D GRE (T1W)	Axial, 32	8.1/4.0	38.0	4.0	256×128	NA	NA	FCM
Kim, 2014 [34]	Retro.	80	(27-68), 44	GE, 1.5	Fat-suppressed 2D FSE (T2W)	Sagittal	5500-7150/82	20.0	1.5	256×160	NA	Dedicated 8-channel bilateral	FCM
					Fat-suppressed 3D Fast SGRE (T2W)	Sagittal	6.2/2.5	20.0	1.5	256×160	10	Dedicated 8-channel bilateral	
Nie, 2010 [35]	NA	321	(25-84), 54	Philips, 1.5	Non-fat-suppressed 3D SGRE (T1W)	Axial, 32	8.1/4.0	(32.0-38.0)	4.0	256×128	20	Dedicated 4-channel phased-array	FCM
Wang, 2013 [2]	Retro.	99	47.2±12.1	GE, 1.5/3.0	Non-fat-suppressed (T1W)	Axial	NA	NA	2.0	NA	NA	Dedicated bilateral phased-array	FCM
Bertrand, 2015 [36]	Pros.	182	(25-29)	NA, 1.5/3.0	Non-fat- & fat-suppressed 3D Fast GRE (T1W)	Axial & Coronal	NA	(32.0-40.0)	NA	NA	NA	Dedicated RF coil	FCM

Table 2.1. Continued.

Author, Year [Reference]	Study design	Subject number	Age range, average (Years) or Mean ± SD	MR Scanner Manufacturer, Field Strength (Tesla, T)	MRI Sequence	Orientation, Slice #	TR/TE (ms)	FOV (cm)	Slice Thickness (mm)	Matrix size	Flip angle (°)	Breast coil	Segmentation method
Bertrand, 2016 [37]	Pros.	172	(25-29)	NA, 1.5/3.0	Non-fat- & fat-suppressed 3D Fast GRE (T1W)	NA	NA	(32.0-40.0)	NA	NA	NA	Dedicated RF coil	FCM
Dorgan, 2012 [38]	NA	174	(25-29)	NA, 1.5/3.0	Non-fat- & fat-suppressed 3D Fast GRE (T1W)	Axial & Coronal	NA	(32.0-40.0)	NA	NA	NA	Dedicated RF coil	FCM
Gabriel, 2013 [39]	NA	182	(25-29)	NA, 1.5/3.0	Non-fat- & fat-suppressed 3D Fast GRE (T1W)	Axial & Coronal	NA	(32.0-40.0)	NA	NA	NA	Dedicated RF coil	FCM
Jung, 2015 [40]	Pros.	180	(25-29)	NA, 1.5/3.0	Non-fat- & fat-suppressed 3D Fast GRE (T1W)	Axial & Coronal	NA	(32.0-40.0)	NA	NA	NA	Dedicated RF coil	FCM
Jung, 2016 [41]	Pros.	177	(25-29)	NA, 1.5/3.0	Non-fat- & fat-suppressed 3D Fast GRE (T1W)	Axial & Coronal	NA	(32.0-40.0)	NA	NA	NA	Dedicated RF coil	FCM
Dorgan, 2013 [42]	C.S.	176	(27.0-27.3), 27.2	NA, 1.5/3.0	Non-fat- & fat-suppressed 3D Fast GRE (T1W)	Axial & Coronal	NA	(32.0-40.0)	NA	NA	NA	Dedicated RF coil	FCM
Jung, 2015 [43]	Pros.	177	(25-29)	NA, 1.5/3.0	Non-fat- & fat-suppressed 3D Fast GRE (T1W)	Axial & Coronal	NA	NA	NA	NA	NA	Dedicated RF coil	NA

Table 2.1. Continued.

Author, Year [Reference]	Study design	Subject number	Age range, average (Years) or Mean ± SD	MR Scanner Manufacturer, Field Strength (Tesla, T)	MRI Sequence	Orientation, Slice #	TR/TE (ms)	FOV (cm)	Slice Thickness (mm)	Matrix size	Flip angle (°)	Breast coil	Segmentation method
Jones, 2015 [44]	C.S.	172	(25-29)	NA, 1.5/3.0	Non-fat- & fat-suppressed 3D Fast GRE (T1W)	Axial & Coronal	NA	NA	NA	NA	NA	Dedicated RF coil	NA
Chen, 2012 [45]	NA	34	(20-64), 35	GE, 1.5	Non-fat-suppressed 2D FSE (T1W)	Axial	607/9.0	38.0	2.0	256×192	NA	Dedicated 8-channel bilateral	FCM & N3
				GE, 3.0	Non-fat-suppressed 2D FSE (T1W)	Axial	650/9.0	38.0	2.0	256×192	NA	Dedicated 8-channel bilateral	
				Philips, 3.0	Non-fat-suppressed 2D FSE (T1W)	Axial	650/9.0	33.0	2.0	328×384	NA	Dedicated 16-channel bilateral	
				Siemens, 1.5	Non-fat-suppressed 2D FSE (T1W)	Axial	650/9.8	33.0	2.0	330×384	20	Dedicated 4-channel bilateral	
Chen, 2015 [46]	NA	32	(22-53), 41	Siemens, 1.5	Non-fat-suppressed 2D FSE (T1W)	Axial	650/9.8	33.0	2.0	256×256 & 512×512	NA	Dedicated 4-channel bilateral	FCM & N3
Chen, 2013 [47]	NA	44	(28-82), 47	Philips, 3.0	Non-fat-suppressed 2D TSE (T1W)	Axial	800/8.6	(31.0-38.0)	2.0	480×480	90	Dedicated 4-channel bilateral	FCM & N3
					Fat-suppressed 3D GRE (T1W)	Axial	6.2/1.26	(31.0-36.0)	2.0	480×480	12	Dedicated 4-channel bilateral	

Table 2.1. Continued.

Author, Year [Reference]	Study design	Subject number	Age range, average (Years) or Mean ± SD	MR Scanner Manufacturer, Field Strength (Tesla, T)	MRI Sequence	Orientation, Slice #	TR/TE (ms)	FOV (cm)	Slice Thickness (mm)	Matrix size	Flip angle (°)	Breast coil	Segmentation method
Chan, 2011 [48]	NA	30	Pre:(N=24) (23-48), 29 Post:(N=6) (51-61), 57	Siemens, 1.5	Non-fat-suppressed 3D GRE (T1W)	Axial	11/4.7	35.0	2.0	256×256	20	4-channel dual-mode	FCM & N3
Choi, 2017 [49]	Retro.	38	(32-79), 45	Philips, 3.0	Non-fat-suppressed SE (T2W)	Axial	620/10	(20.0-34.0)	3.0	332×332	NA	Dedicated 7-channel bilateral	FCM & N3
					STIR & SE-EPI (DW)	Axial	3265/54	35.0	4.0	288×288	90	Dedicated 7-channel bilateral	
Chen, 2013 [50]	NA	24	(23-48), 29	Siemens, 1.5	Non-fat-suppressed 3D Fast GRE (T1W)	Axial	11/4.7	35.0	2.0	256×256	20	4-channel dual-mode	FCM & N3
Clendenen, 2013 [51]	NA	9	(24-31)	Siemens, 3.0	Non-fat-suppressed 3D VIBE (T1W)	Axial	4.19/1.62	26.9× 20.2× 28.8	0.6×0.6×1	448×336 ×288	12	Dedicated 7-channel bilateral	FCM & N3
					3-Point Dixon Non-fat-suppressed 3D FLASH (T1W)	Axial	7.6/3.37, 4.17. 4.96	NA	0.88×0.88× 1.5	NA	10	Dedicated 7-channel bilateral	
McDonald, 2014 [52]	Retro.	103	47 ± 11	Philips, 3.0	EPI-Parallel Imaging (DWI)	NA	5336/61	36.0	5.0	240×240	NA	Dedicated 16 channel bilateral	Semi-automated Interactive Threshold

Table 2.1. Continued.

Author, Year [Reference]	Study design	Study participants	Age range, average (Years) or Mean ± SD	MR Scanner Manufacturer, Field Strength (Tesla, T)	MRI Sequence	Orientation, Slice #	TR/TE (ms)	FOV (cm)	Slice Thickness (mm)	Matrix size	Flip angle (o)	Breast coil	Segmentation method
Tagliafico, 2013 [5]	Pros.	48	(35-67), 41	GE, 3.0	3D Fast SGRE & VIBRANT (T1W)	NA	6.2/3.0	NA	NA	350×350	10	Dedicated 8-channel bilateral	Semi-automated Interactive Threshold
					IDEAL	NA	4380/130.872	NA	NA	360×360	90	Dedicated 8-channel bilateral	
Tagliafico, 2014 [3]	NA	48	(35-67), 41	GE, 3.0	TSE (T1W)	NA	600/9.0	NA	4.0	350×350	90	Dedicated 8-channel bilateral	Semi-automated Interactive Threshold
					TSE (T2W)	NA	5200/103	NA	4.0	350×350	90	Dedicated 8-channel bilateral	
					VIBRANT	NA	6.2/3.0	NA	1.2	350×350	10	Dedicated 8-channel bilateral	
					IDEAL	NA	4380/130	NA	1.2	360×360	90	Dedicated 8-channel bilateral	
Chen, 2013 [53]	NA	24	(23-48), 29.4	Siemens, 1.5	Non-fat-suppressed 3D GRE (T1W)	Axial	11/4.7	35.0	2.0	256×256	20	NA	Semi-automated Interactive Threshold
Ha, 2016 [30]	Fe.	60	54.2	GE, 1.5/3.0	Fat-suppressed Fast SGRE (T1W)	Axial	17/2.4	(18.0-22.0)	2.0	256×192	35	8-channel breast array	Semi-automated (In-house software)

Table 2.1. Continued.

Author, Year [Reference]	Study design	Study participants	Age range, average (Years) or Mean ± SD	MR Scanner Manufacturer, Field Strength (Tesla, T)	MRI Sequence	Orientation, Slice #	TR/TE (ms)	FOV (cm)	Slice Thickness (mm)	Matrix size	Flip angle (°)	Breast coil	Segmentation method
Lodger, 2016 [54]	NA	10	(23-50), 31	Siemens, 1.5	HR/LR 3D GRE (PDW)	Axial	7.34/4.77, 2.39	NA	NA	NA	4	Sentinelle variable coil geometry	Semi-automated (In-house software)
					HR/LR 3D GRE (T1W)	Axial	7.34/4.77, 2.39	NA	NA	NA	25	Sentinelle variable coil geometry	
					LR 2D SE (T1W)	Axial	500/12	NA	7.0	NA	NA	Sentinelle variable coil geometry	
Wengert, 2015 [55]	Pros.	43	(21-71), 38	Siemens, 3.0	Dixon	Axial, 192	NA/6.0, 2.45, 2.67	NA	NA	352×352	6	Dedicated 4-channel bilateral	Fully-automated (AUQV)
O'Flynn, 2014 [56]	Retro.	33	(N=17): (33-49), 43 (N=16): (27-49), 40	Siemens, 1.5	Fat-suppressed SS-EPI (DWI)	Axial	6300/83	34.0	5.0	NA	NA	Dedicated 4-channel bilateral	Dedicated IDL based software for ADC calculation
Kim, 2016 [57]	Pros.	57	(32-74), 50.8	Siemens, 3.0	Fat-suppressed TSE (T2W)	Sagittal	7623/91	22×22	3.0	320×246	NA	Dedicated 4-breast array	Manually
					Fat-suppressed SS-EPI (DWI)	Axial	5200/74	340×179	5.0	80×190	NA	Dedicated 4-breast array	

Table 2.1. Continued.

Author, Year [Reference]	Study design	Study participants	Age range, average (Years) or Mean ± SD	MR Scanner Manufacturer, Field Strength (Tesla, T)	MRI Sequence	Orientation, Slice #	TR/TE (ms)	FOV (cm)	Slice Thickness (mm)	Matrix size	Flip angle (o)	Breast coil	Segmentation method
Kim, 2016 [57]	Pros.	57	(32-74), 50.8	Siemens, 3.0	Fat-suppressed 3D FLASH (T1W)	Sagittal	4.5/1.6	22×22	2.0	352×292	20	Dedicated 4-breast array	Manually

Abbreviations: Ret.: retrospective; Pros.: prospective; C.S.: cross-sectional; F.: feasibility; Pre.: pre-menopausal; Post.: post-menopausal; T1W: T1-weighted; T2W: T2-weighted; SPAIR: spectral attenuated inversion recovery; TSE: turbo spin-echo; SGRE: spoiled gradient-echo; VIBRANT: volume image breast assessment; GRE: gradient-echo; FSE: fast spin-echo; STIR: short-TI inversion recovery; DWI: diffusion-weighted imaging; VIBE: volumetric interpolated breath-hold examination; FLASH: fast low angle shot; IDEAL: iterative decomposition of water and fat with echo asymmetry and least squares estimation; HR: high-resolution; LR: low-resolution; PDW: proton density-weighted; SS-EPI: single shot- echo-planar imaging; FCM: fuzzy c-mean clustering algorithm; N3: non-parametric non-uniformity normalization; AUQV: automated user-independent quantitative volumetric

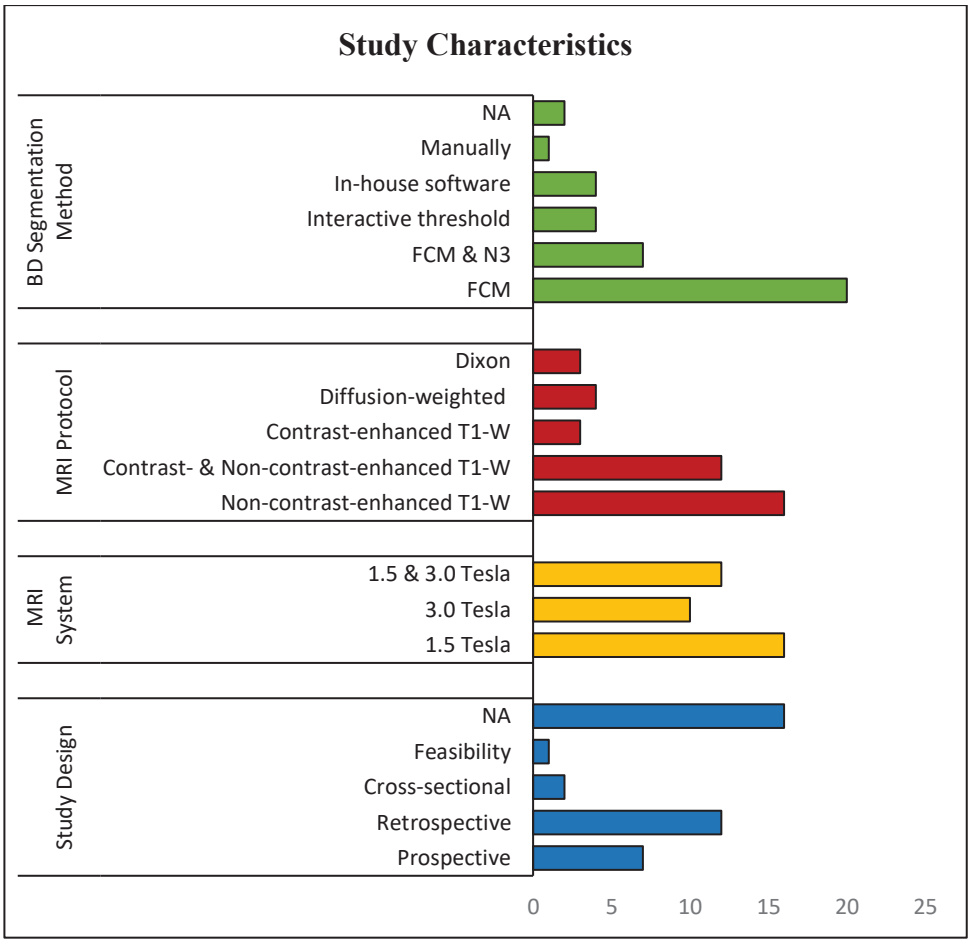

Figure 2.2. Flowchart of the study characteristics (study design, MRI system, MRI sequence, breast density (BD) segmentation method) of 38 studies.

2.4.3 Subgroup Analyses

The final inclusion consisted of a total of twenty-one studies in the meta-analyses; the forest plots and pooled results are shown in Figure 2.3.

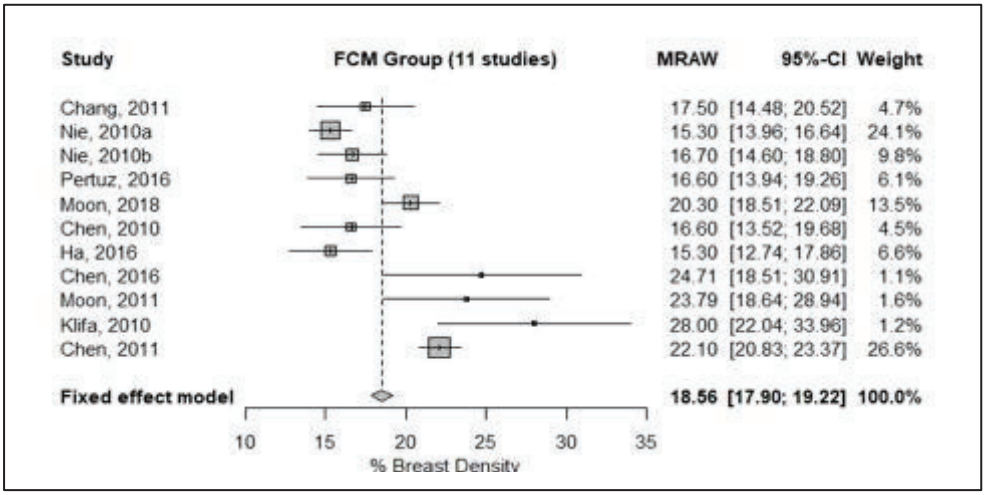
Study
FCM Group (11 studies)
MRAW
95%-CI
Weight
Chang, 2011 17.50 [14.48; 20.52] 4.7%
Nie, 2010a 15.30 [13.96; 16.64] 24.1%
Nie, 2010b 16.70 [14.60; 18.80] 9.8%
Pertuz, 2016 16.60 [13.94; 19.26] 6.1%
Moon, 2018 20.30 [18.51; 22.09] 13.5%
Chen, 2010 16.60 [13.52; 19.68] 4.5%
Ha, 2016 15.30 [12.74; 17.86] 6.6%
Chen, 2016 24.71 [18.51; 30.91] 1.1%
Moon, 2011 23.79 [18.64; 28.94] 1.6%
Klifa, 2010 28.00 [22.04; 33.96] 1.2%
Chen, 2011 22.10 [20.83; 23.37] 26.6%
Fixed effect model 18.56 [17.90; 19.22] 100.0%
10 15 20 25 30 35
% Breast Density

(A)

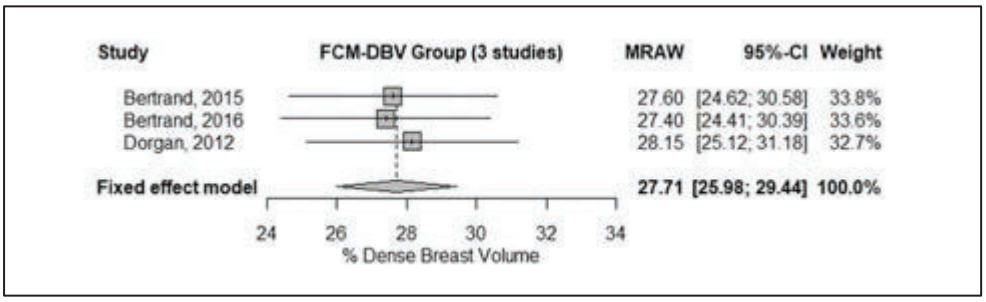
Study
FCM-DBV Group (3 studies)
MRAW
95%-CI
Weight
Bertrand, 2015 27.60 [24.62; 30.58] 33.8%
Bertrand, 2016 27.40 [24.41; 30.39] 33.6%
Dorgan, 2012 28.15 [25.12; 31.18] 32.7%
Fixed effect model 27.71 [25.98; 29.44] 100.0%
24 26 28 30 32 34
% Dense Breast Volume

(B)

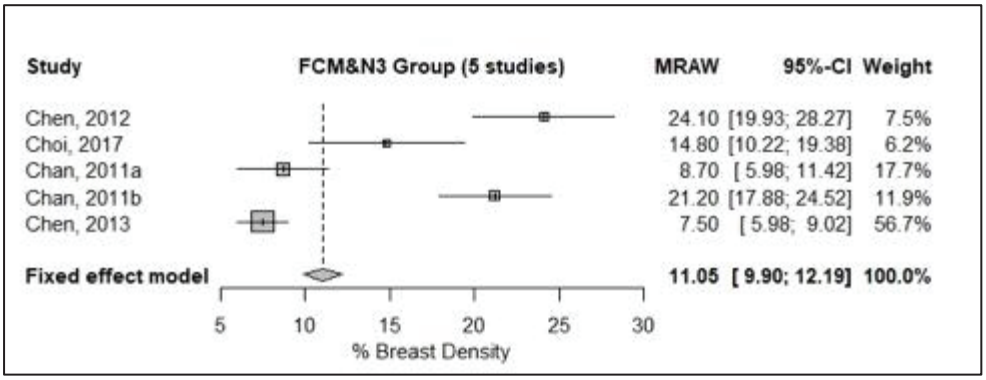
Study
FCM&N3 Group (5 studies)
MRAW
95%-CI
Weight
Chen, 2012 24.10 [19.93; 28.27] 7.5%
Choi, 2017 14.80 [10.22; 19.38] 6.2%
Chan, 2011a 8.70 [5.98; 11.42] 17.7%
Chan, 2011b 21.20 [17.88; 24.52] 11.9%
Chen, 2013 7.50 [5.98; 9.02] 56.7%
Fixed effect model 11.05 [9.90; 12.19] 100.0%
5 10 15 20 25 30
% Breast Density

(C)

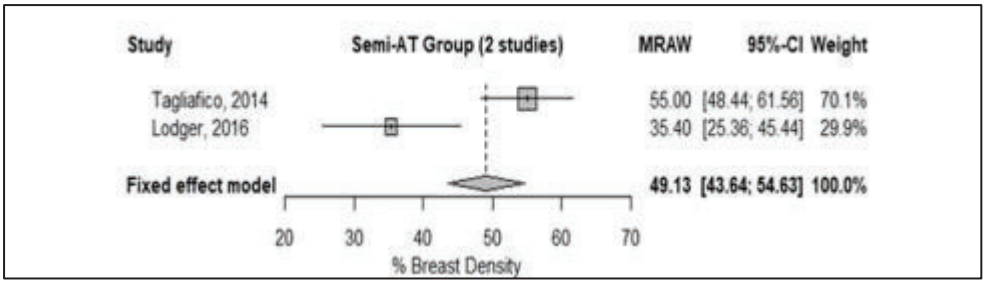
Study
Semi-AT Group (2 studies)
MRAW
95%-CI
Weight
Tagliafico, 2014 55.00 [48.44; 61.56] 70.1%
Lodger, 2016 35.40 [25.36; 45.44] 29.9%
Fixed effect model 49.13 [43.64; 54.63] 100.0%
20 30 40 50 60 70
% Breast Density

(D)

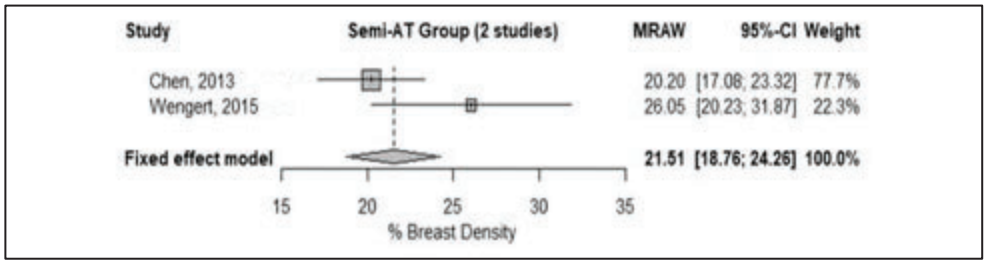

(E)

Figure 2.3. Forest plot of the study means, and 95% confidence limits of the breast density among 21 included studies in the subgroup meta-analyses. **(A)** Fixed effect meta-analysis of the fuzzy c-mean clustering (FCM) group of studies of % breast density. **(B)** Fixed effect meta-analysis of the FCM group of studies of %dense breast volume. **(C)** fixed effect meta-analysis of the FCM and N3 group of studies of % breast density. **(D)** fixed effect meta-analysis of the semi-automated threshold group of studies of % breast density. **(E)** fixed effect meta-analysis of the semi-automated threshold group of studies of % breast density.

2.4.3.1 Fuzzy C-mean Clustering (FCM)

The FCM subgroup consisted of 13 studies, of which, 10 studies reported breast density as a percentage breast density (% BD),[1,11,25–32] whereas 3 studies as a percentage of the dense breast volume (% DBV).[36–38] On one hand, 10 studies with inclusion of 634 patients were included, as Figure 2.3A shows, there is a wide range of mean values as well as standard deviation (SDs) from those studies, which indicated enormous heterogeneity among study means (Cochran's Q test: $X^2 = 86.93$, $P < 0.0001$). Indeed, there is a substantial heterogeneity among study variances (Bartlett's test: $X^2 = 110.59$, $P < 0.0001$). On the other hand, three studies with inclusion of 528 patients were analyzed. Figure 2.3B shows there is a high level of homogeneity among study means (Cochran's Q test: $X^2 = 0.13$, $P = 0.94$), and a high level of homogeneity among study variances (Bartlett's test: $X^2 = 0.12$, $P = 0.94$), which would be expected as those studies used an identical combination of MR technique and breast density segmentation/measurement approach.

2.4.3.2 FCM and Nonparametric Nonuniformity Normalization (N3)

The FCM and N3 subgroup included 4 studies with inclusion of 126 patients,[45,48–50] as Figure 2.3C shows, there is a wide range of mean values as well as SDs from those studies, which indicated tremendous heterogeneity among study means (Cochran's Q test: $X^2 = 99.94$, $P < 0.0001$). Indeed, there is a substantial heterogeneity among study variances (Bartlett's test: $X^2 = 45.41$, $P < 0.0001$), which would be expected as those studies used different MR breast-imaging protocols.

2.4.3.3 Interactive Semi-Automated Threshold

Two studies[3,54] comprising of 58 patients were included in the analysis, which indicated a considerable heterogeneity among study means (Cochran's Q test: $X^2 = 10.26$, $P = 0.0014$). In contrast, there was no evidence of heterogeneity among study variances (Bartlett's test: $X^2 = 1.61$, $P = 0.2072$). On the other hand, two studies with inclusion of 67 patients[53,55] were analyzed as shown in Figure 2.3E, there was no evidence of heterogeneity among study means (Cochran's Q test: $X^2 = 3.01$, $P = 0.0825$), which would be expected as those studies used the same MRI technique and breast density measurement. However, there is a substantial heterogeneity among study variances (Bartlett's test: $X^2 = 18.84$, $P < 0.0001$).

2.4.4 Cluster Analysis

The results obtained from the clustering analysis "Dendrogram using Single Linkage" are shown in Figure 2.4. From this data, it can be seen that a hierarchical diagram showing various distances (0-25) at which studies joined various groups. On that basis, six clusters were identified. A list of cluster membership, study means, SDs, and CVs

(expressed as a percentage) is shown in Table 2.3. A scatter plot of the study means versus SDs is shown in Figure 2.5, the legend in the scatter plot indicates the number of studies in each cluster. Cluster markers with solid fill indicate clusters with two or more studies, whereas open markers indicate singletons. Cluster 1 included nine studies that analysed breast density with a combination of contrast and non-contrast T1-weighted either with 2D spin echo or 3D gradient echo**;** however, Choi et al[49] used diffusion-weighted scanning technique. From the data in Table 2.3, it is apparent that the CVs are varied in value, but in Choi's study[49] the CV is almost 100% because of the mean and SD are almost identical. In contrast, the CVs for Chan et al[48] and Chen et al[53] are much lower than the rest of the included studies, largely because of the small SDs and the breast segmentation methods being used which are FCM & N3 and interactive semi-automated threshold algorithms, respectively.

Table 2.2. Sample size, Mean, and SD of breast volume, fibroglandular volume, and percent of breast density of the (21) included studies in the subgroup meta-analyses.

Author, Year [Reference]	Breast Volume, BV (cm^3)		Fibroglandular Volume, FV (cm^3)			Breast Density, BD (%)	
	Mean	SD	Mean	SD	N	Mean	SD
Chang, 2011 [25]	681	-	100	58	38	17.50	9.50
Nie, 2010 [26]	-	-	104	62	141	15.30	8.10
	-	-	112	73	89	16.70	10.10
Perutz, 2016 [27]	2210	1125	297	128	68	16.60	11.20
Moon, 2018 [28]	537.59	287.74	-	-	89	20.30	8.60
Chen, 2010 [29]	-	-	-	-	35	16.6 0	9.30
Ha, 2016 [30]	-	-	-	-	60	15.30	10.07
Chen, 2016 [31]	537.59	287.74	-	-	23	24.71	15.16
Moon, 2011 [32]	544.90	207.41	-	-	40	23.79	16.62
Klifa, 2010 [11]	-	-	-	-	35	28.0	18.00
Chen, 2011 [1]	358	174	79	66	16	22.10	2.60
Bertrand, 2015 [36]	413.5	364.3	104.2	70.6	182	27.60	20.50
Bertrand, 2016 [37]	418.7	369.3	104.7	70.3	172	27.40	20.00
Dorgan, 2012 [38]	-	-	104.67	71.28	174	28.15	20.39
Chen, 2012 [45]	528	263	117	82	34	24.10	12.40
Choi, 2017 [49]	-	-	-	-	38	14.80	14.40
Chan, 2011 [48]	-	-	-	-	6	8.70	3.40
	-	-	-	-	24	21.20	8.30
Chen, 2013 [50]	-	-	-	-	24	7.50	3.80
Tagliafico, 2014 [3]	-	-	-	-	48	55.00	23.20
Lodger, 2016 [54]	482.6	296.2	135.2	56.2	10	35.40	16.20
Chen, 2013 [53]	-	-	48.1 (ml)	24.7 (ml)	24	20.20	7.80
Wengert, 2015 [55]	1462.43	803.38	-	-	43	26.05	19.47

In contrast, cluster 2 consisted of 8 studies that assessed breast density with a combination of contrast- and non-contrast-enhanced T1-weighted with 3D gradient echo, however, Chen et al[31] and Chen et al[45] used non-contrast- and contrast-enhanced T1-weighted with 2D spin-echo, respectively. Indeed, Chen et al[45] analyzed breast density using FCM and N3 algorithms. From the data in Figure 2.5 and Table 2.3 (Cluster 2), it is apparent that the CVs are almost within a closed range except for Chen et al[45] where the CV is much lower than the remaining studies because of the small SD and the breast segmentation method that previously mentioned. Also, Wengert et al[55] used Dixon method as a technical protocol for breast-imaging, although they measured the breast density using in-house customized software, the mean and SD are not different to the other included studies. The most striking result to emerge from the data in Figure 2.5 and Table 2.3 (Cluster 3–6) is the Chen et al[1] study (i.e., Cluster 3), although it used non-contrast-enhanced T1-weighted with 3D gradient echo and analyzed breast density by FCM algorithm, the CV (11.67%) is much lower than the remaining studies, mainly because of the small SD.

Cluster 4 included two studies Chan et al[48] and Chen et al[50] that assessed breast density using FCM and N3 algorithms and non-contrast-enhanced T1-weighted with 3D gradient echo. As can be seen from the data in Figure 2.5 and Table 2.3 (Cluster 3–6) the study means and SDs are not different. In contrast to this Cluster 5, the Tagliafico et al[3] study used 3D contrast-enhanced T1-weighted gradient echo sequence and analyzed the breast density by semi-automated interactive threshold, in particular, (MedDensity). As Figure 2.5 and Table 2.3 (Cluster 3–6) show, the study mean is much higher than the remaining studies, largely because of the technical method used. Finally, cluster 6 consisted of Lodger et al,[54] this is the only study that used proton

density weighted sequence. Detailed information of clustering membership, study means, SDs, and CVs is shown in Table 2.3, Figures 2.4 and 2.5.

Switching from technology groupings of studies to groupings identified by the cluster analysis, meta-analysis of cluster 1 revealed that the study means, and study variances are both heterogeneous (Cochran's test for heterogeneity of study means, $X^2 = 22.26$, $P = 0.0045$, and Bartlett's test for heterogeneity of study variances, $X^2 = 21.47$, $P = 0.0060$, see Figure 2.6A). When Choi et al[49] was excluded (because of the very large CV), the cluster has improved somewhat, which would be expected as this study used different protocols (i.e. diffusion-weighted imaging). It can be seen from the data in Figure 2.6B that the study variances are no longer heterogeneous ($X^2 = 8.84$, $P = 0.2641$), although the study means remain heterogeneous ($X^2 = 19.54$, $P = 0.0066$). In contrast, meta-analysis of cluster 2 indicated that the study means are not heterogeneous ($X^2 = 4.77$, $P = 0.6874$), while the study variances are mildly heterogeneous ($X^2 = 15.54$, $P = 0.0206$, see Figure 2.7).

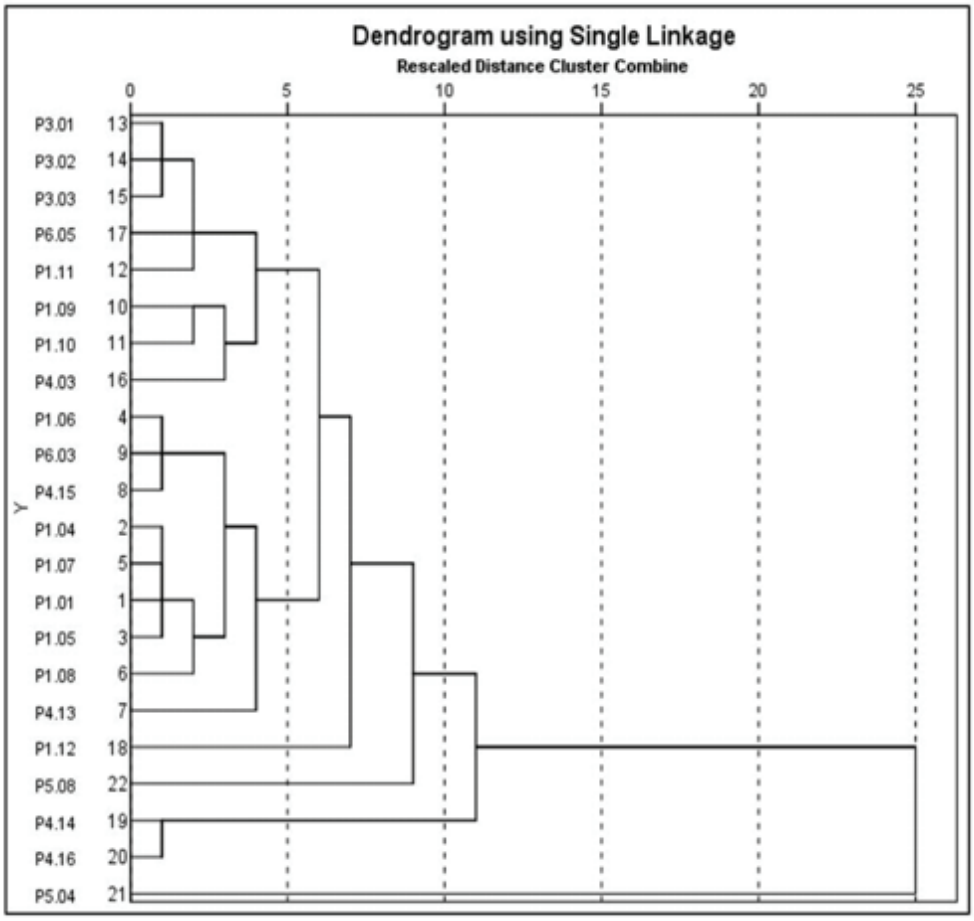

Figure 2.4. Dendrogram clustering analysis using "single linkage" method of the study means, and study SD_S among 21 included studies in the subgroup meta-analysis.

Table 2.3. Study size (N), mean, SD, CV, and cluster membership of the included studies.

Study Code	Author, Year [Reference]	N	Mean	SD	CV	Cluster Membership
P1.01	Chang, 2011 [25]	38	17.50	9.50	54.29	1
P1.04	Nie, 2010 [26]	89	16.70	10.10	60.48	1
P1.05	Pertuz, 2016 [27]	68	16.60	11.20	67.47	1
P1.06	Moon, 2018 [28]	89	20.30	8.60	42.36	1
P1.07	Chen, 2010 [29]	35	16.60	9.30	56.02	1
P1.08	Ha, 2016 [30]	60	15.30	10.07	65.82	1
P4.13	Choi, 2017 [49]	38	14.80	14.40	97.30	1
P4.15	Chen, 2011 [48]	24	21.20	8.30	39.15	1
P6.03	Chen, 2013 [53]	24	20.20	7.80	38.61	1
P1.09	Chen, 2016 [31]	23	24.71	15.16	61.35	2
P1.10	Moon, 2011 [32]	40	23.79	16.62	69.86	2
P1.11	Klifa, 2010 [11]	35	28.00	18.00	64.29	2
P3.01	Bertrand,2015 [36]	182	27.60	20.50	74.28	2
P3.02	Bertrand, 2016 [37]	172	27.40	20.00	72.99	2
P3.03	Dorgan, 2012 [38]	174	28.15	20.39	72.43	2
P4.03	Chen, 2012 [45]	34	24.10	12.40	51.45	2
P6.05	Wengert, 2015 [55]	43	26.05	19.47	74.74	2
P1.12	Chen, 2011 [1]	16	22.10	2.60	11.76	3
P4.14	Chan, 2011 [48]	6	8.70	3.40	39.08	4
P4.16	Chen, 2013 [50]	24	7.50	3.80	50.67	4
P5.04	Tagliafico, 2014 [3]	48	55.00	23.20	42.18	5
P5.08	Lodger, 2016 [54]	10	33.40	16.20	45.76	6

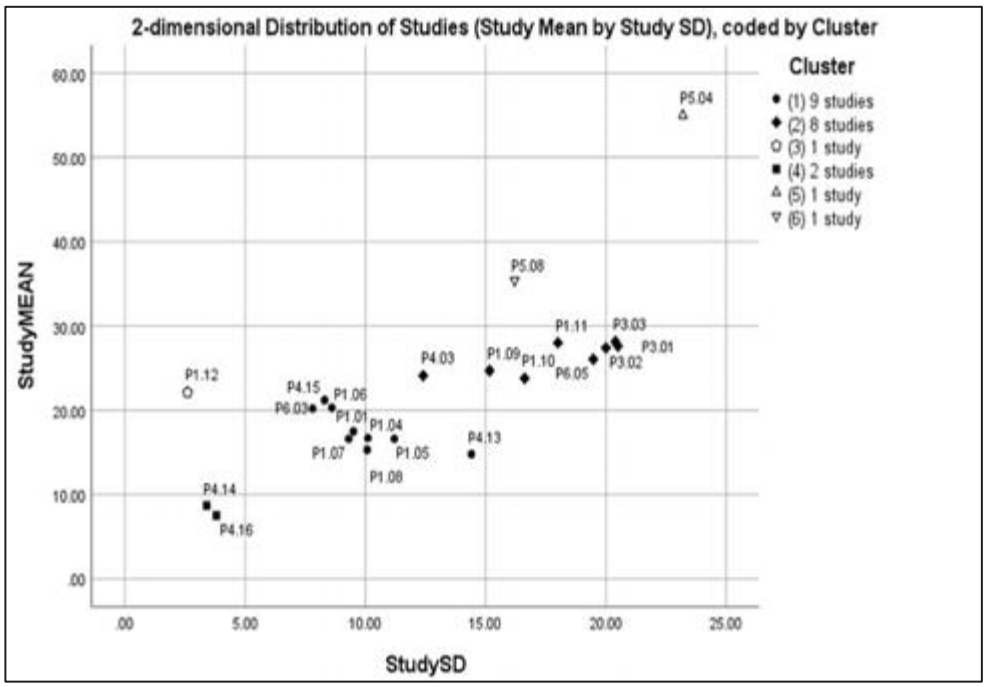

(A)

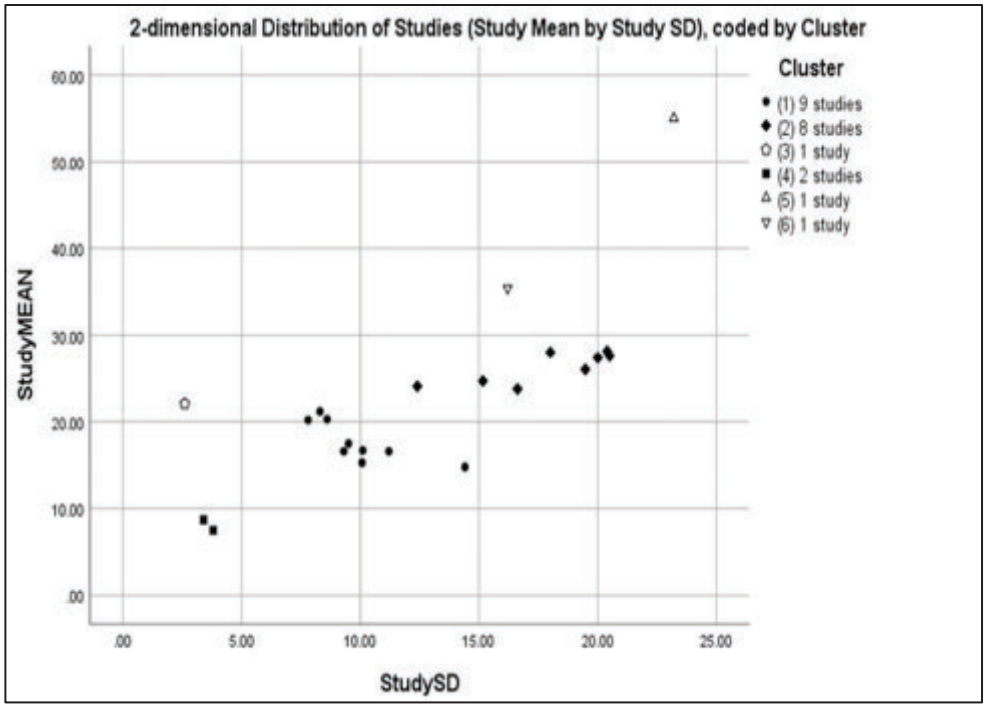

(B)

Figure 2.5. Scatter plot of the study means versus SD_s using 6-clusters memberships of the 21 included studies in the subgroup meta-analyses. legend indicates the number of studies in each cluster, solid fill represents cluster with two or more studies, while open markers represent singleton study. Scatter plot of study means versus SD_s with study codes **(A)** and without study codes **(B)**.

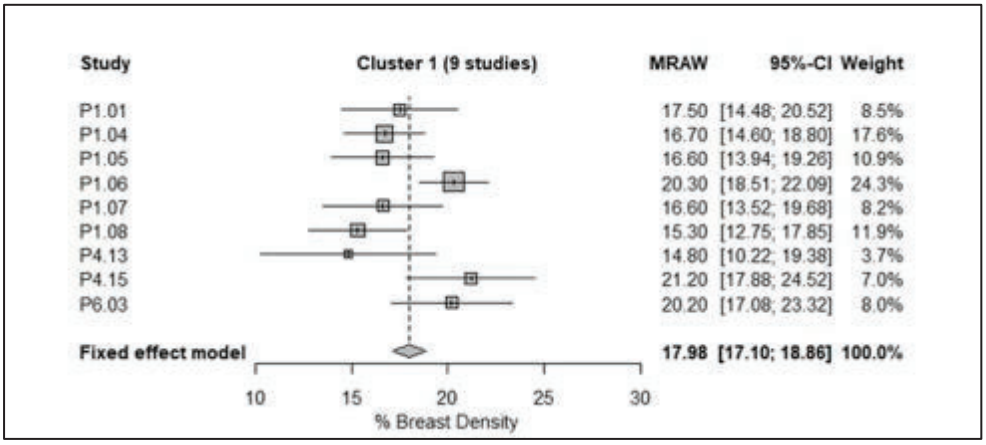

(A)

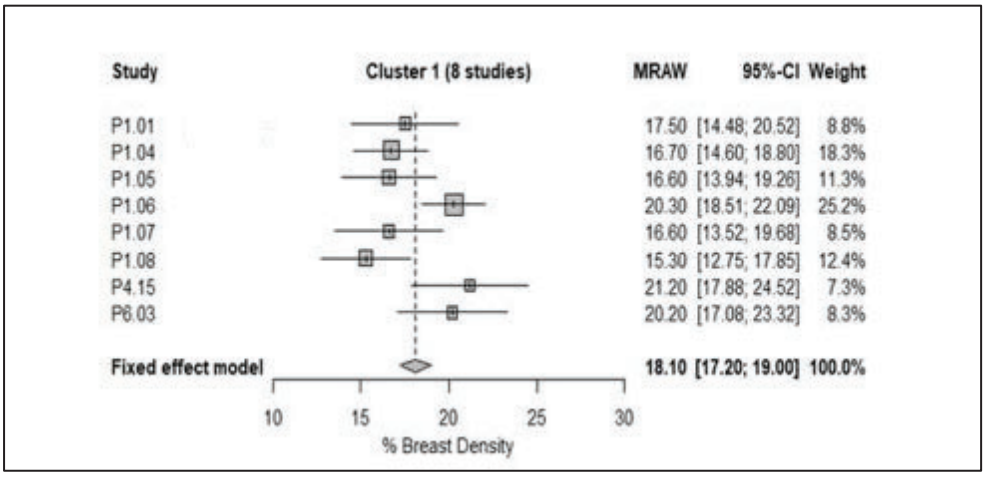

(B)

Figure 2.6. Forest plot of the study means, and 95% confidence limits of the studies in cluster 1 with/without P4.13 (Choi et al[49]) of % breast density. **(A)** fixed effect meta-analysis of the studies in cluster 1 (9 studies) of % breast density. **(B)** Fixed effect meta-analysis of the studies in cluster 1 (8 studies) of % breast density.

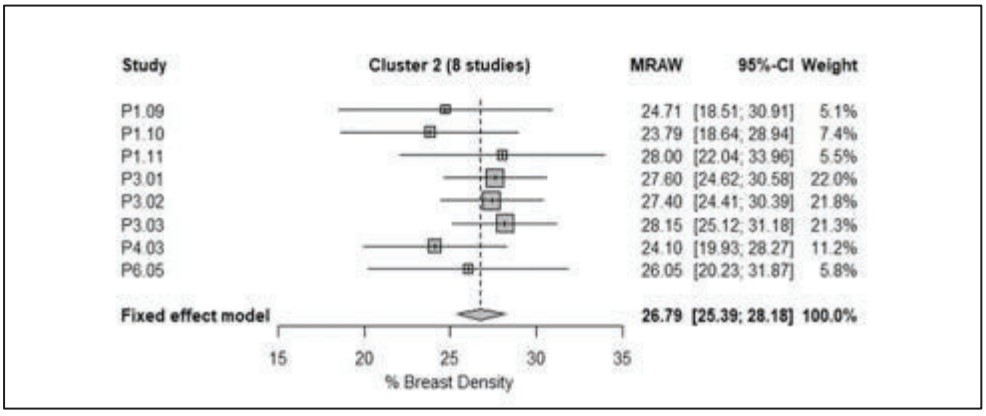

Figure 2.7. Forest plot of the study means, and 95% confidence limits of the studies in cluster 2 (8 studies) of % breast density.

2.5 Discussion

The present systematic review and meta-analysis was performed to analyze the current studies on quantitative breast density using MRI and to determine the most appropriate technical/operational protocol. Through reviewing 38 studies from the literature, despite many methods and protocols available, no gold standard has been established with a wide range of heterogeneous methods or protocols used in these studies. To the best of our knowledge, this is the first comprehensive systematic review and meta-analysis of pooling the results of all breast density segmentation/measurement methods using MRI data. The analysis indicated that the non-contrast-enhanced T1-weighted acquisition was commonly utilized among all MR breast-imaging protocols. Another important finding of this analysis was that the FCM is the most frequently used algorithm amongst the breast density segmentation/measurement methods. Also, the results showed that a high level of heterogeneity was mainly associated with the breast-imaging protocols and the breast density segmentation/measurement methods.

Further attempts have been made by using clustering methods and meta-analysis to identify groups of studies which are as homogeneous as possible within groups and as heterogeneous as possible between groups. The included studies were grouped together into clusters based on their nearest neighbor Euclidean distances. On that basis, clusters 1 and 2 were considered as the most valuable results. Briefly, cluster 1 consisted of 9 studies,[25–30,48,49,53] as shown from the data in Table 2.3 and Figure 2.6A that the CVs are varied in value, but in Choi et al[49] the CV is almost 100% because of the mean and SD are almost identical. This result may be explained by the fact that among the 8 studies,[11,31,32,36–38,45,55] the breast-imaging protocol was a combination of contrast- and non-contrast-enhanced T1-weighted either with 2D spin echo or 3D

gradient echo, while in Choi et al[49] the MRI protocol used was diffusion-weighted imaging. Consequently, it is advisable to exclude it from the meta-analysis to reduce the heterogeneity within cluster 1. Consistent with this hypothesis, the results have improved in somewhat, even though the study variances are not heterogeneous ($P > 0.05$), the study means are heterogeneous ($P < 0.05$) (Figure 2.6B). Although exclusion of Choi et al[49] did not reduce the heterogeneity, these results should be interpreted with caution. The discrepancy could be largely attributed to that although the MR breast-imaging protocols are not dissimilar (i.e., contrast- and non-contrast-enhanced T1-weighted), the breast segmentation/measurement methods are vice versa (i.e., FCM, FCM and N3, and in-house customized software). In contrast, cluster 2 included 8 studies, in 3 of these studies the breast density was reported as a (%DBV), while the remaining as a (% BD). Among these studies, the contrast- and non-contrast-enhanced T1-weighted was often used. From the data in Table 2.3 and Figure 2.7, it is apparent that the study means are not dissimilar ($P > 0.05$), although the study variances are heterogeneous ($P < 0.05$). Among the 21 studies included in the cluster analysis, although the fixed effect meta-analysis of cluster 2 has improved slightly, the heterogeneity within group still exist. There are two likely causes for this heterogeneity: the applied MR breast-imaging protocol and the used breast density segmentation/measurement methods.

Although the study has successfully confirmed the variation in the breast density segmentation/measurement methods using MRI data, the findings are subject to several limitations. First, the heterogeneity of study aims, the study design utilized, and the technical/operational methods applied, for instance, the MR breast-imaging protocol, MR scanner manufacturer, and the static magnetic field strength present challenges for performing the meta-analysis. Second, the breast density

segmentation/measurement algorithm used is another limitation. Although we classified the included studies into discrete subgroups (i.e., FCM, FCM and N3, and interactive semi-automated threshold), and applied stratified analyses, the heterogeneity remains. Third, the definition of the breast density was inconsistent because some studies reported it as a percentage of dense breast volume, while the others as a percentage of breast density. Fourth, among the 38 studies included in this analysis, only 21 studies were eligible for meta-analysis due to the statistical requirements for the input values that should be in identical expression of measurement and dispersion. In addition, some of the included studies used the same set of the subject multiple times for different purpose and feature. Even though we decided to rectify the issue by selecting one of the results of data at random, or by any meaningful clinical criterion, the heterogeneity continues to exist. Notwithstanding these limitations, the study further supports the idea of developing a standard MRI protocol for the quantitative assessment of breast density.

Future research can be suggested according to findings of this review. A recent study has reported the feasibility of creating a realistic 3D printed breast phantom for quality control purpose.[58] Thus, we consider 3D printing technique can be used to develop a patient-specific 3D printed breast phantom with different amounts of breast composition to quantify the volume of FGT. Further, the 3D printed model can be used to examine several MR breast-imaging protocols not only to measure the breast density but also to assess the impact of implementing various image quality parameters (i.e., FOV, matrix size and slice thickness) on the segmentation/measurement of breast density. Finally, the accuracy of different breast density/FGT segmentation methods can be determined.

2.6 Conclusion

This systematic review and meta-analysis confirms and substantiates the variation among the breast density segmentation/measurement methods using MRI. Furthermore, subgroup meta-analyses and further clustering methods indicated that a significant heterogeneity within and between groups exist. The analysis confirmed that the non-contrast-enhanced T1-weighted acquisition was commonly utilized among all MR breast-imaging protocols and the FCM is the most frequently used algorithm amongst the breast density segmentation/measurement methods. Future work will need to determine the most appropriate protocol and method for quantifying breast density using MRI.

2.7 References

1. Chen JH, Chang YC, Chang D, Wang YT, Nie K, Chang RF, Nalcioglu O, Huang CS, Su MY. Reduction of breast density following tamoxifen treatment evaluated by 3-D MRI: Preliminary study. Magn Reson Imaging. 2011; 29(1):91-98.
2. Wang J, Azziz A, Fan B, Malkov S, Klifa C, Newitt D, Yitta S, Hylton N, Kerlikowske K, Shepherd JA. Agreement of mammographic measures of volumetric breast density to MRI. PloS ONE. 2013; 8(12):e81653.
3. Tagliafico A, Bignotti B, Tagliafico G, Astengo D, Martino L, Airaldi S, Signori A, Sormani MP, Houssami N, Calabrese M. Breast density assessment using a 3T MRI system: Comparison among different sequences. PLoS ONE. 2014; 9(6):e99027.

4. Lienart V, Carly B, Kang X, Guzy L, Sajovitz AM, Liebens F. Effect of preventive hormonal therapy on breast density: A systematic qualitative review. Sci World. 2014; 2014:942386.
5. Tagliafico A, Tagliafico G, Astengo D, Airaldi S, Calabrese M, Houssami N. Comparative estimation of percentage breast tissue density for digital mammography, digital breast tomosynthesis, and magnetic resonance imaging. Breast Cancer Res Treat. 2013; 138(1):311-317.
6. Li H, Weiss WA, Medved M, Abe H, Newstead GM, Karczmar GS, Giger ML. Breast density estimation from high spectral and spatial resolution MRI. J Med Imaging. 2016; 3(4):044507.
7. Wu S, Weinstein SP, Conant EF, Kontos D. Automated fibroglandular tissue segmentation and volumetric density estimation in breast MRI using an atlas-aided fuzzy C-means method. Med Phys. 2013; 40(12):122302.
8. Ding J, Stopeck AT, Gao Y, Marron MT, Wertheim BC, Altbach MI, Galons JP, Roe DJ, Wang F, Maskarinec G, Thomson CA. Reproducible automated breast density measure with no ionizing radiation using fat-water decomposition MRI. Magn Reson Imaging. 2018; 48(4):971-981.
9. Sak MA, Littrup PJ, Duric N, Mullooly M, Sherman ME, Gierach GL. Current and future methods for measuring breast density: a brief comparative review. Breast Cancer Manag. 2015; 4(4):209-221.
10. Niukkanen A, Arponen O, Nykänen A, Masarwah A, Sutela A, Liimatainen T, Vanninen R, Sudah M. Quantitative volumetric K-means cluster segmentation of fibroglandular tissue and skin in breast MRI. J Digit Imaging. 2018; 31(4):425-434.

11. Klifa C, Carballido-Gamio J, Wilmes L, Laprie A, Shepherd J, Gibbs J, Fan B, Noworolski S, Hylton N. Magnetic resonance imaging for secondary assessment of breast density in a high-risk cohort. Magn Reson Imaging. 2010; 28(1):8-15.
12. Ertas G, Doran SJ, Leach MO. A computerized volumetric segmentation method applicable to multi-centre MRI data to support computer-aided breast tissue analysis, density assessment and lesion localization. Med Biol Eng Comput. 2017; 55(1):57-68.
13. Petridou E, Kibiro M, Gladwell C, Malcolm P, Toms A, Juette A, Borga M, Leinhard OD, Romu T, Kasmai B, Denton E. Breast fat volume measurement using wide-bore 3 T MRI: Comparison of traditional mammographic density evaluation with MRI density measurements using automatic segmentation. Clin Radiol. 2017; 72(7):565-572.
14. American College of Radiology. ACR BI-RADS® Atlas: Breast Imaging Reporting and Data System; American College of Radiology: Reston, VA, USA, 2013.
15. Mainiero MB, Lourenco A, Mahoney MC, Newell MS, Bailey L, Barke LD, D'Orsi C, Harvey JA, Hayes MK, Huynh PT. ACR appropriateness criteria breast cancer screening. J Am Coll Radiol. 2016; 13(11):R45–R49.
16. Timmers JM, van Doorne-Nagtegaal HJ, Verbeek AL, Den Heeten GJ, Broeders MJ. A dedicated BI-RADS training programme: Effect on the inter-observer variation among screening radiologists. Eur J Radiol. 2012; 81(9):2184–2188.
17. Nayeem F, Ju H, Brunder DG, Nagamani M, Anderson KE, Khamapirad T, Lu LJ. Similarity of fibroglandular breast tissue content measured from magnetic

resonance and mammographic images and by a mathematical algorithm. Int J Breast Cancer. 2014; 2014:961679.

18. Lin M, Chan S, Chen JH, Chang D, Nie K, Chen ST, Lin CJ, Shih TC, Nalcioglu O, Su MY. A new bias field correction method combining N3 and FCM for improved segmentation of breast density on MRI. Med Phys. 2011; 38(1):5-14.
19. Doran SJ, Hipwell JH, Denholm R, Eiben B, Busana M, Hawkes DJ, Leach MO, Silva ID. Breast MRI segmentation for density estimation: Do different methods give the same results and how much do differences matter? Med Phys. 2017; 44(9):4573-4592.
20. Tagliafico A, Tagliafico G, Tosto S, Chiesa F, Martinoli C, Derchi LE, Calabrese M. Mammographic density estimation: comparison among BI-RADS categories, a semi-automated software and a fully automated one. Breast J. 2009; 18(1):35-40.
21. Boston RC, Schnall MD, Englander SA, Landis JR, Moate PJ. Estimation of the content of fat and parenchyma in breast tissue using MRI T1 histograms and phantoms. Magn Reson Imaging. 2005; 23(4):591-599.
22. Lu LJ, Nishino TK, Johnson RF, Nayeem F, Brunder DG, Ju H, Leonard Jr MH, Grady JJ, Khamapirad T. Comparison of breast tissue measurements using magnetic resonance imaging, digital mammography and a mathematical algorithm. Phys Med Biol. 2012; 57(21):6903.
23. Moher D, Shamseer L, Clarke M, Ghersi D, Liberati A, Petticrew M, Shekelle P, Stewart LA. Preferred reporting items for systematic review and meta-analysis protocols (PRISMA-P) 2015 statement. Syst Rev. 2015; 4(1):1-9.

24. Stewart LA, Clarke M, Rovers M, Riley RD, Simmonds M, Stewart G, Tierney JF. Preferred reporting items for a systematic review and meta-analysis of individual participant data: the PRISMA-IPD statement. JAMA. 2015; 313(16):1657-1665.
25. Chang DH, Chen JH, Lin M, Bahri S, Hon JY, Mehta RS, Nie K, Hsiang DJ, Nalcioglu O, Su MY. Comparison of breast density measured on MR images acquired using fat-suppressed versus nonfat-suppressed sequences. Med Phys. 2011; 38(11):5961-5968.
26. Nie K, Chang D, Chen JH, Hsu CC, Nalcioglu O, Su MY. Quantitative analysis of breast parenchymal patterns using 3D fibroglandular tissues segmented based on MRI. Med Phys. 2010; 37(1):217-226.
27. Pertuz S, McDonald ES, Weinstein SP, Conant EF, Kontos D. Fully automated quantitative estimation of volumetric breast density from digital breast tomosynthesis images: Preliminary results and comparison with digital mammography and MR imaging. Radiology. 2016; 279(1):65-74.
28. Moon WK, Chang JF, Lo CM, Chang JM, Lee SH, Shin SU, Huang CS, Chang RF. Quantitative breast density analysis using tomosynthesis and comparison with MRI and digital mammography. Comput Methods Programs Biomed. 2018; 154:99-107.
29. Chen JH, Nie K, Bahri S, Hsu CC, Hsu FT, Shih HN, Lin M, Nalcioglu O, Su MY. Decrease in breast density in the contralateral normal breast of patients receiving neoadjuvant chemotherapy: MR imaging evaluation. Radiology. 2010; 255(1):44-52.
30. Ha R, Mema E, Guo X, Mango V, Desperito E, Ha J, Wynn R, Zhao B. Quantitative 3D breast magnetic resonance imaging fibroglandular tissue

analysis and correlation with qualitative assessments: A feasibility study. Quant Imaging Med Surg. 2016; 6(2):144-150.

31. Chen JH, Lee YW, Chan SW, Yeh DC, Chang RF. Breast density analysis with automated whole-breast ultrasound: Comparison with 3-D magnetic resonance imaging. Ultrasound Med Biol. 2016; 42(5):1211-1220.
32. Moon WK, Shen YW, Huang CS, Luo SC, Kuzucan A, Chen JH, Chang RF. Comparative study of density analysis using automated whole breast ultrasound and MRI. Med Phys. 2011; 38(1):382-389.
33. Nie K, Chang D, Chen JH, Shih TC, Hsu CC, Nalcioglu O, Su MY. Impact of skin removal on quantitative measurement of breast density using MRI. Med Phys. 2010; 37(1):227-233.
34. Kim JY, Cho N, Jeyanth JX, Kim WH, Lee SH, Gweon HM, Moon WK. Smaller reduction in 3D breast density associated with subsequent cancer recurrence in patients with breast cancer receiving adjuvant tamoxifen therapy. Am J Roentgenol. 2014; 202(4):912-921.
35. Nie K, Su MY, Chau MK, Chan S, Nguyen H, Tseng T, Huang Y, McLaren CE, Nalcioglu O, Chen JH. Age-and race-dependence of the fibroglandular breast density analysed on 3D MRI. Med Phys. 2010; 37(6Part1):2770-2776.
36. Bertrand KA, Baer HJ, Orav EJ, Klifa C, Shepherd JA, Van Horn L, Snetselaar L, Stevens VJ, Hylton NM, Dorgan JF. Body fatness during childhood and adolescence and breast density in young women: A prospective analysis. Breast Cancer Res. 2015; 17(1):1-10.
37. Bertrand KA, Baer HJ, Orav EJ, Klifa C, Kumar A, Hylton NM, LeBlanc ES, Snetselaar LG, Van Horn L, Dorgan JF. Early life body fatness, serum anti-

müllerian hormone, and breast density in young adult women. Cancer Epidemiol Biomark Prev. 2016; 25(7):1151-1157.

38. Dorgan JF, Klifa C, Shepherd JA, Egleston BL, Kwiterovich PO, Himes JH, Gabriel KP, Van Horn L, Snetselaar LG, Stevens VJ, Barton BA. Height, adiposity and body fat distribution and breast density in young women. Breast Cancer Res. 2012; 14(4):1-12.
39. Gabriel KP, Klifa C, Pérez A, Kriska AM, High RR, Snetselaar L, Dorgan JF. Adolescent and young adult exposure to physical activity and breast density. Med Sci Sports Exerc. 2013; 45(8):1515.
40. Jung S, Stanczyk FZ, Egleston BL, Snetselaar LG, Stevens VJ, Shepherd JA, Van Horn L, LeBlanc ES, Paris K, Klifa C, Dorgan JF. Endogenous sex hormones and breast density in young women. Cancer Epidemiol Biomark Prev. 2015; 24(2):369-378.
41. Jung S, Goloubeva O, Klifa C, LeBlanc ES, Snetselaar LG, Van Horn L, Dorgan JF. Dietary fat intake during adolescence and breast density among young women. Cancer Epidemiol Biomark Prev. 2016; 25(6):918-926.
42. Dorgan JF, Klifa C, Deshmukh S, Egleston BL, Shepherd JA, Kwiterovich PO, Van Horn L, Snetselaar LG, Stevens VJ, Robson AM, Lasser NL. Menstrual and reproductive characteristics and breast density in young women. Cancer Causes Control. 2013; 24(11):1973-1983.
43. Jung S, Egleston BL, Chandler DW, Van Horn L, Hylton NM, Klifa CC, Lasser NL, LeBlanc ES, Paris K, Shepherd JA, Snetselaar LG. Adolescent endogenous sex hormones and breast density in early adulthood. Breast Cancer Res. 2015;17(1):1-9.

44. Jones JA, Hartman TJ, Klifa CS, Coffman DL, Mitchell DC, Vernarelli JA, Snetselaar LG, Van Horn L, Stevens VJ, Robson AM, Himes JH. Dietary energy density is positively associated with breast density among young women. J Acad Nut Diet. 2015; 115(3):353-359.
45. Chen JH, Chan S, Liu YJ, Yeh DC, Chang CK, Chen LK, Pan WF, Kuo CC, Lin M, Chang DH, Fwu PT. Consistency of breast density measured from the same women in four different MR scanners. Med Phys. 2012; 39(8):4886-4895.
46. Chen JH, Chan S, Tang YT, Hon JS, Tseng PC, Cheriyan AT, Shah NR, Yeh DC, Lee SK, Chen WP, McLaren CE. Impact of positional difference on the measurement of breast density using MRI. Med Phys. 2015; 42(5):2268-2275.
47. Chen JH, Pan WF, Kao J, Lu J, Chen LK, Kuo CC, Chang CK, Chen WP, McLaren CE, Bahri S, Mehta RS. Effect of taxane-based neoadjuvant chemotherapy on fibroglandular tissue volume and percent breast density in the contralateral normal breast evaluated by 3T MR. NMR Biomed. 2013; 26(12):1705-1713.
48. Chan S, Su MY, Lei FJ, Wu JP, Lin M, Nalcioglu O, Feig SA, Chen JH. Menstrual cycle–related fluctuations in breast density measured by using three-dimensional MR imaging. Radiology. 2011; 261(3):744-751.
49. Choi YJ, Chen JH, Yu HJ, Li Y, Su MY. Impact of different analytic approaches on the analysis of the breast fibroglandular tissue using diffusion weighted imaging. Bio Med Res Int. 2017; 2017:1094354.
50. Chen JH, Chan S, Yeh DC, Fwu PT, Lin M, Su MY. Response of bilateral breasts to the endogenous hormonal fluctuation in a menstrual cycle evaluated using 3D MRI. Magn Reson Imaging. 2013; 31(4):538-544.

51. Clendenen TV, Zeleniuch-Jacquotte A, Moy L, Pike MC, Rusinek H, Kim S. Comparison of 3-point dixon imaging and fuzzy C-means clustering methods for breast density measurement. Magn Reson Imaging. 2013; 38(2):474-481.
52. McDonald ES, Schopp JG, Peacock S, DeMartini WB, Rahbar H, Lehman CD, Partridge SC. Diffusion-weighted MRI: Association between patient characteristics and apparent diffusion coefficients of normal breast fibroglandular tissue at 3 T. Am J Roentgenol. 2014; 202(5):W496-W502.
53. Chen JH, Chen WP, Chan S, Yeh DC, Su MY, McLaren CE. Correlation of endogenous hormonal levels, fibroglandular tissue volume and percent density measured using 3D MRI during one menstrual cycle. Ann Oncol. 2013; 24(9):2329-2335.
54. Ledger AE, Scurr ED, Hughes J, Macdonald A, Wallace T, Thomas K, Wilson R, Leach MO, Schmidt MA. Comparison of Dixon sequences for estimation of percent breast fibroglandular tissue. PloS ONE. 2016; 11(3):e0152152.
55. Wengert GJ, Helbich TH, Vogl WD, Baltzer P, Langs G, Weber M, Bogner W, Gruber S, Trattnig S, Pinker K. Introduction of an automated user–independent quantitative volumetric magnetic resonance imaging breast density measurement system using the Dixon sequence: Comparison with mammographic breast density assessment. Investig Radiol. 2015; 50(2):73-80.
56. O'flynn EA, Wilson RM, Allen SD, Locke I, Scurr E, deSouza NM. Diffusion-weighted imaging of the high-risk breast: Apparent diffusion coefficient values and their relationship to breast density. Magn Reson Imaging. 2014; 39(4):805-811.
57. Kim JY, Suh HB, Kang HJ, Shin JK, Choo KS, Nam KJ, Lee SW, Jung YL, Bae YT. Apparent diffusion coefficient of breast cancer and normal

fibroglandular tissue in diffusion-weighted imaging: the effects of menstrual cycle and menopausal status. Breast Cancer Res Treat. 2016; 157(1):31-40.

58. He Y, Liu Y, Dyer BA, Boone JM, Liu S, Chen T, Zheng F, Zhu Y, Sun Y, Rong Y, Qiu J. 3D printed breast phantom for multi-purpose and multi-modality imaging. Quant Imaging Med Surg. 2019; 9(1):63-74.

3. Chapter 3

Development of Patient-Specific 3D-Printed Breast Phantom Using Silicone and Peanut Oils for Magnetic Resonance Imaging

3.1 Abstract

Background: Despite increasing reports of 3D printing in medical applications, the use of 3D printing in breast imaging is limited, thus, personalized 3D-printed breast model could be a novel approach to overcome current limitations in utilizing breast magnetic resonance imaging (MRI) for quantitative assessment of breast density. **Purpose:** The aim of this study is to develop a patient-specific 3D-printed breast phantom and to identify the most appropriate materials for simulating the MR imaging characteristics of fibroglandular and adipose tissues. **Methods:** A patient-specific 3D-printed breast model was generated using 3D-printing techniques for the construction of the hollow skin and fibroglandular region shells. Then, the T1 relaxation times of the five selected materials (agarose gel, silicone rubber with/without fish oil, silicone oil, and peanut oil) were measured on a 3T MRI system to determine the appropriate ones to represent the MR imaging characteristics of fibroglandular and adipose tissues. Results were then compared to the reference values of T1 relaxation times of the corresponding tissues: 1,324.42±167.63 and 449.27±26.09 ms, respectively. Finally, the materials that matched the T1 relaxation times of the respective tissues were used to fill the 3D-printed hollow breast shells. **Results:** The silicone and peanut oils were found to closely resemble the T1 relaxation times and imaging characteristics of these two tissues, which are 1,515.8±105.5 and 405.4±15.1 ms, respectively. The agarose gel with different concentrations, ranging from 0.5 to 2.5 wt%, was found to have the longest T1 relaxation times. **Conclusions:** A patient-specific 3D-printed breast phantom was successfully designed and constructed using silicone and peanut oils to simulate the MR imaging characteristics of fibroglandular and adipose tissues. The phantom can be used to investigate different MR breast imaging protocols for the quantitative assessment of breast density.

Keywords Magnetic resonance imaging (MRI); T1 and T2 relaxation times; fibroglandular-tissue; breast density; 3D-printing; fused deposition modelling (FDM); digital light processing (DLP); polylactic acid (PLA); photopolymer resin; silicone oil; peanut oil

3.2 Introduction

Breast magnetic resonance imaging (MRI) is a well- established approach in the diagnosis of breast disease, and it has become an important modality in the screening of women at high-risk of breast cancer, preoperative staging of newly diagnosed breast cancer, and follow-up of breast cancer treatment.[1-3] Hence, the European Society of Breast Imaging (EUSOBI) has recommended that breast MRI be used as an adjuvant modality in women at high- risk of developing breast cancer,[3] for those with (BRCA-positive genetic mutation carriers), family history, and/or high breast density.[4]

Breast density, a measure of fibroglandular, dense tissue relative to fatty, non-dense tissue, is an independent risk factor of breast cancer.[5-7] Consistent with this risk relationship, women who have dense breasts have a likelihood of developing breast cancer that is fourfold higher than those with fatty breasts.[8,9] Currently various methods have been developed and introduced to segment/ measure breast density using MRI: the utilization of a clustering algorithm, the segmentation of glandular and fatty tissues with an interactive thresholding algorithm, a logistic function approach and a curve-fitting algorithm; each has its advantages and limitations.[10-14] However, there are certain drawbacks associated with the use of these algorithms as most of them are interpreted as measurements with a semi-automatic thresholding and segmentation methods. Likewise, different MR breast- imaging protocols have been used to differentiate between adipose and fibroglandular tissues ranging from non- contrast-

enhanced T1-weighted to contrast-enhanced T1- weighted and diffusion-weighted acquisitions.[15-19] Despite improvements in the quantitative assessment of breast density using MR imaging, there has been no general agreement about the optimal scanning protocol in this aspect. A recent systematic review and meta-analysis about the quantitative assessment of breast density has confirmed these variations among breast segmentation/measurement methods and MR breast-imaging protocols.[20]

In recent years, there has been an increasing interest in 3D printing techniques, which are being used in different medical domains such as cardiovascular disease, orthopaedic surgery, prosthetics, and neurosurgery.[21-24] 3D-printed models have been shown to assist in the development of many surgical implants, which can improve the individual's understanding of such a complex anatomical structure.[21] Several studies have produced anthropomorphic breast phantoms for X-ray imaging, but there is still insufficient data available for MR imaging.[25-30] Carton et al[25] developed a 3D anthropomorphic breast phantom for the evaluation of image quality of 2D and 3D breast X-ray imaging systems. This phantom was based on a computational model and a rapid prototyping technique to generate breast phantom with different compositions, sizes, and shapes by using a tissue-equivalent material.[25] While the phantom has effectively demonstrated a heterogeneous distribution of the fibroglandular and adipose tissues that can be analogous to the clinical breast images, it has certain limitations in terms of its fabrication method and application. The phantom has been printed in slabs form, which is very complicated to manufacture and it is a time-consuming process.[25]

Although some research has been carried out on the use of 3D printing techniques to develop a breast phantom for MR imaging, only few studies have attempted to

generate a personalized 3D-printed breast phantom based on a realistic breast MR images that can be similar to the anatomical structures seen in human tissues.[26-30] Burfeindt et al[26] reported a new and convenient synthetic procedure to develop an MRI-derived 3D-printed breast phantom for the preclinical use in microwave breast-imaging experiments. Although the phantom has successfully simulated the dielectric properties of the biological breast tissues, it has been designed for microwave breast-imaging rather than for MR imaging system.[26] Furthermore, the importance of realistic phantom structure in the assessment of photoacoustic breast imaging systems for the purpose of simulating the acoustic and optical breast tissues properties was demonstrated in a study by Dantuma et al,[27] in which a semi-anthropomorphic 3D-printed moulds derived from a MRI segmented numerical breast model was developed to produce real breast morphology using polyvinyl chloride plastisol (PVCP). However, there are limits to how far the phantom that has been designed for ultrasound and photoacoustic imaging can be used to simulate the MR imaging characteristics of breast tissues.[27] Moreover, He et al[28] developed a 3D-printed breast phantom for machine calibration and image optimization in multi-modalities imaging, where a mixture of PVC powder and softener (i.e., dioctyl terephthalate) was used as a tissue-mimicking material (TMM) of breast tissues.

Although the study has successful demonstrated the simulation of breast structures, it has certain limitations in terms of the lack of the appearance, variability, and heterogeneity of structures that are presented in the physiological tissues.[28] Another potential limitation is that the T1 and T2 relaxation times of the materials were measured and found to be shorter than those reported in the physiological human breast tissues.[28,29] While most of the aforementioned phantoms address their objectives in the medical imaging discipline, there are currently no phantoms available to evaluate

the breast density based on a realistic morphology of breast structures derived from a MR images of human tissues. Likewise, uncertainties still exist about the most appropriate TMMs that can be used to simulate the MR- related characteristics and appearance of breast structures, particularly fibroglandular tissue. Such a personalized 3D-printed breast model could be used to examine different MR breast-imaging protocols not only to evaluate the breast density but also to determine the impact of applying various image quality parameters on the segmentation/ measurement methods of breast density. Therefore, the aim of this study is to develop a patient-specific 3D-printed breast phantom and to identify the most appropriate materials for simulating the MR imaging characteristics of fibroglandular and adipose tissues.

3.3 Methods

3.3.1 Patient Data

Ethical approval was obtained from Curtin University's Human Research Ethics Committee (HREC) and King Fahd Armed Forces Hospital's (Jeddah) Research and Ethics Committee. A random sample of patients with no history of breast disease was retrospectively reviewed from an existing breast MRI database. The criteria for selecting the subjects were the following: no previous surgery, no radiotherapy treatment on the chest wall, no history of breast cancer, and a Breast Imaging-Reporting and Data System (BI-RADS) classification of 1, indicating a negative likelihood of cancer. A 46-year-old woman was identified by a senior radiology resident to match the selection criteria. The breast MRI examination was performed using 1.5T system (MAGNETOM Aera, Siemens, Germany) with a dedicated breast coil (18 channels). The MR breast imaging protocol was chosen based on the recommendations of a recent systematic review and meta-analysis[20] as high-resolution

non-contrast-enhanced T1-weighted images to allow a precise differentiation between adipose and fibroglandular tissues: TR/TE 11.8/6.0 ms; matrix size 384×384; slice thickness 0.9 mm with no gap.

3.3.2 Image Post-processing and Segmentation Process

A series of image post-processing and segmentation of the volumetric data was performed. First, the anonymized Digital Imaging and Communications in Medicine (DICOM) MR images were imported into the commercially available software Analyze 12.0 (AnalyzeDirect, Inc., Lexana, KS, USA) to segment the non-contrast-enhanced T1-weighted breast images. Second, the breast's boundary was delineated manually to distinguish the breast's body from the surrounding tissues (pectoral muscle, heart, lungs, and thorax) on each 2D slice based on grayscale intensity, displayed in a histogram. Then, the 3D breast volume was created by these 2D images and was subsequently used to design the 3D-printed breast model. Finally, the 3D segmented MR breast volume was saved as a standard tessellation language (STL) file for further image post- processing and 3D printing. Figure 3.1 presents a schematic flowchart of the process of developing a patient-specific 3D-printed breast model using MRI data. For more details, the phantom consists of three main parts: the outer shell, simulating the skin layer, and the internal structures, which include fibroglandular and fat tissues, imitating the breast composition. To generate the skin shell, the STL file containing the 3D segmented MR breast volume was imported into the Blender software, version 2.79b (Blender Foundation, Amsterdam, Netherlands) to hollow the model and ensure that all the internal structures were perfectly extracted.

On the other hand, the DICOM MR breast dataset was loaded into the 3D Slicer software, version 4.10.2 [National Alliance for Medical Image Computing (NA-MIC)]

to segment out the fibroglandular tissue and ensure that all the surrounding structures were completely removed. To increase reliability of the segmentation, each slice was segmented in different orientations using the threshold function, which was adjusted manually. This approach was used to threshold the DICOM dataset so that only the fibroglandular tissue structures were kept in the final segmented data. Subsequently, the segmented fibroglandular model was saved as a STL file and imported into the (version 3.5.474, Autodesk Inc., San Rafael, CA, USA) open-source software for further edit. Any deformities or free-floating objects were removed, and any holes were fixed during the editing process.

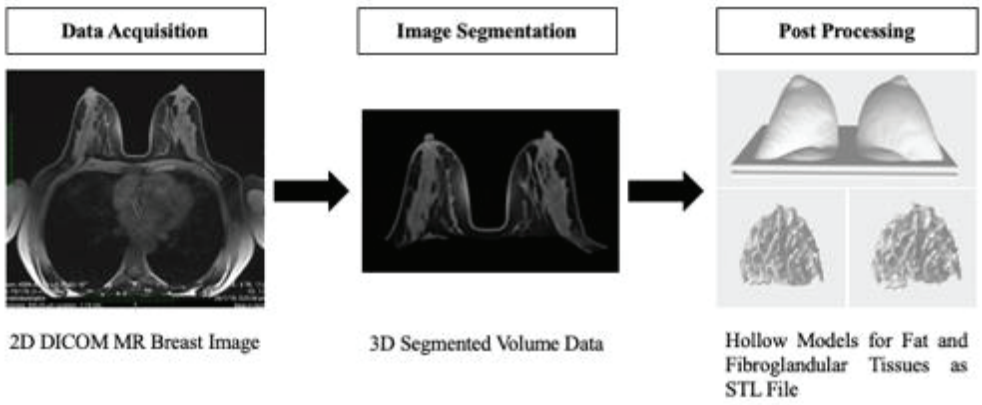

Figure 3.1. Schematic flowchart demonstrates the process of developing a patient-specific 3D-printed breast model.

3.3.3 Overview and Breast Phantom Design

This part is divided into three sections, each detailing the construction process related to the 3D-printed breast model components.

3.3.3.1 Skin Layer

Based on the dimensions of a realistic tissue, the outer phantom shell had an average thickness of 3.0 mm, which corresponds to the normal skin thickness. The cover of the skin shell was designed using a computer-aided design (CAD) software. The skin shell and the cover were fabricated with fused deposition modelling (FDM) technology using polylactic acid (PLA) (Polymaker, Shanghai, China) on a Raise3D N2 Plus 3D printer (Raise3D, Irvine, CA, USA). The skin shell was printed with a layer height of 0.15 mm, average printing time of 40 hours, and a resolution of 12.5 μm (Figure 3.2).

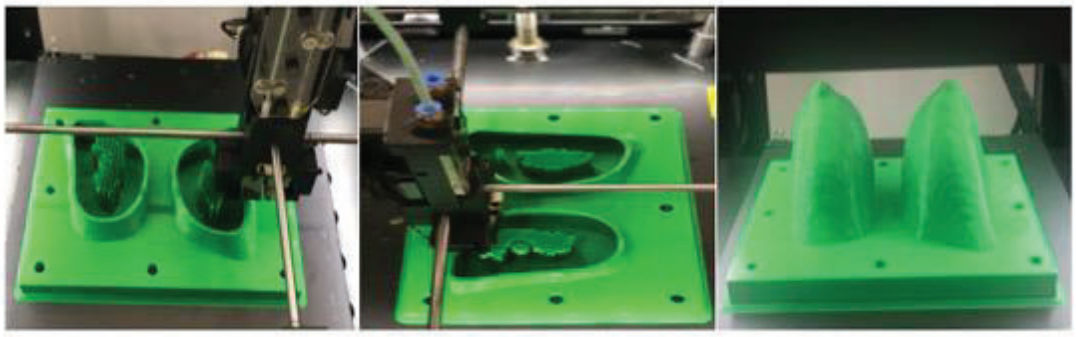

Figure 3.2. External structure of the patient-specific 3D-printed breast phantom that consists of 3 mm thick skin layer and compartments to be filled with fibroglandular and adipose tissues models.

3.3.3.2 Fibroglandular Region

The fibroglandular models constitute the internal component of the 3D-printed breast phantom. While various definitions of the term “breast density” have been proposed, in this study, the term “fibroglandular tissue” is used to refer to the breast density. Naturally, the fibroglandular region contains variable shapes and/or volumes of glandular tissue, includes fibrous or connective tissue. In clinical practice, the evaluation of fibroglandular tissue is based on a subjective assessment recommended by the American College of Radiology (ACR) BI-RADS, which is commonly used for

mammography but also for MRI. The BI-RADS atlas can be described as a classification system that characterises breast density on the basis of the amount of fibroglandular tissue into four categories: (I) almost entirely fat, (II) scattered fibroglandular tissue, (III) heterogeneous fibroglandular tissue, and (IV) extreme fibroglandular tissue.[31,32]

In order to simulate the MR imaging characteristics, the 3D fibroglandular models were designed as hollow structures with an average thickness of 2.0 mm. The fibroglandular models were fabricated using the digital light processing (DLP) technology on an Anycubic Photon S 3D DLP UV resin printer (Shenzhen Anycubic Technology Co. Ltd., Shenzhen, China) using white photopolymer resin (Magma H LINE Photopolymer Resin) from Magma Filament, Malaysia. A curing time of 10 sec per layer, a layer thickness of 0.05 mm, and a resolution of 47 μm were used to fabricate the fibroglandular models. The printing duration for both left and right fibroglandular models was about 17 hours (Figure 3.3).

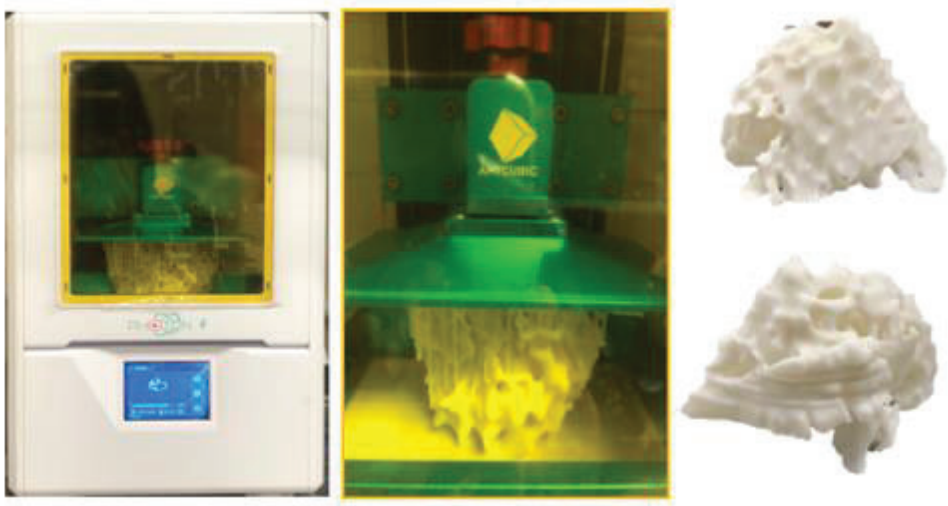

Figure 3.3. Fabrication of the hollow fibroglandular models using the Anycubic photon S high-resolution 3D DLP UV resin printer. The thickness of the wall is 2.0 mm. DLP, digital light processing.

3.3.3.3 Fat/Adipose Region

This region comprises a considerable part of the 3D-printed breast model. It consists of a selected material that simulates the MR imaging relaxation times of adipose tissue.

3.3.3.4 Fibroglandular TMMs

Agarose gels with different concentrations vary in their ability to simulate the MR imaging characteristics of T1 and T2 relaxation times of an extensive range of human tissues.[33,34] In a study investigating the T1 and T2 relaxation times of four sample phantom liquids, Gach et al[33] found that silicone oil had the longest T1 and T2 times on a 3T MRI system: 1,068.29±5.95 and 566.40±4.68 ms, respectively. These results provide further support to the hypothesis that agarose gel or silicone oil could be used to mimic the MR imaging characteristics of fibroglandular tissue based on T1 and/or T2 relaxation times. Thus, four different raw materials were scanned to determine which one could be used to mimic the T1 and/or T2 relaxation times of fibroglandular tissue. The candidate materials were silicone oil with a viscosity of 50 mm^2/s at 25 °C (TEX Chemical Inc., Country), agarose (Thermo Fisher, Waltham, MA, USA), silicone rubber RTV (Craftiviti Sdn. Bhd., Selangor, Malaysia), and fish oil (Blackmores, Sydney, Australia) (Figure 3.4).

3.3.3.5 Fat/Adipose TMMs

As Niebuhr et al[35] reported, olive oil successfully simulates the MR imaging relaxation times of adipose tissue in abdominal and pelvic tissues measured *in-vivo*. In another study, Niebuhr et al[34] found that peanut oil efficiently simulates the MR imaging characteristics of subcutaneous fat for pelvis phantoms. Peanut oil was preferred in this study for several reasons, including its relatively similar MR imaging

characteristics (T1 and T2 relaxation times) for adipose tissue, its translucent appearance, and its high oxidation stability.[34,35] These characteristics suggest that peanut oil could be a performed material to mimic the T1 and/or T2 relaxation times of breast adipose tissue. Two types of peanut oil were scanned for testing: peanut oil Basso (raw material: Arachis hypogea; price: US$ 5/1L; Basso), and peanut oil Pressed Purity (raw materials: oleic acid (96.2%) and linoleic acid (13.2%), price: US$18/1.5L, Proteco Oils) (Figure 3.4).

3.3.4 Breast Phantom Construction

The T1 relaxation times of the five selected materials (agarose gel, silicone rubber with/without fish oil, silicone oil, and peanut oil) were measured at room temperature using a 3T MRI system to determine which ones could be used to mimic the MR imaging characteristics of fibroglandular and adipose tissues. The results were then compared to the reference values of T1 relaxation times of the corresponding tissues. Following this, the materials that matched the T1 relaxation times of the respective tissues were chosen to fill the 3D-printed hollow breast shells.

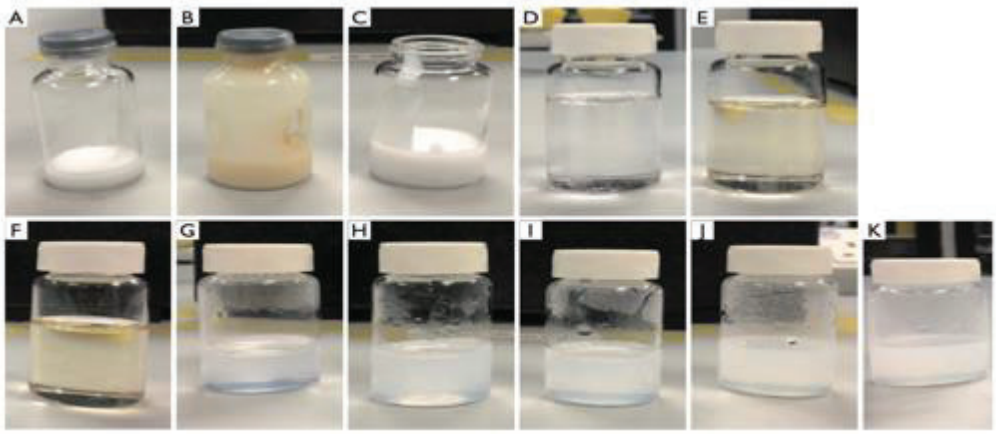

Figure 3.4. Test raw materials. **(A)** Silicone rubber; **(B)** silicone rubber with fish oil; **(C)** fresh silicone rubber; **(D)** silicone oil with a viscosity of 50 mm^2/s; **(E)** peanut oil (basso); **(F)** peanut oil (pressed purity); **(G)** agarose gel 0.5 wt%; **(H)** agarose gel 1.0 wt%; **(I)** agarose gel 1.5 wt%; **(J)** agarose gel 2.0 wt%; **(K)** agarose gel 2.5 wt%.

3.4 Results

3.4.1 3D-printed Hollow Models

The 3D-printed models of the hollow skin and fibroglandular region shells were scanned on a 3T MRI system (MAGNETOM Prisma, Siemens Healthcare, Erlangen, Germany) to check whether the models printed with the PLA or the photopolymer resin produce MR signals corresponding with these tissue features. Fortunately, no MR signal was observed from scanning the 3D-printed hollow models, indicating the possibility of using these materials for breast structure simulation and further patient models. It is important to note that the selected materials were checked when the 3D printing was initially performed and then checked again at the end of the breast phantom construction.

3.4.2 Sample Characteristics

The five selected materials were scanned on the same 3T MRI system, with the materials placed in the 18-channel body and 32-channel spine coils. The MR breast scanning was chosen based on the institutional clinical protocol using 3D T1- and T2-weighted turbo spin echo (TSE) sequences: TR/TE 650.0/10.0 ms; matrix size 384×384; slice thickness 2.9 mm; no gap, and TR/TE 6,080.0/78.0 ms; matrix size 384×384; slice thickness 4.0 mm; no gap, respectively.

Figure 3.5 presents the MR imaging T1 relaxation times of the five materials (agarose gel, silicone rubber with/without fish oil, silicone oil, and peanut oil) simulating the breast composition. Figure 3.5D shows that the T1-weighted image of the silicone oil was associated with a mid-grey signal intensity, which is usually related to water-based tissues characterized by a moderate T1 relaxation time. On the other hand, Figure

3.5E,F shows that the T1-weighted images of the peanut oils indicated a high signal intensity, which was within expectation, as fat-based tissues have a short T1 relaxation time. In contrast, the T1-weighted images of the agarose gel with different concentrations, 0.5 to 2.5 wt%; were associated with low signal intensity, which is mainly observed in free water and other fluids (Figure 3.5G,H,I,J,K).

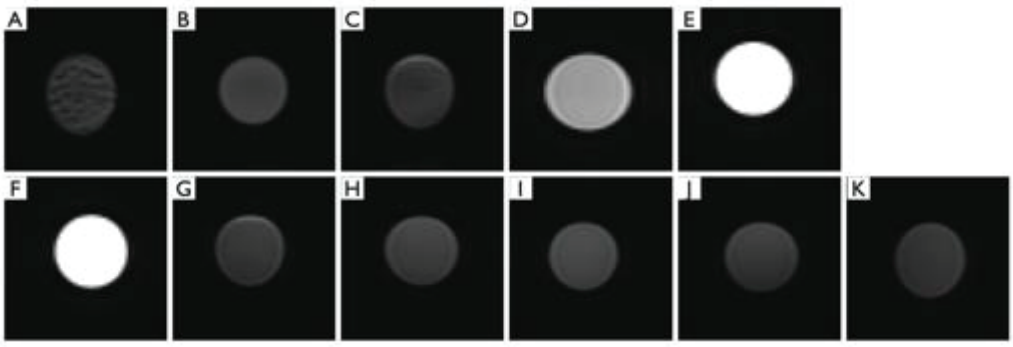

Figure 3.5. T1-weighted images. **(A)** Silicone rubber; **(B)** silicone rubber with fish oil; **(C)** fresh silicone rubber; **(D)** silicone oil with a viscosity of 50 mm^2/s; **(E)** peanut oil (basso); **(F)** peanut oil (pressed purity); **(G)** agarose gel 0.5 wt%; **(H)** agarose gel 1.0 wt%; **(I)** agarose gel 1.5 wt%; **(J)** agarose gel 2.0 wt%; **(K)** agarose gel 2.5 wt%.

3.4.3 T1 Relaxation Times of the Sample Characteristics

The T1 relaxation times of these five materials are listed in Table 3.1. Silicone oil had a T1 relaxation time similar to that of fibroglandular tissue: 1,515.8±105.5 ms. In contrast, the Basso and Pressed Purity peanut oils had T1 relaxation times analogous to that of adipose tissue: 405.4±15.1 and 404.1±10.5 ms, respectively. For comparison, the T1 and T2 relaxation times of fibroglandular and adipose tissues measured using a 1.5T and a 3T MRI system are presented in Table 3.2.

As shown in Table 3.1, the agarose gel with different concentrations, ranging from 0.5 to 2.5 wt%, had the longest T1 relaxation times, which are similar to that of free water. The interesting finding is that the lowest concentration was associated with the highest

T1 relaxation time. Overall, the results presented in Table 3.1 and Figure 3.5 indicate that the silicone and peanut oils closely resemble the MR imaging T1 relaxation times of the fibroglandular and adipose tissues, respectively. Therefore, these materials were chosen to fill the 3D-printed hollow models.

Figure 3.6 provides an overview of the construction process of the 3D-printed breast phantom. The two fibroglandular shell models were filled with a silicone oil and then sealed using UV-curable photopolymer resin. Following this, the filled fibroglandular shell models were fixed inside the skin shell model using acrylic-based adhesive. Further, the space between the fibroglandular and skin shell models was filled with peanut oil. A home-made silicone gasket and cover were used to enclose the breast phantom. Finally, the cover was tighten using the commercially available polycarbonate bolt and nuts.

Table 3.1. T1 Relaxation times of different materials for tissue surrogates used in the experiment.

Phantom, TMM	**T1 (average SD, ms), 3T Siemens MR Scanner**
Fibroglandular shell	No signal
Skin/outer shell	No signal
Silicone rubber	577.2 ± 107.8
Silicone rubber with fish oil	902.1 ± 120.5
Fresh Silicone rubber	638.3 ± 108.5
Silicone oil 50 mm^2/s *	1515.8 ± 105.5
Peanut oil (Basso)	405.4 ± 15.1
Peanut Oil (Pressed Purity)	404.1 ± 10.5
Agarose gel 0.5 wt%	4015.5 ± 100.2
Agarose gel 1.0 wt%	3877.8 ± 130.5
Agarose gel 1.5 wt%	3404.8 ± 255.9
Agarose gel 2.0 wt%	3572.6 ± 100.4
Agarose gel 2.5 wt%	3617.2 ± 101.5

*, Viscosity unit. TMM, tissue-mimicking material.

Table 3.2. T1 and T2 Relaxation times of the breast tissues at 1.5T and 3T using FSE-IR scans.[36]

Tissue (reference)	T1 (average SD, ms), 1.5T	T2 (average SD, ms), 1.5T	T1 (average SD, ms), 3T	T2 (average SD, ms), 3T
Adipose/Fat	372.04 ± 8.6	53.33 ± 2.11	449.27 ± 26.09	52.96 ± 1.54
Fibroglandular	1135.98 ± 151.37	57.51 ± 10.15	1324.42 ± 167.63	54.36 ± 9.35

FSE-IR, Fast Spin Echo-Inversion Recovery.

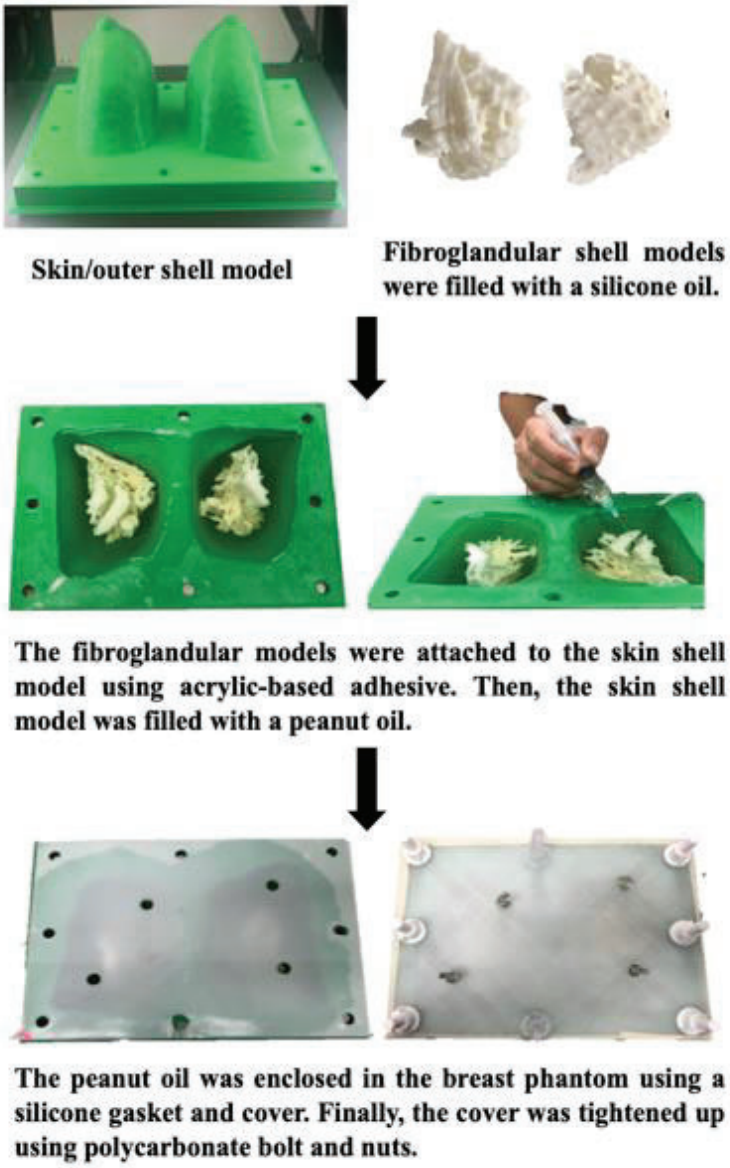

Figure 3.6. Flow chart showing 3D construction of the breast phantom. 3D-printing technique was used to create the hollow shells for skin and fibroglandular regions. Fibroglandular and adipose tissues were simulated using silicone and peanut oils, respectively.

3.4.4 Scanning of the 3D-printed Breast Phantom

The MR images of the phantom were acquired following the same breast imaging protocols described in the Results, Sample Characteristics. The phantom was scanned in a prone position using a dedicated 18-channel breast coil. Figure 3.7 shows the T1- and T2-weighted MR images of a patient-specific 3D-printed breast phantom using silicone and peanut oils as surrogates of the fibroglandular and adipose tissues, respectively. These oils presented an acceptable level of contrast and MR-related characteristics in both the T1- and the T2-weighted images. One of the most noticeable features of this phantom is that it is slightly inhomogeneous. However, this feature simulates the considerable inhomogeneity as often observed among the irregular distribution of the patient. Overall, the results shown in Table 3.1 and Figure 3.5 indicate that the MR imaging T1 relaxation times of the silicone and peanut oils used for the simulation of fibroglandular and adipose tissues are similar to their respective reference values reported in the literature.

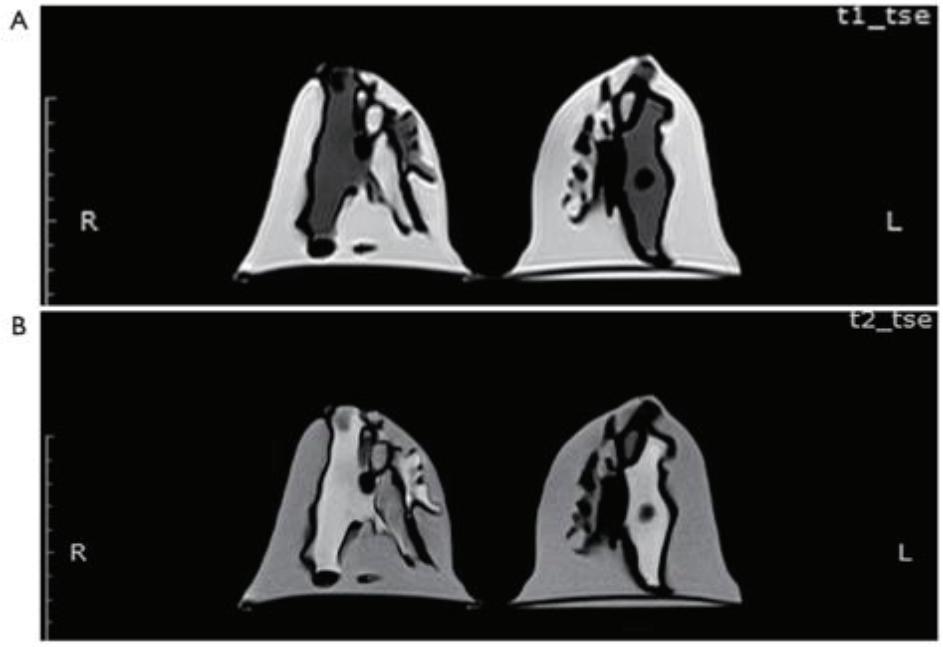

Figure 3.7. MR images of the 3D-printed breast phantom. **(A)** T1-weighted image; **(B)** T2-weighted image using TSE scans. TSE, turbo spin echo.

3.5 Discussion

This study aimed to develop a patient-specific 3D-printed breast phantom and to determine the most appropriate materials for simulating the MR imaging characteristics of fibroglandular and adipose tissues. Anthropomorphic shapes of skin and fibroglandular tissues were constructed using 3D-printing techniques based on the segmentations of breast MR images from a selected healthy patient's data. All the 3D skin and fibroglandular region shells were designed as hollow structures using PLA and photopolymer resin. Since no MR signal was generated by the 3D-printed hollow models of those corresponding shells, different materials were selected to search for suitable ones with silicone oil and peanut oil being the most appropriate materials with similar T1 relaxation times to fibroglandular and adipose tissues.

It was assumed that the T1 relaxation times would effectively supplement and extend our knowledge about the selected materials since most organs' T1 values are five times longer than their T2 values. A comparison of the T1 relaxation times of the scanned materials with breast structure and literature reports showed that the silicone and peanut oils closely resemble the MR imaging T1 relaxation times of the fibroglandular and adipose tissues, respectively. Surprisingly, this study did not find a significant difference in the T1 relaxation times between different concentrations of agarose gel, which exhibited long T1 relaxation times, similar to that of water. Nevertheless, the agarose gel can be mixed with a gadolinium-based contrast agent for T1 adaptation, and can thus be used to simulate the MR imaging relaxation times of a wide range of human tissues. However, this would be costly and requires precautions when handling the contrast agent. Another unexpected finding was the slight difference in the T1 relaxation times between the Basso and Pressed Purity peanut oils. However, the

observed difference was not significant. It is also worth noting that the Basso peanut oil was preferable due to its purity, availability, and low cost.

The most important clinically relevant finding was that the silicone and peanut oils demonstrated an acceptable level of contrast and MR-related characteristics of breast structures in both the T1- and the T2-weighted images. These findings are in line with Niebuhr et al,[34] who suggested that peanut oil efficiently simulates the MR imaging characteristics of subcutaneous fat for pelvis phantoms. In accordance with the present results, previous studies demonstrated that silicone oil with a viscosity of 50 mm^2/s had the longest T1 and T2 relaxation times on a 3T MRI system.[33,35] However, silicone oil was not previously used for simulating the MR-related characteristics of breast structures, particularly fibroglandular tissue. Thus, this study presents interesting findings to encourage more research along this direction in breast phantom.

The observed correlation between silicone oil's T1 relaxation time and fibroglandular tissue could be attributed to its chemical composition and physical properties such as viscosity and density. This preliminary finding: suggests that silicone and peanut oils can be used to efficiently simulate the MR imaging characteristics of breast structures and produce further models. An implication of this is the possibility to examine different MR breast imaging protocols to identify the most appropriate for the quantitative assessment of breast density. For future investigations, it might be possible to use different chemical compositions and physical properties of silicone oils to evaluate the MR imaging relaxation times of breast structures. Since the relationship between silicone oil and fibroglandular tissue has not been studied, further research is required to better understand it.

Although the study has successfully designed and constructed a patient-specific 3D-printed breast phantom, the findings are subject to several limitations. The study was not specifically designed to evaluate the mechanical properties of breast tissue components, such as elastic modulus or tissue strength. Examining the mechanical features along with the physical properties of selected materials could provide an idea of their characteristics and allow more detailed comparisons to the human breast tissue. Moreover, there are certain drawbacks to the use of 3D printing techniques for the construction of skin and fibroglandular hollow shells. One of them is the potential risk for some of the connected structures to break easily during the cleaning process. For this reason, several models of varying wall thicknesses, ranging between 1.0 and 2.5 mm, were printed. However, increasing the thickness of photopolymer resin can cause considerable deformation of the fibroglandular structure. Another potential limitation is due to the complexity of the fibroglandular structure, with holes formed in the final mould. For this reason, a wrapping process was performed manually for each model to ensure that all the small gaps had been completely sealed.

A further study on a patient-specific 3D-printed breast phantom will be conducted with a focus on different percentages of fibroglandular tissue. This can correspond to the four categories of the ACR BI-RADS atlas, thus allowing an estimation of the volumes of fibroglandular tissue. Varying its proportions will allow the quantitative assessments of breast density to be performed.

3.6 Conclusion

In this study, a patient-specific 3D-printed breast phantom was successfully constructed using silicone and peanut oils to simulate the MR-related characteristics of breast fibroglandular and adipose tissues. The proposed methodologies can be used as a preliminary work for breast structure simulations and the construction of further patient models using MRI dataset. The phantom can be used to test different breast MR imaging protocols to determine the optimum scanning parameters and analysis algorithms for the quantitative assessment of breast density.

3.7 References

1. Sardanelli F, Boetes C, Borisch B, Decker T, Federico M, Gilbert FJ, Helbich T, Heywang-Köbrunner SH, Kaiser WA, Kerin MJ, Mansel RE. Magnetic resonance imaging of the breast: Recommendations from the EUSOMA working group. Eur J Cancer. 2010; 46(8):1296-1316.
2. Londero V, Zuiani C, Linda A, Girometti R, Bazzocchi M, Sardanelli F. High-risk breast lesions at imaging-guided needle biopsy: Usefulness of MRI for treatment decision. Am J Roentgenol. 2012; 199(2):W240-W250.
3. Mann RM, Balleyguier C, Baltzer PA, Bick U, Colin C, Cornford E, Evans A, Fallenberg E, Forrai G, Fuchsjäger MH, Gilbert FJ, Helbich TH, Heywang-Köbrunner SH, Camps-Herrero J, Kuhl CK, Martincich L, Pediconi F, Panizza P, Pina LJ, Pijnappel RM, Pinker-Domenig K3, Skaane P, Sardanelli F. European Society of Breast Imaging (EUSOBI), with language review by Europa Donna–The European Breast Cancer Coalition. Breast MRI: EUSOBI recommendations for women's information. Eur Radiol. 2015; 25:3669-3678.

4. Heller SL, Yeong Lin LL, Melsaether AN, Moy L, Gao Y. Hormonal Effects on Breast Density, Fibroglandular Tissue, and Background Parenchymal Enhancement. Radiographics. 2018; 38(4):983-996.
5. Chen JH, Chang YC, Chang D, Wang YT, Nie K, Chang RF, Nalcioglu O, Huang CS, Su MY. Reduction of breast density following tamoxifen treatment evaluated by 3-D MRI: Preliminary study. Magn Reson Imaging. 2011; 29(1):91-98.
6. Wang J, Azziz A, Fan B, Malkov S, Klifa C, Newitt D, Yitta S, Hylton N, Kerlikowske K, Shepherd JA. Agreement of mammographic measures of volumetric breast density to MRI. PLoS ONE. 2013; 8(12):e81653.
7. Tagliafico A, Bignotti B, Tagliafico G, Astengo D, Martino L, Airaldi S, Signori A, Sormani MP, Houssami N, Calabrese M. Breast density assessment using a 3T MRI system: Comparison among different sequences. PLoS ONE. 2014; 9(6):e99027.
8. Lienart V, Carly B, Kang X, Guzy L, Sajovitz AM, Liebens F. Effect of preventive hormonal therapy on breast density: A systematic qualitative review. Sci World. 2014; 2014:942386.
9. Tagliafico A, Tagliafico G, Astengo D, Airaldi S, Calabrese M, Houssami N. Comparative estimation of percentage breast tissue density for digital mammography, digital breast tomosynthesis, and magnetic resonance imaging. Breast Cancer Res Treat. 2013; 138(1):311-317.
10. Nayeem F, Ju H, Brunder DG, Nagamani M, Anderson KE, Khamapirad T, Lu LJ. Similarity of fibroglandular breast tissue content measured from magnetic resonance and mammographic images and by a mathematical algorithm. Int J Breast Cancer. 2014; 2014:961679.

11. Lin M, Chan S, Chen JH, Chang D, Nie K, Chen ST, Lin CJ, Shih TC, Nalcioglu O, Su MY. A new bias field correction method combining N3 and FCM for improved segmentation of breast density on MRI. Med Phys. 2011; 38(1):5-14.
12. Doran SJ, Hipwell JH, Denholm R, Eiben B, Busana M, Hawkes DJ, Leach MO, Silva ID. Breast MRI segmentation for density estimation: Do different methods give the same results and how much do differences matter? Med Phys. 2017; 44(9):4573-4592.
13. Tagliafico A, Tagliafico G, Tosto S, Chiesa F, Martinoli C, Derchi LE, Calabrese M. Mammographic density estimation: comparison among BI-RADS categories, a semi-automated software and a fully automated one. Breast. 2009; 18(1):35-40.
14. Boston RC, Schnall MD, Englander SA, Landis JR, Moate PJ. Estimation of the content of fat and parenchyma in breast tissue using MRI T1 histograms and phantoms. Magn Reson Imaging. 2005; 23(4):591-599.
15. Klifa C, Carballido-Gamio J, Wilmes L, Laprie A, Shepherd J, Gibbs J, Fan B, Noworolski S, Hylton N. Magnetic resonance imaging for secondary assessment of breast density in a high-risk cohort. Magn Reson Imaging. 2010; 28(1):8-15.
16. Chang DH, Chen JH, Lin M, Bahri S, Yu HJ, Mehta RS, Nie K, Hsiang DJ, Nalcioglu O, Su MY. Comparison of breast density measured on MR images acquired using fat-suppressed versus non-fat-suppressed sequences. Med Phys. 2011; 38(11):5961-5968.

17. Choi YJ, Chen JH, Yu HJ, Li Y, Su MY. Impact of Different Analytic Approaches on the Analysis of the Breast Fibroglandular Tissue Using Diffusion Weighted Imaging. Biomed Res Int. 2017; 2017:1094354.
18. McDonald ES, Schopp JG, Peacock S, DeMartini WB, Rahbar H, Lehman CD, Partridge SC. Diffusion-weighted MRI: Association between patient characteristics and apparent diffusion coefficients of normal breast fibroglandular tissue at 3 T. Am J Roentgenol. 2014; 202(5):W496-W502.
19. Ledger AE, Scurr ED, Hughes J, Macdonald A, Wallace T, Thomas K, Wilson R, Leach MO, Schmidt MA. Comparison of Dixon sequences for estimation of percent breast fibroglandular tissue. PLoS ONE. 2016; 11(3):e0152152.
20. Sindi R, Sá Dos Reis C, Bennett C, Stevenson G, Sun Z. Quantitative Measurements of Breast Density Using Magnetic Resonance Imaging: A Systematic Review and Meta-Analysis. J Clin Med. 2019; 8(5):745.
21. Matsumoto JS, Morris JM, Foley TA, Williamson EE, Leng S, McGee KP, Kuhlmann JL, Nesberg LE, Vrtiska TJ. Three-dimensional physical modelling: Applications and experience at Mayo Clinic. Radiographics. 2015; 35(7):1989-2006.
22. Sun Z, Lau I, Wong YH, Yeong CH. Personalized three-dimensional printed models in congenital heart disease. J Clin Med. 2019; 8(4):522.
23. Perica ER, Sun Z. A Systematic Review of Three-dimensional Printing in Liver Disease. J Digit Imaging. 2018; 31(5):692-701.
24. Sun Z, Liu D. A systematic review of clinical value of three-dimensional printing in renal disease. Quant Imaging Med Surg. 2018; 8(3):311-325.

25. Carton AK, Bakic P, Ullberg C, Derand H, Maidment AD. Development of a physical 3D anthropomorphic breast phantom. Med Phys. 2011; 38(2):891-896.
26. Burfeindt MJ, Colgan TJ, Mays RO, Shea JD, Behdad N, Van Veen BD, Hagness SC. MRI-Derived 3-D-Printed Breast Phantom for Microwave Breast Imaging Validation. IEEE Antennas Wirel Propag Lett. 2012; 11:1610-1613.
27. Dantuma M, van Dommelen R, Manohar S. Semi-anthropomorphic photoacoustic breast phantom. Biomed Opt Express. 2019; 10(11):5921-5939.
28. He Y, Liu Y, Dyer BA, Boone JM, Liu S, Chen T, Zheng F, Zhu Y, Sun Y, Rong Y, Qiu J. 3D-printed breast phantom for multi-purpose and multi-modality imaging. Quant Imaging Med Surg. 2019; 9(1):63-74.
29. He Y, Qin S, Dyer BA, Zhang H, Zhao L, Chen T, Zheng F, Sun Y, Shi L, Rong Y, Qiu J. Characterizing mechanical and medical imaging properties of polyvinyl chloride- based tissue-mimicking materials. J Appl Clin Med Phys. 2019; 20(7):176-183.
30. Freed M, de Zwart JA, Loud JT, El Khouli RH, Myers KJ, Greene MH, Duyn JH, Badano A. An anthropomorphic phantom for quantitative evaluation of breast MRI. Med Phys. 2011; 38(2):743-753.
31. American College of Radiology. ACR BI-RADS® Atlas: Breast Imaging Reporting and Data System. Reston: American College of Radiology, 2013.
32. Mainiero MB, Lourenco A, Mahoney MC, Newell MS, Bailey L, Barke LD, D'Orsi C, Harvey JA, Hayes MK, Huynh PT, Jokich PM, Lee SJ, Lehman CD, Mankoff DA, Nepute JA, Patel SB, Reynolds HE, Sutherland ML, Haffty BG. ACR Appropriateness Criteria Breast Cancer Screening. J Am Coll Radiol. 2016; 13(11):R45-R49.

33. Gach HM. T1 and T2 and complex permittivities of mineral oil, silicone oil, and glycerol at 0.35, 1.5, and 3 T. Med Phys. 2019; 46(4):1785-1792.
34. Niebuhr NI, Johnen W, Echner G, Runz A, Bach M, Stoll M, Giske K, Greilich S, Pfaffenberger A. The ADAM-pelvis phantom-an anthropomorphic, deformable and multimodal phantom for MRgRT. Phys Med Biol. 2019; 64(4):04NT05.
35. Niebuhr NI, Johnen W, Güldaglar T, Runz A, Echner G, Mann P, Möhler C, Pfaffenberger A, Jäkel O, Greilich S. Radiological properties of tissue surrogates used in a multimodality deformable pelvic phantom for MR-guided radiotherapy. Med Phys. 2016; 43(2):908-916.
36. Rakow-Penner R, Daniel B, Yu H, Sawyer-Glover A, Glover GH. Relaxation times of breast tissue at 1.5 T and 3T measured using IDEAL. J Magn Reson Imaging. 2006; 23(1):87-91.

4. Chapter 4

Quantitative Measurement of Breast Density Using Personalized 3D-Printed Breast Model for Magnetic Resonance Imaging

4.1 Abstract

Despite the development and implementation of several MRI techniques for breast density assessments, there is no consensus on the optimal protocol in this regard. This study aimed to determine the most appropriate MRI protocols for the quantitative assessment of breast density using a personalized 3D-printed breast model. The breast model was developed using silicone and peanut oils to simulate the MRI related-characteristics of fibroglandular and adipose breast tissues, and then scanned on a 3T MRI system using non-fat-suppressed and fat-suppressed sequences. Breast volume, fibroglandular tissue volume, and percentage of breast density from these imaging sequences were objectively assessed using Analyze 14.0 software. Finally, the repeated-measures analysis of variance (ANOVA) was performed to examine the differences between the quantitative measurements of breast volume, fibroglandular tissue volume, and percentage of breast density with respect to the corresponding sequences. The volume of fibroglandular tissue and the percentage of breast density were significantly higher in the fat-suppressed sequences than in the non-fat-suppressed sequences ($p < 0.05$); however, the difference in breast volume was not statistically significant ($p = 0.529$). Further, a fat-suppressed T2-weighted with turbo inversion recovery magnitude (TIRM) imaging sequence was superior to the non-fat- and fat-suppressed T1- and T2-weighted sequences for the quantitative measurement of breast density due to its ability to represent the exact breast tissue compositions. This study shows that the fat-suppressed sequences tended to be more useful than the non-fat-suppressed sequences for the quantitative measurements of the volume of fibroglandular tissue and the percentage of breast density.

Keywords MRI; fibroglandular tissue; breast density; 3D-printed model; fat suppression; TIRM

4.2 Introduction

Breast density, a measure of dense fibroglandular tissue relative to non-dense fatty tissue, has been determined as an independent risk factor for developing breast cancer.[1–4] Previous studies have reported that the potential risk of breast cancer in women with dense breasts is three- to five-fold higher than in women with fatty breasts.[5–7] Recent developments in breast cancer screening have intensified the need for a standardized imaging protocol and/or measurement method for the evaluation of breast density predominantly for women at an elevated risk of developing breast cancer, such as those with high breast density.[4,8–10] A considerable amount of literature has been published on the assessment of breast density with several methods and algorithms proposed to segment and/or measure breast density using MRI datasets.[11–19] Nevertheless, research has consistently shown that these methods/algorithms seem to have certain drawbacks, mostly due to the use of a semi-automatic approach or a high-level of dependency on user interaction. Likewise, numerous MR breast-imaging protocols have been applied to the screening and/or the assessment of breast density, ranging from contrast- to non-contrast-enhanced imaging with or without the implementation of fat-suppression techniques.[3,4,8–10,20–25] To date, there has been little consensus on the optimal MR breast-imaging protocol and measurement method for breast density screening and/or assessment, especially in the context of women with dense breast tissues.

The dynamic contrast-enhanced (DCE)-MRI technique has been widely used for the screening of women at high risk of breast cancer and has been included in standard clinical breast MRI protocols.[4,8] Despite its long clinical success, DCE-MRI has certain disadvantages, such as long scanning time, high cost, and potential harm caused

by the contrast agent.[4,26] Although contradictory findings have been reported in the literature about the precipitation and accumulation of gadolinium contrast-based agents in the brain, there is no general agreement regarding the risk of repeated gadolinium administration.[4,27–29] Nevertheless, questions have been raised about the safety of prolonged use of DCE-MRI as a primary screening method for the detection of breast cancer and/or the assessment of breast density. On the other hand, the fat-suppression technique has been suggested in breast MRI to improve the visibility of pathology, contrast enhancement, and image quality, thus allowing for better differentiation between dense fibroglandular and non-dense fatty tissues.[17,30] It has been combined with other techniques and/or sequence types due to the difficulty of eliminating the high signal intensity associated with fatty tissues.[17,30] Several methods have been proposed for fat suppression in breast MRI, including chemical shift spectral-selective saturation (CHESS) based on the chemical shift variation between fat and water, inversion recovery (IR) based on variation in T1 relaxation time, hybrid CHESS–inversion recovery methods, and Dixon fat–water separation based on phase variation between fat and water signals at different echo times (TEs).[3,17,20,30–32]

Non-fat-suppressed and fat-suppressed T1-weighted images are frequently used with either 2D spin echo (SE) or 3D gradient echo (GRE) in standard clinical breast MRI protocols.[8,17] Nevertheless, there is no consensus as to which of these sequences/techniques is the most efficient in this regard. The American College of Radiology (ACR) has recommended that the fat-suppressed images with high spatial resolution be used in clinical breast MRI protocols as images acquired with this sequence can eliminate misregistration, which mainly occurs when a patient moves during the acquisition of pre- and post-contrast images.[8,17] However, this recommendation contrasts with that of the European Society of Breast Imaging

(EUSOBI), which considers non-fat-suppressed sequences based on the acquisition of subtraction images more useful.[17,33] Despite this, there seems to be some consensus that other breast MRI techniques, including T2-weighted images, DCE, and diffusion-weighted imaging (DWI), tend to benefit from its combination with fat-suppression techniques for several reasons.[1,8,17,30] For instance, turbo inversion recovery magnitude (TIRM), a type of inversion recovery sequence with the advantage of short image acquisition time, has been widely used in the delineation of tumor and/or lymphatic spread and could possibly be combined with fat-suppression technique for the assessment of breast density.[4,34] Patient-specific 3D-printed breast models, derived from a patient's MR imaging data and comparable to the anatomical structures of human tissues, can be a valuable tool for examining different breast MRI protocols, testing the radio frequency coils, and evaluating system performance.[35–42] The aim of this study is to determine the most appropriate MR breast-imaging protocols for the quantitative assessment of breast density using a personalized 3D-printed breast model based on an objective comparison between the non-fat-suppressed and fat-suppressed sequences. We hypothesize that fat-suppressed sequences allow for more accurate assessment of breast density while TIRM with fat-suppressed sequence further enhances its accuracy in quantitative assessment of breast density.

4.3 Materials and Methods

4.3.1 Study Subject: A Personalized 3D-Printed Breast Model

A personalized 3D-printed breast model which was developed in our previous study[43] used 3D-printing techniques and tissue-mimicking materials (TMMs) with the intention of simulating the MR-related characteristics of fibroglandular and adipose breast tissues for the quantitative assessment of breast density. The model consisted of

two main parts: an outer shell to simulate the breast outline, and an inner shell filled with silicone and peanut oils to mimic the internal breast compositions. The results showed that the silicone and peanut oils successfully resemble the MR-imaging characteristics and T1 relaxation times of fibroglandular and adipose breast tissues, respectively.[43] This combination of findings further supports the hypothesis that such a model could be used to examine different MR breast-imaging protocols in order to determine the optimum for the quantitative assessment of breast density. Figure 4.1 demonstrates the schematic flowchart of the construction process for developing a personalized 3D-printed breast model.

4.3.2 MR Scanning Protocol

The 3D-printed breast model was scanned on a 3T MRI system (MAGNETOM Prisma, Siemens Healthcare, Erlangen, Germany) in a prone position using a dedicated 18-channel breast coil. Different MR imaging sequences were applied to improve the visibility of structure and contrast enhancement, thus allowing for better differentiation between fatty non-glandular and glandular structures. The site's standard clinical breast MRI protocols of the site were used with no further modification and/or adjustment to the technical parameters. Table 4.1 displays the image acquisition parameters of the six MR imaging sequences used in this study.

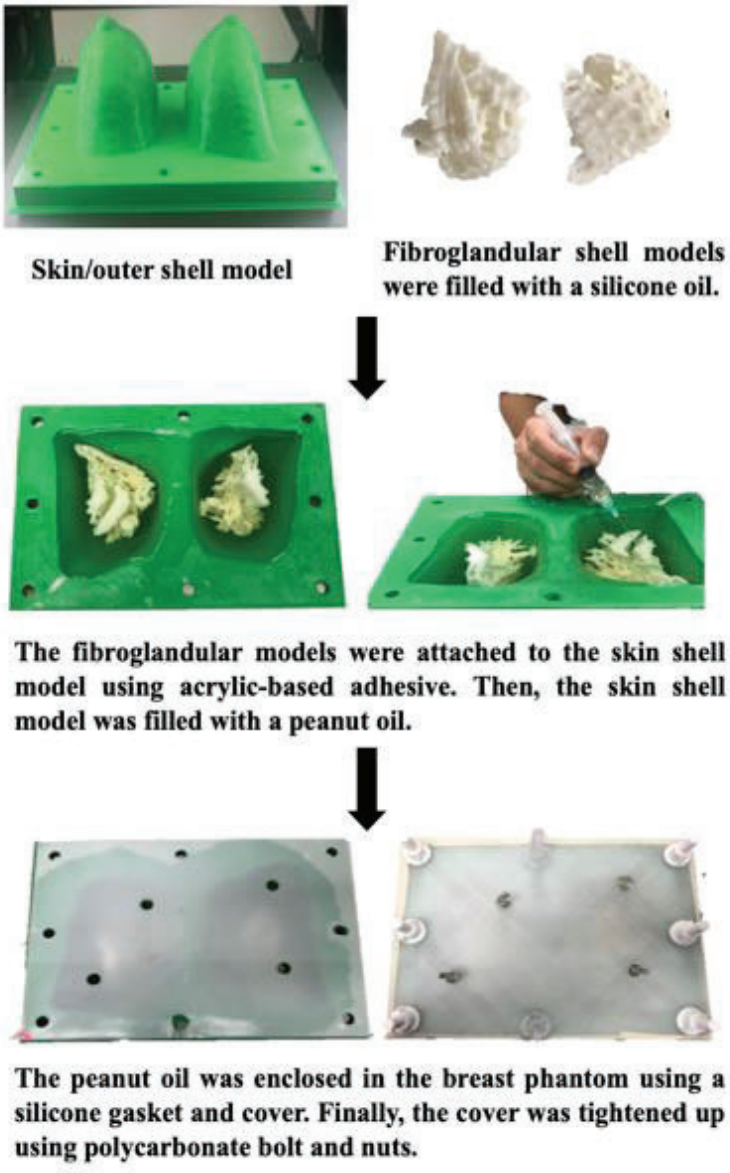

Figure 4.1. Flow chart demonstrates the construction process of the personalized 3D-printed breast model for MRI.[43]

4.3.3 Quantitative Measurement: Breast Volume, Fibroglandular Tissue Volume, and Percentage of Breast Density

Breast volume and fibroglandular tissue volume were objectively measured with a semi-automated segmentation method using a commercially available biomedical imaging software, Analyze V 14.0 (AnalyzeDirect, Inc., Lexana, KS, USA). Two steps

were performed to measure the percentage of breast density from MRI data: breast segmentation and fibroglandular tissue segmentation. The purpose of breast segmentation is to separate the breast's body from the surrounding structure and/or background, while fibroglandular tissue segmentation separates the glandular from the fatty tissue.

To differentiate the breast's body from the background, the breast's boundary was first delineated semi-automatically using an interactive tool based on the threshold signal intensity function by setting seed points on a series of 2D axial slices comprising the entire breast volume. The minimum and maximum threshold limits were then adjusted to define the region of interest. The software spontaneously interpolated between these slices and generated a mask of the whole breast volume. Once the breast's body was segmented out, an automated method incorporating several morphological processing operations and spatial filters were used to segment out the fibroglandular tissue from the surrounding fatty tissue. Upon completion of this segmentation process, the breast volume and fibroglandular tissue volume were measured using a 3D-measurement tool based on the size intensity function. The percentage of breast density was then computed as the ratio of the fibroglandular tissue volume relative to the total breast volume. Finally, the results were analyzed to assess the differences between the measurement of breast volume, fibroglandular tissue volume, and percentage of breast density based on the different MRI sequences.

4.3.4 Data Synthesis

The acquisition of the different MRI sequences and the implementation of several fat-suppression techniques, as applied in the proposed study, are considered to be

technically heterogeneous. To address this complexity and provide more objective comparisons, the six MRI sequence compartments were re-configured into a two-way cross-classification, namely two fat-suppression categories: non-fat-suppression MRI sequences (i.e., MR Seq. 1, 2, and 3) and fat-suppression MRI sequences (i.e., MR Seq. 4, 5, and 6). For the purpose of the analysis, the segmentation processes of both the breast volume and the fibroglandular tissue volume were performed three times, thus extracting three segments from each MRI sequence. Subsequently, the measurements were conducted three times with respect to the volume of the breast, the volume of the fibroglandular tissue, and, thereby, the percentage of the breast density.

4.3.5 Statistical Analysis

Statistical analyses were conducted using NCSS V 19.0.5 (NCSS, LLC., Kaysville, UT, USA). The repeated-measures analysis of variance (ANOVA) was performed to examine the difference between the quantitative measurements of breast volume, fibroglandular tissue volume, and percentage of breast density with regard to the non-fat-suppressed and fat-suppressed MRI sequences. This variance model was employed to account for the variation both between sequences (i.e., between subjects) and within repeated measurements (i.e., within subjects). Significance levels were set at the 5% level. Descriptive data and box plots were also produced for all variables, demonstrating the distribution and median of breast volume, fibroglandular tissue volume, and percentage of breast density measured in the non-fat-suppressed and fat-suppressed imaging groups.

Table 4.1. Image acquisition parameters of the MR breast-imaging sequences using a personalized 3D-printed breast model.

No.	MRI sequence	Acquisition type	Orientation, Slice No.	TR (ms)	TE (ms)	TI (ms)	FOV (mm)	Matrix size	Slice thickness (mm)	Flip angle (°)	NSA	Scan time (min)
1.	Non-fat-suppressed TSE (T2W)	2D	Axial, 33	6080	78	-	350×350	336×448	4.0	80	1	1.10
2.	Non-fat-suppressed TSE (T1W)	2D	Axial, 37	709	10	-	350×350	224×320	2.9	130	2	2.38
3.	Non-fat-suppressed TSE SPACE (T1W)	3D	Axial, 88	600	3.4	-	400×400	256×256	1.6	120	2	2.47
4.	Fat-suppressed TSE SPACE (T1W)	3D	Axial, 88	1500	3.4	-	400×400	256×256	1.6	120	1	4.58
5.	Fat-suppressed TSE SPACE SPAIR (T1W)	3D	Axial, 88	1500	3.4	-	400×400	256×256	1.6	120	1	4.58
6.	Fat-suppressed IR/PFP TIRM (T2W)	2D	Axial, 37	4120	70	230	340×340	358×448	3.0	80	2	1.51

Abbreviations: TR: repetition time; TE: echo time; TI: inversion time; FOV: field-of-view; NSA: number of signal averages/excitations; 2D: two-dimensional; 3D: three-dimensional; TSE: turbo (fast) spin-echo; T1W: T1-weighted; T2W: T2-weighted; SPACE: sampling perfection with application optimized contrasts using different flip angle evolution; SPAIR: spectral attenuation inversion recovery; SE: spin-echo; IR: inversion recovery; PFP: partial fourier phase; TIRM: turbo inversion recovery magnitude.

4.4 Results

4.4.1 Scanning of the Personalized 3D-Printed Breast Model

Figure 4.2 shows the MR images of the personalized 3D-printed breast model using silicone and peanut oils as surrogates for fibroglandular and fatty breast tissues, respectively, for the various scanning sequences. These oils produced a reasonable level of contrast and MR-related characteristics amongst the T1- and T2-weighted images with and without the implementation of the fat-suppression techniques. Although the most noticeable feature of the personalized 3D-printed breast model was that it was somewhat inhomogeneous, this feature nevertheless mimics the substantial inhomogeneity sometimes encountered in patients' irregular distributions. The used tissue-mimicking materials for simulating the MR imaging characteristics for fibroglandular and adipose tissues have been induced similar appearance, variability, and heterogeneity of the breast structures that seen in the physiological tissues.

The suppression of fat signals in the T1-weighted images with both SPACE and SPAIR acquisitions did not substantially increase the contrast enhancement or visualization between the dense fibroglandular and non-dense fatty structures (Figure 4.2D, E). A possible explanation for this could be that these types of acquisitions are highly affected by inhomogeneity in the magnetic field, demonstrating inhomogeneous fat suppression in the fatty structures. On the contrary, Figure 4.2F shows that the fat-suppressed T2-weighted image with TIRM acquisition demonstrated a homogenous high signal intensity in the fibroglandular structure and a low signal intensity in the fatty structure for both the right and left breasts. The suppression of fat signals significantly improved the contrast between the

fibroglandular and fatty structures, further enhanced visualization, and provided more anatomical information which may assist in the segmentation and/or quantification of breast density.

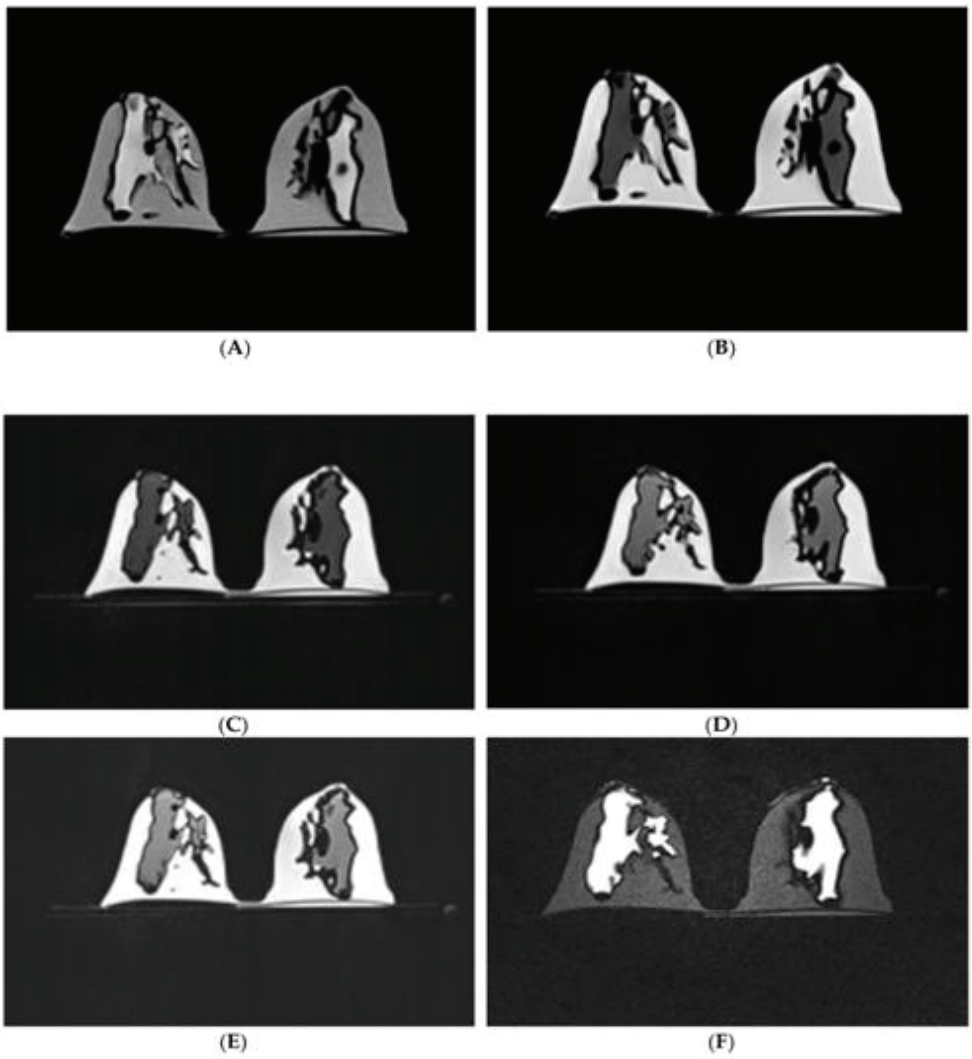

Figure 4.2. Central axial slice of a personalized 3D-printed breast model for the different MR imaging pulse sequences. **(A)** Non-fat-suppressed TSE (T2W); **(B)** Non-fat-suppressed TSE (T1W); **(C)** Non-fat-suppressed TSE SPACE (T1W); **(D)** Fat-suppressed TSE SPACE (T1W); **(E)** Fat-suppressed TSE SPACE SPAIR (T1W); **(F)** Fat-suppressed IR/PFP TIRM (T2W). For pulse sequences, refer to Table 4.1.

4.4.2 Quantitative Measurement of Breast Volume, Fibroglandular Tissue Volume, and Percentage of Breast Density

Table 4.2 displays the quantitative measurements (mean and standard deviations) of the breast volume, fibroglandular tissue volume, and percentage of breast density for the different MRI sequences. For the SPACE T1-weighted images (i.e., MR Seq. 3 and 4), there was evidence of a difference in breast density between the non-fat-suppressed sequence (7.719 ± 0.366%) and the fat-suppressed sequence (11.698 ± 0.351%). This difference can be explained by the direct relationship between fibroglandular tissue volume and breast density, as shown in Table 4.2, the volume of fibroglandular tissue measured in the fat-suppressed sequence (i.e., MR Seq. 4) was higher than that in the non-fat-suppressed sequence (i.e., MR Seq. 3): 53.940 ± 1.083 cm^3 and 34.261 ± 1.809 cm^3, respectively.

For the breast density assessment, there was a substantial difference between the non-fat-suppressed sequence (5.401 ± 0.165%) and the fat-suppressed sequence (9.498 ± 0.930%) measured in the T2-weighted images, MR Seq. 1 and MR Seq. 6, respectively. This difference might explain the relatively good improvement in the contrast between the fibroglandular and fatty structures (Figure 4.2F) owing to the implementation of the fat-suppression technique, which had a major effect on the segmentation process and, therefore, the measurement of breast density. By contrast, the means of the breast density for the non-fat suppressed (i.e., MR Seq. 2) and the fat-suppressed (i.e., MR Seq. 5) were 7.733 ± 0.365% and 10.467 ± 0.084%, respectively. A comparison of MR Seq. 2 and MR Seq. 5 revealed that the breast volume, fibroglandular tissue volume, and percentage of breast density measured in the fat-

suppressed sequence tended to be higher than that measured in the non-fat-suppressed sequence (Table 4.2).

Table 4.2. Results of the estimated mean and standard deviation of breast volume, fibroglandular tissue volume, and percentage of breast density for the different MRI sequences using a personalized 3D-printed breast model.

MRI sequence*	Breast volume (cm^3)		Fibroglandular tissue volume (cm^3)		Breast density (%)	
	Mean	SD	Mean	SD	Mean	SD
Non-fat-suppression group (MR Sequences 1, 2, and 3)						
MR Seq. 1 (N = 3)	592.291	5.065	31.984	0.735	5.401	0.165
MR Seq. 2 (N = 3)	388.793	4.159	30.067	1.159	7.733	0.365
MR Seq. 3 (N = 3)	443.884	11.913	34.261	1.809	7.719	0.366
Combined (N = 9)	474.989	91.406	32.104	2.144	6.952	1.194
Fat-suppression group (MR Sequences 4, 5, and 6)						
MR Seq. 4 (N = 3)	461.188	4.699	53.940	1.083	11.698	0.351
MR Seq. 5 (N = 3)	462.948	11.882	48.456	1.140	10.467	0.084
MR Seq. 6 (N = 3)	715.784	32.097	67.794	3.623	9.498	0.930
Combined (N = 9)	546.640	128.031	56.730	8.854	10.555	1.077

*For pulse sequences, refer to Table 4.1.

4.4.3 Comparison of Measurements Between Non-Fat-Suppression and Fat-Suppression Groups

Table 4.3 demonstrates the results (mean, standard error, F-ratio, and P-value) of the repeated-measures ANOVA of breast volume, fibroglandular tissue volume, and percentage of breast density with respect to the non-fat-suppression and fat-suppression groups. The box plots of these parameters for the two groups are shown in Figure 4.3.

Table 4.3. Results of the repeated-measures ANOVA, including total mean, standard error (SE), F-ratio, probability level (Prob level) of breast volume, fibroglandular tissue volume, and percentage of breast density between two imaging groups: non-fat-suppressed and fat-suppressed MRI pulse sequences.

Breast Density Parameter	Non-fat-suppressed (N = 9)		Fat-suppressed (N = 9)		F-ratio	Prob level**
	Mean	SE (4 df*)	Mean	SE (4 df*)		
Breast volume (cm^3)	474.989	73.639	546.640	73.639	0.47	0.5293
Fibroglandular tissue volume (cm^3)	32.104	4.158	56.730	4.158	17.54	0.0138
Breast density (%)	6.952	0.709	10.555	0.709	12.90	0.0229

*The degrees of freedom; **The significance level of the F-ratio (the probability that the difference between data is significant or not). The significant difference between the quantitative measurements of breast volume, fibroglandular volume, and percentage of breast density based on the non-fat suppressed and the fat-suppressed MRI sequences was determined at the 5% level.

For breast volume, although the mean measured from the non-fat-suppression group (474.989 cm3) tended to be lower than that from the fat-suppression group (546.640 cm^3), the difference was not statistically significant (p = 0.5293), with an F-ratio of 0.47 and a standard error for both means of 73.639. However, for the fibroglandular

tissue volume and the percentage of breast density, the repeated-measures ANOVA showed that the difference between the non-fat-suppression group and the fat-suppression group was statistically significant at the 5% level. The values measured from the non-fat-suppression group were lower than those from the fat-suppression group, as shown in Table 4.2; Table 4.3. The mean volume of fibroglandular tissue was 32.104 cm^3 for the non-fat-suppression group and 56.730 cm^3 for the fat-suppression group, which was statistically significant ($F = 17.54$; $p = 0.0138$), with a standard error of 4.158. Likewise, there was a significant difference ($F = 12.90$; $p = 0.0229$) between the two groups: the mean breast density measured in the non-fat-suppression group (6.952%) tended to be lower than that of the fat-suppression group (10.555%), with a standard error for both means of 0.709.

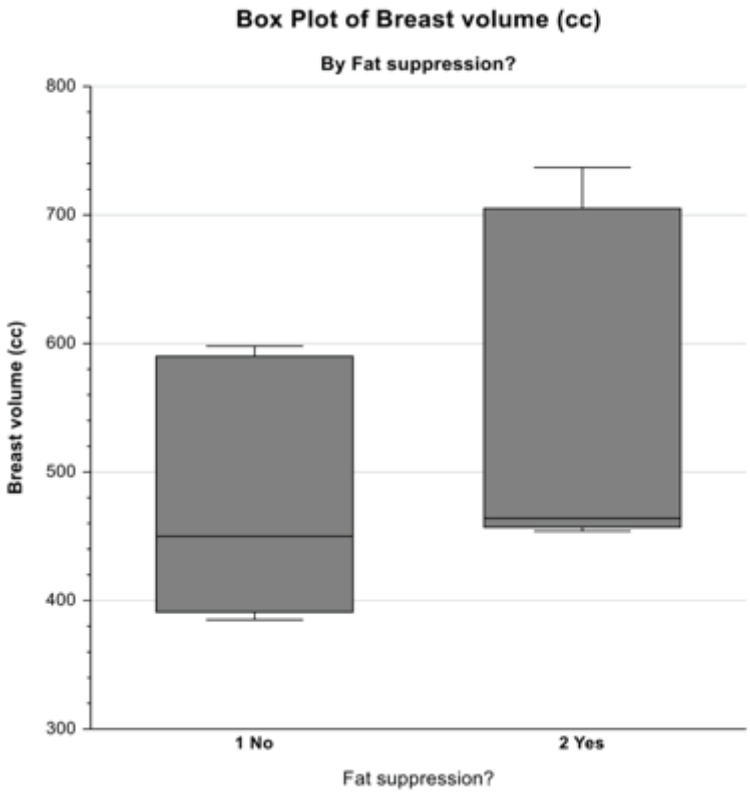

(A)

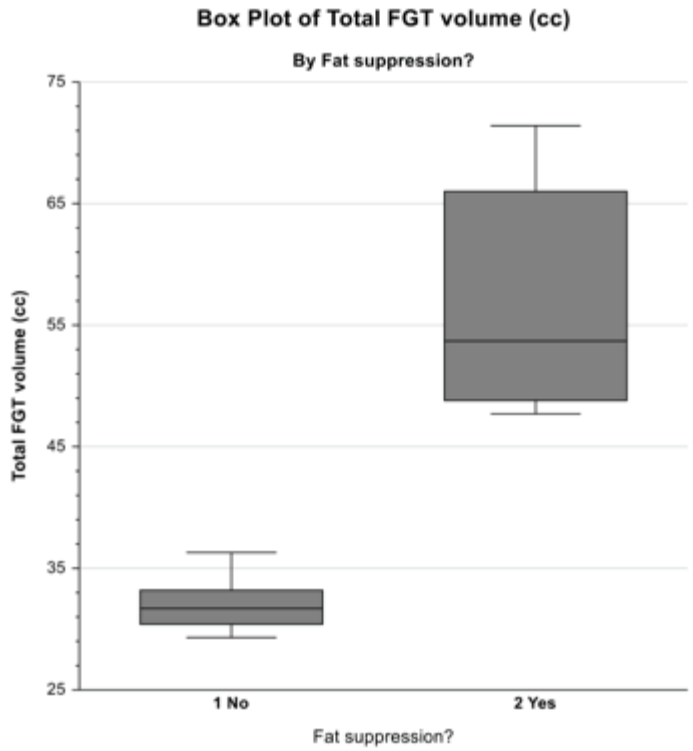

(B)

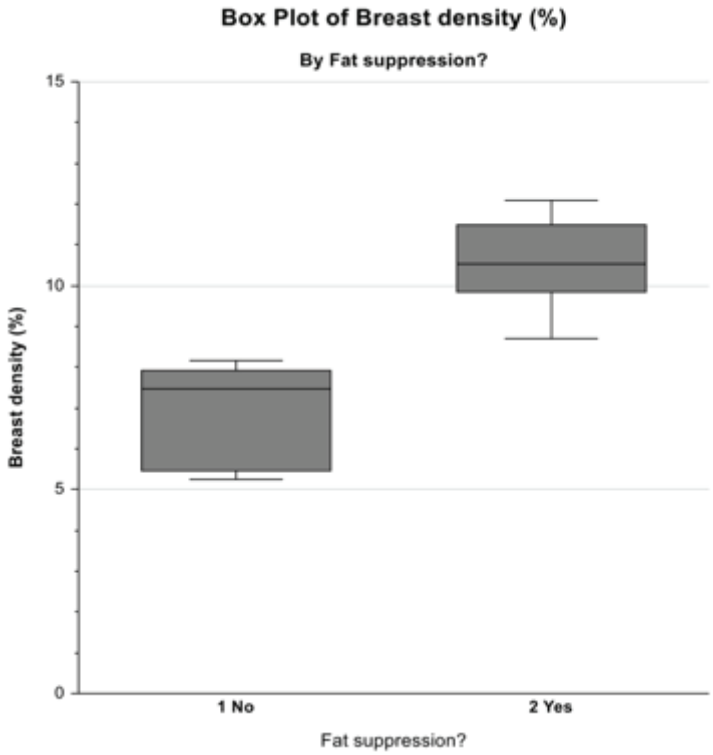

(C)

Figure 4.3. Box plots demonstrate the distribution and median of three main parameters: **(A)** breast volume, **(B)** fibroglandular tissue volume, and **(C)** percentage of breast density measured on the non-fat-suppressed and the fat-suppressed MRI sequences. The six MRI sequences compartments were re-configured into a two-way cross-classification, namely two fat-suppression categories. As shown,

"1/No" is the non-fat-suppression, "2/Yes" is the fat-suppression, which are on the x-axis, while the three parameters measured with respect to these two corresponding categories are on the y-axis.

4.5 Discussion

Recently, for women with an elevated risk of developing breast cancer, such as those with high breast density, the importance of establishing a standardized MRI protocol and/or measurement method for the assessment of breast density has increased in clinical and research domains. Although fat-suppressed and non-fat-suppressed sequences have frequently been included for both T1- and T2-weighted images in clinical breast MRI protocol, there is no agreement on which of these sequences should be used in this regard.[1,8,17,30] The current study was designed to determine the most appropriate MRI sequence for the quantitative assessment of breast density using a personalized 3D-printed breast model[43] based on an objective comparison between fat-suppressed and non-fat-suppressed sequences. Six MRI sequences were acquired and categorized into fat-suppression and non-fat-suppression categories to examine the difference between the quantitative measurements of breast volume, fibroglandular tissue volume, and percentage of breast density between these two imaging groups.

Comparing the two fat-suppression groups, the repeated-measures ANOVA showed that the differences between the non-fat-suppressed and fat-suppressed MRI sequences (i.e., MR Seq. 1, 2, and 3 and MR Seq. 4, 5, and 6) were statistically significant at the 5% level for both fibroglandular tissue volume and percentage of breast density. On the contrary, the observed difference between these corresponding sequences was not statistically significant with respect to breast volume. The current findings seem to be consistent with other research documenting that the assessment of breast density is considered to fluctuate with MRI sequences and with the application of fat-suppression

techniques.[3,16,17] A comparison of our results with Chang et al,[17] who suggested that breast volumes measured in T1-weighted sequences with and without fat suppression were almost identical for a similar case, is encouraging. Although their results differed from the current study, given that the breast density parameters were analyzed only on the T1-weighted sequences, they are still consistent with our findings, which showed that there was no evidence of a difference in the breast volumes between the non-fat-suppression and the fat-suppression groups (Table 4.3). A possible explanation for this could be that the measurement of breast volumes based on these two groups was not considerably influenced by the applied imaging techniques and/or segmentation method. Despite the breast volumes measured from the T2-weighted sequences with and without fat suppression being higher than those of the T1-weighted sequences, the difference between the two imaging groups was not significant. This can be attributed to the matrix sizes of the T2-weighted images used with the non-fat-suppressed and fat-suppressed sequences (i.e., MR Seq. 1 and 6), which were 336 × 448 and 358 × 448, respectively.

However, there was a statistically significant difference between fibroglandular tissue volume and percentage of breast density, indicating higher values in the fat-suppressed sequences (MR Seq. 4, 5, and 6) compared to the non-fat-suppressed sequences (MR Seq. 1, 2, and 3), as shown in Tables 4.2 and 4.3. This difference can be explained in part by the relatively good contrast enhancement and/or visualization observed between the fibroglandular and the fatty structures resulting from the suppression of fat signals, as was evident in the TIRM with fat-suppressed T2-weighted image (Figure 4.2F). Although the signal-to-noise ratio and tissue contrast in the non-fat-suppressed images were higher than those in the fat-suppressed images, the results for the fat-suppression group were significantly higher than those for the non-fat-suppression

group. Nevertheless, the scanning times for the fat-suppressed sequences were longer than those for the non-fat-suppressed sequences, except for the TIRM, which was 1 min 51 s. As shown in Table 4.2, breast volume, fibroglandular tissue volume, and percentage of breast density analyzed with TIRM were considerably higher than those of the T1- and T2-weighted sequences with and without fat suppression. Compared to these sequences, the observed increase in breast density parameters from the T2-weighted and TIRM acquisition was probably due to their individual characteristics: the T2-weighted image with fat-suppression technique is known to improve fluid intensity visualization, while TIRM is known to provide more anatomical information.[4,44] Similar findings were obtained by Bu et al,[4] who suggested that the combined DWI and TIRM could be used as an alternative imaging protocol for the screening of women with dense breast tissue. Despite being preliminary findings, our study indicates that TIRM could be incorporated with fat-suppression techniques for the assessment of breast density. Therefore, the fat-suppressed T2-weighted image with TIRM acquisition can be a promising technique for the quantitative assessment of breast density, although further research should be conducted to verify this suggestion.

Overall, the observed differences in breast density measurements between the fat-suppression and non-fat-suppression groups can be attributed to several factors: the segmentation method, image quality, scanning/technical parameters, and tissue contrast achieved by using different MRI pulse sequences. There are, however, other possible reasons; the applied fat-suppression techniques are more susceptible to magnetic field inhomogeneity, especially in the case of the 3T MRI system, where the field heterogeneity can be more protuberant. As shown in Figure 4.2, the high levels of inhomogeneity in both the fat-suppressed and non-fat-suppressed images might be

the major factor—if not the only factor—that can cause such a variation in the segmentation and/or quantification of breast density parameters.

Although this study suggests that the fat-suppressed sequences are more useful than the non-fat-suppressed sequences for the segmentation/measurement of fibroglandular tissue volume and breast density, it is subject to several limitations. First, the assessment of breast density parameters was carried out on a developed 3D-printed breast model using silicone and peanut oils as tissue-equivalent materials and may not reflect the exact distribution of both fibroglandular and fatty structures as seen in human breast tissues. This limitation could be addressed by further research with the use of more realistic breast models for MRI scanning. Second, the high levels of inhomogeneity in both the fat-suppressed and non-fat-suppressed images could have influenced the segmentation and breast density measurements. This is unavoidable due to the complexity of the MRI scanning sequences. Third, the breast density parameters were segmented and measured using a semi-automated method, which implies that the prospective source of variation between such measurements could be due to a high level of dependency on user interaction. For this reason, multiple segmentations/measurements of the breast density parameters were consistently conducted by the same observer to minimize potential intra-observer variations. However, the applicability of the proposed segmentation and measurement method is relatively high as an interactive 3D tool and would be more useful in the long-term assessment of breast density. Finally, with the implementation of different imaging techniques, acquisition types, and fat-suppression methods, caution must be applied as the findings might not be transferable to clinical practice without further investigation.

For future research, a greater focus on the TIRM with a fat-suppression technique could produce interesting findings on the quantification of breast density, especially for women at high risk of developing breast cancer. Quantitative assessment of breast density parameters in participants' clinical breast MRI datasets, could also be used to investigate and validate this observation.

4.6 Conclusion

A significant difference was found between the non-fat-suppression and fat-suppression MRI sequences for the quantitative measurements of the volume of fibroglandular tissue and the percentage of breast density. In general, the findings suggest that fat-suppressed sequences are an efficient scanning technique that reflects the exact composition of breast tissues. TIRM with fat-suppressed T2-weighted sequence can be a promising imaging protocol for the segmentation and/or quantification of breast density. Further research is required to verify these findings so that the optimal breast MRI protocols can be developed for clinical application.

4.7 References

1. Chen JH, Chang YC, Chang D, Wang YT, Nie K, Chang RF, Nalcioglu O, Huang CS, Su MY. Reduction of breast density following tamoxifen treatment evaluated by 3-D MRI: Preliminary study. Magn Reson Imaging. 2011; 29(1):91-98.
2. Wang J, Azziz A, Fan B, Malkov S, Klifa C, Newitt D, Yitta S, Hylton N, Kerlikowske K, Shepherd JA. Agreement of mammographic measures of volumetric breast density to MRI. PLoS ONE. 2013; 8(12):e81653.

3. Tagliafico A, Bignotti B, Tagliafico G, Astengo D, Martino L, Airaldi S, Signori A, Sormani MP, Houssami N, Calabrese M. Breast density assessment using a 3T MRI system: Comparison among different sequences. PLoS ONE. 2014; 9(6):e99027.
4. Bu Y, Xia J, Joseph B, Zhao X, Xu M, Yu Y, Qi S, Shah KA, Wang S, Hu J. Non-contrast MRI for breast screening: Preliminary study on detectability of benign and malignant lesions in women with dense breasts. Breast Cancer Res Treat. 2019; 177(3):629–639.
5. Nelson HD, Zakher B, Cantor A, Fu R, Griffin J, O'Meara ES, Buist DS, Kerlikowske K, Van Ravesteyn NT, Trentham-Dietz A, Mandelblatt JS. Risk factors for breast cancer for women aged 40 to 49 years: A systematic review and meta-analysis. Ann Intern Med. 2012; 156(9):635–648.
6. McCormack VA, Dos Santos Silva I. Breast density and parenchymal patterns as markers of breast cancer risk: A meta-analysis. Cancer Epidem Biomar. 2006; 15(6): 1159–1169.
7. Kerlikowske K, Ichikawa L, Miglioretti DL, Buist DS, Vacek PM, Smith-Bindman R, Yankaskas B, Carney PA, Ballard-Barbash R. Longitudinal measurement of clinical mammographic breast density to improve estimation of breast cancer risk. J Natl Cancer Inst. 2007; 99(5):386–395.
8. Sindi R, Sá Dos Reis C, Bennett C, Stevenson G, Sun Z. Quantitative Measurements of Breast Density Using Magnetic Resonance Imaging: A Systematic Review and Meta-Analysis. J Clin Med. 2019; 8(5):745.
9. Sindi R, Sun Z. Optimal protocols for quantitative assessment of breast density using magnetic resonance imaging. Australas Med J. 2019; 12(6):186–188.

10. Warner E, Messersmith H, Causer P, Eisen A, Shumak R, Plewes D. Systematic review: Using magnetic resonance imaging to screen women at high risk for breast cancer. Ann Intern Med. 2008; 148(9):671–679.
11. Nayeem F, Ju H, Brunder DG, Nagamani M, Anderson KE, Khamapirad T, Lu LJ. Similarity of fibroglandular breast tissue content measured from magnetic resonance and mammographic images and by a mathematical algorithm. Int J Breast Cancer. 2014; 2014:961679.
12. Lin M, Chan S, Chen JH, Chang D, Nie K, Chen ST, Lin CJ, Shih TC, Nalcioglu O, Su MY. A new bias field correction method combining N3 and FCM for improved segmentation of breast density on MRI. Med Phys. 2011; 38(1):5-14.
13. Doran SJ, Hipwell JH, Denholm R, Eiben B, Busana M, Hawkes DJ, Leach MO, Silva ID. Breast MRI segmentation for density estimation: Do different methods give the same results and how much do differences matter? Med Phys. 2017; 44(9):4573-4592.
14. Tagliafico A, Tagliafico G, Tosto S, Chiesa F, Martinoli C, Derchi LE, Calabrese M. Mammographic density estimation: comparison among BI-RADS categories, a semi-automated software and a fully automated one. Breast. 2009; 18(1):35-40.
15. Boston RC, Schnall MD, Englander SA, Landis JR, Moate PJ. Estimation of the content of fat and parenchyma in breast tissue using MRI T1 histograms and phantoms. Magn Reson Imaging. 2005; 23(4):591-599.
16. Lu LJ, Nishino TK, Johnson RF, Nayeem F, Brunder DG, Ju H, Leonard Jr MH, Grady JJ, Khamapirad T. Comparison of breast tissue measurements

using magnetic resonance imaging, digital mammography and a mathematical algorithm. Phys Med Biol. 2012; 57(21):6903–6927.

17. Chang DH, Chen JH, Lin M, Bahri S, Yu HJ, Mehta RS, Nie K, Hsiang DJ, Nalcioglu O, Su MY. Comparison of breast density measured on MR images acquired using fat-suppressed versus non-fat-suppressed sequences. Med Phys. 2011; 38(11):5961-5968.
18. Nie K, Chang D, Chen JH, Hsu CC, Nalcioglu O, Su MY. Quantitative analysis of breast parenchymal patterns using 3D fibroglandular tissues segmented based on MRI. Med Phys. 2010; 37(1):217–226.
19. Pertuz S, McDonald ES, Weinstein SP, Conant EF, Kontos D. Fully automated quantitative estimation of volumetric breast density from digital breast tomosynthesis images: Preliminary results and comparison with digital mammography and MR imaging. Radiology. 2016; 279(1):65–74.
20. Ledger AE, Scurr ED, Hughes J, Macdonald A, Wallace T, Thomas K, Wilson R, Leach MO, Schmidt MA. Comparison of Dixon sequences for estimation of percent breast fibroglandular tissue. PLoS ONE. 2016; 11(3):e0152152.
21. Miyazaki M, Wheaton A, Kitane S. Enhanced fat suppression technique for breast imaging. J Magn Reson Imaging. 2013; 38(4):981–986.
22. Kalovidouri A, Firmenich N, Delattre BM, Picarra M, Becker CD, Montet X, Botsikas D. Fat suppression techniques for breast MRI: Dixon versus spectral fat saturation for 3D T1-weighted at 3 T. Radiol Med. 2017; 122(10):731–742.
23. Le-Petross H, Kundra V, Szklaruk J, Wei W, Hortobagyi GN, Ma J. Fast three-dimensional dual echo Dixon technique improves fat suppression in breast MRI. J Magn Reson Imaging. 2010; 31(4):889–894.

24. Dogan BE, Ma J, Hwang K, Liu P, Yang WT. T1-weighted 3D dynamic contrast-enhanced MRI of the breast using a dual-echo Dixon technique at 3 T. J Magn Reson Imaging. 2011; 34(4):842–851.
25. Clauser P, Pinker K, Helbich TH, Kapetas P, Bernathova M, Baltzer PA. Fat saturation in dynamic breast MRI at 3 Tesla: Is the Dixon technique superior to spectral fat saturation? A visual grading characteristics study. Eur Radiol. 2014; 24(9):2213–2219.
26. An YY, Kim SH, Kang BJ. Differentiation of malignant and benign breast lesions: Added value of the qualitative analysis of breast lesions on diffusion-weighted imaging (DWI) using readout-segmented echo-planar imaging at 3.0 T. PLoS ONE. 2017; 12(3):e0174681.
27. Beckett KR, Moriarity AK, Langer JM. Safe use of contrast media: What the radiologist needs to know. Radiographics. 2015; 35(6):1738–1750.
28. Kanda T, Fukusato T, Matsuda M, Toyoda K, Oba H, Kotoku JI, Haruyama T, Kitajima K, Furui S. Gadolinium-based contrast agent accumulates in the brain even in subjects without severe renal dysfunction: Evaluation of autopsy brain specimens with inductively coupled plasma mass spectroscopy. Radiology. 2015; 276(1):228–232.
29. Ramalho M, Ramalho J, Burke LM, Semelka RC. Gadolinium retention and toxicity—An update. Adv Chronic Kidney Dis. 2017; 24(3):138–146.
30. Del Grande F, Santini F, Herzka DA, Aro MR, Dean CW, Gold GE, Carrino JA. Fat-suppression techniques for 3-T MR imaging of the musculoskeletal system. Radiographics. 2014; 34(1):217–233.
31. McRobbie DW, Moore EA, Graves MJ, Prince MR. MRI from Picture to Proton. Cambridge University Press; 2017.

32. Brown MA, Semelka RC, Dale BM. MRI: Basic principles and applications. John Wiley & Sons, Inc; 2015.
33. Mann RM, Kuhl CK, Kinkel K, Boetes C. Breast MRI: Guidelines from the European society of breast imaging. Eur Radiol. 2008; 18(7):1307-1318.
34. Hauer MP, Uhl M, Allmann KH, Laubenberger J, Zimmerhackl LB, Langer M. Comparison of turbo inversion recovery magnitude (TIRM) with T2-weighted turbo spin-echo and T1-weighted spin-echo MR imaging in the early diagnosis of acute osteomyelitis in children. Pediatr Radiol. 1998; 28(11):846–850.
35. Freed M, Badal A, Jennings RJ, de Las Heras H, Myers KJ, Badano A. X-ray properties of an anthropomorphic breast phantom for MRI and x-ray imaging. Phys Med Biol. 2011; 56(12):3513–3533.
36. Carton AK, Bakic P, Ullberg C, Derand H, Maidment AD. Development of a physical 3D anthropomorphic breast phantom. Med Phys. 2011; 38(2):891-896.
37. Mazzara GP, Briggs RW, Wu Z, Steinbach BG. Use of a modified polysaccharide gel in developing a realistic breast phantom for MRI. Magn Reson Imaging. 1996; 14(6):639–648.
38. Liney GP, Tozer DJ, Turnbull LW. A simple and realistic tissue-equivalent breast phantom for MRI. J Magn Reson Imaging. 1999; 10(6):968–971.
39. Freed M, de Zwart JA, Loud JT, El Khouli RH, Myers KJ, Greene MH, Duyn JH, Badano A. An anthropomorphic phantom for quantitative evaluation of breast MRI. Med Phys. 2011; 38(2):743-753.

40. Burfeindt MJ, Colgan TJ, Mays RO, Shea JD, Behdad N, Van Veen BD, Hagness SC. MRI-Derived 3-D-Printed Breast Phantom for Microwave Breast Imaging Validation. IEEE Antennas Wirel Propag Lett. 2012; 11:1610-1613.
41. Dantuma M, van Dommelen R, Manohar S. Semi-anthropomorphic photoacoustic breast phantom. Biomed Opt Express. 2019; 10(11):5921-5939.
42. He Y, Liu Y, Dyer BA, Boone JM, Liu S, Chen T, Zheng F, Zhu Y, Sun Y, Rong Y, Qiu J. 3D-printed breast phantom for multi-purpose and multi-modality imaging. Quant Imaging Med Surg. 2019; 9(1):63-74.
43. Sindi R, Wong YH, Yeong CH, Sun Z. Development of patient-specific 3D-printed breast phantom using silicone and peanut oils for magnetic resonance imaging. Quant Imaging Med Surg. 2020; 10(6):1237–1248.
44. Westra C, Dialani V, Mehta TS, Eisenberg RL. Using T2-weighted sequences to more accurately characterize breast masses seen on MRI. Am J Roentgenol. 2014; 202(3):183–190.

5. Chapter 5

Quantitative Measurement of Breast Density in a High-risk Group Using Fat-suppressed and Non-fat-suppressed T2-weighted Magnetic Resonance Imaging Sequences

5.1 Abstract

Background: T2-weighted imaging is one of the standard magnetic resonance imaging (MRI) protocols used in breast scanning. However, the relative role of T2-weighted images with/without the use of fat-suppression techniques in the quantitative assessment of breast density remains limited across a variety of T2-weighted sequences. **Purpose:** This study aimed to investigate the difference between the quantitative measurements of breast volume, fibroglandular tissue volume, and percentage of breast density of two MR techniques, the non-fat-suppressed versus the fat-suppressed T2-weighted imaging sequences in a cohort of 11 high-risk women. **Methods:** Breast volume, fibroglandular tissue volume, and percentage of breast density from these imaging techniques were quantitatively measured using the Analyze 14.0 software. Averages of repeated-measures observations were conducted using the Bland-Altman comparison of measurements to examine the difference between the non-fat-suppressed and fat-suppressed T2-weighted sequences with regard to the quantitative assessments of breast density parameters. **Results:** The results revealed no indication of measurement bias between the non-fat-suppressed and fat-suppressed T2-weighted imaging sequences with respect to breast density parameters, and no evidence to reject the presumption that the differences were normally distributed. Although the volume of fibroglandular tissue and the percentage of breast density were higher in the non-fat-suppressed sequence than in the fat-suppressed sequence, the differences were not statistically significant ($p > 0.05$). **Conclusions:** This study showed no substantial differences between the non-fat-suppressed and fat-suppressed sequences in the quantitative measurement of breast density parameters; however, further studies with inclusion of a larger sample size are required to validate the complementary role of T2-weighted imaging in this regard.

Keywords MRI; fibroglandular tissue; adipose tissue; breast density; segmentation; non-fat-suppressed T2-weighted image; fat-suppressed T2-weighted image; TSE; STIR

5.2 Introduction

Breast density, a measure of dense fibroglandular tissue compared to fatty, non-dense tissue, is an independent risk factor for breast cancer.[1-4] Evidence suggests that the prospective risk of breast cancer is three to five times higher for women with dense breasts than for women with fatty breasts.[5-7] Most information about breast density estimation and screening for breast cancer is obtained through full-field digital mammography (FFDM), a two-dimensional imaging technique.[8, 9] However, the evaluation of breast density based on mammograms is limited due to tissue overlapping, variations in breast compression, and inappropriate positioning, which can lead to artefacts and insufficient imaging of breast tissue.[10, 11] Magnetic resonance imaging (MRI), an adjuvant modality of breast imaging, has been proposed to be used in women at high risk of developing breast cancer, such as those with the breast cancer susceptibility gene (BRCA-positive genetic mutation carriers), a family history of breast cancer, and high breast density.[12-15] MRI has been used to estimate actual breast density because it provides a three-dimensional volume representation of breast structure with excellent soft tissue contrast, which assists in the differentiation between fibroglandular and fatty, or adipose tissues.[16-19]

Conventionally, the evaluation of breast density is based on a qualitative approach recommended by the American College of Radiology (ACR) Breast Imaging

Reporting and Data System (BI-RADS), which classifies density into four categories based on the amount of fibroglandular tissue: 1) almost entirely fat; 2) scattered fibroglandular tissue; 3) heterogeneous fibroglandular tissue; and 4) extreme fibroglandular tissue.[20, 21] Despite standardization guidelines, however, research has consistently shown that BI-RADS scores are subjective and vary between readers, resulting in inter- and even intra-reader variability.[22-24] Various methods of quantifying breast density, with a variety of algorithms or techniques documented in the literature, have been proposed to address this limitation.[25-31] Nevertheless, in the quantitative assessment of breast density, these methods were based on a semi-automatic thresholding and/or segmentation methodology, and much uncertainty remains about the optimal method in this regard.[25-32] Similarly, for the evaluation of breast density, different MR breast-imaging protocols and/or sequences have been used, varying from contrast- to non-contrast-enhanced imaging with/without the application of fat-suppression techniques.[3, 4, 32-40]

The inversion-based technique known as the short-TI inversion recovery (STIR) sequence is among the most widely used fat-suppression techniques in breast imaging due to its insensitivity to B_0 and B_1 heterogeneity.[41, 42] STIR is obtained by a 180° non-spectral-selective inversion pulse followed by either a single 90° pulse or a pair of 90° and 180° pulses for inversion recovery (IR) and spin-echo (SE) imaging, respectively.[36, 38, 41-43] Although fat-suppression techniques have been shown to enhance the visibility of pathology, contrast enhancement, and image quality, thereby allowing for a better differentiation between fibroglandular and fatty tissue, no agreement has yet been reached on which MR breast-imaging protocols are appropriate for the quantitative assessment of breast density, particularly for women at high risk of developing breast cancer.[41, 44] Fundamentally, the MRI studies used

T2-weighted images to identify diseased tissue in almost all parts of the body; while T2-weighted turbo spin-echo (TSE) pulse sequences have been widely reported in breast MRI to help classify lesion characterization and thus improve the differential diagnosis, their complementary role in breast density assessment remains largely unexplored.[45-48]

The primary aim of this study was to investigate the differences between the quantitative measurements of breast volume, fibroglandular tissue volume, and percentage of breast density of two MR techniques, non-fat-suppressed T2-weighted TSE versus fat-suppressed T2-weighted STIR imaging sequences, in a cohort of high-risk women. The tested hypothesis was that the T2-weighted image features with/without the use of fat-suppression techniques can assist in the differentiation of fibroglandular and fatty tissue, allowing for more accurate measurement of breast density parameters, thus highlighting the potential risk of developing breast cancer in high-risk women.

5.3 Materials and Methods

5.3.1 Study Subjects and MR Scanning Protocol

The study group consisted of 11 female subjects who had breast MRI examinations conducted between 2009 and 2010. All participants were cancer-free but at high risk of developing breast cancer and confirmed to be normal without prior breast surgery or radiation therapy on the chest wall. MRI studies were performed on a 1.5T system (Philips, Best, The Netherlands) in a prone position using a dedicated bilateral 8-channel breast coil. The imaging protocol included axial non-fat-suppressed T2-weighted TSE and fat-suppressed T2-weighted STIR images. The version of two-

dimensional-STIR imaging used in this study employed a 180° non-spectral-selective inversion pulse followed by a single 90° pulse for the fat-suppression technique. In all cases, both the imaging acquisitions used for the quantitative assessment of breast density parameters were acquired before the injection of contrast for the T1-weighted dynamic contrast-enhanced imaging. Table 5.1 shows the image acquisition parameters of the MRI sequences used in this study.

5.3.2 Quantitative Measurement: Breast Volume, Fibroglandular Tissue Volume, and Percentage of Breast Density

With a semi-automated segmentation/measurement method, breast volume and fibroglandular tissue volume were quantitatively assessed using commercially available biomedical imaging software, Analyze V 14.0 (AnalyzeDirect, Inc., Lexana, KS, USA). Two steps were implemented to measure the percentage of breast density from MRI volumes: breast segmentation and fibroglandular tissue segmentation. Breast segmentation is proposed to separate the breast's body from the surrounding structure, while segmentation of fibroglandular tissue separates the glandular tissue from the fatty tissue.

The breast's boundary was first semi-automatically delineated to separate the breast's body from the surrounding structures, using an interactive method based on the threshold signal intensity function by placing seed points on a series of 2D axial slices comprising the whole volume of the breast. To identify the region of interest, the minimum and maximum threshold limits were then modified. The software impulsively interpolated between these slices and produced a mask of the entire breast volume. Once the breast segmentation process was completed, an automated method, using a variety of morphological processes and spatial filters, was carried out to

segment the fibroglandular tissue from the surrounding fatty tissue. Following this, the volume of the breast and the volume of fibroglandular tissue were quantified using a 3D-measuring tool based on the size intensity function. Finally, the ratio of the fibroglandular tissue volume relative to the total breast volume was determined as the percentage of breast density.

5.3.3 Data Synthesis

In this retrospective study, the MRI data for 11 high-risk women were examined. The women were recruited from The Cancer Imaging Archive (TCIA) Public Access (https://www.cancerimagingarchive.net), and both non-fat-suppressed T2-weighted TSE and fat-suppressed T2-weighted STIR images were available for them. For each woman, a two-fold segmentation of both the breast volume and the fibroglandular tissue volume was performed, thus extracting two segments of each MRI sequence. Consequently, the measurements were conducted twice with respect to the breast volume, the fibroglandular tissue volume, and thus the percentage of breast density. Finally, the average of each pair of values was calculated as a final observation for each patient/MRI sequence combination and reflected as an estimate of the true numerical value of each of the subjects of interest in the analysis (i.e. breast density parameters). This aimed to avoid the variance from causing significant underestimation/overestimation of other variance components.

5.3.4 Statistical Analysis

Statistical analyses were conducted using NCSS V 19.0.5 (NCSS, LLC. Kaysville, Utah, USA). Averages of repeated-measures observations through the Bland-Altman comparison of measurements were conducted to examine the difference between the

non-fat-suppressed T2-weighted TSE and the fat-suppressed T2-weighted STIR MRI sequences with regard to the quantitative measurements of breast volume, fibroglandular tissue volume, and percentage of breast density. The null hypothesis was that the differences between the two MRI sequences would all be zero throughout the range.

The Bland-Altman model was employed to test the outcomes on the assumption that both measurement methods (i.e. two MRI sequences) would yield exactly the same numerical value of the metric of interest (i.e. breast volume, fibroglandular tissue volume, and percentage of breast density) and provide a graphical representation of bias, if any, in one method relative to the other. The Bland-Altman scatter plots were produced for the two MRI sequences, demonstrating the difference against the average, which illustrates a system with zero bias of one method relative to the other with respect to breast volume, fibroglandular tissue volume, and percentage of breast density. The normality assumptions of the datasets distributed were also examined using the Shapiro-Wilk, Skewness, Kurtosis, and Omnibus tests. Statistical significance was evaluated using the one-sample t-test as appropriate and set at the 5% level.

Table 5.1. Image acquisition parameters of the MR breast-imaging sequences used in this study.

Patient No.	MRI sequence	Acquisition type	Orientation, Slice No.	TR (ms)	TE (ms)	TI (ms)	FOV (mm)	Matrix size	Slice thickness (mm)	Flip angle (°)	NSA	Scan time (min)
1.	Non-fat-suppressed T2W (TSE)	2D	Axial, 84	4132.6	120.0		640×640	333×464	2.0	90	3	4.33
	Fat-suppressed T2W (STIR)			4344.9	70.0	165	640×640	304×332	2.0	90	2	4.43
2.	Non-fat-suppressed T2W (TSE)	2D	Axial, 84	4130.0	120.0		560×560	433×540	2.0	90	3	5.57
	Fat-suppressed T2W (STIR)			4347.7	70.0	165	480×480	304×332	2.0	90	2	4.43
3.	Non-fat-suppressed T2W (TSE)	2D	Axial, 84	4132.6	120.0		576×576	367×500	2.0	90	3	4.75
	Fat-suppressed T2W (STIR)			4344.9	70.0	165	576×576	342×364	2.0	90	2	4.95
4.	Non-fat-suppressed T2W (TSE)	2D	Axial, 86	4375.8	120.0		576×576	367×512	2.0	90	3	5.03
	Fat-suppressed T2W (STIR)			4655.2	70.0	165	576×576	342×368	2.0	90	2	5.30
5.	Non-fat-suppressed T2W (TSE)	2D	Axial, 86	4375.7	120.0		528×528	333×456	2.0	90	3	4.59
	Fat-suppressed T2W (STIR)			4655.2	70.0	165	512×512	304×328	2.0	90	2	4.74
6.	Non-fat-suppressed T2W (TSE)	2D	Axial, 86	4375.7	120.0		480×480	300×412	2.0	90	3	4.15
	Fat-suppressed T2W (STIR)			4655.3	70.0	165	480×480	266×300	2.0	90	2	4.18
7.	Non-fat-suppressed T2W (TSE)	2D	Axial, 84	4132.6	120.0		480×480	300×408	2.0	90	3	3.92
	Fat-suppressed T2W (STIR)			4347.7	70.0	165	480×480	304×324	2.0	90	2	4.43

Table 5.1. Continued.

Patient No.	MRI sequence	Acquisition type	Orientation, Slice No.	TR (ms)	TE (ms)	TI (ms)	FOV (mm)	Matrix size	Slice thickness (mm)	Flip angle (°)	NSA	Scan time (min)
8.	Non-fat-suppressed T2W (TSE)	2D	Axial, 84	4132.6	120.0		640×640	383×524	2.0	90	3	4.95
	Fat-suppressed T2W (STIR)			4344.9	70.0	165	640×640	361×384	2.0	90	2	5.21
9.	Non-fat-suppressed T2W (TSE)	2D	Axial, 84	4128.2	120.0		528×528	367×440	2.0	90	3	4.74
	Fat-suppressed T2W (STIR)			4347.6	70.0	165	448×448	304×340	2.0	90	2	4.43
10.	Non-fat-suppressed T2W (TSE)	2D	Axial, 84	4132.6	120.0		640×640	383×524	2.0	90	3	4.95
	Fat-suppressed T2W (STIR)			4344.9	70.0	165	640×640	361×384	2.0	90	2	5.21
11.	Non-fat-suppressed T2W (TSE)	2D	Axial, 80	4862.0	120.0		432×432	267×380	2.0	90	3	3.30
	Fat-suppressed T2W (STIR)			4344.9	70.0	165	432×432	247×276	2.0	90	2	3.64

Abbreviations: TR: repetition time; TE: echo time; TI: inversion time; FOV: field-of-view; NSA: number of signal averages/excitations; T2W: T2-weighted; TSE: turbo spin-echo; STIR: short-TI inversion recovery; 2D: two-dimensional.

5.4 Results

5.4.1 Quantitative Measurement of Breast Volume, Fibroglandular Tissue Volume, and Percentage of Breast Density

Table 5.2 provides the quantitative measurements (average and SD) of the breast volume, fibroglandular tissue volume, and percentage of breast density measured on these two MRI sequences. The differences between the two MRI sequences and their averages are highlighted in Table 5.3.

5.4.2 Comparison of Measurements Between Non-fat-suppressed and Fat-suppressed T2-weighted MRI Sequences

Table 5.4 lists the descriptive statistics, including mean, SD, 95% confidence interval limits, and other values for the breast density parameters. Table 5.5 demonstrates the results of the Bland-Altman analyses for breast volume, fibroglandular tissue volume, and percentage of breast density measured on the two MRI sequences, while Table 5.6 shows the tests of normality of differences assumption. Figure 5.1 plots the Bland-Altman comparison of the MRI sequences (i.e. the difference between the two MRI sequences against their average) with respect to breast density parameters. Figure 5.2 displays the degree of agreement between the non-fat-suppressed T2-weighted TSE and the fat-suppressed T2-weighted STIR MRI sequences for each of the breast density parameters.

In the whole group of 11 patients, although the breast volume measured from the non-fat-suppressed T2-weighted TSE sequence, 2745.978 ± 1469.893 cm^3 (average ± Std Dev), was lower than that of the fat-suppressed T2-weighted STIR sequence, 2885.557

± 1568.706 cm^3, the difference was not statistically significant (t = -1.960, p = 0.078), with a mean difference of -139.579 ± 236.191 cm^3 and a standard error of 71.214.

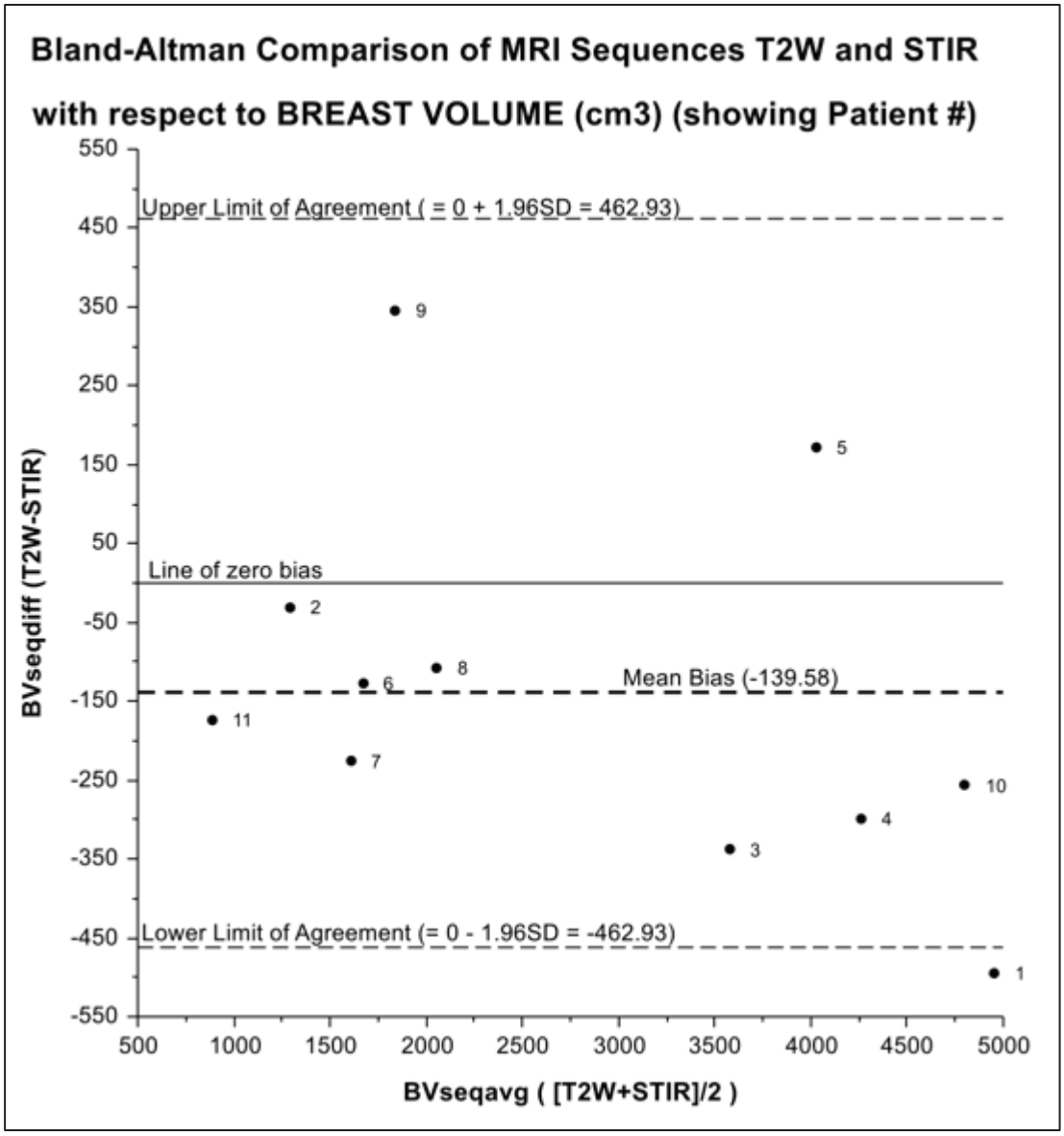

(A)

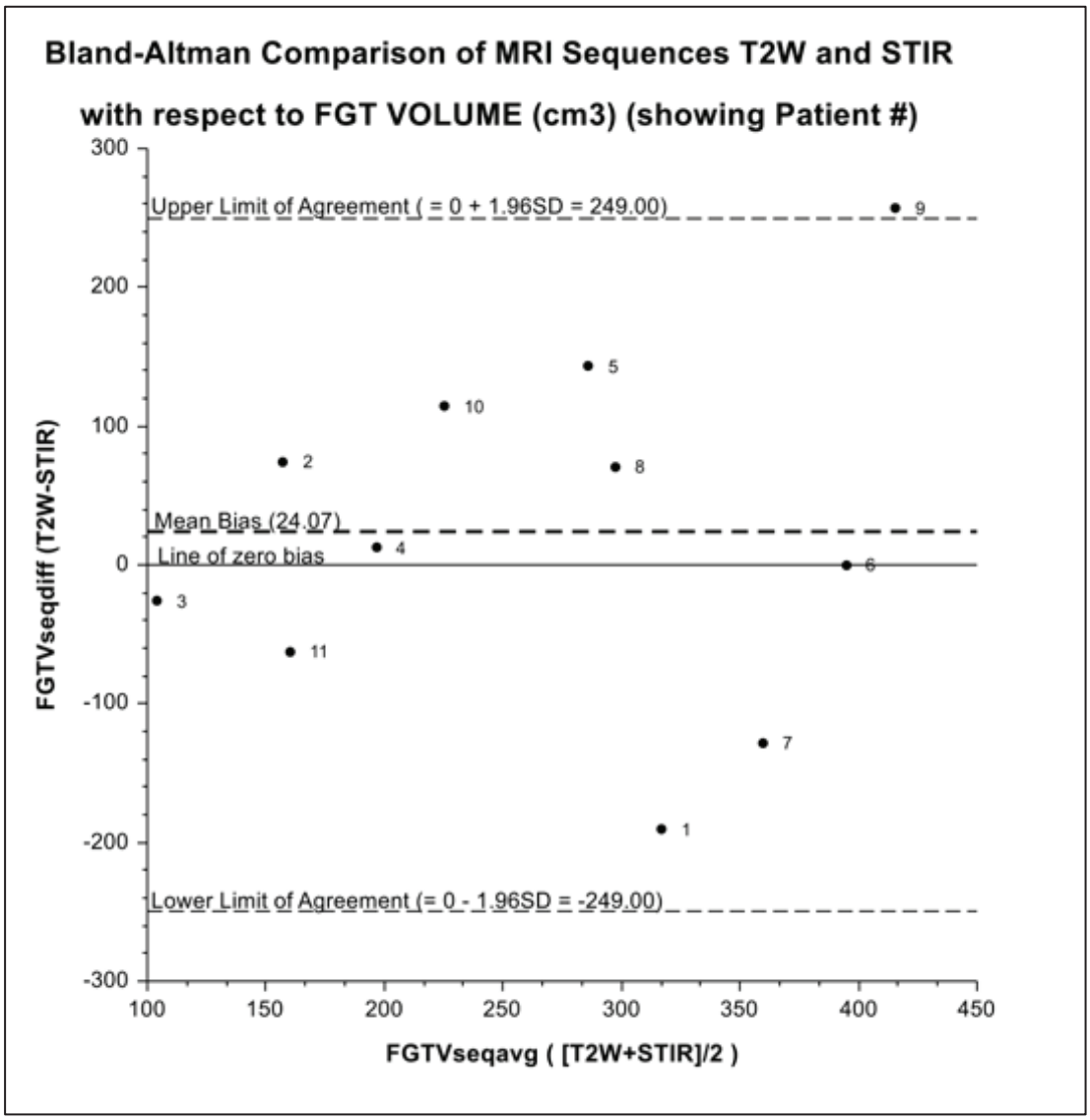
Bland-Altman Comparison of MRI Sequences T2W and STIR
with respect to FGT VOLUME (cm3) (showing Patient #)
Upper Limit of Agreement (= 0 + 1.96SD = 249.00)
Mean Bias (24.07)
Line of zero bias
Lower Limit of Agreement (= 0 - 1.96SD = -249.00)
FGTVseqdiff (T2W-STIR)
FGTVseqavg ([T2W+STIR]/2)
300
200
100
0
-100
-200
-300
100
150
200
250
300
350
400
450
9
5
10
2
8
4
6
3
11
7
1

(B)

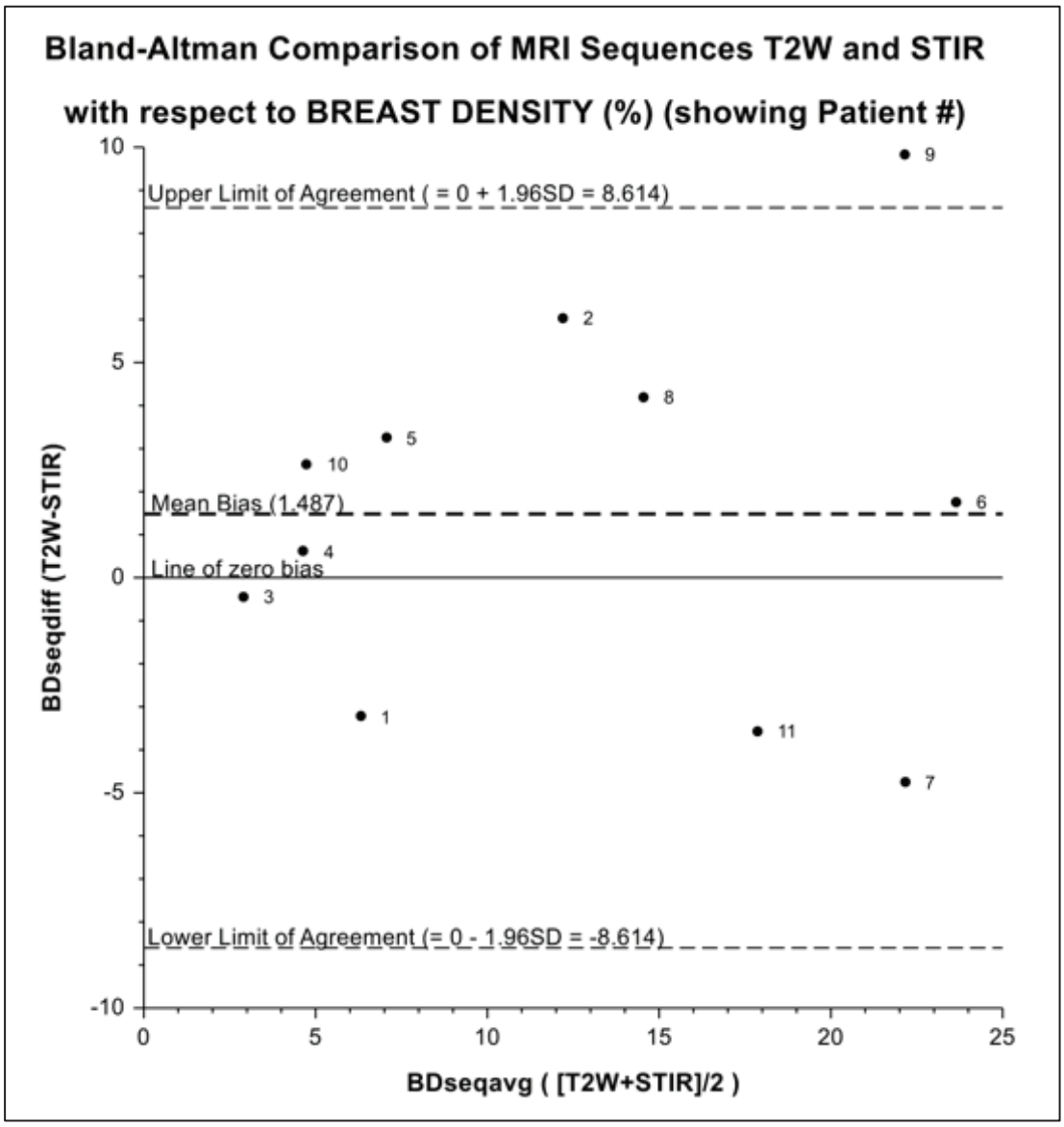

(C)

Figure 5.1. Bland-Altman plots for the breast density parameters agreement analysis (N = 11). **(A)** breast volume, **(B)** fibroglandular tissue volume, and **(C)** percentage of breast density measured from the non-fat-suppressed T2-weighted TSE and fat-suppressed T2-weighted STIR MR sequences. The average of the breast density parameters of the two sequences is on the x-axis, while the estimated mean difference (a measure of the bias between the two sequences) is on the y-axis. Limits of agreement are shown as solid, black lines with 95% confidence intervals (as light dotted black line), and bias (as dark dotted black line) with 95% confidence interval. Note that the limits of agreement are calculated as the mean difference ± 1.96 Std Dev, where the Std Dev is determined from the array of difference value. The factor 1.96 indicates the assumption that the difference values are normally distributed. The upper and lower limits of the agreement 1.96 Std Dev are displayed above and below zero, not the mean difference. The differences between the two MRI sequences and their averages are listed in Table 5.3, while the Bland-Altman analyses, including the bias and limits of agreement are in Table 5.5.

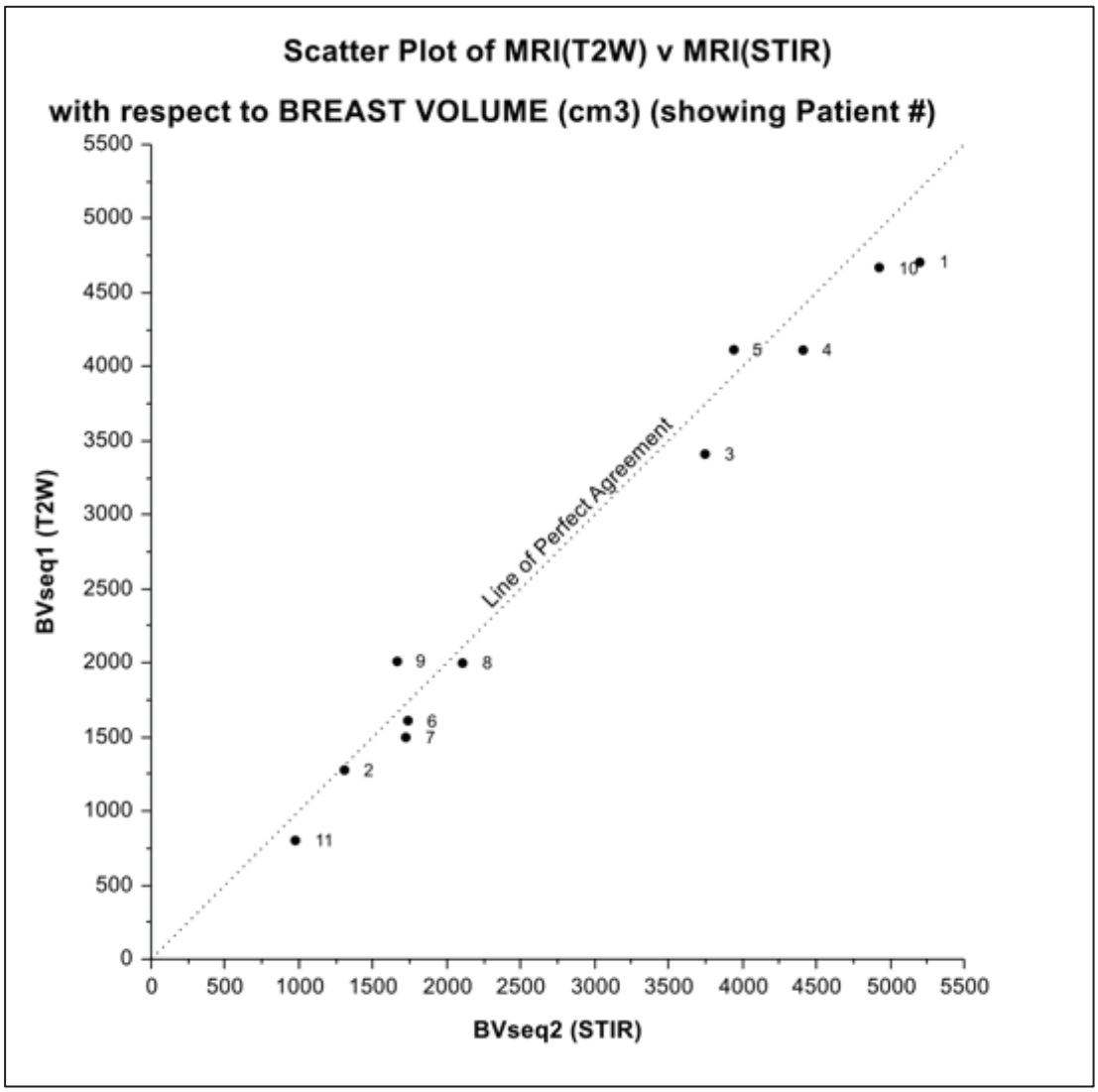
Scatter Plot of MRI(T2W) v MRI(STIR)
with respect to BREAST VOLUME (cm3) (showing Patient #)
BVseq1 (T2W)
BVseq2 (STIR)
Line of Perfect Agreement
0
500
1000
1500
2000
2500
3000
3500
4000
4500
5000
5500
1
2
3
4
5
6
7
8
9
10
11

(A)

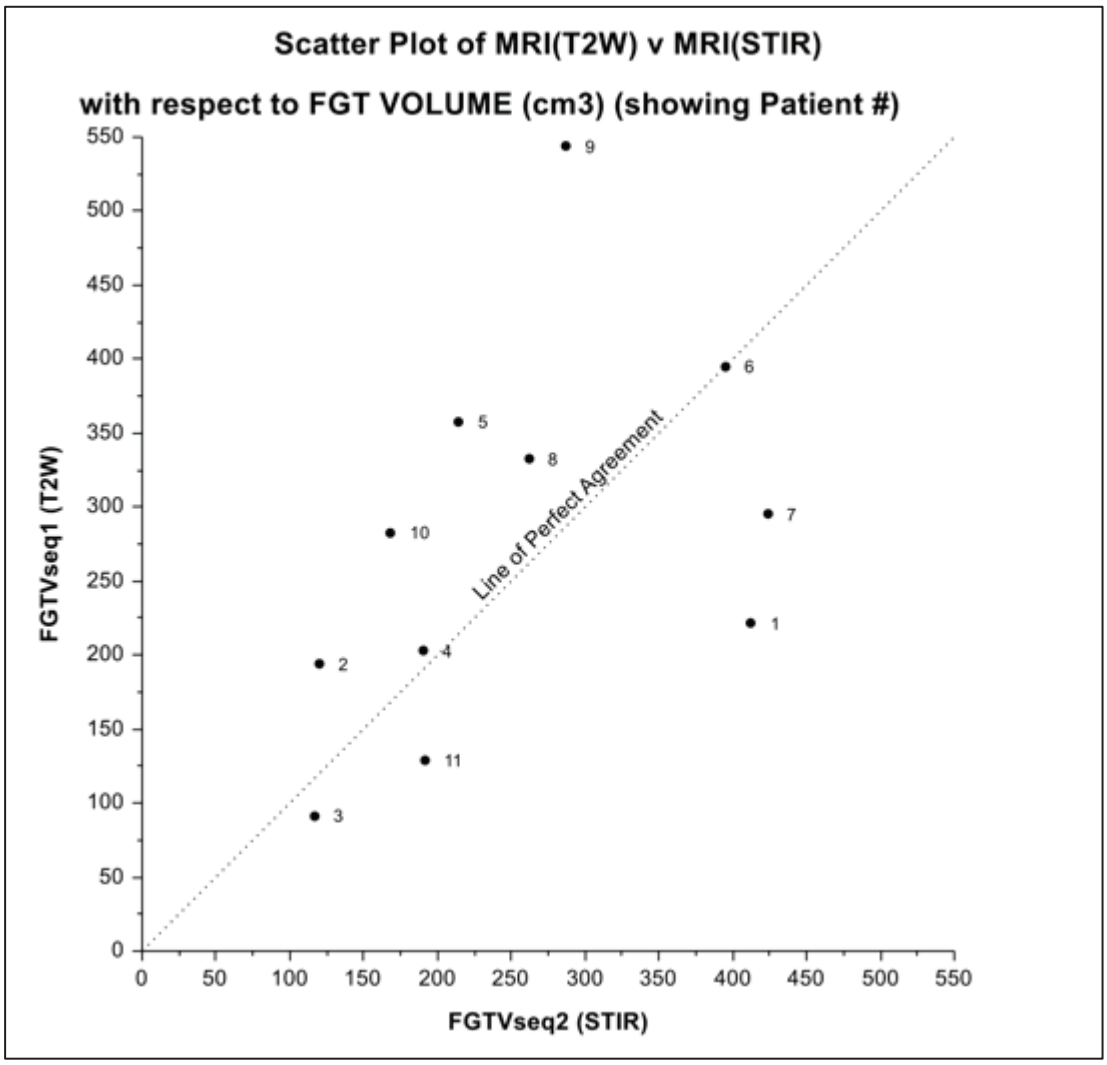
Scatter Plot of MRI(T2W) v MRI(STIR)
with respect to FGT VOLUME (cm3) (showing Patient #)
FGTVseq1 (T2W)
FGTVseq2 (STIR)
Line of Perfect Agreement
9
6
5
8
7
10
1
2
4
11
3
0
50
100
150
200
250
300
350
400
450
500
550

(B)

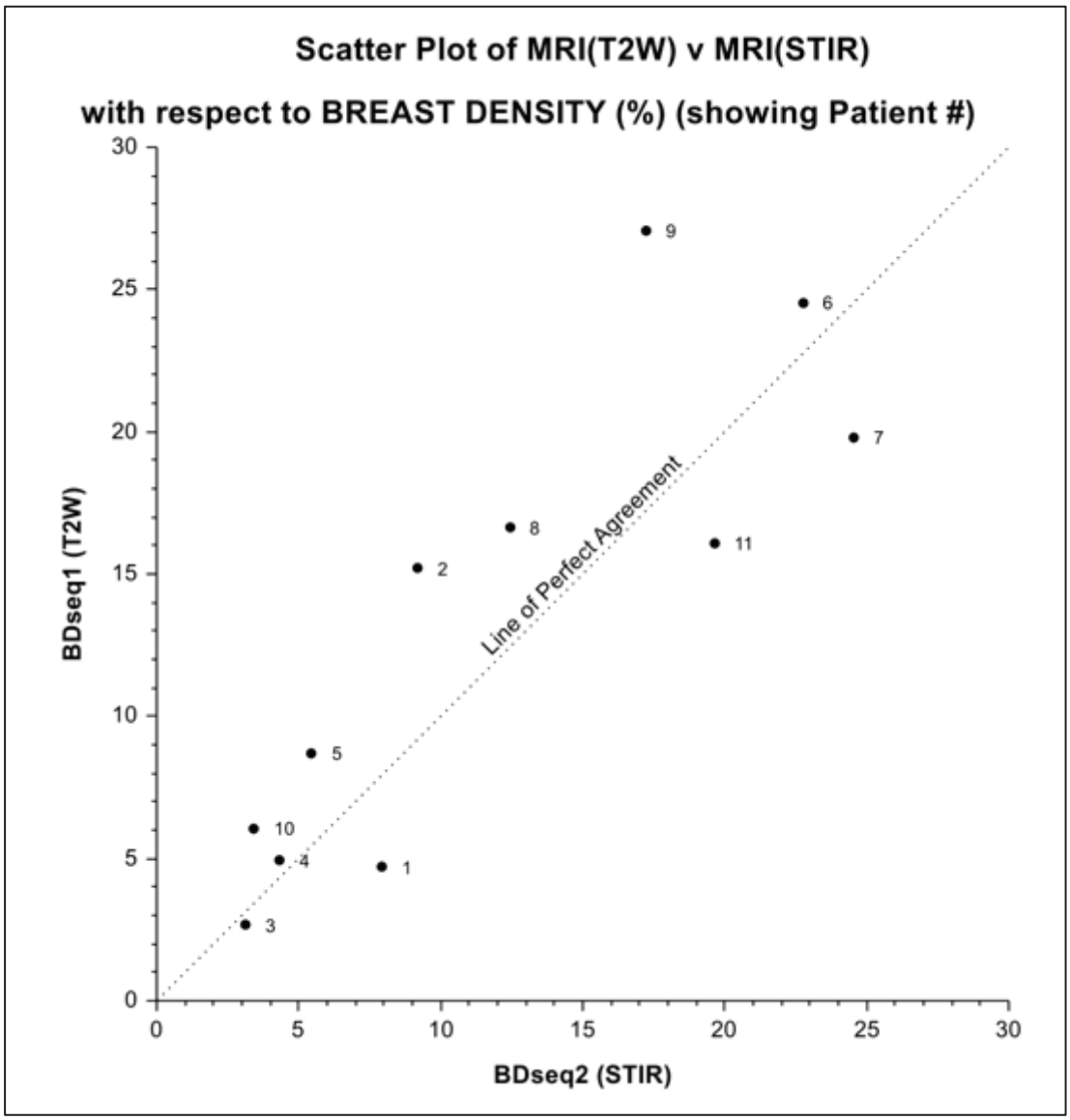

(C)

Figure 5.2. Scatter plots display the degree of agreement between the non-fat-suppressed T2-weighted TSE and the fat-suppressed T2-weighted STIR MRI sequences for **(A)** breast volume, **(B)** fibroglandular tissue volume, and **(C)** percentage of breast density. The breast density parameters (A, B, and C) measured from the fat-suppressed T2-weighted STIR MRI sequence are on the x-axis; from the non-fat-suppressed T2-weighted TSE MRI sequence are on the y-axis. The dotted black line shows the line of equality (i.e., the line of perfect agreement); the Bland-Altman correlation of 1 indicates perfect agreement, while the value of 0 indicates complete discord. The level of agreements between the two MRI sequences are listed in Table 5.4, with a correlation coefficient of 0.990 for breast volume, 0.458 for fibroglandular tissue volume, and 0.858 for percentage of breast density.

The 95% tolerance limits of agreement were -602.513, 323.355. Likewise, there was no significant difference (t = 0.628, p = 0.544) between the volume of fibroglandular tissue measured on the non-fat-suppressed T2-weighted TSE sequence, 276.909 ± 129.250 cm^3, and the fat-suppressed T2-weighted STIR sequence, 252.844 ± 113.393 cm^3, with a mean difference of 24.065 ± 127.041 cm^3 and a standard error of 38.304. The 95% tolerance limits of agreement were -224.935, 273.066. Further, the percentage of breast density was 13.308 ± 8.429% for the non-fat-suppressed T2-weighted TSE sequence and 11.821 ± 7.989% for the fat-suppressed T2-weighted STIR sequence, which was not statistically significant (t = 1.122, p = 0.288), with a mean difference of 1.487 ± 4.395% and a standard error of 1.325. Consequently, the fat-suppressed T2-weighted sequence appeared to result in a lower reading, by between -1.466 and 4.439 (95% confidence limits), than that of the non-fat-suppressed T2-weighted sequence. Despite this observation, the 95% tolerance limits of agreement (-7.127 and 10.101) were wide apart to give preference to one sequence over the other with respect to the quantitative measurement of breast density, as shown in Table 5.5.

The most prominent finding to emerge from the data was the comparatively high standard deviation of breast density parameters, which resulted in high individual variation among patients. However, the estimate of the standard deviations of the differences in both breast volume and breast density decreased, as some of the influence of repeated measurement error was accordingly eliminated. The results also indicated, as shown in Table 5.4, that the level of agreement between the non-fat-suppressed T2-weighted TSE and the fat-suppressed T2-weighted STIR MRI sequences had a correlation coefficient of 0.990 for breast volume, 0.458 for fibroglandular tissue volume, and 0.858 for percentage of breast density. Although the

breast volume measured on the non-fat-suppressed and the fat-suppressed T2-weighted MRI sequences was almost correlated (r = 0.990), as shown in Figure 5.2A, there was no evidence of agreement between the two measurement sequences.

From the data in Figure 5.1A, it is apparent that the differences in breast volume between the non-fat-suppressed and the fat-suppressed T2-weighted MRI sequences for patients 1, 3, 4, and 10 were -494.768, -337.405, -299.050, and -255.885, respectively, suggesting a rise in negative bias with increasing volumes. Nevertheless, there was a small negative bias associated with small breast volumes in patients 2, 6, and 8, with a mean difference of -31.246, -127.223, and -107.728, respectively. In contrast to breast volumes, however, there was a considerable dispersion in the volume of fibroglandular tissue and the percentage of breast density measured in the fat-suppressed and non-fat-suppressed T2-weighted sequences, as shown in Figures 5.2B and C, which made the bias more difficult to detect.

Overall, the results indicated that no evidence of measurement bias was found between the non-fat-suppressed T2-weighted TSE and the fat-suppressed T2-weighted STIR MRI sequences; furthermore, there was no proof to reject the hypothesis that the differences are normally distributed, since the majority of the mean difference is allocated between the upper and lower limits of the agreement, as shown in Figure 5.1

Table 5.2. Results of the estimated mean and standard deviation of breast volume, fibroglandular tissue volume, and percentage of breast density for high-risk women using non-fat-suppressed T2-weighted TSE (Non-fat-sup) and fat-suppressed T2-weighted STIR (Fat-sup) MRI sequences.

Patient No.	Breast Volume (cm^3)		Fibroglandular Tissue Volume (cm^3)		Breast Density (%)	
	Non-fat-sup	Fat-sup	Non-fat-sup	Fat-sup	Non-fat-sup	Fat-sup
	(Average ± Std Dev*)		(Average ± Std Dev)		(Average ± Std Dev)	
1.	4704.994 ± 65.824	5199.762 ± 69.849	221.663 ± 2.766	412.044 ± 5.566	4.712 ± 0.125	7.924 ± 0.001
2.	1276.573 ± 55.662	1307.819 ± 18.326	194.122 ± 5.251	120.019 ± 6.744	15.212 ± 0.252	9.182 ± 0.644
3.	3410.015 ± 159.200	3747.420 ± 110.919	91.110 ± 0.190	116.867 ± 4.800	2.675 ± 0.130	3.122 ± 0.220
4.	4111.758 ± 129.505	4410.808 ± 112.994	203.099 ± 0.272	190.414 ± 1.649	4.942 ± 0.162	4.319 ± 0.148
5.	4114.339 ± 136.961	3942.410 ± 207.191	357.578 ± 1.452	214.143 ± 2.613	8.695 ± 0.254	5.438 ± 0.219
6.	1610.203 ± 59.582	1737.426 ± 92.531	394.813 ± 10.743	395.112 ± 3.372	24.524 ± 0.240	22.768 ± 1.018
7.	1497.314 ± 31.837	1722.762 ± 101.423	295.482 ± 78.072	423.934 ± 63.778	19.794 ± 5.635	24.541 ± 2.257
8.	1999.096 ± 3.499	2106.824 ± 25.886	332.697 ± 31.276	262.204 ± 6.461	16.641 ± 1.535	12.448 ± 0.460
9.	2010.286 ± 9.746	1664.973 ± 36.490	544.060 ± 16.391	286.927 ± 6.915	27.066 ± 0.947	17.233 ± 0.038
10.	4669.732 ± 145.690	4925.616 ± 12.496	282.503 ± 18.919	168.012 ± 4.897	6.046 ± 0.217	3.411 ± 0.108
11.	801.447 ± 3.427	975.309 ± 56.272	128.875 ± 3.048	191.609 ± 10.022	16.080 ± 0.312	19.649 ± 0.106

* Standard deviation.

Table 5.3. Difference between the non-fat-suppressed T2-weighted TSE (Non-fat-sup) and fat-suppressed T2-weighted STIR (Fat-sup) MRI sequences and their average for breast volume, fibroglandular tissue volume, and percentage of breast density measured in high-risk women.

Patient No.	Breast Volume (cm^3)		Fibroglandular Tissue Volume (cm^3)		Breast Density (%)	
	Difference*	Average**	Difference	Average	Difference	Average
1.	-494.768	4952.378	-190.381	316.853	-3.212	6.318
2.	-31.246	1292.196	74.104	157.070	6.030	12.197
3.	-337.405	3578.717	-25.757	103.989	-0.447	2.898
4.	-299.050	4261.283	12.685	196.757	0.623	4.630
5.	171.929	4028.375	143.435	285.861	3.258	7.066
6.	-127.223	1673.814	-0.299	394.962	1.756	23.646
7.	-225.448	1610.038	-128.453	359.708	-4.747	22.168
8.	-107.728	2052.960	70.493	297.450	4.193	14.545
9.	345.313	1837.629	257.133	415.493	9.833	22.149
10.	-255.885	4797.674	114.492	225.257	2.635	4.729
11.	-173.862	888.378	-62.734	160.242	-3.569	17.864

* The difference between the two MRI sequences = (Non-fat-sup - Fat-sup); ** the average of the two MRI sequences = (Non-fat-sup + Fat-sup)/2.

Table 5.4. Descriptive statistics of breast volume, fibroglandular tissue volume, and percentage of breast density measured on the non-fat-suppressed T2-weighted TSE (Non-fat-sup) and fat-suppressed T2-weighted STIR (Fat-sup) MRI sequences in high-risk women.

Variable	Count	Mean	Std Dev*	95.0% LCL of Mean	95.0% LCL of Mean
Breast Volume (cm^3)					
Non-fat-sup	1	2745.978	1469.893	1758.490	3733.465
Fat-sup	1	2885.557	1568.706	1831.686	3939.428
Difference	1	-139.579	236.191	-298.255	19.096
Correlation Coefficient = 0.990; SE ** **(10 df***) = 71.214; Prob Level**** **= 0.078; T-Statistics = -1.960**					
Fibroglandular Tissue Volume (cm)					
Non-fat-sup	1	276.909	129.250	190.078	363.740
Fat-sup	1	252.844	113.393	176.665	329.022
Difference	1	24.065	127.041	-61.282	109.413
Correlation Coefficient = 0.458; SE (10 df) = 38.304; Prob Level = 0.544; T-Statistics = 0.628					
Breast Density (%)					
Non-fat-sup	1	13.308	8.429	7.645	18.971
Fat-sup	1	11.821	7.989	6.454	17.188
Difference	1	1.487	4.395	-1.466	4.439
Correlation Coefficient = 0.858; SE (10 df) = 1.325; Prob Level = 0.288; T-Statistics = 1.122					

* Standard deviation; ** Standard error; *** The degrees of freedom; **** The significance level of the F-ratio (i.e., the probability that the difference between data is significant or not). The significant difference between the quantitative measurements of the breast volume, the fibroglandular volume, and the percentage of breast density measured on the non-fat suppressed T2-weighted TSE and the fat-suppressed T2-weighted STIR MRI sequences was determined at the 5% level using the one-sample t-test.

Table 5.5. Bland-Altman Analysis (Bias and limits of agreement) for breast volume, fibroglandular tissue volume, and percentage of breast density between the non-fat-suppressed T2-weighted TSE (Non-fat-sup) and fat-suppressed T2-weighted STIR (Fat-sup) MRI sequences.

Variable	Count	Mean	Std Dev	95.0% LCL of Mean	95.0% LCL of Mean
Breast Volume (cm^3)					
Bias (Difference)	1	-139.579	236.191	-298.255	19.096
Lower Limit of Agreement	1	-602.513	125.646	-882.470	-322.557
Upper Limit of Agreement	1	323.355	125.646	43.399	603.311
Fibroglandular Tissue Volume (cm^3)					
Bias (Difference)	1	24.065	127.041	-61.282	109.413
Lower Limit of Agreement	1	-224.935	67.582	-375.516	-74.354
Upper Limit of Agreement	1	273.066	67.582	122.484	423.647
Breast Density (%)					
Bias (Difference)	1	1.487	4.395	-1.466	4.439
Lower Limit of Agreement	1	-7.128	2.338	-12.337	-1.918
Upper Limit of Agreement	1	10.101	2.338	4.891	15.310

Table 5.6. Test of normality of differences assumption for breast volume, fibroglandular tissue volume, and percentage of breast density between the non-fat-suppressed T2-weighted TSE and fat-suppressed T2-weighted STIR MRI sequences.

Assumption	Variable	Value	Prob Level	Decision (α = 0.050)
Shapiro-Wilk	Breast Volume Fibroglandular Tissue Volume Breast Density	0.950 0.992 0.971	0.642 0.999 0.893	Cannot reject normality
Skewness	Breast Volume Fibroglandular Tissue Volume Breast Density	1.243 0.106 0.497	0.214 0.916 0.619	Cannot reject normality
Kurtosis	Breast Volume Fibroglandular Tissue Volume Breast Density	0.754 0.226 0.008	0.451 0.821 0.994	Cannot reject normality
Omnibus	Breast Volume Fibroglandular Tissue Volume Breast Density	2.113 0.062 0.247	0.348 0.969 0.884	Cannot reject normality

5.5 Discussion

Although T2-weighted imaging has been confirmed as a standard part of clinical breast MRI protocols across a variety of T2-weighted sequences, the relative role of T2-weighted images with/without the use of fat-suppression techniques in the quantitative assessment of breast density remains limited. It was hypothesized that the T2-weighted imaging features can assist in the differentiation between fibroglandular and fatty tissue, and allow for more accurate measurement of breast density. In this study, the non-fat-suppressed T2-weighted TSE and the fat-suppressed T2-weighted STIR MR imaging sequences were compared in 11 women with an increased risk of developing breast cancer with regard to their quantitative measurements of breast volume, fibroglandular tissue volume, and percentage of breast density. The results showed that there was no indication of measurement bias between the non-fat-suppressed and the fat-suppressed T2-weighted imaging sequences with respect to breast density parameters, and that there was no evidence to refute the presumption that the differences were normally distributed.

Although the breast volume measured in the fat-suppressed T2-weighted sequence was slightly higher than that in the non-fat-suppressed T2-weighted sequence and the difference was close to significant ($p = 0.078$), the findings showed no significant difference in the breast density parameters analyzed from the two imaging techniques. A possible explanation for these results could be that the skin is more prominent on the fat-suppressed images than on the non-fat-suppressed images; this could be the cause of such a difference in measurements, although it was considered as part of the breast volume for both sequences. Even though the signal-to-noise ratio was much higher for the non-fat-suppressed images than for the fat-suppressed images,[44, 49] the

difference can also be explained in part by the contrast between the breast tissues and the surrounding tissues. Although it was well defined in both sequences, it could be a source of variation in the segmentation and/or measurement of breast volume and breast density outcomes. A previous study showed that the breast volume, fibroglandular tissue volume, and percentage of breast density measured in the T1-weighted sequences with and without fat-suppression techniques are highly correlated.[44] Although these results differed from the current study, which specified that the breast density parameters were quantified on the T1-weighted images, they are consistent with our findings, which showed that the breast volumes measured on the non-fat-suppressed and the fat-suppressed sequences were almost identical.

As the quantification of breast density parameters was based on different density prototypes, the findings showed that the difference in breast volume between the non-fat-suppressed and the fat-suppressed T2-weighted MRI sequences could be classified into two patterns: the first indicates small negative differences associated with small volumes, while the second indicates large negative differences associated with large volumes, as shown in Figure 5.1A. This clustering in both the non-fat-suppressed and the fat-suppressed T2-weighted sequences suggests that a systematic effect may be a reason for this rather than a random variation. However, the volume of fibroglandular tissue and the percentage of breast density measured in both sequences were noticeably dispersed, making the bias more difficult to detect, as shown in Figures 5.1B and C. It is possible, therefore, that the segmentation method of the breast volume and fibroglandular tissue volume may have been affected by the variation of the subject, although this needs to be confirmed by future research.

Another important finding arising from this study was that the percentage of breast density measured on the non-fat-suppressed T2-weighted sequence was subsequently increased compared to the fat-suppressed T2-weighted sequence because of the increased fibroglandular tissue volume and decreased breast volume. The assessment of breast density varies with pulse sequence, image quality, and fibroglandular tissue segmentation. This may result in a profound effect on the efficiency of the segmentation and/or measurement method and consequently on the results of breast density parameters. The segmentation and/or measurement of breast density parameters could be affected by the various levels of inhomogeneity in both the fat-suppressed and non-fat-suppressed MR images. The difference could also be attributed to the fact that breast MRI is obtained with a surface coil covering a wide region, which results in varying signal strength depending on the location of the tissue being imaged.

While this study reported that no substantial difference was observed between the non-fat-suppressed and the fat-suppressed T2-weighted imaging sequences for the quantitative measurement of breast density parameters, the findings are subject to certain limitations. First, the type of fat suppression used in this study relied on an inversion-based approach, which is just one of several methods; caution must be used, as it might not be possible to extrapolate the results to all fat-suppression techniques. Second, although the acquisition of the non-fat-suppressed and fat-supressed sequences was based on a two-dimensional imaging, the scanning parameters, such as field-of-view and matrix size, were relatively different; this may play a role in the segmentation and/or measurement of breast density; however, caution should be applied because the results may not applicable to clinical practice without further investigations. Further research to examine the impact of the scanning/technical parameters on the quantitative measurement of breast density would be suggested.

Third, the association of breast density parameters and the T2-weighted imaging sequences could not be further explored, as the sample size was limited. It must be acknowledged that the small sample size was selected because of the expected complexity of recruiting cancer-free patients at high risk of developing breast cancer. Nevertheless, a further study with a larger sample size to determine exactly how the non-fat-suppressed and fat-suppressed T2-weighted sequences influence the quantification of breast density would be desirable. Further, the study is limited by the lack of information about the patient age; this may highlight the potential correlation between age dependency and the results, thus explaining the disparity between the two MRI sequences with respect to the patterns of breast density parameters, because the distribution of fibroglandular tissue varies from age to age and from person to person. Finally, using a semi-automated method, the breast density parameters were segmented and measured; this means that the prospective cause of such a discrepancy between the non-fat-suppressed and fat-suppressed sequences could be due to a high degree of reliance on user interaction. In future studies, it might be possible to use deep learning method to segment breast and fibroglandular tissue,[50, 51] in which the degree of difference between the non-fat-suppressed and fat-suppressed T2-weighted imaging sequences could be more accurately assessed with regard to the quantitative measurement of breast density in MRI volumes.

5.6 Conclusion

Of the two types of scanning techniques used in this study, there seems to be no substantial difference between the non-fat-suppressed and fat-suppressed MR pulse sequences for the quantitative measurement of breast density parameters; however, a

much larger study is required to determine the complementary role of T2-weighted imaging in this regard.

5.7 References

1. Chen JH, Chang YC, Chang D, Wang YT, Nie K, Chang RF, Nalcioglu O, Huang CS, Su MY. Reduction of breast density following tamoxifen treatment evaluated by 3-D MRI: Preliminary study. Magn Reson Imaging. 2011; 29(1):91-98.
2. Wang J, Azziz A, Fan B, Malkov S, Klifa C, Newitt D, Yitta S, Hylton N, Kerlikowske K, Shepherd JA. Agreement of mammographic measures of volumetric breast density to MRI. PLoS ONE. 2013; 8(12):e81653.
3. Tagliafico A, Bignotti B, Tagliafico G, Astengo D, Martino L, Airaldi S, Signori A, Sormani MP, Houssami N, Calabrese M. Breast density assessment using a 3T MRI system: Comparison among different sequences. PLoS ONE. 2014; 9(6):e99027.
4. Bu Y, Xia J, Joseph B, Zhao X, Xu M, Yu Y, Qi S, Shah KA, Wang S, Hu J. Non-contrast MRI for breast screening: Preliminary study on detectability of benign and malignant lesions in women with dense breasts. Breast Cancer Res Treat. 2019; 177(3):629–639.
5. Nelson HD, Zakher B, Cantor A, Fu R, Griffin J, O'Meara ES, Buist DS, Kerlikowske K, van Ravesteyn NT, Trentham-Dietz A. Risk factors for breast cancer for women aged 40 to 49 years: A systematic review and meta-analysis. Ann Intern Med. 2012; 156(9):635–648.

6. McCormack VA, dos Santos Silva I. Breast density and parenchymal patterns as markers of breast cancer risk: A meta-analysis. Cancer Epidem Biomar. 2006; 15(6):1159–1169.
7. Kerlikowske K, Ichikawa L, Miglioretti DL, Buist DS, Vacek PM, Smith-Bindman R, Yankaskas B, Carney PA, Ballard-Barbash R. Longitudinal measurement of clinical mammographic breast density to improve estimation of breast cancer risk. J Natl Cancer Inst. 2007; 99(5):386–395.
8. Choi G, Woo OH, Shin HS, Jang S, Cho KR, Seo BK. Comparison of two-dimensional synthesized mammogram (2DSM) and conventional full-field digital mammogram (FFDM) for evaluation of breast cancer. Clin Imaging. 2017; 43:170-174.
9. Park JM, Franken JR EA, Garg M, Fajardo LL, Niklason LT. Breast tomosynthesis: Present considerations and future applications. Radiographics. 2007; 27(Suppl_1):S231-S240.
10. Li H, Weiss WA, Medved M, Abe H, Newstead GM, Karczmar GS, Giger ML. Breast density estimation from high spectral and spatial resolution MRI. J Med Imaging. 2016; 3(4):044507.
11. Wu S, Weinstein SP, Conant EF, Kontos D. Automated fibroglandular tissue segmentation and volumetric density estimation in breast MRI using an atlas-aided fuzzy C-means method. Med Phys. 2013; 40(12):122302.
12. Sardanelli F, Boetes C, Borisch B, Decker T, Federico M, Gilbert FJ, Helbich T, Heywang-Köbrunner SH, Kaiser WA, Kerin MJ, Mansel RE. Magnetic resonance imaging of the breast: Recommendations from the EUSOMA working group. Eur J Cancer. 2010; 46(8):1296–1316.

13. Londero V, Zuiani C, Linda A, Girometti R, Bazzocchi M, Sardanelli F. High-risk breast lesions at imaging-guided needle biopsy: Usefulness of MRI for treatment decision. Am J Roentgenol. 2012; 199(2):W240–W250.
14. Mann RM, Balleyguier C, Baltzer PA, Bick U, Colin C, Cornford E, Evans A, Fallenberg E, Forrai G, Fuchsjäger MH, Gilbert FJ. Breast MRI: EUSOBI recommendations for women's information. Eur Radiol. 2105; 25(12):3669-3678.
15. Heller SL, Yeong Lin LL, Melsaether AN, Moy L, Gao Y. Hormonal Effects on Breast Density, Fibroglandular Tissue, and Background Parenchymal Enhancement. Radiographics. 2018; 38(4):983-996.
16. Klifa C, Carballido-Gamio J, Wilmes L, Laprie A, Shepherd J, Gibbs J, Fan B, Noworolski S, Hylton N. Magnetic resonance imaging for secondary assessment of breast density in a high-risk cohort. Magn Reson Imaging. 2010; 28(1):8–15.
17. Niukkanen A, Arponen O, Nykänen A, Masarwah A, Sutela A, Liimatainen T, Vanninen R, Sudah M. Quantitative volumetric K-means cluster segmentation of fibroglandular tissue and skin in breast MRI. J Digit Imaging. 2018; 31(4):425-434.
18. Ertas G, Doran SJ, Leach MO. A computerized volumetric segmentation method applicable to multi-center MRI data to support computer-aided breast tissue analysis, density assessment and lesion localization. Med Biol Eng Comput. 2017; 55(1):57-68.
19. Petridou E, Kibiro M, Gladwell C, Malcolm P, Toms A, Juette A, Borga M, Leinhard OD, Romu T, Kasmai B, Denton E. Breast fat volume measurement using wide-bore 3 T MRI: Comparison of traditional mammographic density

evaluation with MRI density measurements using automatic segmentation. Clin Radiol. 2017; 72(7):565-572.

20. American College of Radiology. ACR BI-RADS® Atlas: Breast Imaging Reporting and Data System; American College of Radiology: Reston, VA, USA, 2013.
21. Mainiero MB, Lourenco A, Mahoney MC, Newell MS, Bailey L, Barke LD, D'Orsi C, Harvey JA, Hayes MK, Huynh PT, Jokich PM. ACR appropriateness criteria breast cancer screening. J Am Coll Radiol. 2016; 13(11):45-49.
22. Timmers JM, van Doorne-Nagtegaal HJ, Verbeek AL, Den Heeten GJ, Broeders MJ. A dedicated BI-RADS training programme: Effect on the inter-observer variation among screening radiologists. Eur Radiol. 2012; 81(9):2184-2188.
23. Lazarus E, Mainiero MB, Schepps B, Koelliker SL, Livingston LS. BI-RADS lexicon for US and mammography: Interobserver variability and positive predictive value. Radiology. 2006; 239(2):385-391.
24. Ciatto S, Houssami N, Apruzzese A, Bassetti E, Brancato B, Carozzi F, Catarzi S, Lamberini MP, Marcelli G, Pellizzoni R, Pesce B. Categorizing breast mammographic density: Intra-and interobserver reproducibility of BI-RADS density categories. The Breast. 2005; 14(4):269-275.
25. Nayeem F, Ju H, Brunder DG, Nagamani M, Anderson KE, Khamapirad T, Lu LJ. Similarity of fibroglandular breast tissue content measured from magnetic resonance and mammographic images and by a mathematical algorithm. Int J Breast Cancer. 2014; 2014:961679.
26. Lin M, Chan S, Chen JH, Chang D, Nie K, Chen ST, Lin CJ, Shih TC, Nalcioglu O, Su MY. A new bias field correction method combining N3 and

FCM for improved segmentation of breast density on MRI. Med Phys. 2011; 38(1):5-14.

27. Doran SJ, Hipwell JH, Denholm R, Eiben B, Busana M, Hawkes DJ, Leach MO, Silva ID. Breast MRI segmentation for density estimation: Do different methods give the same results and how much do differences matter? Med Phys. 2017; 44(9):4573-4592.
28. Tagliafico A, Tagliafico G, Tosto S, Chiesa F, Martinoli C, Derchi LE, Calabrese M. Mammographic density estimation: comparison among BI-RADS categories, a semi-automated software and a fully automated one. Breast. 2009; 18(1):35-40.
29. Boston RC, Schnall MD, Englander SA, Landis JR, Moate PJ. Estimation of the content of fat and parenchyma in breast tissue using MRI T1 histograms and phantoms. Magn Reson Imaging. 2005; 23(4):591-599.
30. Lu LJ, Nishino TK, Johnson RF, Nayeem F, Brunder DG, Ju H, Leonard Jr MH, Grady JJ, Khamapirad T. Comparison of breast tissue measurements using magnetic resonance imaging, digital mammography and a mathematical algorithm. Phys Med Biol. 2012; 57(21):6903.
31. Nie K, Chen JH, Chan S, Chau MK, Yu HJ, Bahri S, Tseng T, Nalcioglu O, Su MY. Development of a quantitative method for analysis of breast density based on three-dimensional breast MRI. Med Phys. 2008; 35(12):5253-5262.
32. Sindi R, Sá Dos Reis C, Bennett C, Stevenson G, Sun Z. Quantitative measurements of breast density using magnetic resonance imaging: A systematic review and meta-analysis. J Clin Med. 2019; 8(5):745.
33. Sindi R, Sun Z. Optimal protocols for quantitative assessment of breast density using magnetic resonance imaging. Australas Med J. 2019; 12(6):186–188.

34. Warner E, Messersmith H, Causer P, Eisen A, Shumak R, Plewes D. Systematic review: Using magnetic resonance imaging to screen women at high risk for breast cancer. Ann Intern Med. 2008; 148(9):671–679.
35. Ledger AE, Scurr ED, Hughes J, Macdonald A, Wallace T, Thomas K, Wilson R, Leach MO, Schmidt MA. Comparison of Dixon sequences for estimation of percent breast fibroglandular tissue. PLoS ONE. 2016; 11(3):e0152152.
36. Miyazaki M, Wheaton A, Kitane S. Enhanced fat suppression technique for breast imaging. J Magn Reson Imaging. 2013; 38(4):981-986.
37. Kalovidouri A, Firmenich N, Delattre BM, Picarra M, Becker CD, Montet X, Botsikas D. Fat suppression techniques for breast MRI: Dixon versus spectral fat saturation for 3D T1-weighted at 3 T. Radiol Med. 2017; 122(10):731-742.
38. Le-Petross H, Kundra V, Szklaruk J, Wei W, Hortobagyi GN, Ma J. Fast three-dimensional dual echo Dixon technique improves fat suppression in breast MRI. J Magn Reson Inaging. 2010; 31(4):889-894.
39. Dogan BE, Ma J, Hwang K, Liu P, Yang WT. T1-weighted 3D dynamic contrast-enhanced MRI of the breast using a dual-echo Dixon technique at 3 T. J Magn Reson Imaging. 2011; 34(4):842-851.
40. Clauser P, Pinker K, Helbich TH, Kapetas P, Bernathova M, Baltzer PA. Fat saturation in dynamic breast MRI at 3 Tesla: is the Dixon technique superior to spectral fat saturation? A visual grading characteristics study. Eur Radiol. 2014; 24(9):2213-2219.
41. Del Grande F, Santini F, Herzka DA, Aro MR, Dean CW, Gold GE, Carrino JA. Fat-suppression techniques for 3-T MR imaging of the musculoskeletal system. Radiographics. 2014; 34(1):217-233.

42. Mamourian AC. Practical MR Physics: And Case File of MR Artefacts and Pitfalls. Oxford University Press; 2010.
43. Hendrick RE. Breast MRI: fundamentals and technical aspects. Springer Science & Business Media; 2007.
44. Chang DH, Chen JH, Lin M, Bahri S, Yu HJ, Mehta RS, Nie K, Hsiang DJ, Nalcioglu O, Su MY. Comparison of breast density measured on MR images acquired using fat-suppressed versus nonfat-suppressed sequences. Med Phys. 2011; 38(11):5961-5968.
45. Kuhl CK, Klaschik S, Mielcarek P, Gieseke J, Wardelmann E, Schild HH. Do T2-weighted pulse sequences help with the differential diagnosis of enhancing lesions in dynamic breast MRI? J Magn Reson Imaging. 1999; 9(2):187-196.
46. Gallego-Ortiz C, Martel AL. Using quantitative features extracted from T2-weighted MRI to improve breast MRI computer-aided diagnosis (CAD). PLoS ONE. 2017; 12(11):e0187501.
47. Santamaría G, Velasco M, Bargalló X, Caparrós X, Farrús B, Luis Fernández P. Radiologic and pathologic findings in breast tumors with high signal intensity on T2-weighted MR images. Radiographics. 2010; 30(2):533-548.
48. Moran CJ, Hargreaves BA, Saranathan M, Lipson JA, Kao J, Ikeda DM, Daniel BL. 3D T2-weighted spin echo imaging in the breast. J Magn Reson Imaging. 2014; 39(2):332-338.
49. Mann RM, Kuhl CK, Kinkel K, Boetes C. Breast MRI: Guidelines from the European society of breast imaging. Eur Radiol. 2008; 18(7):1307-1318.
50. Dalmış MU, Litjens G, Holland K, Setio A, Mann R, Karssemeijer N, Gubern-Mérida A. Using deep learning to segment breast and fibroglandular tissue in MRI volumes. Med Phys. 2017; 44(2):533-546.

51. Saffari N, Rashwan HA, Abdel-Nasser M, Kumar Singh V, Arenas M, Mangina E, Herrera B, Puig D. Fully Automated Breast Density Segmentation and Classification Using Deep Learning. Diagnostics. 2020; 10(11):988.

6. Chapter 6

Conclusions and Future Directions

6.1 Conclusions

This study was performed to investigate the quantitative assessments of breast density using breast MR imaging protocols with the aim of determining the optimal breast MRI protocol. Through both phantom experiments and clinical data analysis, expected outcomes are achieved with significant findings as reported below.

A systematic review and meta-analysis study was conducted to evaluate the existing research on quantitative assessment of breast density using MRI data. This was the first comprehensive systematic review and meta-analysis of pooling the results of 38 studies reporting all breast density segmentation/measurement methods and scanning protocols using MRI data. Results of the analysis are summarised as follows:

- The review confirmed high levels of heterogeneity within the breast density studies, primarily due to the applications of MR breast-imaging protocols and the use of breast density segmentation/measurement methods.
- The study revealed that the assessment of breast density varied with pulse sequence, image quality, and fibroglandular tissue segmentation. This may result in a profound effect on the efficiency of the segmentation and/or measurement method and consequently on the results of breast density parameters.
- The analysis confirmed that the non-contrast-enhanced T1-weighted acquisition was commonly utilized among all MR breast-imaging protocols and the FCM is the most frequently used algorithm amongst the breast density segmentation/measurement methods.

This research successfully identified the appropriate materials for simulating the MRI related-characteristics of fibroglandular and adipose breast tissues, and developed a personalized 3D-printed breast model using 3D-printing techniques and tissue mimicking materials for the assessment of breast density. Outcomes are stated as follows:

- Anthropomorphic shapes of skin and fibroglandular tissues were constructed using 3D-printing techniques based on the segmentations of breast MR images from a selected healthy patient's data.
- All the 3D skin and fibroglandular region shells were designed as hollow structures using polylactic acid and photopolymer resin.
- The silicone and peanut oils were found to closely resemble the T1 relaxation times and imaging characteristics of fibroglandular and adipose breast tissues, respectively.
- The phantom was used to test different breast MR imaging protocols to determine the optimum scanning parameters for the quantitative assessment of breast density.

The breast density parameters were quantitatively assessed using a personalized 3D-printed breast model and an objective comparison between the non-fat-suppressed and fat-suppressed MRI sequences. Findings are summarised as follows:

- The volume of fibroglandular tissue and the percentage of breast density were significantly higher in the fat-suppressed sequences than in the non-fat-suppressed sequences; however, the difference in breast volume was not statistically significant.

- The fat-suppressed sequences tended to be more useful than the non-fat-suppressed sequences for the quantitative measurements of the volume of fibroglandular tissue and the percentage of breast density.
- A fat-suppressed T2-weighted with turbo inversion recovery magnitude (TIRM) imaging sequence was superior to the non-fat- and fat-suppressed T1- and T2-weighted sequences for the quantitative measurement of breast density due to its ability to represent the exact breast tissue compositions.
- The segmentation and/or measurement of breast density parameters could be affected by the various levels of inhomogeneity in both the fat-suppressed and non-fat-suppressed MR images.
- The difference could also be attributed to the fact that breast MRI is obtained with a surface coil covering a wide region, which results in varying signal strength depending on the location of the tissue being imaged.

Finally, the breast density parameters were quantitatively assessed in a cohort of high-risk women based on an objective comparison between the fat-suppressed and non-fat-suppressed T2-weighted MRI. Key findings are stated as follows:

- The results revealed no indication of measurement bias between the non-fat-suppressed and fat-suppressed T2-weighted imaging sequences with respect to breast density parameters, and no evidence to reject the presumption that the differences were normally distributed.
- Although the breast volume measured in the fat-suppressed T2-weighted sequence was slightly higher than that in the non-fat-suppressed T2-weighted sequence and the difference was close to significant, the findings showed no

significant difference in the breast density parameters analyzed from the two imaging techniques.

- This study showed no substantial differences between the non-fat-suppressed and fat-suppressed T2-weighted imaging sequences in the quantitative measurement of breast density parameters; however, further studies with inclusion of a larger sample size are required to validate the complementary role of T2-weighted imaging in this regard.
- Although the acquisition of the non-fat-suppressed and fat-supressed sequences was based on a two-dimensional imaging, the scanning parameters, such as field-of-view and matrix size, were relatively different; this may play a role in the segmentation and/or measurement of breast density, and therefore in the results.
- The type of fat suppression used in this study relied on an inversion-based approach, which is just one of several methods; caution must be used, as it might not be possible to extrapolate the results to all fat-suppression techniques.

6.2 Future Directions

This research has intensified the need for a standardized imaging protocol and/or measurement method for the evaluation of breast density predominantly for women at an elevated risk of developing breast cancer, for those with high breast density. The study showed how 3D-printing techniques and tissue mimicking materials can be used to construct a customized breast model for the quantitative assessment of breast density. The findings also indicate that the silicone and peanut oils can effectively

mimic the T1 relaxation times and MR imaging characteristics of fibroglandular and adipose breast tissues. The proposed methodologies can be used as a preliminary work for breast structure simulations and the development of further patient models based on MRI datasets.

Although the fat-suppressed sequences were more useful for the quantitative measurements of the volume of fibroglandular tissue and the percentage of breast density in a patient-specific 3D-printed breast model than the non-fat-suppressed sequences, this work was limited by the fact that breast density parameters were segmented and measured using a semi-automated method, which indicates that the prospective cause of such a difference between the aforementioned imaging sequences could be due to a high degree of reliance on user interaction.

A fat-suppressed T2-weighted with TIRM imaging sequence was superior to the non-fat- and fat-suppressed T1- and T2-weighted sequences for the quantitative measurement of breast density due to its ability to represent the exact breast tissue compositions. Despite being preliminary findings, the study indicates that TIRM could be incorporated with fat-suppression techniques for the assessment of breast density. The fat-suppressed T2-weighted image with TIRM acquisition can be a promising technique for the quantitative assessment of breast density, although further research should be conducted to verify this suggestion. Despite the fact that there were no substantial differences between the non-fat-suppressed and fat-suppressed T2-weighted imaging sequences for the quantitative measurement of breast density parameters in a cohort of high-risk women, the study's findings are constrained by the small sample size.

Many questions and potential research directions have emerged as a result of this study, which would need to be investigated further. Some suggestions for future research are as follows:

- 3D-printed breast models can be used to guide breast reconstructive surgery to improve clinical outcomes. This can be enhanced further by the use of a variety of customized breast implants in different shapes and sizes.
- A more realistic breast phantom with different amounts of breast composition could be created using 3D-printing technique and tissue mimicking materials. This can correspond to the four categories of the ACR BI-RADS atlas, allowing an estimation of the volume of fibroglandular tissue, and thus breast density.
- Another possible area of future research would be to examine more closely the observed correlations between silicone oil's T1 relaxation time and fibroglandular tissue.
- Multiple MR breast-imaging protocols are suggested, not only to measure the breast density but also to assess the impact of implementing various image quality parameters (i.e., FOV, matrix size and slice thickness) on the segmentation/measurement of breast density.
- More research would be required to evaluate the Analyze 14.0 software's effectiveness in the segmentation/measurement of breast density, especially in the differentiation between fibroglandular and fatty tissues.
- A further study with a larger sample size would be desirable to determine exactly how the non-fat-suppressed and fat-suppressed T2-weighted imaging sequences influence the quantification of breast density, and thus allowing more robust conclusions to be drawn.

- Deep learning methods may be used to segment breast and fibroglandular tissue, in which the degree of difference between the non-fat-suppressed and fat-suppressed imaging sequences could be more accurately assessed in terms of the efficiency and accuracy of quantitative measurement of breast density in MRI volumes.

7. Appendix I: Statements of contributions of others

Journal: Journal of Clinical Medicine

Paper Title: Quantitative Measurements of Breast Density Using Magnetic Resonance Imaging: A Systematic Review and Meta-Analysis

Reference: Sindi R, Sá Dos Reis C, Bennett C, Stevenson G, Sun Z. Quantitative measurements of breast density using magnetic resonance imaging: a systematic review and meta-analysis. Journal of Clinical Medicine. 2019; 8(5): 745.

	Conception and Design	Acquisition of Data and Method	Data Conditioning and Manipulation	Analysis and Statistical Method	Interpretation and Discussion	Final Approval	Total % Contribution
Co-Author 1 (Rooa Sindi)	50	80	80	30	80	10	55
Co-Author 1 Acknowledgment: I acknowledge that these represent my contribution to the above research output Signed: Rooa Sindi							
Co-Author 2 (Cláudia Sá Dos Reis)					5	20	4
Co-Author 2 Acknowledgment: I acknowledge that these represent my contribution to the above research output Signed:							
Co-Author 3 (Colleen Bennett)					5	20	4
Co-Author 3 Acknowledgment: I acknowledge that these represent my contribution to the above research output Signed: Colleen Bennett							
Co-Author 4 (Gil Stevenson)				70	5	20	16
Co-Author 4 Acknowledgment: I acknowledge that these represent my contribution to the above research output Signed:							
Co-Author 5 (Zhonghua Sun)	50	20	20		5	30	21
Co-Author 5 Acknowledgment: I acknowledge that these represent my contribution to the above research output Signed:							
Total %	100	100	100	100	100	100	100

8. Appendix II: Statements of contributions of others

Journal: Quantitative Imaging in Medicine and Surgery

Paper Title: Development of Patient-Specific 3D-Printed Breast Phantom Using Silicone and Peanut Oils for Magnetic Resonance Imaging.

Reference: Sindi R, Wong YH, Yeong CH, Sun Z. Development of patient-specific 3D-printed breast phantom using silicone and peanut oils for magnetic resonance imaging. Quant Imaging Med Surg. 2020; 10(6): 1237-1248.

	Conception and Design	Acquisition of Data and Method	Data Conditioning and Manipulation	Analysis and Statistical Method	Interpretation and Discussion	Final Approval	Total % Contribution
Co-Author 1 (Rooa Sindi)	50	50	60	60	80	30	55
Co-Author 1 Acknowledgment: I acknowledge that these represent my contribution to the above research output Signed: 							
Co-Author 2 (YH Wong)	25	25	15	20		10	15.8
Co-Author 2 Acknowledgment: I acknowledge that these represent my contribution to the above research output Signed: 							
Co-Author 3 (CH Yeong)	25	25	15	10		10	14.2
Co-Author 3 Acknowledgment: I acknowledge that these represent my contribution to the above research output Signed: 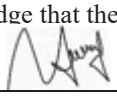							
Co-Author 4 (Zhonghua Sun)			10	10	20	50	15
Co-Author 4 Acknowledgment: I acknowledge that these represent my contribution to the above research output Signed: 							
Total %	100	100	100	100	100	100	100

9. Appendix III: Statements of contributions of others

Journal: Diagnostics

Paper Title: Quantitative Measurement of Breast Density Using Personalized 3D-Printed Breast Model for Magnetic Resonance Imaging

Reference: Sindi R, Wong YH, Yeong CH, Sun Z. Quantitative Measurement of Breast Density Using Personalized 3D-Printed Breast Model for Magnetic Resonance Imaging. Diagnostics. 2020; 10(10): 793.

	Conception and Design	Acquisition of Data and Method	Data Conditioning and Manipulation	Analysis and Statistical Method	Interpretation and Discussion	Final Approval	Total % Contribution
Co-Author 1 (Rooa Sindi)	50	50	80	30	80	30	53
Co-Author 1 Acknowledgment: I acknowledge that these represent my contribution to the above research output Signed: 							
Co-Author 2 (YH Wong)	25	25				10	10
Co-Author 2 Acknowledgment: I acknowledge that these represent my contribution to the above research output Signed: 							
Co-Author 3 (CH Yeong)	25	25				10	10
Co-Author 3 Acknowledgment: I acknowledge that these represent my contribution to the above research output Signed: 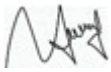							
Co-Author 4 (Zhonghua Sun)			20	70	20	50	27
Co-Author 4 Acknowledgment: I acknowledge that these represent my contribution to the above research output Signed: 							
Total %	100	100	100	100	100	100	100

10. Appendix IV: Statements of contributions of others

Journal: Australasian Medical Journal

Paper Title: Optimal Protocols for Quantitative Assessment of Breast Density Using Magnetic Resonance Imaging

Reference: Sindi R, Sun Z. Optimal protocols for quantitative assessment of breast density using magnetic resonance imaging. Australas Med J. 2019; 12(6): 186-188.

	Conception and Design	Acquisition of Data and Method	Data Conditioning and Manipulation	Analysis and Statistical Method	Interpretation and Discussion	Final Approval	Total % Contribution
Co-Author 1 (Rooa Sindi)	50	50	50	50	50	50	50
Co-Author 1 Acknowledgment: I acknowledge that these represent my contribution to the above research output Signed: 							
Co-Author 2 (Zhonghua Sun)	50	50	50	50	50	50	50
Co-Author 5 Acknowledgment: I acknowledge that these represent my contribution to the above research output  Signed:							
Total %	100	100	100	100	100	100	100

11. Appendix V: Statements of contributions of others

Journal: Australasian Medical Journal

Paper Title: Personalized Three-dimensional Printed Breast Model for Quantitative Assessment of Breast Density Using Magnetic Resonance Imaging

Reference: Sindi R, Sun Z. Personalized three-dimensional printed breast model for quantitative assessment of breast density using magnetic resonance imaging. Australas Med J. 2020; 13(7): 234-238.

	Conception and Design	Acquisition of Data and Method	Data Conditioning and Manipulation	Analysis and Statistical Method	Interpretation and Discussion	Final Approval	Total % Contribution
Co-Author 1 (Rooa Sindi)	50	50	50	50	50	50	50
Co-Author 1 Acknowledgment: I acknowledge that these represent my contribution to the above research output Signed: 							
Co-Author 2 (Zhonghua Sun)	50	50	50	50	50	50	50
Co-Author 5 Acknowledgment: I acknowledge that these represent my contribution to the above research output  Signed:							
Total %	100	100	100	100	100	100	100

Journal of
Clinical Medicine

MDPI

Review

Quantitative Measurements of Breast Density Using Magnetic Resonance Imaging: A Systematic Review and Meta-Analysis

Rooa Sindi [1], Cláudia Sá Dos Reis [1,2,3,*], Colleen Bennett [1], Gil Stevenson [4] and Zhonghua Sun [1,*]

[1] Discipline of Medical Radiation Sciences, School of Molecular and Life Sciences, Curtin University, Perth, Western Australia 6845, Australia; rooa.sindi@postgrad.curtin.edu.au (R.S.); colleen.bennett@curtin.edu.au (C.B.)
[2] School of Health Sciences (HESAV), University of Applied Sciences and Arts Western Switzerland (HES-SO), Av. de Beaumont 21, 1011 Lausanne, Switzerland
[3] CISP—Centro de Investigação em Saúde Pública, Escola Nacional de Saúde Pública, Universidade NOVA de Lisboa, 1600-560 Lisboa, Portugal
[4] Real Statistics, Bangor, County Down BT19 7PX, UK; real_statistics@btinternet.com (G.S.)
* Correspondence: z.sun@curtin.edu.au (Z.S.); claudia.sadosreis@hesav.ch (C.S.D.R.); Tel: +61-8-9266-7509 (Z.S.); Tel: +41-21-316-8143 (C.S.D.R.)

Abstract: Breast density, a measure of dense fibroglandular tissue relative to non-dense fatty tissue, is confirmed as an independent risk factor of breast cancer. Although there has been an increasing interest in the quantitative assessment of breast density, no research has investigated the optimal technical approach of breast MRI in this aspect. Therefore, we performed a systematic review and meta-analysis to analyze the current studies on quantitative assessment of breast density using MRI and to determine the most appropriate technical/operational protocol. Databases (PubMed, EMBASE, ScienceDirect, and Web of Science) were searched systematically for eligible studies. Single arm meta-analysis was conducted to determine quantitative values of MRI in breast density assessments. Combined means with their 95% confidence interval (CI) were calculated using a fixed-effect model. In addition, subgroup meta-analyses were performed with stratification by breast density segmentation/measurement method. Furthermore, alternative groupings based on statistical similarities were identified via a cluster analysis employing study means and standard deviations in a Nearest Neighbor/Single Linkage. A total of 38 studies matched the inclusion criteria for this systematic review. Twenty-one of these studies were judged to be eligible for meta-analysis. The results indicated, generally, high levels of heterogeneity between study means within groups and high levels of heterogeneity between study variances within groups. The studies in two main clusters identified by the cluster analysis were also subjected to meta-analyses. The review confirmed high levels of heterogeneity within the breast density studies, considered to be due mainly to the applications of MR breast-imaging protocols and the use of breast density segmentation/measurement methods. Further research should be performed to determine the most appropriate protocol and method for quantifying breast density using MRI.

Keywords: Magnetic resonance imaging; breast density; fibroglandular-tissue; systematic review and meta-analysis; cluster analysis; segmentation; FCM; breast-imaging protocol; non-contrast-enhanced T1-weighted

1. Introduction

Breast density, a measure of dense fibroglandular tissue relative to non-dense fatty tissue, is an independent risk factor for breast cancer [1–3]. Consistent with this risk relationship, women who

have dense breasts have a likelihood of developing breast cancer that is fourfold higher than those with fatty breasts [4,5]. Most of the information regarding breast density has been acquired with two-dimensional imaging, which is mammography. However, the evaluation of breast density based on mammograms is limited due to the overlapping of tissues, variations in breast compression, and inappropriate positioning that lead to artefacts (skin folder) and inclusion of insufficient breast tissue [6,7]. These factors could affect mammography's performance for precise, reliable measurements of small changes in breast density over brief timespans [8,9].

Magnetic resonance imaging (MRI), an alternative imaging modality in breast imaging can estimate the actual breast density value because it provides a three-dimensional volume assessment of breast tissue, with excellent contrast resolution in the differentiation between fibroglandular and fatty tissues [10–13]. Conventionally, breast density is assessed qualitatively using the American College of Radiology (ACR) Breast Imaging-Reporting and Data System (BI-RADS) atlas, which is a classification system commonly used for mammography, according to which density has four categories based on the amount of fibroglandular tissue: "(1) almost entirely fat, (2) scattered fibroglandular tissue, (3) heterogeneous fibroglandular dense and (4) extreme fibroglandular tissue" [14,15]. The interpretations of these four categories are also applied for MRI. Despite its long clinical success, the BI-RADS scoring atlas is subjective and varies between readers, even within the same reader [16]. To overcome a subjective assessment of breast density and to reduce inter- and intra-reader variability, different methods for quantitative breast density have been proposed, with a range of algorithms or methods reported in the literature [17–22]. Each of these methods were shown to have advantages and limitations through the use of semi-automatic thresholding and segmentation approaches for quantitative assessment of breast density.

There is no doubt that MRI is one of the most useful modalities for breast imaging and that the analysis of breast density in quantitative synthesis is a well-established approach. In spite of the fact that extensive research has been carried out on breast density measurements, no consensus has been reached about the optimal approach to quantify breast density using MRI. Therefore, the purpose of this review is to analyze the current methods for the quantitative assessment of breast density using MRI over the past decade of publications. Due to the expected heterogeneity of MRI scanning protocols, both systematic review and meta-analysis were performed to analyze the available studies.

2. Materials and Methods

This systematic review and meta-analysis were performed according to the Preferred Reporting Items for Systematic Reviews and Meta-Analysis (PRISMA) criteria [23,24]. No ethics committee approval was required.

2.1. Search Strategy and Eligibility Criteria

A systematic literature review was conducted of studies that analyzed breast density in a quantitative pattern using MRI. Briefly, a search for studies published between 1 January 2009 and 31 December 2018 was conducted in different databases: PubMed (MEDLINE, U.S. National Library of Medicine and National Institutes of Health, Bethesda, MD, USA), EMBASE (Elsevier, Amsterdam, The Netherlands), ScienceDirect (Elsevier, Amsterdam, The Netherlands), and Web of Science (Clarivate Analytics, Philadelphia, PA, USA) using the search terms detailed below.

Systematic search expressions were employed using MeSH (medical subject headings) in PubMed and the thesaurus in EMBASE, ScienceDirect, and Web of Science. A search structure was based on combining three main terms as follows: "breast density," "quantitative analysis," and "MRI." The exact search expressions were "Breast Density" (MeSH term) OR "fibroglandular tissue" (Text word) OR "breast densit*" (Text word) OR "FGT" (Text word) OR "FT" (Text word) OR "fibroglandular densit*" (Text word) AND "Quantitative analysis" (Subject heading) AND "Magnetic Resonance Imaging" (MeSH term) OR "nuclear magnetic resonance imaging" (Text word) OR "MRI" (Text word) OR "magnetic resonance imaging" (Text word). The criteria for selecting the studies for eligibility were based on their title, abstract, and subsequently the full text, this was performed independently by two reviewers (R.S. and Z.S.). Studies addressing the quantitative

analysis of breast density using MRI were considered eligible for inclusion and also studies on human subjects since 2009 had to be published in peer-reviewed journals and written in English. For study inclusion, the subjects must have undergone breast MRI studies and the breast density measurement method is known. Eligible studies were retrieved, and full manuscripts were read. No restricted conditions have been applied in terms of study characteristics, the purpose of study, and the results. Publications were only included in the analysis if the measurement of breast density had been performed in a quantitative manner regardless of the MRI technique or breast density segmentation/measurement method.

2.2. Data Extraction

On completing the eligibility screening, the process of data extraction from the included studies was carried out manually by the same two reviewers. Descriptive data were extracted for all variables as follows: the first author's surname; year of publication; journal of publication; study type; total number of participants/patients; mean age; age range of participants/patients; MRI technique (pulse sequence/breast-imaging protocol and static magnetic field strength); and breast segmentation/measurement method. For each study analyzed, estimates of breast volume, fibroglandular-tissue volume and percentage breast density were recorded using descriptive statistics, arithmetic means and standard deviations, whenever appropriate. Due to the heterogeneous nature of this analysis, some of the included studies produced their results in a median and interquartile range (IQR). Accordingly, the researchers decided to stratify results and excluded them from the meta-analysis only.

2.3. Data Synthesis

The combinations of MRI techniques and the applied breast segmentation/measurement methods encountered in the studies were considered to be technologically heterogeneous. To address this issue and acquire more reasonable estimates, the analyses were stratified by breast segmentation method into three discrete groups (fuzzy c-mean clustering (FCM), FCM and nonparametric nonuniformity normalization (N3), and signal intensity thresholding). In each sub meta-analysis, the number of the included studies were selected on the basis of a degree of homogeneity of their breast density segmentation/measurement results.

2.4. Statistical Analysis

The measurement of breast density as ascertained by MRI using semi- or fully-automated segmentation method was assessed. The primary outcome was the percentage breast density (%BD). Data input for each study within a group consisted of the study size (N), the 'raw' study mean (i.e., with no re-scaling or standardization), and the study standard deviation. The data was analyzed by the *"metamean"* function in the *"meta"* package in the R system, Version 3.4.1 (http://www.r-project.org/). This facilitates the meta-analysis of a single arm trial, as opposed to the traditional two arm trial with a control group and a treatment group, equivalent to a one-way analysis of variance. A forest plot was generated, displaying the individual study (%BD) means with 95% confidence interval (CI) limits, inverse variance study weights, and the pooled mean and confidence limits. Heterogeneity of study means was assessed using Cochran's Q-test, and heterogeneity of study variances was assessed with Bartlett's test. A conclusion to pool studies requires both heterogeneity tests to be non-significant at the 5% level.

As an alternative to grouping the studies on a technological basis, a cluster analysis was run to investigate any similarities between studies with respect to two attributes, namely study mean and study standard deviation. The International Business Machines Statistical Package for the Social Sciences (IBM SPSS) Statistics software Version 25.0 was used for cluster analysis. The procedure provides for a wide selection of combinations of distance measures and clustering methods, but for the current application, the simplest of these was chosen, namely Euclidean distance and nearest neighbor agglomeration. This algorithm calculates a proximity matrix of distances between all

possible pairs of studies and allocates the closest pair into a cluster, then examines the remaining clusters to identify which is the next nearest or whether there is a pair that are closer to one another, and so on.

3. Results

3.1. Literature Search

Figure 1 presents an overview of the systematic search of the literature through different databases. The complete search yielded 941 studies. After removing duplicates (n = 70), 871 were screened, based on their titles, which resulted in 765 being excluded, followed by 27 of the remaining studies being excluded on the basis of their abstracts. Of the remaining 79 studies, the full manuscript was retrieved and reviewed. Forty-one studies did not meet the selection inclusion criteria: no adequate breast density data (n = 20), qualitative analysis (n = 12), editorials (n = 4), conference abstracts (n = 3), post-mortem study (n = 1), and phantom study (n = 1). Finally, 38 studies attained the inclusion criteria [1–3,5,11,25–57] and were included in the analysis as shown in Table 1.

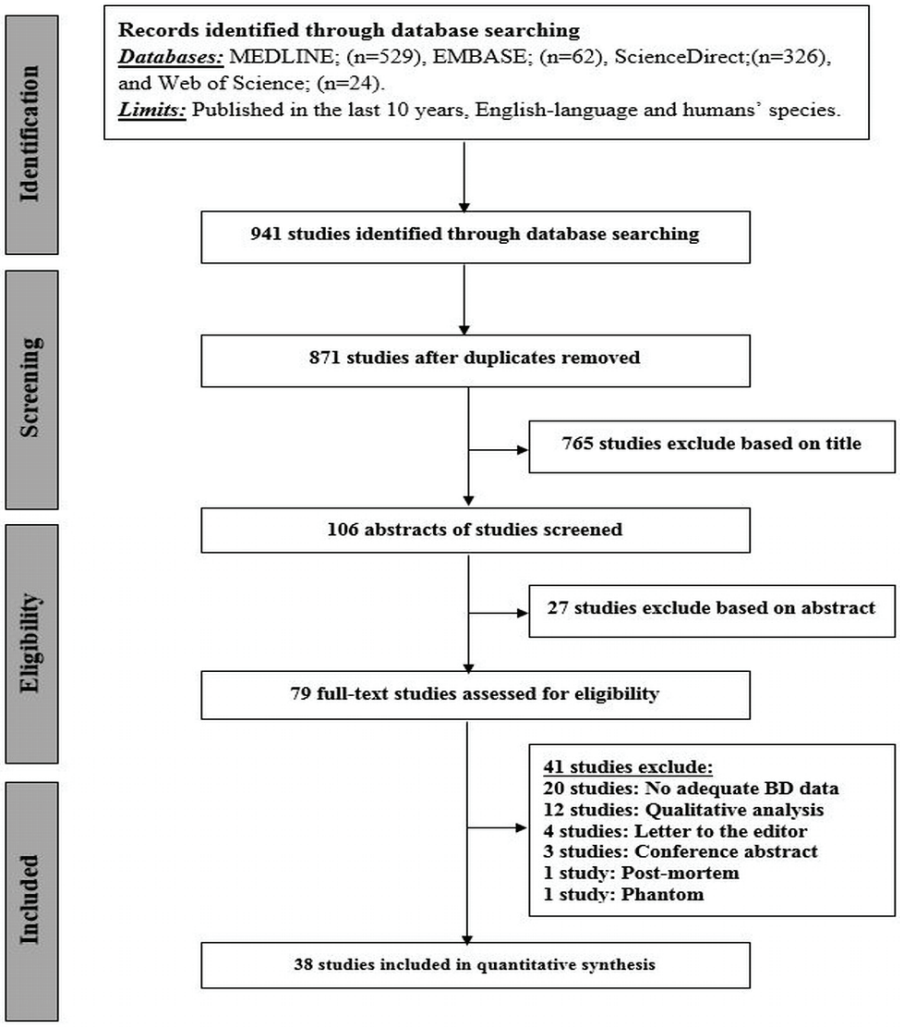

Figure 1. Preferred Reporting Items for Systematic Reviews and Meta-Analysis (PRISMA) flowchart of systematic review and meta-analysis of the excluded and included studies.

3.2. Systematic Review

Table 1 demonstrates some of the main characteristics of the 38 included studies, while Figure 2 shows details of the study design and MRI system used in these studies. Several MRI sequences were used to enable the precise differentiation between adipose and fibroglandular tissues; of these, non-contrast-enhanced T1-weighted was widely used either with 2D spin echo or 3D gradient echo. In fact, 16 studies (41.03%) used non-contrast-enhanced T1-weighted [1,2,26–29,31,33,35,44,45,48–51,53], while in 12 studies (30.77%) non-contrast-enhanced images were integrated with contrast-enhanced images [25,36–44,47,49]. In terms of breast density segmentation/measurement, the majority of the studies (20 studies; 51.28%) used FCM clustering algorithm [1,2,11,25–29,31–42], while 7 studies (17.95%) used FCM and N3 algorithm [45–51], 4 studies (10.26%) interactive thresholding algorithm [3,5,52,53], 4 studies (10.26%) in-house customized software [29,53–55], one study (2.56%) manual software [57]; however, two studies did not provide the information [43,44].

Among the thirty-eight studies included in the systematic review and meta-analysis, 21 studies qualified for meta-analysis since they reported the percent breast density using an identical expression of measurement and dispersion [1,3,11,25–32,36–38,45,48–50,53–55] (Table 2). However, for the remaining 17 studies, the percent breast density was reported in different format: in eight of these studies, it was defined as a median and interquartile range (IQR) [2,39–44,47], and in the other nine, it was reported either in different measurement unit or the subject's sets were not independent, due to multiple usage [5,33–35,46,51,52,56,57]. To perform the meta-analysis precisely, all the measured quantities should be reported in an identical expression of measurement and dispersion, thus we decided to exclude them from the meta-analysis.

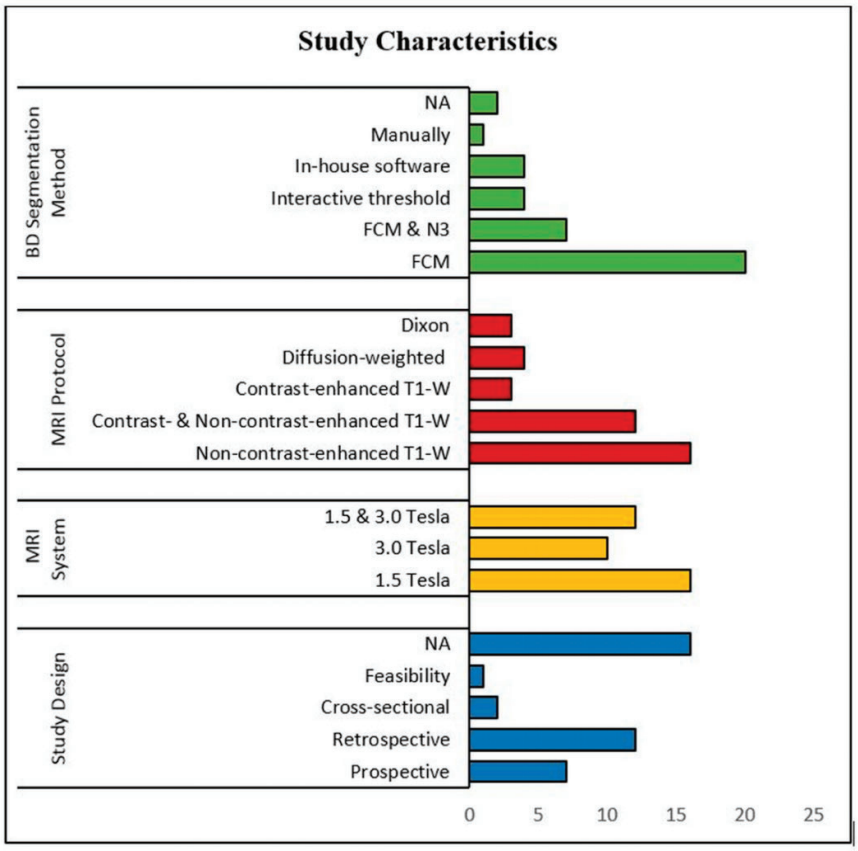

Figure 2. Flowchart of the study characteristics (study design, MRI system, MRI sequence, Breast Density (BD) segmentation method) of 38 studies.

3.4. Subgroup Analyses

The final inclusion consisted of a total of twenty-one studies in the meta-analyses; the forest plots and pooled results are shown in Figure 3.

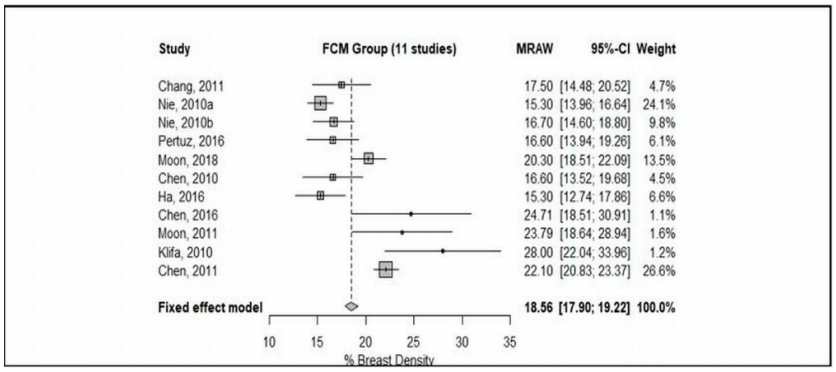

(**A**)

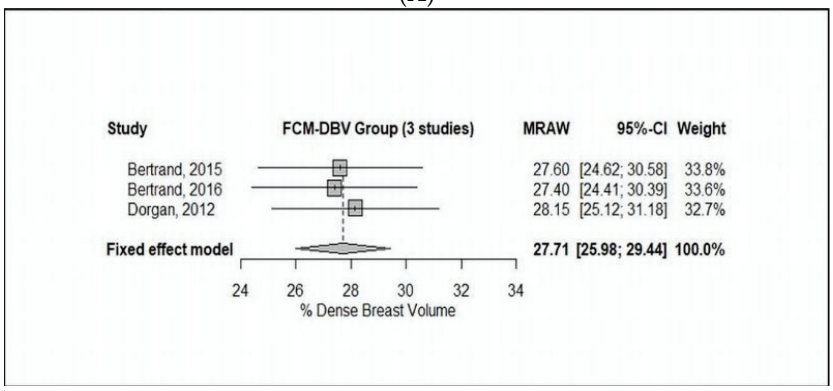

(**B**)

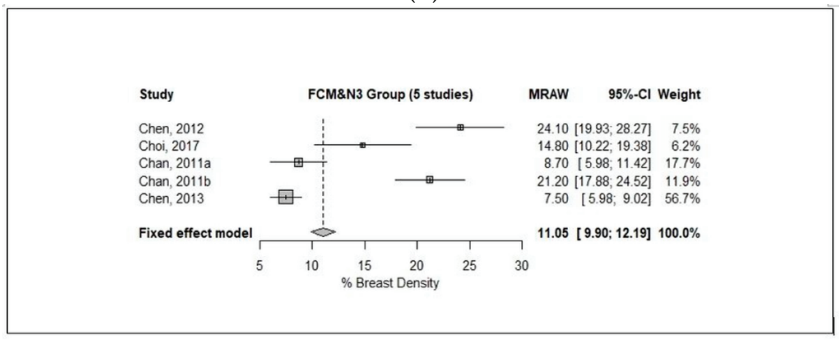

(**C**)

Figure 3. *Cont.*

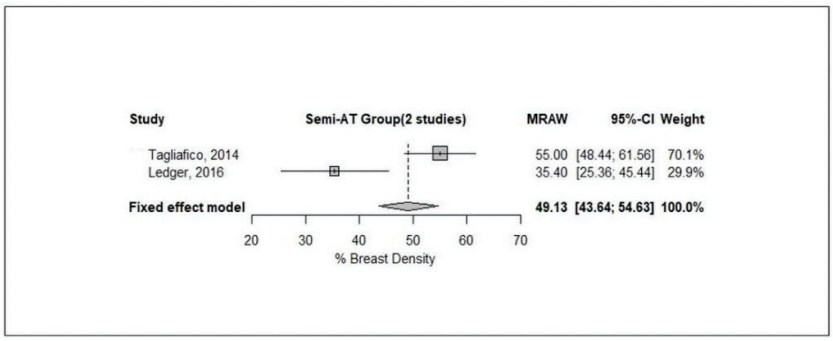

(**D**)

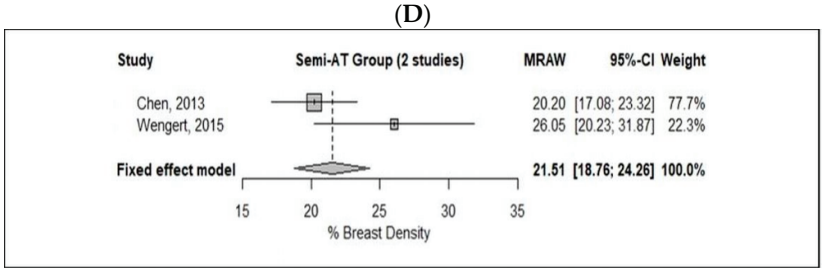

(**E**)

Figure 3. Forest plot of the study means, and 95% confidence limits of the breast density among 21 included studies in the subgroup meta-analyses. (**A**) Fixed effect meta-analysis of the fuzzy c-mean clustering (FCM) group of studies of % breast density. (**B**) Fixed effect meta-analysis of the FCM group of studies of % dense breast volume. (**C**) Fixed effect meta-analysis of the FCM and N3 group of studies of % breast density. (**D**) Fixed effect meta-analysis of the semi-automated threshold group of studies of % breast density. (**E**) Fixed effect meta-analysis of the semi-automated threshold group of studies of % breast density.

3.4.1. Fuzzy C-mean Clustering (FCM)

The FCM subgroup consisted of 13 studies, of which, 10 studies reported breast density as a percentage breast density (% BD) [1,11,25–32], whereas 3 studies as a percentage of the dense breast volume (% DBV) [36–38]. On one hand, 10 studies with inclusion of 634 patients were included, as Figure 3A shows, there is a wide range of mean values as well as standard deviation (SDs) from those studies, which indicated enormous heterogeneity among study means (Cochran's Q test: $X^2 = 86.93$, $P < 0.0001$). Indeed, there is a substantial heterogeneity among study variances (Bartlett's test: $X^2 = 110.59$, $P < 0.0001$). On the other hand, three studies with inclusion of 528 patients were analyzed. Figure 3B shows there is a high level of homogeneity among study means (Cochran's Q test: $X^2 = 0.13$, $P = 0.94$), and a high level of homogeneity among study variances (Bartlett's test: $X^2 = 0.12$, $P = 0.94$), which would be expected as those studies used an identical combination of MR technique and breast density segmentation/measurement approach.

3.4.2. FCM and Nonparametric Nonuniformity Normalization (N3)

The FCM and N3 subgroup included 4 studies with inclusion of 126 patients [45,48–50], as Figure 3C shows, there is a wide range of mean values as well as SDs from those studies, which indicated tremendous heterogeneity among study means (Cochran's Q test: $X^2 = 99.94$, $P < 0.0001$). Indeed, there is a substantial heterogeneity among study variances (Bartlett's test: $X^2 = 45.41$, $P < 0.0001$), which would be expected as those studies used different MR breast-imaging protocols.

Table 1. Characteristics of the included studies in the systematic review and meta-analysis.

Author, year of publication	Study design	Study participants	Age range, average (Years) or Mean ± SD	MR Scanner Manufacturer, Field Strength (Tesla)	MRI Sequence	Orientation, Slice No.	TR/TE (ms)	FOV (cm)	Slice Thickness (mm)	Matrix size	Flip angle (°)	Breast coil	Segmentation method
Chang, 2011 [25]	Retro.	38	28–82, 48	Philips, 3.0	Fat-suppressed 3D SPAIR	Axial, 160	6.20/1.26	3.01–38.0	1.0	480 × 480	12	NA	FCM
					Non-fat-suppressed 2D TSE	Axial, 84	800/8.6	31.0–38.0	2.0	480 × 480	90	NA	
Nie, 2010 [26]	NA	230	50 ± 11.0	Philips, 1.5	Non-fat-suppressed 3D SGRE (T1W)	Axial, 32	8.1/4.0	31.0–38.0	4.0	256 × 256	20	NA	FCM
Pertuz, 2016 [27]	Retro.	68	24–82, 52	Siemens, 1.5	Non-fat-suppressed (T1W)	NA	NA	NA	2.4–3.5	512 × 512	NA	NA	FCM
Moon, 2018 [28]	Retro.	98	51.81 ± 11.08	GE, 1.5	Non-fat-suppressed (T1W)	Axial	6.2/2.1	20.0	1.0	512 × 217	NA	NA	FCM
Chen, 2010 [29]	Retro.	35	45 ± 7	Philips, 1.5	Non-fat-suppressed 3D SGRE (T1W)	Axial, 32	8.1/4.0	38.0	3.0–4.0	256 × 128	20	Dedicated 4-channel phased array	FCM
Chen, 2016 [31]	Retro.	23	40.5 ± 8.2	Philips, 3.0	Non-fat-suppressed 2D TSE (T1W)	Axial, 90	654/9.0	33.0	2.0	328 × 384	NA	NA	FCM
Moon, 2011 [32]	Retro.	40	50.9 ± 9.4	GE, 1.5	Fat-suppressed 3D GRE (T1W) (VIBRANT)	Sagittal, 144–192	6.1/2.5	19.0	1.5	512 × 512	NA	NA	FCM
Klifa, 2010 [11]	Retro.	35	28–59, 43	GE, 1.5	Fat-suppressed 3D Fast GRE (T1W)	Axial, 60	8.0/4.2	NA	2.0	NA	20	Dedicated bilateral phased array	FCM
Chen, 2011 [1]	Retro.	16	33–51, 43	GE, 1.5	Non-fat-suppressed 3D (T1W)	Axial, 56	7.4/3.3	30	2.0	512 × 512	NA	Dedicated 8-channel bilateral	FCM

Nie, 2010 [33]	Retro.	50	NA	Philips, 1.5	Non-fat-suppressed 3D GRE (T1W)	Axial, 32	8.1/4.0	38.0	4.0	256 × 128	20	NA	FCM
Kim, 2014 [34]	Retro.	80	27–68, 44	GE, 1.5	Fat-suppressed 2D FSE (T2W)	Sagittal	5500-7150/82	20.0	1.5	256 × 160	NA	Dedicated 8-channel bilateral	FCM
					Fat-suppressed 3D Fast SGRE (T2W)	Sagittal	6.2/2.5	20.0	1.5	256 × 160	10	Dedicated 8-channel bilateral	
Nie, 2010 [35]	Retro.	321	54 ± 12	Philips, 1.5	Non-fat-suppressed 3D SGRE (T1W)	Axial, 32	8.1/4.0	32.0–38.0	4.0	256 × 128	20	Dedicated 4-channel phased-array	FCM
Wang, 2013 [2]	Retro.	99	47.2 ± 12.1	GE, 1.5/3.0	Non-fat-suppressed (T1W)	Axial	NA	NA	2.0	NA	NA	Dedicated bilateral phased-array	FCM
Bertrand, 2015 [36]	Pros.	182	25–29	NA, 1.5/3.0	Non-fat- and fat-suppressed 3D Fast GRE (T1W)	Axial and Coronal	NA	32.0–40.0	NA	NA	NA	Dedicated RF coil	FCM
Bertrand, 2016 [37]	Pros.	172	25–29	NA, 1.5/3.0	Non-fat- and fat-suppressed 3D Fast GRE (T1W)	NA	NA	32.0–40.0	NA	NA	NA	Dedicated RF coil	FCM
Dorgan, 2012 [38]	Retro.	174	25–29	NA, 1.5/3.0	Non-fat- and fat-suppressed 3D Fast GRE (T1W)	Axial and Coronal	NA	32.0–40.0	NA	NA	NA	Dedicated RF coil	FCM
Gabriel, 2013 [39]	NA	182	25–29	NA, 1.5/3.0	Non-fat- and fat-suppressed 3D Fast GRE (T1W)	Axial and Coronal	NA	32.0–40.0	NA	NA	NA	Dedicated RF coil	FCM
Jung, 2015 [40]	Pros.	180	25–29	NA, 1.5/3.0	Non-fat- and fat-suppressed 3D Fast GRE (T1W)	Axial and Coronal	NA	32.0–40.0	NA	NA	NA	Dedicated RF coil	FCM
Jung, 2016 [41]	Pros.	177	25–29	NA, 1.5/3.0	Non-fat- and fat-suppressed 3D Fast GRE (T1W)	Axial and Coronal	NA	32.0–40.0	NA	NA	NA	Dedicated RF coil	FCM

Dorgan, 2013 [42]	C.S.	176	27.0–27.3, 27.2	NA, 1.5/3.0	Non-fat- and fat-suppressed 3D Fast GRE (T1W)	Axial and Coronal	NA	32.0–40.0	NA	NA	NA	Dedicated RF coil	FCM
Jung, 2015 [43]	Pros.	177	25–29	NA, 1.5/3.0	Non-fat- and fat-suppressed 3D Fast GRE (T1W)	Axial and Coronal	NA	NA	NA	NA	NA	Dedicated RF coil	NA
Jones, 2015 [44]	C.S.	172	25–29	NA, 1.5/3.0	Non-fat- and fat-suppressed 3D Fast GRE (T1W)	Axial and Coronal	NA	NA	NA	NA	NA	Dedicated RF coil	NA
Chen, 2012 [45]	Pros.	34	20–64, 35	GE, 1.5	Non-fat-suppressed 2D FSE (T1W)	Axial	607/9.0	38.0	2.0	256 × 192	NA	Dedicated 8-channel bilateral	FCM and N3
				GE, 3.0	Non-fat-suppressed 2D FSE (T1W)	Axial	650/9.0	38.0	2.0	256 × 192	NA	Dedicated 8-channel bilateral	
				Philips, 3.0	Non-fat-suppressed 2D FSE (T1W)	Axial	650/9.0	33.0	2.0	328 × 384	NA	Dedicated 16-channel bilateral	
				Siemens, 1.5	Non-fat-suppressed 2D FSE (T1W)	Axial	650/9.8	33.0	2.0	330 × 384	20	Dedicated 4-channel bilateral	
Chen, 2015 [46]	NA	32	22–53, 41	Siemens, 1.5	Non-fat-suppressed 2D FSE (T1W)	Axial	650/9.8	33.0	2.0	256 × 256 and 512 × 512	NA	Dedicated 4-channel bilateral	FCM and N3
Chen, 2013 [47]	NA	44	28–82, 47	Philips, 3.0	Non-fat-suppressed 2D TSE (T1W)	Axial	800/8.6	31.0–38.0	2.0	480 × 480	90	Dedicated 4-channel bilateral	FCM and N3
					Fat-suppressed 3D GRE (T1W)	Axial	6.2/1.26	31.0–36.0	2.0	480 × 480	12	Dedicated 4-channel bilateral	
Chan, 2011 [48]	NA	30	Pre: (N = 24) 23–48, 29 Post: (N = 6) 51–61, 57	Siemens, 1.5	Non-fat-suppressed 3D GRE (T1W)	Axial	11/4.7	35.0	2.0	256 × 256	20	4-channel dual-mode	FCM and N3

Table 1. *Cont.*

Choi, 2017 [49]	Retro.	38	32–79, 45	Philips, 3.0	Non-fat-suppressed SE (T1W)	Axial	620/10	20.0–34.0	3.0	332 × 332	NA	Dedicated 7-channel bilateral	FCM and N3
					STIR and SE-EPI (DW)	Axial	3265/54	35.0	4.0	288 × 288	90	Dedicated 7-channel bilateral	
Chen, 2013 [50]	NA	24	23–48, 29	Siemens, 1.5	Non-fat-suppressed 3D Fast GRE (T1W)	Axial	11/4.7	35.0	2.0	256 × 256	20	4-channel dual-mode	FCM and N3
Clendenen, 2013 [51]	NA	9	24–31	Siemens, 3.0	Non-fat-suppressed 3D VIBE (T1W)	Axial	4.19/1.62	26.9 × 20.2 × 28.8	0.6 × 0.6 × 1	448 × 336 × 288	12	Dedicated 7-channel bilateral	FCM and N3
					3-Point Dixon Non-fat-suppressed 3D FLASH (T1W)	Axial	7.6/3.37, 4.17. 4.96	NA	0.88 × 0.88 × 1.5	NA	10	Dedicated 7-channel bilateral	
McDonald, 2014 [52]	Retro.	103	47 ± 11	Philips, 3.0	EPI-Parallel Imaging (DWI)	NA	5336/61	36.0	5.0	240 × 240	NA	Dedicated 16 channel bilateral	Semi-automated Interactive Threshold
Tagliafico, 2013 [5]	Pros.	48	35–67, 41	GE, 3.0	3D Fast SGRE and Fat-suppressed 3D GRE (T1W) (VIBRANT)	NA	6.2/3.0	NA	NA	350 × 350	10	Dedicated 8-channel bilateral	Semi-automated Interactive Threshold
					IDEAL	NA	4380/130. 872	NA	NA	360 × 360	90	Dedicated 8-channel bilateral	

Table 1. *Cont.*

Tagliafico, 2014 [3]	NA	48	35–67, 41	GE, 3.0	TSE (T1W)	NA	600/9.0	NA	4.0	350 × 350	90	Dedicated 8-channel bilateral	Semi-automated Interactive Threshold
					TSE (T2W)	NA	5200/103	NA	4.0	350 × 350	90	Dedicated 8-channel bilateral	
					Fat-suppressed 3D GRE (T1W) (VIBRANT)	NA	6.2/3.0	NA	1.2	350 × 350	10	Dedicated 8-channel bilateral	
					IDEAL	NA	4380/130	NA	1.2	360 × 360	90	Dedicated 8-channel bilateral	
Chen, 2013 [53]	NA	24	23–48, 29.4	Siemens, 1.5	Non-fat-suppressed 3D GRE (T1W)	Axial	11/4.7	35.0	2.0	256 × 256	20	NA	Semi-automated Interactive Threshold
Ha, 2016 [30]	Retro.	60	54.2	GE, 1.5/3.0	Fat-suppressed Fast SGRE (T1W)	Axial	17/2.4	18.0-22.0	2.0	256 × 192	35	8-channel breast array	Semi-automated (In-house software)
Ledger, 2016 [54]	Retro.	10	23–50, 31	Siemens, 1.5	HR/LR 3D GRE (PDW)	Axial	7.34/4.77, 2.39	NA	NA	NA	4	Sentinelle variable coil geometry	Semi-automated (In-house software)
					HR/LR 3D GRE (T1W)	Axial	7.34/4.77, 2.39	NA	NA	NA	25	Sentinelle variable coil geometry	
					LR 2D SE (T1W)	Axial	500/12	NA	7.0	NA	NA	Sentinelle variable coil geometry	
Wengert, 2015 [55]	Pros.	43	21–71, 38	Siemens, 3.0	Dixon	Axial, 192	NA/6.0, 2.45, 2.67	NA	NA	352 × 352	6	Dedicated 4-channel bilateral	Fully-automated (AUQV)
O'Flynn, 2014 [56]	Retro.	33	(N = 17): 33–49, 43 (N = 16): 27–49, 40	Siemens, 1.5	Fat-suppressed SS-EPI (DWI)	Axial	6300/83	34.0	5.0	NA	NA	Dedicated 4-channel bilateral	Dedicated IDL based software for ADC calculation

Table 1. *Cont.*

Kim, 2016 [57]	Pros.	57	32–74, 50.8	Siemens, 3.0	Fat-suppressed TSE (T2W)	Sagittal	7623/91	22 × 22	3.0	320 × 246	NA	Dedicated 4-breast array	Manually
					Fat-suppressed SS-EPI (DWI)	Axial	5200/74	340 × 179	5.0	80 × 190	NA	Dedicated 4-breast array	
					Fat-suppressed 3D FLASH (T1W)	Sagittal	4.5/1.6	22 × 22	2.0	352 × 292	20	Dedicated 4-breast array	

Abbreviations: Retro.: retrospective; Pros.: prospective; C.S.: cross-sectional; Pre.: pre-menopausal; Post.: post-menopausal; T1W: T1-weighted; T2W: T2-weighted; SPAIR: spectral attenuated inversion recovery; TSE: turbo spin-echo; SGRE: spoiled gradient-echo; VIBRANT: volume image breast assessment; GRE: gradient-echo; FSE: fast spin-echo; STIR: short-TI inversion recovery; DWI: diffusion-weighted imaging; VIBE: volumetric interpolated breath-hold examination; FLASH: fast low angle shot; IDEAL: iterative decomposition of water and fat with echo asymmetry and least squares estimation; HR: high-resolution; LR: low-resolution; PDW: proton density-weighted; SS-EPI: single shot- echo-planar imaging; FCM: fuzzy c-mean clustering algorithm; N3: non-parametric non-uniformity normalization; AUQV: automated user-independent quantitative volumetric.

Table 2. Sample size, Mean, and SD of breast volume, fibroglandular volume, and percent of breast density of the (21) included studies in the subgroup meta-analyses.

Author, Year	Breast Volume, BV (cm^3)		Fibroglandular Volume, FV (cm^3)			Breast Density, BD (%)	
	Mean	SD	Mean	SD	N	Mean	SD
Chang, 2011 [25]	681	359	100	58	38	17.50	9.50
Nie, 2010 [26]	-	-	104	62	141	15.30	8.10
	-	-	112	73	89	16.70	10.10
Perutz, 2016 [27]	2210	1125	297	128	68	16.60	11.20
Moon, 2018 [28]	537.59	287.74	-	-	89	20.30	8.60
Chen, 2010 [29]	-	-	-	-	35	16.6 0	9.30
Ha, 2016 [30]	-	-	-	-	60	15.30	10.07
Chen, 2016 [31]	537.59	287.74	-	-	23	24.71	15.16
Moon, 2011 [32]	544.90	207.41	-	-	40	23.79	16.62
Klifa, 2010 [11]	-	-	-	-	35	28.0	18.00
Chen, 2011 [1]	358	174	79	66	16	22.10	2.60
Bertrand, 2015 [36]	413.5	364.3	104.2	70.6	182	27.60	20.50
Bertrand, 2016 [37]	418.7	369.3	104.7	70.3	172	27.40	20.00
Dorgan, 2012 [38]	-	-	104.67	71.28	174	28.15	20.39
Chen, 2012 [45]	528	263	117	82	34	24.10	12.40
Choi, 2017 [49]	-	-	-	-	38	14.80	14.40
Chan, 2011 [48]	-	-	-	-	6	8.70	3.40
	-	-	-	-	24	21.20	8.30
Chen, 2013 [50]	-	-	-	-	24	7.50	3.80
Tagliafico, 2014 [3]	-	-	-	-	48	55.00	23.20
Ledger, 2016 [54]	482.6	296.2	135.2	56.2	10	35.40	16.20
Chen, 2013 [53]	-	-	48.1	24.7	24	20.20	7.80
Wengert, 2015 [55]	1462.43	803.38	-	-	43	26.05	19.47

3.4.3. Interactive Semi-Automated Threshold

Two studies [3,54] comprising of 58 patients were included in the analysis, which indicated a considerable heterogeneity among study means (Cochran's Q test: $X^2 = 10.26$, $P = 0.0014$). In contrast, there was no evidence of heterogeneity among study variances (Bartlett's test: $X^2 = 1.61$, $P = 0.2072$).

On the other hand, two studies with inclusion of 67 patients [53,55] were analyzed as shown in Figure 3E, there was no evidence of heterogeneity among study means (Cochran's Q test: $X^2 = 3.01$, $P = 0.0825$), which would be expected as those studies used the same MRI technique and breast density measurement. However, there is a substantial heterogeneity among study variances (Bartlett's test: $X^2 = 18.84$, $P < 0.0001$).

3.5. Cluster Analysis

The results obtained from the clustering analysis "Dendrogram using Single Linkage" are shown in Figure 4. From this data, it can be seen that a hierarchical diagram showing various distances (0–25) at which studies joined various groups. On that basis, six clusters were identified. A list of cluster membership, study means, SDs, and coefficient of variations (CVs) (expressed as a percentage) is shown in Table 3. A scatter plot of the study means versus SDs is shown in Figure 5, the legend in the scatter plot indicates the number of studies in each cluster. Cluster markers with solid fill indicate clusters with two or more studies, whereas open markers indicate singletons. Cluster 1 included nine studies that analyzed breast density with a combination of contrast and non-contrast T1-weighted either with 2D spin echo or 3D gradient echo**;** however, Choi [49] used diffusion-weighted scanning technique. From the data in Table 3 (Cluster 1), it is apparent that the CVs are varied in value, but in Choi's study [49] the CV is almost 100% because of the mean and SD are almost identical. In contrast, the CVs for Chan [48] and Chen [53] are much lower than the rest of the included studies, largely

because of the small SDs and the breast segmentation methods being used which are FCM and N3 and interactive semi-automated threshold algorithms, respectively.

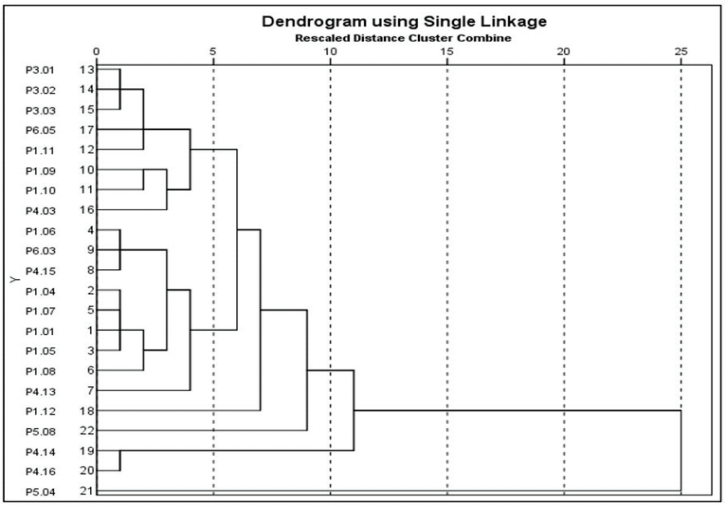

Figure 4. Dendrogram clustering analysis using "Single Linkage" method of the study means, and study SDs among 21 included studies in the subgroup meta-analyses.

Table 3. Study size (N), mean, SD, coefficient of variations (CV), and cluster membership of the included studies.

Study Code	Author, Year	N	Mean	SD	CV	Cluster Membership
P1.01	Chang, 2011 [25]	38	17.50	9.50	54.29	1
P1.04	Nie, 2010 [26]	89	16.70	10.10	60.48	1
P1.05	Pertuz, 2016 [27]	68	16.60	11.20	67.47	1
P1.06	Moon, 2018 [28]	89	20.30	8.60	42.36	1
P1.07	Chen, 2010 [29]	35	16.60	9.30	56.02	1
P1.08	Ha, 2016 [30]	60	15.30	10.07	65.82	1
P4.13	Choi, 2017 [49]	38	14.80	14.40	97.30	1
P4.15	Chan, 2011 [48]	24	21.20	8.30	39.15	1
P6.03	Chen, 2013 [53]	24	20.20	7.80	38.61	1
P1.09	Chen, 2016 [31]	23	24.71	15.16	61.35	2
P1.10	Moon, 2011 [32]	40	23.79	16.62	69.86	2
P1.11	Klifa, 2010 [11]	35	28.00	18.00	64.29	2
P3.01	Bertrand,2015 [36]	182	27.60	20.50	74.28	2
P3.02	Bertrand, 2016 [37]	172	27.40	20.00	72.99	2
P3.03	Dorgan, 2012 [38]	174	28.15	20.39	72.43	2
P4.03	Chen, 2012 [45]	34	24.10	12.40	51.45	2
P6.05	Wengert, 2015 [55]	43	26.05	19.47	74.74	2
P1.12	Chen, 2011 [1]	16	22.10	2.60	11.76	3
P4.14	Chan, 2011 [48]	6	8.70	3.40	39.08	4
P4.16	Chen, 2013 [50]	24	7.50	3.80	50.67	4
P5.04	Tagliafico, 2014 [3]	48	55.00	23.20	42.18	5
P5.08	Ledger, 2016 [54]	10	33.40	16.20	45.76	6

In contrast, cluster 2 consisted of 8 studies that assessed breast density with a combination of contrast- and non-contrast-enhanced T1-weighted with 3D gradient echo, however, Chen [31] and Chen [45] used non-contrast- and contrast-enhanced T1-weighted with 2D spin-echo, respectively. Indeed, Chen [45] analyzed breast density using FCM and N3 algorithms. From the data in Figure 5

and Table 3 (Cluster 2), it is apparent that the CVs are almost within a closed range except for Chen [45] where the CV is much lower than the remaining studies because of the small SD and the breast segmentation method that previously mentioned. Also, Wengert [55] used Dixon method as a technical protocol for breast-imaging, although they measured the breast density using in-house customized software, the mean and SD are not different to the other included studies. The most striking result to emerge from the data in Figure 5 and Table 3 (Cluster 3–6) is the Chen [1] study (i.e., Cluster 3), although it used non-contrast-enhanced T1-weighted with 3D gradient echo and analyzed breast density by FCM algorithm, the CV (11.67%) is much lower than the remaining studies, mainly because of the small SD.

Cluster 4 included two studies Chan [48] and Chen [50] that assessed breast density using FCM and N3 algorithms and non-contrast-enhanced T1-weighted with 3D gradient echo. As can be seen from the data in Figure 5 and Table 3 (Cluster 3–6) the study means and SDs are not different. In contrast to this Cluster 5, the Tagliafico study [3] used 3D contrast-enhanced T1-weighted gradient echo sequence and analyzed the breast density by semi-automated interactive threshold, in particular, (MedDensity). As Figure 5 and Table 3 (Cluster 3–6) show, the study mean is much higher than the remaining studies, largely because of the technical method used. Finally, cluster 6 consisted of Lodger [54], this is the only study that used proton density weighted sequence. Detailed information of clustering membership, study means, SDs, and CVs is shown in Table 3, Figures 4 and 5.

Switching from technology groupings of studies to groupings identified by the cluster analysis, meta-analysis of cluster 1 revealed that the study means, and study variances are both heterogeneous (Cochran's test for heterogeneity of study means, $X^2 = 22.26$, $P = 0.0045$, and Bartlett's test for heterogeneity of study variances, $X^2 = 21.47$, $P = 0.0060$, see Figure 6A). When Choi [49] was excluded (because of the very large CV), the cluster has improved somewhat, which would be expected as this study used different protocols (i.e. diffusion-weighted imaging). It can be seen from the data in Figure 6B that the study variances are no longer heterogeneous ($X^2 = 8.84$, $P = 0.2641$), although the study means remain heterogeneous ($X^2 = 19.54$, $P = 0.0066$). In contrast, meta-analysis of cluster 2 indicated that the study means are not heterogeneous ($X^2 = 4.77$, $P = 0.6874$), while the study variances are mildly heterogeneous ($X^2 = 15.54$, $P = 0.0206$, see Figure 7).

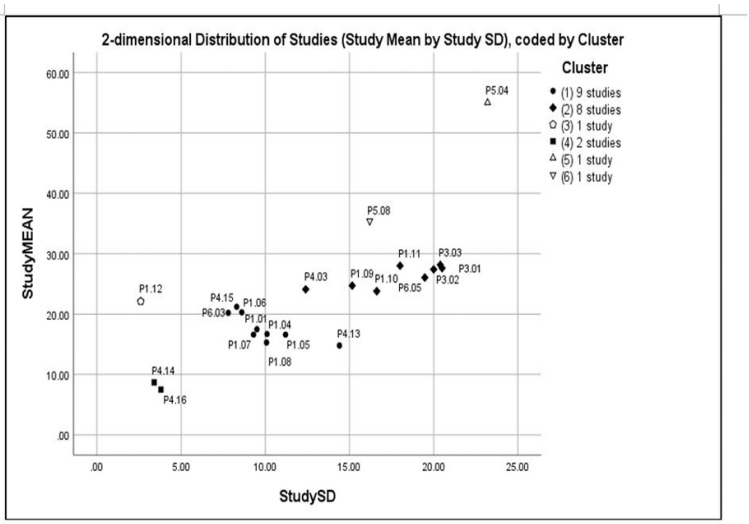

(**A**)

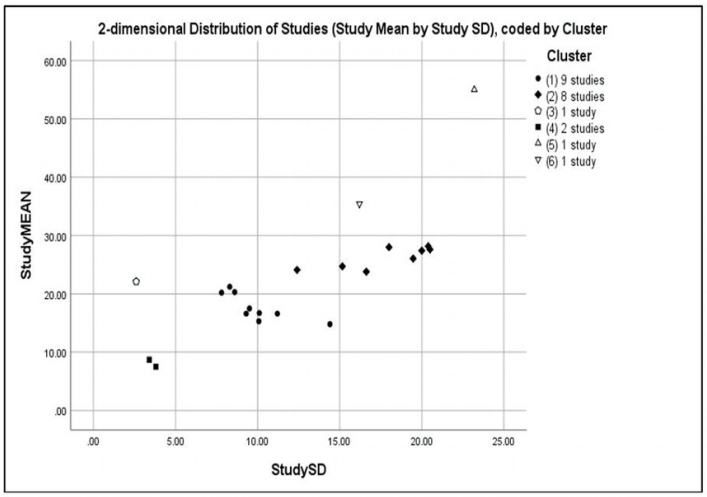

(**B**)

Figure 5. Scatter plot of the study means versus SDs using 6-clusters memberships of the 21 included studies in the subgroup meta-analyses. Legend indicates the number of studies in each cluster, solid fill represents clusters with two or more studies, while open markers represent singleton study. Scatterplot of study means versus SDs with study codes (**A**) and without study codes (**B**).

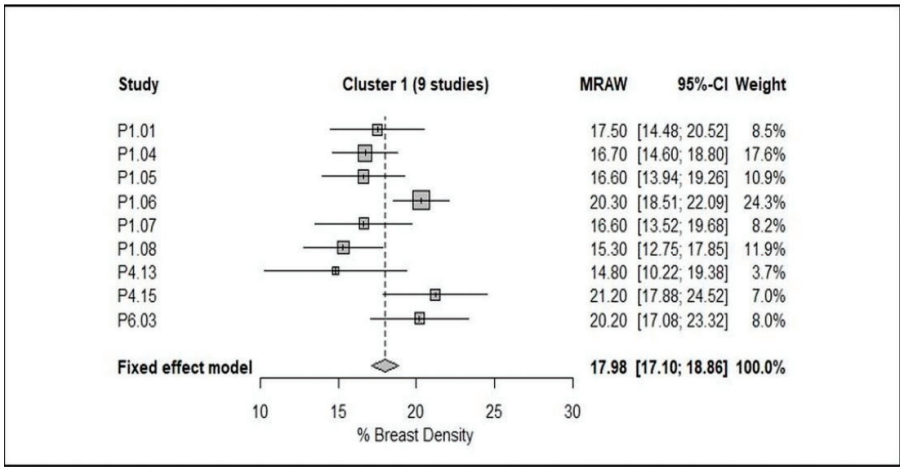

(**A**)

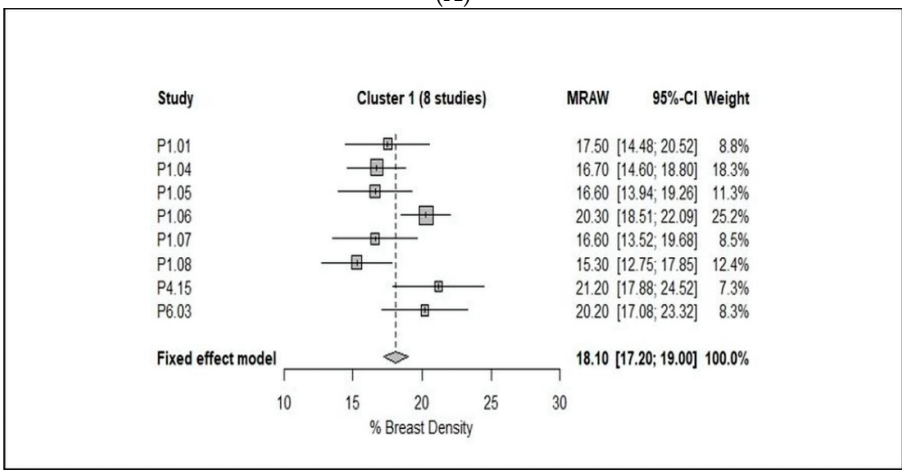

(**B**)

Figure 6. Forest plot of the study means, and 95% confidence limits of the studies in Cluster 1 with/without P4.13 (Choi, 2017) of % breast density. (**A**) Fixed effect meta-analysis of the studies in Cluster 1 (9 studies) of % breast density. (**B**) Fixed effect meta-analysis of the studies in Cluster 1 (8 studies) of % breast density.

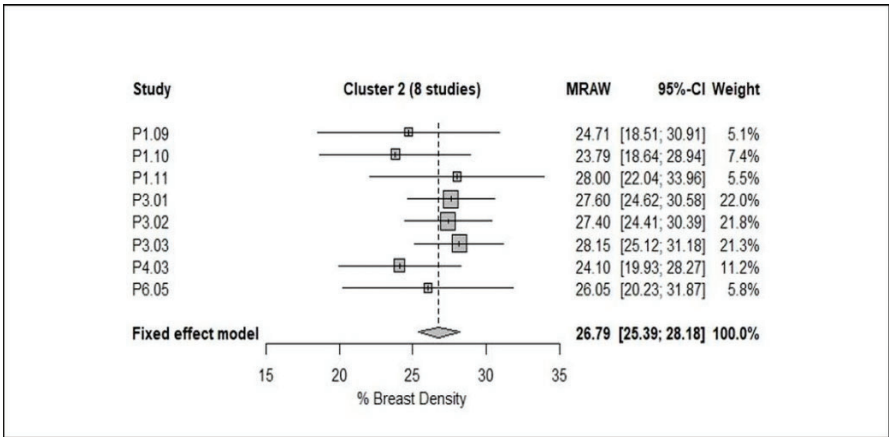

Figure 7. Forest plot of the study means, and 95% confidence limits of the studies in Cluster 2 (8 studies) of % breast density.

4. Discussion

The present systematic review and meta-analysis was performed to analyze the current studies on quantitative breast density using MRI and to determine the most appropriate technical/operational protocol. Through reviewing 38 studies from the literature, despite many methods and protocols available, no gold standard has been established with a wide range of heterogeneous methods or protocols used in these studies. To the best of our knowledge, this is the first comprehensive systematic review and meta-analysis of pooling the results of all breast density segmentation/measurement methods using MRI data. The analysis indicated that the non-contrast-enhanced T1-weighted acquisition was commonly utilized among all MR breast-imaging protocols. Another important finding of this analysis was that the FCM is the most frequently used algorithm amongst the breast density segmentation/measurement methods. Also, the results showed that a high level of heterogeneity was mainly associated with the breast-imaging protocols and the breast density segmentation/measurement methods.

Further attempts have been made by using clustering methods and meta-analysis to identify groups of studies which are as homogeneous as possible within groups and as heterogeneous as possible between groups. The included studies were grouped together into clusters based on their nearest neighbor Euclidean distances. On that basis, clusters 1 and 2 were considered as the most valuable results. Briefly, cluster 1 consisted of 9 studies [25–30,48,49,53], as shown from the data in Table 3 and Figure 6A that the CVs are varied in value, but in Choi [49] the CV is almost 100% because of the mean and SD are almost identical. This result may be explained by the fact that among the 8 studies [11,31,32,36–38,45,55], the breast-imaging protocol was a combination of contrast- and non-contrast-enhanced T1-weighted either with 2D spin echo or 3D gradient echo, while in Choi [49] the MRI protocol used was diffusion-weighted imaging. Consequently, it is advisable to exclude it from the meta-analysis to reduce the heterogeneity within cluster 1. Consistent with this hypothesis, the results have improved in somewhat, even though the study variances are not heterogeneous ($P > 0.05$), the study means are heterogeneous ($P < 0.05$) (Figure 6B). Although exclusion of Choi [49] did not reduce the heterogeneity, these results should be interpreted with caution. The discrepancy could be largely attributed to that although the MR breast-imaging protocols are not dissimilar (i.e., contrast- and non-contrast-enhanced T1-weighted), the breast segmentation/measurement methods are vice versa (i.e., FCM, FCM and N3, and in-house customized software). In contrast, cluster 2 included 8 studies, in 3 of these studies the breast density was reported as a (%DBV), while the remaining as a (% BD). Among these studies, the contrast- and non-contrast-enhanced T1-weighted was often used. From the data in Table 3 and Figure 7, it is apparent that the study means are not dissimilar ($P > 0.05$), although the study variances are heterogeneous ($P < 0.05$). Among the 21 studies included in the cluster analysis, although the fixed effect meta-analysis of cluster 2 has improved slightly, the heterogeneity within group still exist. There are two likely causes for this heterogeneity: the applied MR breast-imaging protocol and the used breast density segmentation/measurement methods.

Although the study has successfully confirmed the variation in the breast density segmentation/measurement methods using MRI data, the findings are subject to several limitations. First, the heterogeneity of study aims, the study design utilized, and the technical/operational methods applied, for instance, the MR breast-imaging protocol, MR scanner manufacturer, and the static magnetic field strength present challenges for performing the meta-analysis. Second, the breast density segmentation/measurement algorithm used is another limitation. Although we classified the included studies into discrete subgroups (i.e., FCM, FCM and N3, and interactive semi-automated threshold), and applied stratified analyses, the heterogeneity remains. Third, the definition of the breast density was inconsistent because some studies reported it as a percentage of dense breast volume, while the others as a percentage of breast density. Fourth, among the 38 studies included in this analysis, only 21 studies were eligible for meta-analysis due to the statistical requirements for the input values that should be in identical expression of measurement and dispersion. In addition, some of the included studies used the same set of the subject multiple times for different purpose and feature. Even though we decided to rectify the issue by selecting one of the results of data at random,

or by any meaningful clinical criterion, the heterogeneity continues to exist. Notwithstanding these limitations, the study further supports the idea of developing a standard MRI protocol for the quantitative assessment of breast density.

Future research can be suggested according to findings of this review. A recent study has reported the feasibility of creating a realistic 3D printed breast phantom for quality control purpose [58]. Thus, we consider 3D printing technique can be used to develop a patient-specific 3D printed breast phantom with different amounts of breast composition to quantify the volume of FGT. Further, the 3D printed model can be used to examine several MR breast-imaging protocols not only to measure the breast density but also to assess the impact of implementing various image quality parameters (i.e., FOV, matrix size and slice thickness) on the segmentation/measurement of breast density. Finally, the accuracy of different breast density/FGT segmentation methods can be determined.

5. Conclusion

This systematic review and meta-analysis confirms and substantiates the variation among the breast density segmentation/measurement methods using MRI. Furthermore, subgroup meta-analyses and further clustering methods indicated that a significant heterogeneity within and between groups exist. The analysis confirmed that the non-contrast-enhanced T1-weighted acquisition was commonly utilized among all MR breast-imaging protocols and the FCM is the most frequently used algorithm amongst the breast density segmentation/measurement methods. Future work will need to determine the most appropriate protocol and method for quantifying breast density using MRI.

Author contribution: Conceptualization: R.S and Z.S; data analysis: R.S and G.S; Writing—original draft preparation: R.S; Writing—review and editing: R.S, C.S, C.B, G.S. and Z.S.

Conflicts of Interest: Authors declare no conflicts of interest.

References

1. Chen, J.H.; Chang, Y.C.; Chang, D.; Wang, Y.T.; Nie, K.; Chang, R.F.; Nalcioglu, O.; Huang, C.S.; Su, M.Y. Reduction of breast density following tamoxifen treatment evaluated by 3-D MRI: Preliminary study. *Magn. Reson. Imaging* **2011**, *29*, 91–98.
2. Wang, J.; Azziz, A.; Fan, B.; Malkov, S.; Klifa, C.; Newitt, D.; Yitta, S.; Hylton, N.; Kerlikowske, K.; Shepherd, J.A. Agreement of mammographic measures of volumetric breast density to MRI. *PloS ONE* **2013**, *8*, e81653.
3. Tagliafico, A.; Bignotti, B.; Tagliafico, G.; Astengo, D.; Martino, L.; Airaldi, S.; Signori, A.; Sormani, M.P.; Houssami, N.; Calabrese, M. Breast density assessment using a 3T MRI system: Comparison among different sequences. *PLoS ONE* **2014**, *9*, e99027.
4. Lienart, V.; Carly, B.; Kang, X.; Guzy, L.; Sajovitz, A.M.; Liebens, F. Effect of preventive hormonal therapy on breast density: A systematic qualitative review. *Sci. World J.* **2014**, *2014*, 942386.
5. Tagliafico, A.; Tagliafico, G.; Astengo, D.; Airaldi, S.; Calabrese, M.; Houssami, N. Comparative estimation of percentage breast tissue density for digital mammography, digital breast tomosynthesis, and magnetic resonance imaging. *Breast Cancer Res. Treat.* **2013**, *138*, 311–317.
6. Li, H.; Weiss, W.A.; Medved, M.; Abe, H.; Newstead, G.M.; Karczmar, G.S.; Giger, M.L. Breast density estimation from high spectral and spatial resolution MRI. *J. Med. Imaging* **2016**, *3*, 044507.
7. Wu, S.; Weinstein, S.P.; Conant, E.F.; Kontos, D. Automated fibroglandular tissue segmentation and volumetric density estimation in breast MRI using an atlas-aided fuzzy C-means method. *Med. Phys.* **2013**, *40*, 122302.
8. Ding, J.; Stopeck, A.T.; Gao, Y.; Marron, M.T.; Wertheim, B.C.; Altbach, M.I.; Galons, J.P.; Roe, D.J.; Wang, F.; Maskarinec, G.; Thomson, C.A. Reproducible automated breast density measure with no ionizing radiation using fat-water decomposition MRI. *Magn. Reson. Imaging* **2018**, *48*, 971–981.
9. Sak, M.A.; Littrup, P.J.; Duric, N.; Mullooly, M.; Sherman, M.E.; Gierach, G.L. Current and future methods for measuring breast density: a brief comparative review. *Breast Cancer Manag.* **2015**, *4*, 209–221.

10. Niukkanen, A.; Arponen, O.; Nykänen, A.; Masarwah, A.; Sutela, A.; Liimatainen, T.; Vanninen, R.; Sudah, M. Quantitative volumetric K-means cluster segmentation of fibroglandular tissue and skin in breast MRI. *J. Digit. Imaging* **2018**, *31*, 425–434.
11. Klifa, C.; Carballido-Gamio, J.; Wilmes, L.; Laprie, A.; Shepherd, J.; Gibbs, J.; Fan, B.; Noworolski, S.; Hylton, N. Magnetic resonance imaging for secondary assessment of breast density in a high-risk cohort. *Magn. Reson. Imaging* **2010**, *28*, 8–15.
12. Ertas, G.; Doran, S.J.; Leach, M.O. A computerized volumetric segmentation method applicable to multi-centre MRI data to support computer-aided breast tissue analysis, density assessment and lesion localization. *Med. Biol. Eng. Comput.* **2017**, *55*, 57–68.
13. Petridou, E.; Kibiro, M.; Gladwell, C.; Malcolm, P.; Toms, A.; Juette, A.; Borga, M.; Leinhard, O.D.; Romu, T.; Kasmai, B.; Denton, E. Breast fat volume measurement using wide-bore 3 T MRI: comparison of traditional mammographic density evaluation with MRI density measurements using automatic segmentation. *Clin. Radiol.* **2017**, *72*, 565–572.
14. American College of Radiology. *ACR BI-RADS® Atlas: Breast Imaging Reporting and Data System*; American College of Radiology: Reston, VA, USA, 2013.
15. Mainiero MB, Lourenco A, Mahoney MC, Newell MS, Bailey L, Barke LD, D'Orsi C, Harvey JA, Hayes MK, Huynh PT, Jokich PM. ACR appropriateness criteria breast cancer screening. *J. Am. Coll. Radiol*. **2016**, 1, 13, 45-49
16. Timmers, J.M.; van Doorne-Nagtegaal, H.J.; Verbeek, A.L.; Den Heeten, G.J.; Broeders, M.J. A dedicated BI-RADS training programme: Effect on the inter-observer variation among screening radiologists. *Eur. J. Radiol.* **2012**, *81*, 2184–2188.
17. Nayeem, F.; Ju, H.; Brunder, D.G.; Nagamani, M.; Anderson, K.E.; Khamapirad, T.; Lu, L.J. Similarity of fibroglandular breast tissue content measured from magnetic resonance and mammographic images and by a mathematical algorithm. *Int. J. Breast. Cancer*. **2014**, *2014*, 961679.
18. Lin, M.; Chan, S.; Chen, J.H.; Chang, D.; Nie, K.; Chen, S.T.; Lin, C.J.; Shih, T.C.; Nalcioglu, O.; Su, M.Y. A new bias field correction method combining N3 and FCM for improved segmentation of breast density on MRI. *Med. Phys.* **2011**, *38*, 5–14.
19. Doran, S.J.; Hipwell, J.H.; Denholm, R.; Eiben, B.; Busana, M.; Hawkes, D.J.; Leach, M.O.; Silva, I.D. Breast MRI segmentation for density estimation: Do different methods give the same results and how much do differences matter? *Med. Phys.* **2017**, *44*, 4573–4592.
20. Tagliafico, A.; Tagliafico, G.; Tosto, S.; Chiesa, F.; Martinoli, C.; Derchi, L.E.; Calabrese, M. Mammographic density estimation: Comparison among BI-RADS categories, a semi-automated software and a fully automated one. *Breast J.* **2009**, *18*, 35–40.
21. Boston, R.C.; Schnall, M.D.; Englander, S.A.; Landis, J.R.; Moate, P.J. Estimation of the content of fat and parenchyma in breast tissue using MRI T1 histograms and phantoms. *Magn. Reson. Imaging* **2005**, *23*, 591–599.
22. Lu, L.J.; Nishino, T.K.; Johnson, R.F.; Nayeem, F.; Brunder, D.G.; Ju, H.; Leonard, M.H., Jr.; Grady, J.J.; Khamapirad, T. Comparison of breast tissue measurements using magnetic resonance imaging, digital mammography and a mathematical algorithm. *Phys. Med. Biol.* **2012**, *57*, 6903.
23. Moher, D.; Shamseer, L.; Clarke, M.; Ghersi, D.; Liberati, A.; Petticrew, M.; Shekelle, P.; Stewart, L.A. Preferred reporting items for systematic review and meta-analysis protocols (PRISMA-P) 2015 statement. *Syst. Rev.* **2015**, *4*, 1.
24. Stewart, L.A.; Clarke, M.; Rovers, M.; Riley, R.D.; Simmonds, M.; Stewart, G.; Tierney, J.F. Preferred reporting items for a systematic review and meta-analysis of individual participant data: The PRISMA-IPD statement. *JAMA* **2015**, *313*, 1657–1665.
25. Chang, D.H.; Chen, J.H.; Lin, M.; Bahri, S.; Hon, J.Y.; Mehta, R.S.; Nie, K.; Hsiang, D.J.; Nalcioglu, O.; Su, M.Y. Comparison of breast density measured on MR images acquired using fat-suppressed versus nonfat-suppressed sequences. *Med. Phys.* **2011**, *38*, 5961–5968.
26. Nie, K.; Chang, D.; Chen, J.H.; Hsu, C.C.; Nalcioglu, O.; Su, M.Y. Quantitative analysis of breast parenchymal patterns using 3D fibroglandular tissues segmented based on MRI. *Med. Phys.* **2010**, *37*, 217–226.
27. Pertuz, S.; McDonald, E.S.; Weinstein, S.P.; Conant, E.F.; Kontos, D. Fully automated quantitative estimation of volumetric breast density from digital breast tomosynthesis images: Preliminary results and comparison with digital mammography and MR imaging. *Radiology* **2016**, *279*, 65-74.

28. Moon, W.K.; Chang, J.F.; Lo, C.M.; Chang, J.M.; Lee, S.H.; Shin, S.U.; Huang, C.S.; Chang, R.F. Quantitative breast density analysis using tomosynthesis and comparison with MRI and digital mammography. *Comput. Methods Programs. Biomed.* **2018**, *154*, 99–107.
29. Chen, J.H.; Nie, K.; Bahri, S.; Hsu, C.C.; Hsu, F.T.; Shih, H.N.; Lin, M.; Nalcioglu, O.; Su, M.Y. Decrease in breast density in the contralateral normal breast of patients receiving neoadjuvant chemotherapy: MR imaging evaluation. *Radiology* **2010**, *255*, 44–52.
30. Ha, R.; Mema, E.; Guo, X.; Mango, V.; Desperito, E.; Ha, J.; Wynn, R.; Zhao, B. Quantitative 3D breast magnetic resonance imaging fibroglandular tissue analysis and correlation with qualitative assessments: A feasibility study. *Quant. Imaging Med. Surg.* **2016**, *6*, 144–150.
31. Chen, J.H.; Lee, Y.W.; Chan, S.W.; Yeh, D.C.; Chang, R.F. Breast density analysis with automated whole-breast ultrasound: Comparison with 3-D magnetic resonance imaging. *Ultrasound Med. Biol.* **2016**, *42*, 1211–1220.
32. Moon, W.K.; Shen, Y.W.; Huang, C.S.; Luo, S.C.; Kuzucan, A.; Chen, J.H.; Chang, R.F. Comparative study of density analysis using automated whole breast ultrasound and MRI. *Med. Phys.* **2011**, *38*, 382–389.
33. Nie, K.; Chang, D.; Chen, J.H.; Shih, T.C.; Hsu, C.C.; Nalcioglu, O.; Su, M.Y. Impact of skin removal on quantitative measurement of breast density using MRI. *Med. Phys.* **2010**, *37*, 227–233.
34. Kim, J.Y.; Cho, N.; Jeyanth, J.X.; Kim, W.H.; Lee, S.H.; Gweon, H.M.; Moon, W.K. Smaller reduction in 3D breast density associated with subsequent cancer recurrence in patients with breast cancer receiving adjuvant tamoxifen therapy. *Am. J. Roentgenol.* **2014**, *202*, 912–921.
35. Nie, K.; Su, M.Y.; Chau, M.K.; Chan, S.; Nguyen, H.; Tseng, T.; Huang, Y.; McLaren, C.E.; Nalcioglu, O.; Chen, J.H. Age-and race-dependence of the fibroglandular breast density analysed on 3D MRI. *Med. Phys.* **2010**, *37*, 2770–2776.
36. Bertrand, K.A.; Baer, H.J.; Orav, E.J.; Klifa, C.; Shepherd, J.A.; Van Horn, L.; Snetselaar, L.; Stevens, V.J.; Hylton, N.M.; Dorgan, J.F. Body fatness during childhood and adolescence and breast density in young women: A prospective analysis. *Breast. Cancer. Res.* **2015**, *17*, 95.
37. Bertrand, K.A.; Baer, H.J.; Orav, E.J.; Klifa, C.; Kumar, A.; Hylton, N.M.; LeBlanc, E.S.; Snetselaar, L.G.; Van Horn, L.; Dorgan, J.F. Early life body fatness, serum anti-müllerian hormone, and breast density in young adult women. *Cancer Epidemiol. Biomarkers Prev.* **2016**, *25*, 1151–1157.
38. Dorgan, J.F.; Klifa, C.; Shepherd, J.A.; Egleston, B.L.; Kwiterovich, P.O.; Himes, J.H.; Gabriel, K.P.; Van Horn, L.; Snetselaar, L.G.; Stevens, V.J.; Barton, B.A. Height, adiposity and body fat distribution and breast density in young women. *Breast. Cancer Res.* **2012**, *14*, R107.
39. Gabriel, K.P.; Klifa, C.; Pérez, A.; Kriska, A.M.; High, R.R.; Snetselaar, L.; Dorgan, J.F. Adolescent and young adult exposure to physical activity and breast density. *Med. Sci. Sports Exerc.* **2013**, *45*, 1515.
40. Jung, S.; Stanczyk, F.Z.; Egleston, B.L.; Snetselaar, L.G.; Stevens, V.J.; Shepherd, J.A.; Van Horn, L.; LeBlanc, E.S.; Paris, K.; Klifa, C.; Dorgan, J.F. Endogenous sex hormones and breast density in young women. *Cancer Epidemiol. Biomarkers Prev.* **2015**, *24*, 369–378.
41. Jung, S.; Goloubeva, O.; Klifa, C.; LeBlanc, E.S.; Snetselaar, L.G.; Van Horn, L.; Dorgan, J.F. Dietary fat intake during adolescence and breast density among young women. *Cancer Epidemiol. Biomarkers Prev.* **2016**, *25*, 918–926.
42. Dorgan, J.F.; Klifa, C.; Deshmukh, S.; Egleston, B.L.; Shepherd, J.A.; Kwiterovich, P.O.; Van Horn, L.; Snetselaar, L.G.; Stevens, V.J.; Robson, A.M.; et al. Menstrual and reproductive characteristics and breast density in young women. *Cancer Causes Control* **2013**, *24*, 1973–1983.
43. Jung, S.; Egleston, B.L.; Chandler, D.W.; Van Horn, L.; Hylton, N.M.; Klifa, C.C.; Lasser, N.L.; LeBlanc, E.S.; Paris, K.; Shepherd, J.A.; et al. Adolescent endogenous sex hormones and breast density in early adulthood. *Breast Cancer Res.* **2015**, *17*, 77.
44. Jones, J.A.; Hartman, T.J.; Klifa, C.S.; Coffman, D.L.; Mitchell, D.C.; Vernarelli, J.A.; Snetselaar, L.G.; Van Horn, L.; Stevens, V.J.; Robson, A.M.; et al. Dietary energy density is positively associated with breast density among young women. *J. Acad. Nut. Diet.* **2015**, 115, 353-9.
45. Chen, J.H.; Chan, S.; Liu, Y.J.; Yeh, D.C.; Chang, C.K.; Chen, L.K.; Pan, W.F.; Kuo, C.C.; Lin, M.; Chang, D.H.; et al. Consistency of breast density measured from the same women in four different MR scanners. *Med. Phys.* **2012**, 39, 4886–4895.
46. Chen, J.H.; Chan, S.; Tang, Y.T.; Hon, J.S.; Tseng, P.C.; Cheriyan, A.T.; Shah, N.R.; Yeh, D.C.; Lee, S.K.; Chen, W.P.; et al. Impact of positional difference on the measurement of breast density using MRI. *Med. Phys.* **2015**, *42*, 2268–2275.

47. Chen, J.H.; Pan, W.F.; Kao, J.; Lu, J.; Chen, L.K.; Kuo, C.C.; Chang, C.K.; Chen, W.P.; McLaren, C.E.; Bahri, S.; et al. Effect of taxane-based neoadjuvant chemotherapy on fibroglandular tissue volume and percent breast density in the contralateral normal breast evaluated by 3T MR. *NMR Biomed.* **2013**, *26*, 1705–1713.
48. Chan, S.; Su, M.Y.; Lei, F.J.; Wu, J.P.; Lin, M.; Nalcioglu, O.; Feig, S.A.; Chen, J.H. Menstrual cycle–related fluctuations in breast density measured by using three-dimensional MR imaging. *Radiology* **2011**, *261*, 744–751.
49. Choi, Y.J.; Chen, J.H.; Yu, H.J.; Li, Y.; Su, M.Y. Impact of different analytic approaches on the analysis of the breast fibroglandular tissue using diffusion weighted imaging. *Bio. Med. Res. Int.* **2017**, *2017*, 1094354.
50. Chen, J.H.; Chan, S.; Yeh, D.C.; Fwu, P.T.; Lin, M.; Su, M.Y. Response of bilateral breasts to the endogenous hormonal fluctuation in a menstrual cycle evaluated using 3D MRI. *Magn. Reson. Imaging* **2013**, *31*, 538–544.
51. Clendenen, T.V.; Zeleniuch-Jacquotte, A.; Moy, L.; Pike, M.C.; Rusinek, H.; Kim, S. Comparison of 3-point dixon imaging and fuzzy C-means clustering methods for breast density measurement. *Magn. Reson. Imaging* **2013**, *38*, 474–481.
52. McDonald, E.S.; Schopp, J.G.; Peacock, S.; DeMartini, W.B.; Rahbar, H.; Lehman, C.D.; Partridge, S.C. Diffusion-weighted MRI: Association between patient characteristics and apparent diffusion coefficients of normal breast fibroglandular tissue at 3 T. *Am. J. Roentgenol.* **2014**, *202*, 496–502.
53. Chen, J.H.; Chen, W.P.; Chan, S.; Yeh, D.C.; Su, M.Y.; McLaren, C.E. Correlation of endogenous hormonal levels, fibroglandular tissue volume and percent density measured using 3D MRI during one menstrual cycle. *Ann. Oncol.* **2013**, *24*, 2329–2335.
54. Ledger, A.E.; Scurr, E.D.; Hughes, J.; Macdonald, A.; Wallace, T.; Thomas, K.; Wilson, R.; Leach, M.O.; Schmidt, M.A. Comparison of Dixon sequences for estimation of percent breast fibroglandular tissue. *PloS. ONE* **2016**, *11*, e0152152.
55. Wengert, G.J.; Helbich, T.H.; Vogl, W.D.; Baltzer, P.; Langs, G.; Weber, M.; Bogner, W.; Gruber, S.; Trattnig, S.; Pinker, K. Introduction of an automated user–independent quantitative volumetric magnetic resonance imaging breast density measurement system using the Dixon sequence: Comparison with mammographic breast density assessment. *Invest. Radiol.* **2015**, *50*, 73–80.
56. O'Flynn, E.A.; Wilson, R.M.; Allen, S.D.; Locke, I.; Scurr, E.; deSouza, N.M. Diffusion-weighted imaging of the high-risk breast: Apparent diffusion coefficient values and their relationship to breast density. *Magn. Reson. Imaging* **2014**, *39*, 805–811.
57. Kim, J.Y.; Suh, H.B.; Kang, H.J.; Shin, J.K.; Choo, K.S.; Nam, K.J.; Lee, S.W.; Jung, Y.L.; Bae, Y.T. Apparent diffusion coefficient of breast cancer and normal fibroglandular tissue in diffusion-weighted imaging: The effects of menstrual cycle and menopausal status. *Breast Cancer Res. Treat.* **2016**, *157*, 31–40.
58. He, Y.; Liu, Y.; Dyer, B.A.; Boone, J.M.; Liu, S.; Chen, T.; Zheng, F.; Zhu, Y.; Sun, Y.; Rong, Y.; Qiu, J. 3D-printed breast phantom for multi-purpose and multi-modality imaging. *Quant. Imaging Med. Surg.* **2019**, *9*, 63–74.

Original Article

Development of patient-specific 3D-printed breast phantom using silicone and peanut oils for magnetic resonance imaging

Rooa Sindi[1,2], Yin How Wong[3], Chai Hong Yeong[3], Zhonghua Sun[1]

[1]Discipline of Medical Radiation Sciences, School of Molecular and Life Sciences, Curtin University, Perth, WA, Australia; [2]Radio-diagnostic and Medical Imaging Department, Medical Physics Section, King Fahd Armed Forces Hospital, Jeddah, Kingdom of Saudi Arabia; [3]School of Medicine, Faculty of Health and Medical Sciences, Taylor's University, Subang Jaya, Selangor, Malaysia

Correspondence to: Zhonghua Sun. Professor, Discipline of Medical Radiation Sciences, School of Molecular and Life Sciences, Curtin University, Perth, WA 6845, Australia. Email: z.sun@curtin.edu.au.

Background: Despite increasing reports of 3D printing in medical applications, the use of 3D printing in breast imaging is limited, thus, personalized 3D-printed breast model could be a novel approach to overcome current limitations in utilizing breast magnetic resonance imaging (MRI) for quantitative assessment of breast density. The aim of this study is to develop a patient-specific 3D-printed breast phantom and to identify the most appropriate materials for simulating the MR imaging characteristics of fibroglandular and adipose tissues.

Methods: A patient-specific 3D-printed breast model was generated using 3D-printing techniques for the construction of the hollow skin and fibroglandular region shells. Then, the T1 relaxation times of the five selected materials (agarose gel, silicone rubber with/without fish oil, silicone oil, and peanut oil) were measured on a 3T MRI system to determine the appropriate ones to represent the MR imaging characteristics of fibroglandular and adipose tissues. Results were then compared to the reference values of T1 relaxation times of the corresponding tissues: 1,324.42±167.63 and 449.27±26.09 ms, respectively. Finally, the materials that matched the T1 relaxation times of the respective tissues were used to fill the 3D-printed hollow breast shells.

Results: The silicone and peanut oils were found to closely resemble the T1 relaxation times and imaging characteristics of these two tissues, which are 1,515.8±105.5 and 405.4±15.1 ms, respectively. The agarose gel with different concentrations, ranging from 0.5 to 2.5 wt%, was found to have the longest T1 relaxation times.

Conclusions: A patient-specific 3D-printed breast phantom was successfully designed and constructed using silicone and peanut oils to simulate the MR imaging characteristics of fibroglandular and adipose tissues. The phantom can be used to investigate different MR breast imaging protocols for the quantitative assessment of breast density.

Keywords: Magnetic resonance imaging (MRI); T1 and T2 relaxation times; fibroglandular-tissue; breast density; 3D-printing; fused deposition modelling (FDM); digital light processing (DLP); polylactic acid (PLA); photopolymer resin; silicone oil; peanut oil

Submitted Feb 12, 2020. Accepted for publication Apr 22, 2020.
doi: 10.21037/qims-20-251
View this article at: http://dx.doi.org/10.21037/qims-20-251

Introduction

Breast magnetic resonance imaging (MRI) is a well-established approach in the diagnosis of breast disease, and it has become an important modality in the screening of women at high-risk of breast cancer, preoperative staging of newly diagnosed breast cancer, and follow-up of breast cancer treatment (1-3). Hence, the European Society of Breast Imaging (EUSOBI) has recommended that breast

MRI be used as an adjuvant modality in women at high-risk of developing breast cancer (3), for those with (BRCA-positive genetic mutation carriers), family history, and/or high breast density (4).

Breast density, a measure of fibroglandular, dense tissue relative to fatty, non-dense tissue, is an independent risk factor of breast cancer (5-7). Consistent with this risk relationship, women who have dense breasts have a likelihood of developing breast cancer that is fourfold higher than those with fatty breasts (8,9). Currently various methods have been developed and introduced to segment/measure breast density using MRI: the utilization of a clustering algorithm, the segmentation of glandular and fatty tissues with an interactive thresholding algorithm, a logistic function approach and a curve-fitting algorithm; each has its advantages and limitations (10-14). However, there are certain drawbacks associated with the use of these algorithms as most of them are interpreted as measurements with a semi-automatic thresholding and segmentation methods. Likewise, different MR breast-imaging protocols have been used to differentiate between adipose and fibroglandular tissues ranging from non-contrast-enhanced T1-weighted to contrast-enhanced T1-weighted and diffusion-weighted acquisitions (15-19). Despite improvements in the quantitative assessment of breast density using MR imaging, there has been no general agreement about the optimal scanning protocol in this aspect. A recent systematic review and meta-analysis about the quantitative assessment of breast density has confirmed these variations among breast segmentation/measurement methods and MR breast-imaging protocols (20).

In recent years, there has been an increasing interest in 3D printing techniques, which are being used in different medical domains such as cardiovascular disease, orthopedic surgery, prosthetics, and neurosurgery (21-24). 3D-printed models have been shown to assist in the development of many surgical implants, which can improve the individual's understanding of such a complex anatomical structure (21). Several studies have produced anthropomorphic breast phantoms for X-ray imaging, but there is still insufficient data available for MR imaging (25-30). Carton *et al.* developed a 3D anthropomorphic breast phantom for the evaluation of image quality of 2D and 3D breast X-ray imaging systems. This phantom was based on a computational model and a rapid prototyping technique to generate breast phantom with different compositions, sizes, and shapes by using a tissue-equivalent material (25). While the phantom has effectively demonstrated a heterogeneous distribution of the fibroglandular and adipose tissues that can be analogous to the clinical breast images, it has certain limitations in terms of its fabrication method and application. The phantom has been printed in slabs form, which is very complicated to manufacture and it is a time-consuming process (25).

Although some research has been carried out on the use of 3D printing techniques to develop a breast phantom for MR imaging, only few studies have attempted to generate a personalized 3D-printed breast phantom based on a realistic breast MR images that can be similar to the anatomical structures seen in human tissues (26-30). Burfeindt *et al.* (26) reported a new and convenient synthetic procedure to develop an MRI-derived 3D-printed breast phantom for the preclinical use in microwave breast-imaging experiments. Although the phantom has successfully simulated the dielectric properties of the biological breast tissues, it has been designed for microwave breast-imaging rather than for MR imaging system (26). Furthermore, the importance of realistic phantom structure in the assessment of photoacoustic breast imaging systems for the purpose of simulating the acoustic and optical breast tissues properties was demonstrated in a study by Dantuma *et al.* (27), in which a semi-anthropomorphic 3D-printed moulds derived from a MRI segmented numerical breast model was developed to produce real breast morphology using polyvinyl chloride plastisol (PVCP). However, there are limits to how far the phantom that has been designed for ultrasound and photoacoustic imaging can be used to simulate the MR imaging characteristics of breast tissues (27). Moreover, He *et al.* (28) developed a 3D-printed breast phantom for machine calibration and image optimization in multi-modalities imaging, where a mixture of PVC powder and softener (i.e., dioctyl terephthalate) was used as a tissue-mimicking material (TMM) of breast tissues. Although the study has successful demonstrated the simulation of breast structures, it has certain limitations in terms of the lack of the appearance, variability, and heterogeneity of structures that are presented in the physiological tissues (28). Another potential limitation is that the T1 and T2 relaxation times of the materials were measured and found to be shorter than those reported in the physiological human breast tissues (28,29). While most of the aforementioned phantoms address their objectives in the medical imaging discipline, there are currently no phantoms available to evaluate the breast density based on a realistic morphology of breast structures derived from a MR images of human tissues. Likewise, uncertainties still exist about the most

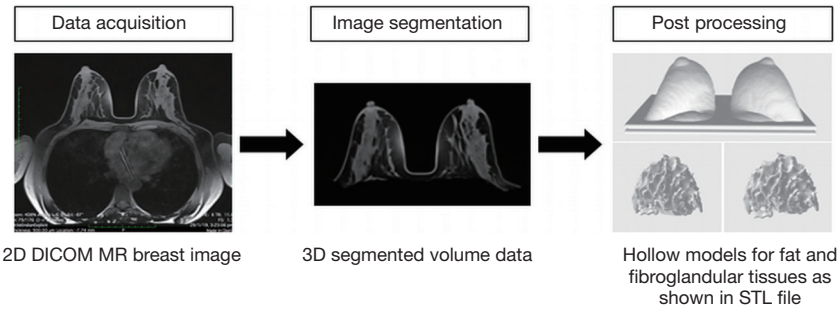

Figure 1 Schematic flowchart demonstrates the process of developing a patient-specific 3D-printed breast model.

appropriate TMMs that can be used to simulate the MR-related characteristics and appearance of breast structures, particularly fibroglandular tissue. Such a personalized 3D-printed breast model could be used to examine different MR breast-imaging protocols not only to evaluate the breast density but also to determine the impact of applying various image quality parameters on the segmentation/measurement methods of breast density. Therefore, the aim of this study is to develop a patient-specific 3D-printed breast phantom and to identify the most appropriate materials for simulating the MR imaging characteristics of fibroglandular and adipose tissues.

Methods

Patient data

Ethical approval was obtained from Curtin University's Human Research Ethics Committee (HREC) and King Fahd Armed Forces Hospital's (Jeddah) Research and Ethics Committee. A random sample of patients with no history of breast disease was retrospectively reviewed from an existing breast MRI database. The criteria for selecting the subjects were the following: no previous surgery, no radiotherapy treatment on the chest wall, no history of breast cancer, and a Breast Imaging-Reporting and Data System (BI-RADS) classification of 1, indicating a negative likelihood of cancer. A 46-year-old woman was identified by a senior radiology resident to match the selection criteria. The breast MRI examination was performed using 1.5T system (MAGNETOM Aera, Siemens, Germany) with a dedicated breast coil (18 channels). The MR breast imaging protocol was chosen based on the recommendations of a recent systematic review and meta-analysis (20) as high-resolution non-contrast-enhanced T1-weighted images to allow a precise differentiation between adipose and fibroglandular tissues: TR/TE 11.8/6.0 ms; matrix size 384×384; slice thickness 0.9 mm with no gap.

Image post-processing and segmentation process

A series of image post-processing and segmentation of the volumetric data was performed. First, the anonymized Digital Imaging and Communications in Medicine (DICOM) MR images were imported into the commercially available software Analyze 12.0 (AnalyzeDirect, Inc., Lexana, KS, USA) to segment the non-contrast-enhanced T1-weighted breast images. Second, the breast's boundary was delineated manually to distinguish the breast's body from the surrounding tissues (pectoral muscle, heart, lungs, and thorax) on each 2D slice based on grayscale intensity, displayed in a histogram. Then, the 3D breast volume was created by these 2D images and was subsequently used to design the 3D-printed breast model. Finally, the 3D segmented MR breast volume was saved as a standard tessellation language (STL) file for further image post-processing and 3D printing. *Figure 1* presents a schematic flowchart of the process of developing a patient-specific 3D-printed breast model using MRI data. For more details, the phantom consists of three main parts: the outer shell, simulating the skin layer, and the internal structures, which include fibroglandular and fat tissues, imitating the breast composition. To generate the skin shell, the STL file containing the 3D segmented MR breast volume was imported into the Blender software, version 2.79b (Blender Foundation, Amsterdam, Netherlands) to hollow the model and ensure that all the internal structures were perfectly extracted.

On the other hand, the DICOM MR breast dataset was loaded into the 3D Slicer software, version 4.10.2 [National Alliance for Medical Image Computing (NA-MIC)] to segment out the fibroglandular tissue and ensure that all

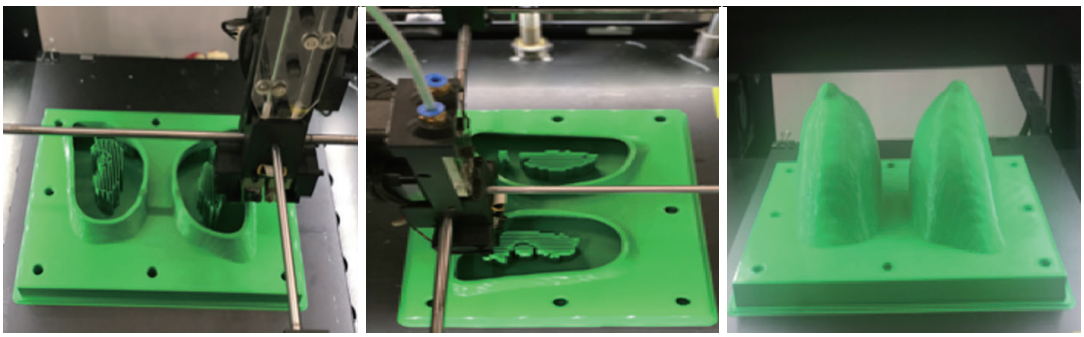

Figure 2 External structure of the patient-specific 3D-printed breast phantom that consists of 3 mm thick skin layer and compartments to be filled with fibroglandular and adipose tissues models.

the surrounding structures were completely removed. To increase reliability of the segmentation, each slice was segmented in different orientations using the threshold function, which was adjusted manually. This approach was used to threshold the DICOM dataset so that only the fibroglandular tissue structures were kept in the final segmented data. Subsequently, the segmented fibroglandular model was saved as a STL file and imported into the (version 3.5.474, Autodesk Inc., San Rafael, CA, USA) open-source software for further edit. Any deformities or free-floating objects were removed, and any holes were fixed during the editing process.

Overview and breast phantom design

This part is divided into three sections, each detailing the construction process related to the 3D-printed breast model components.

Skin layer

Based on the dimensions of a realistic tissue, the outer phantom shell had an average thickness of 3.0 mm, which corresponds to the normal skin thickness. The cover of the skin shell was designed using a computer-aided design (CAD) software. The skin shell and the cover were fabricated with fused deposition modelling (FDM) technology using polylactic acid (PLA) (Polymaker, Shanghai, China) on a Raise3D N2 Plus 3D printer (Raise3D, Irvine, CA, USA). The skin shell was printed with a layer height of 0.15 mm, average printing time of 40 hours, and a resolution of 12.5 µm (*Figure 2*).

Fibroglandular region

The fibroglandular models constitute the internal component of the 3D-printed breast phantom. While various definitions of the term "breast density" have been proposed, in this study, the term "fibroglandular tissue" is used to refer to the breast density. Naturally, the fibroglandular region contains variable shapes and/or volumes of glandular tissue, includes fibrous or connective tissue. In clinical practice, the evaluation of fibroglandular tissue is based on a subjective assessment recommended by the American College of Radiology (ACR) BI-RADS, which is commonly used for mammography but also for MRI. The BI-RADS atlas can be described as a classification system that characterises breast density on the basis of the amount of fibroglandular tissue into four categories: (I) almost entirely fat, (II) scattered fibroglandular tissue, (III) heterogeneous fibroglandular tissue, and (IV) extreme fibroglandular tissue (31,32).

In order to simulate the MR imaging characteristics, the 3D fibroglandular models were designed as hollow structures with an average thickness of 2.0 mm. The fibroglandular models were fabricated using the digital light processing (DLP) technology on an Anycubic Photon S 3D DLP UV resin printer (Shenzhen Anycubic Technology Co. Ltd., Shenzhen, China) using white photopolymer resin (Magma H LINE Photopolymer Resin) from Magma Filament, Malaysia. A curing time of 10 sec per layer, a layer thickness of 0.05 mm, and a resolution of 47 µm were used to fabricate the fibroglandular models. The printing duration for both left and right fibroglandular models was about 17 hours (*Figure 3*).

Fat/adipose region

This region comprises a considerable part of the 3D-printed breast model. It consists of a selected material that simulates the MR imaging relaxation times of adipose tissue.

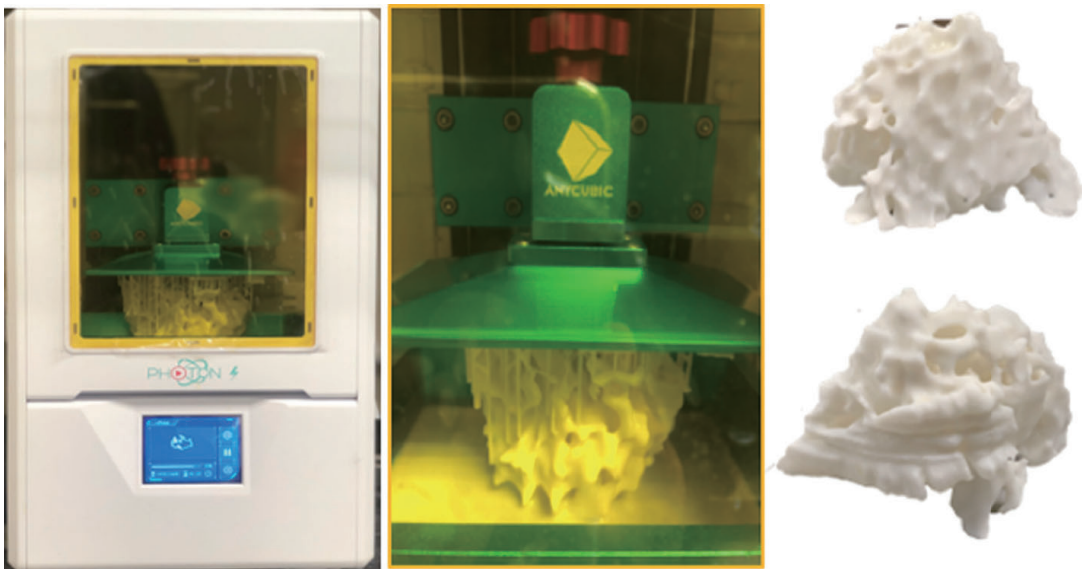

Figure 3 Fabrication of the hollow fibroglandular models using the Anycubic Photon S high-resolution 3D DLP UV resin printer. The thickness of the wall is 2.0 mm. DLP, digital light processing.

Fibroglandular TMMs

Agarose gels with different concentrations vary in their ability to simulate the MR imaging characteristics of T1 and T2 relaxation times of an extensive range of human tissues (33,34). In a study investigating the T1 and T2 relaxation times of four sample phantom liquids, Gach *et al.* (33) found that silicone oil had the longest T1 and T2 times on a 3T MRI system: 1,068.29±5.95 and 566.40±4.68 ms, respectively. These results provide further support to the hypothesis that agarose gel or silicone oil could be used to mimic the MR imaging characteristics of fibroglandular tissue based on T1 and/or T2 relaxation times. Thus, four different raw materials were scanned to determine which one could be used to mimic the T1 and/or T2 relaxation times of fibroglandular tissue. The candidate materials were silicone oil with a viscosity of 50 mm^2/s at 25 ℃ (TEX Chemical Inc., Country), agarose (Thermo Fisher, Waltham, MA, USA), silicone rubber RTV (Craftiviti Sdn. Bhd., Selangor, Malaysia), and fish oil (Blackmores, Sydney, Australia) (*Figure 4*).

Fat/adipose TMMs

As Niebuhr *et al.* (35) reported, olive oil successfully simulates the MR imaging relaxation times of adipose tissue in abdominal and pelvic tissues measured *in-vivo*. In another study, Niebuhr *et al.* (34) found that peanut oil efficiently simulates the MR imaging characteristics of subcutaneous fat for pelvis phantoms. Peanut oil was preferred in this study for several reasons, including its relatively similar MR imaging characteristics (T1 and T2 relaxation times) for adipose tissue, its translucent appearance, and its high oxidation stability (34,35). These characteristics suggest that peanut oil could be a performed material to mimic the T1 and/or T2 relaxation times of breast adipose tissue. Two types of peanut oil were scanned for testing: peanut oil Basso (raw material: Arachis hypogea; price: US$ 5/1L; Basso), and peanut oil Pressed Purity (raw materials: oleic acid (96.2%) and linoleic acid (13.2%), price: US$18/1.5L, Proteco Oils) (*Figure 4*).

Breast phantom construction

The T1 relaxation times of the five selected materials (agarose gel, silicone rubber with/without fish oil, silicone oil, and peanut oil) were measured at room temperature using a 3T MRI system to determine which ones could be used to mimic the MR imaging characteristics of fibroglandular and adipose tissues. The results were then compared to the reference values of T1 relaxation times of the corresponding tissues. Following this, the materials that matched the T1 relaxation times of the respective tissues were chosen to fill the 3D-printed hollow breast shells.

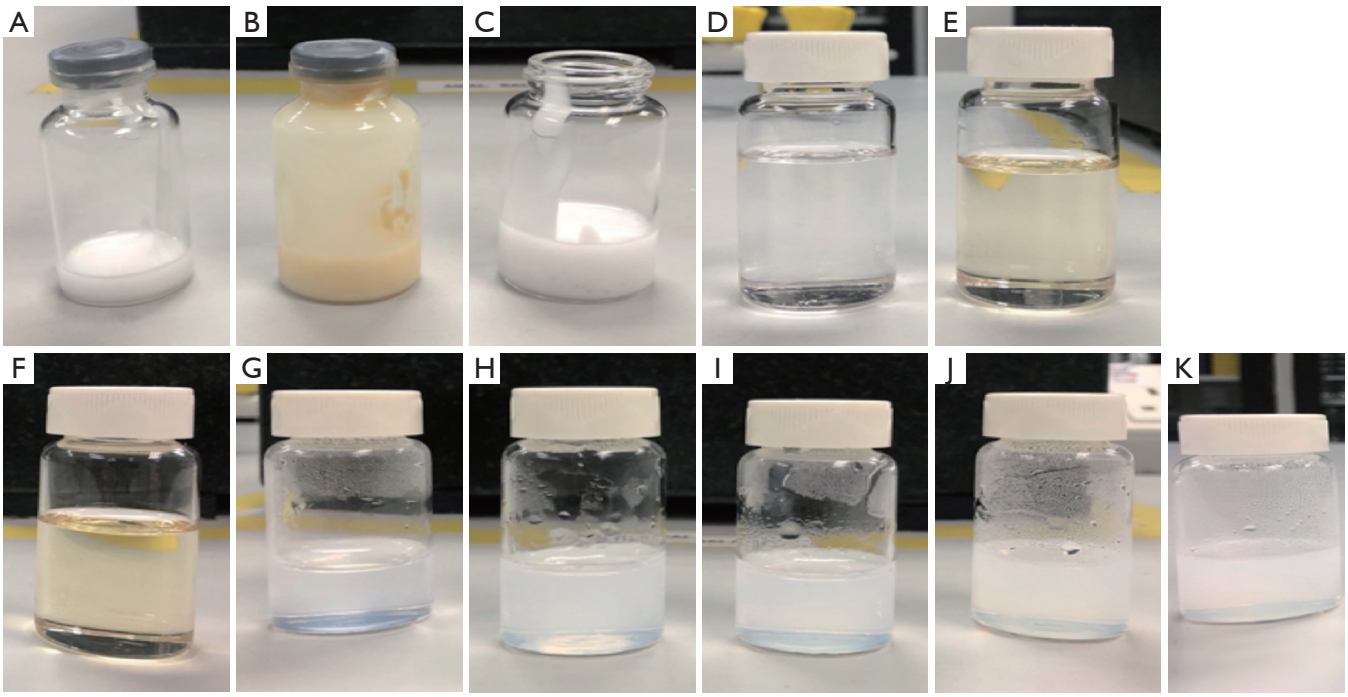

Figure 4 Test raw materials. (A) Silicone rubber; (B) silicone rubber with fish oil; (C) fresh silicone rubber; (D) silicone oil with a viscosity of 50 mm^2/s; (E) peanut oil (Basoo); (F) peanut oil (pressed purity); (G) agarose gel 0.5 wt%; (H) agarose gel 1.0 wt%; (I) agarose gel 1.5 wt%; (J) agarose gel 2.0 wt%; (K) agarose gel 2.5 wt%.

Results

3D-printed hollow models

The 3D-printed models of the hollow skin and fibroglandular region shells were scanned on a 3T MRI system (MAGNETOM Prisma, Siemens Healthcare, Erlangen, Germany) to check whether the models printed with the PLA or the photopolymer resin produce MR signals corresponding with these tissue features. Fortunately, no MR signal was observed from scanning the 3D-printed hollow models, indicating the possibility of using these materials for breast structure simulation and further patient models. It is important to note that the selected materials were checked when the 3D printing was initially performed and then checked again at the end of the breast phantom construction.

Sample characteristics

The five selected materials were scanned on the same 3T MRI system, with the materials placed in the 18-channel body and 32-channel spine coils. The MR breast scanning was chosen based on the institutional clinical protocol using 3D T1- and T2-weighted turbo spin echo (TSE) sequences: TR/TE 650.0/10.0 ms; matrix size 384×384; slice thickness 2.9 mm; no gap, and TR/TE 6,080.0/78.0 ms; matrix size 384×384; slice thickness 4.0 mm; no gap, respectively.

Figure 5 presents the MR imaging T1 relaxation times of the five materials (agarose gel, silicone rubber with/without fish oil, silicone oil, and peanut oil) simulating the breast composition. *Figure 5D* shows that the T1-weighted image of the silicone oil was associated with a mid-grey signal intensity, which is usually related to water-based tissues characterized by a moderate T1 relaxation time. On the other hand, *Figure 5E,F* shows that the T1-weighted images of the peanut oils indicated a high signal intensity, which was within expectation, as fat-based tissues have a short T1 relaxation time. In contrast, the T1-weighted images of the agarose gel with different concentrations, 0.5 to 2.5 wt%; were associated with low signal intensity, which is mainly observed in free water and other fluids (*Figure 5G,H,I,J,K*).

T1 relaxation times of the sample materials

The T1 relaxation times of these five materials are listed in *Table 1*. Silicone oil had a T1 relaxation time similar to

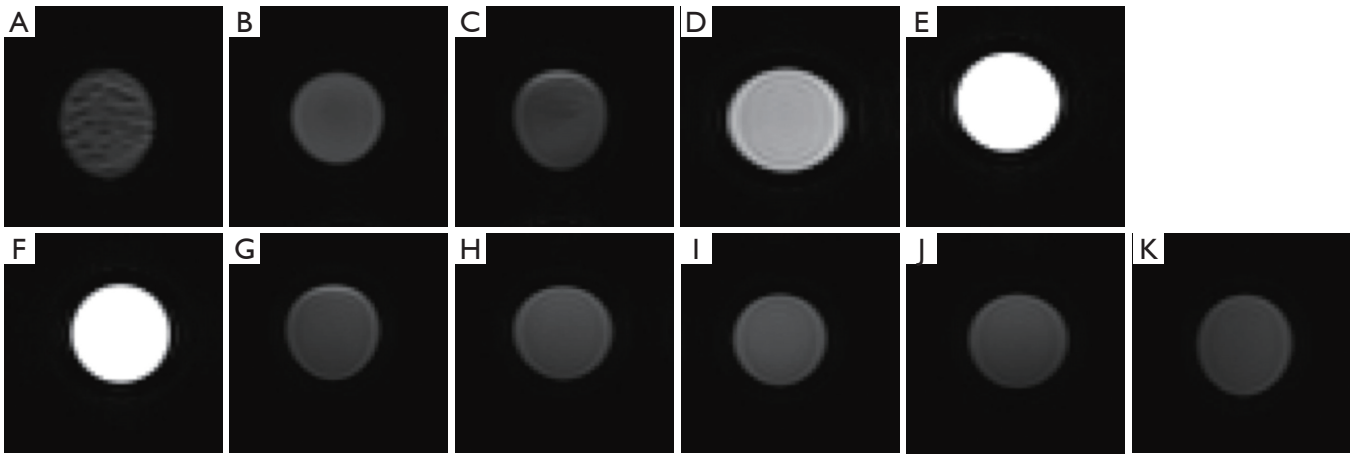

Figure 5 T1-weighted images. (A) Silicone rubber; (B) silicone rubber with fish oil; (C) fresh silicone rubber; (D) silicone oil with a viscosity of 50 mm^2/s; (E) peanut oil (Basoo); (F) peanut oil (Pressed Purity); (G) agarose gel 0.5 wt%; (H) agarose gel 1.0 wt%; (I) agarose gel 1.5 wt%; (J) agarose gel 2.0 wt%; (K) agarose gel 2.5 wt%.

Table 1 T1 Relaxation times of different materials for tissue surrogates used in the experiment

Phantom, TMM	T1 (average SD, ms), 3T Siemens MR Scanner
Fibroglandular shell	No signal
Skin/outer shell	No signal
Silicone rubber	577.2±107.8
Silicone rubber with fish oil	902.1±120.5
Fresh silicone rubber	638.3±108.5
Silicone oil 50 mm^2/s*	1,515.8±105.5
Peanut oil (Basso)	405.4±15.1
Peanut oil (pressed purity)	404.1±10.5
Agarose gel 0.5 wt%	4015.5±100.2
Agarose gel 1.0 wt%	3,877.8±130.5
Agarose gel 1.5 wt%	3,404.8±255.9
Agarose gel 2.0 wt%	3,572.6±100.4
Agarose gel 2.5 wt%	3,617.2±101.5

*, Viscosity unit. TMM, tissue-mimicking material.

that of fibroglandular tissue: 1,515.8±105.5 ms. In contrast, the Basso and Pressed Purity peanut oils had T1 relaxation times analogous to that of adipose tissue: 405.4±15.1 and 404.1±10.5 ms, respectively. For comparison, the T1 and T2 relaxation times of fibroglandular and adipose tissues measured using a 1.5T and a 3T MRI system are presented in *Table 2*.

As shown in *Table 1*, the agarose gel with different concentrations, ranging from 0.5 to 2.5 wt%, had the longest T1 relaxation times, which are similar to that of free water. The interesting finding is that the lowest concentration was associated with the highest T1 relaxation time. Overall, the results presented in *Table 1* and *Figure 5* indicate that the silicone and peanut oils closely resemble the MR imaging T1 relaxation times of the fibroglandular and adipose tissues, respectively. Therefore, these materials were chosen to fill the 3D-printed hollow models.

Figure 6 provides an overview of the construction process of the 3D-printed breast phantom. The two fibroglandular shell models were filled with a silicone oil and then sealed using UV-curable photopolymer resin. Following this, the filled fibroglandular shell models were fixed inside the skin shell model using acrylic-based adhesive. Further, the space between the fibroglandular and skin shell models was filled with peanut oil. A home-made silicone gasket and cover were used to enclose the breast phantom. Finally, the cover was tighten using the commercially available polycarbonate bolt and nuts.

Scanning of the 3D-printed breast phantom

The MR images of the phantom were acquired following the same breast imaging protocols described in the Results, Sample Characteristics. The phantom was scanned in a

Table 2 T1 and T2 Relaxation times of the breast tissues at 1.5T and 3T using FSE-IR scans (36)

Tissue (reference)	T1 (average SD, ms), 1.5T	T2 (average SD, ms), 1.5T	T1 (average SD, ms), 3T	T2 (average SD, ms), 3T
Adipose/fat	372.04±8.6	53.33±2.11	449.27±26.09	52.96±1.54
Fibroglandular	1,135.98±151.37	57.51±10.15	1,324.42±167.63	54.36±9.35

FSE-IR, Fast Spin Echo-Inversion Recovery.

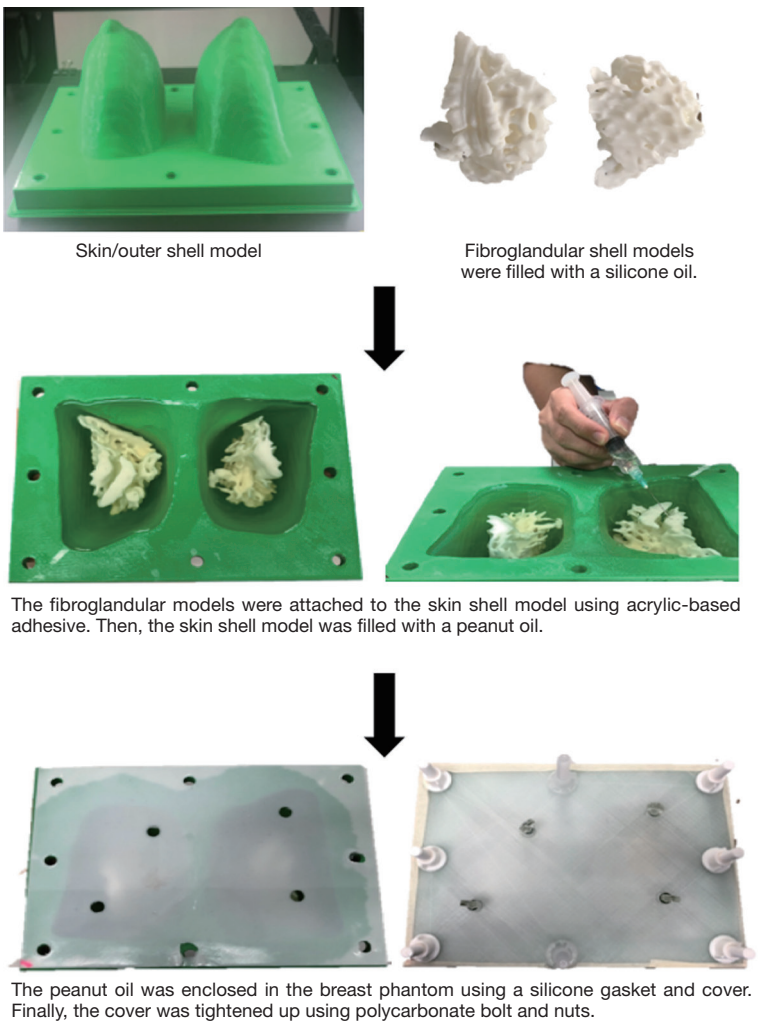

Figure 6 Flow chart showing 3D construction of the breast phantom. 3D printing technique was used to create the hollow shells for skin and fibroglandular regions. Fibroglandular and adipose tissues were simulated using silicone and peanut oils, respectively.

prone position using a dedicated 18-channel breast coil. *Figure* 7 shows the T1- and T2-weighted MR images of a patient-specific 3D-printed breast phantom using silicone and peanut oils as surrogates of the fibroglandular and adipose tissues, respectively. These oils presented an acceptable level of contrast and MR-related characteristics in both the T1- and the T2-weighted images. One of the most noticeable features of this phantom is that it is slightly inhomogeneous. However, this feature simulates the considerable inhomogeneity as often observed among

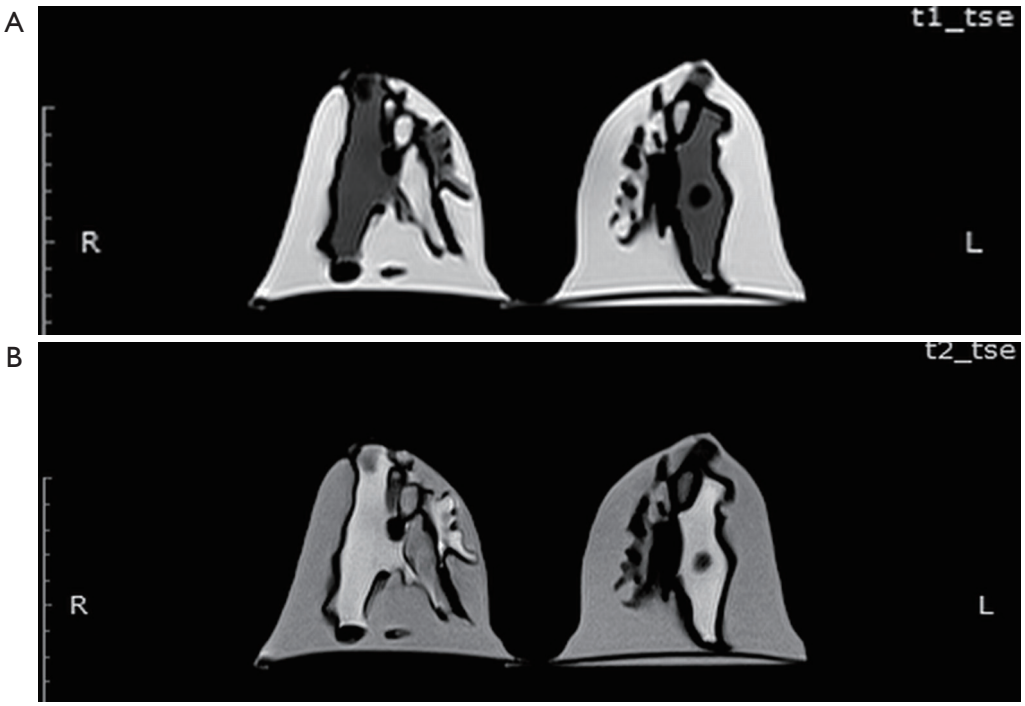

Figure 7 MR images of the 3D printed breast phantom. (A) T1-weighted image; (B) T2-weighted image using TSE scans. TSE, turbo spin echo.

the irregular distribution of the patient. Overall, the results shown in *Table 1* and *Figure 5* indicate that the MR imaging T1 relaxation times of the silicone and peanut oils used for the simulation of fibroglandular and adipose tissues are similar to their respective reference values reported in the literature.

Discussion

This study aimed to develop a patient-specific 3D-printed breast phantom and to determine the most appropriate materials for simulating the MR imaging characteristics of fibroglandular and adipose tissues. Anthropomorphic shapes of skin and fibroglandular tissues were constructed using 3D-printing techniques based on the segmentations of breast MR images from a selected healthy patient's data. All the 3D skin and fibroglandular region shells were designed as hollow structures using PLA and photopolymer resin. Since no MR signal was generated by the 3D-printed hollow models of those corresponding shells, different materials were selected to search for suitable ones with silicone oil and peanut oil being the most appropriate materials with similar T1 relaxation times to fibroglandular and adipose tissues.

It was assumed that the T1 relaxation times would effectively supplement and extend our knowledge about the selected materials since most organs' T1 values are five times longer than their T2 values. A comparison of the T1 relaxation times of the scanned materials with breast structure and literature reports showed that the silicone and peanut oils closely resemble the MR imaging T1 relaxation times of the fibroglandular and adipose tissues, respectively. Surprisingly, this study did not find a significant difference in the T1 relaxation times between different concentrations of agarose gel, which exhibited long T1 relaxation times, similar to that of water. Nevertheless, the agarose gel can be mixed with a gadolinium-based contrast agent for T1 adaptation, and can thus be used to simulate the MR imaging relaxation times of a wide range of human tissues. However, this would be costly and requires precautions when handling the contrast agent. Another unexpected finding was the slight difference in the T1 relaxation times between the Basso and Pressed Purity peanut oils. However, the observed difference was not significant. It is also worth noting that the Basso peanut oil was preferable due to its purity, availability, and low cost.

The most important clinically relevant finding was that the silicone and peanut oils demonstrated an acceptable level of contrast and MR-related characteristics of breast structures in both the T1- and the T2-weighted images. These findings are in line with Niebuhr *et al.* (34), who suggested that peanut oil efficiently simulates the MR imaging characteristics of subcutaneous fat for pelvis phantoms. In accordance with the present results, previous studies demonstrated that silicone oil with a viscosity of 50 mm^2/s had the longest T1 and T2 relaxation times on a 3T MRI system (33,35). However, silicone oil was not previously used for simulating the MR-related characteristics of breast structures, particularly fibroglandular tissue. Thus, this study presents interesting findings to encourage more research along this direction in breast phantom.

The observed correlation between silicone oil's T1 relaxation time and fibroglandular tissue could be attributed to its chemical composition and physical properties such as viscosity and density. This preliminary finding; suggests that silicone and peanut oils can be used to efficiently simulate the MR imaging characteristics of breast structures and produce further models. An implication of this is the possibility to examine different MR breast imaging protocols to identify the most appropriate for the quantitative assessment of breast density. For future investigations, it might be possible to use different chemical compositions and physical properties of silicone oils to evaluate the MR imaging relaxation times of breast structures. Since the relationship between silicone oil and fibroglandular tissue has not been studied, further research is required to better understand it.

Although the study has successfully designed and constructed a patient-specific 3D-printed breast phantom, the findings are subject to several limitations. The study was not specifically designed to evaluate the mechanical properties of breast tissue components, such as elastic modulus or tissue strength. Examining the mechanical features along with the physical properties of selected materials could provide an idea of their characteristics and allow more detailed comparisons to the human breast tissue. Moreover, there are certain drawbacks to the use of 3D printing techniques for the construction of skin and fibroglandular hollow shells. One of them is the potential risk for some of the connected structures to break easily during the cleaning process. For this reason, several models of varying wall thicknesses, ranging between 1.0 and 2.5 mm, were printed. However, increasing the thickness of photopolymer resin can cause considerable deformation of the fibroglandular structure. Another potential limitation is due to the complexity of the fibroglandular structure, with holes formed in the final mould. For this reason, a wrapping process was performed manually for each model to ensure that all the small gaps had been completely sealed.

A further study on a patient-specific 3D-printed breast phantom will be conducted with a focus on different percentages of fibroglandular tissue. This can correspond to the four categories of the ACR BI-RADS atlas, thus allowing an estimation of the volumes of fibroglandular tissue. Varying its proportions will allow the quantitative assessments of breast density to be performed.

Conclusions

In this study, a patient-specific 3D-printed breast phantom was successfully constructed using silicone and peanut oils to simulate the MR-related characteristics of breast fibroglandular and adipose tissues. The proposed methodologies can be used as a preliminary work for breast structure simulations and the construction of further patient models using MRI dataset. The phantom can be used to test different breast MR imaging protocols to determine the optimum scanning parameters and analysis algorithms for the quantitative assessment of breast density.

Acknowledgments

We like to thank King Fahd Armed Forces Hospital, Jeddah, Kingdom of Saudi Arabia, Mrs. Aghadeer Bana, Medical Physicist, and Ms. Khulud Al-Amoudi, Radiology Technologist/Patient Experience Western Regional Head for their cooperation in ethical approval and data collection. We deeply acknowledge the support of Dr. Sarah Bukhari, Senior Radiology Resident for her expertise guidance in gathering the required healthy patient's data.

Funding: This project was funded by the Ministry of Defence, Medical Service Division, Kingdom of Saudi Arabia and Saudi Arabian Cultural Mission (SACM), Australia.

Footnote

Conflicts of Interest: All authors have completed the ICMJE uniform disclosure form (available at http://dx.doi.org/10.21037/qims-20-251). ZS serves as an unpaid associate editor of *Quantitative Imaging in Medicine and Surgery*. The

other authors have no other conflicts of interest to declare.

Ethical Statement: Ethical approval was obtained from relevant institutions for use of MR images to generate patient-specific 3D printed model.

References

1. Sardanelli F, Boetes C, Borisch B, Decker T, Federico M, Gilbert FJ, Helbich T, Heywang-Köbrunner SH, Kaiser WA, Kerin MJ, Mansel RE. Magnetic resonance imaging of the breast: recommendations from the EUSOMA working group. Eur J Cancer 2010;46:1296-316.
2. Londero V, Zuiani C, Linda A, Girometti R, Bazzocchi M, Sardanelli F. High-risk breast lesions at imaging-guided needle biopsy: usefulness of MRI for treatment decision. AJR Am J Roentgenol 2012;199:W240-50.
3. Mann RM, Balleyguier C, Baltzer PA, Bick U, Colin C, Cornford E, Evans A, Fallenberg E, Forrai G, Fuchsjäger MH, Gilbert FJ, Helbich TH, Heywang-Köbrunner SH, Camps-Herrero J, Kuhl CK, Martincich L, Pediconi F, Panizza P, Pina LJ, Pijnappel RM, Pinker-Domenig K3, Skaane P, Sardanelli F; European Society of Breast Imaging (EUSOBI), with language review by Europa Donna–The European Breast Cancer Coalition. Breast MRI: EUSOBI recommendations for women's information. Eur Radiol 2015;25:3669-78.
4. Heller SL, Yeong Lin LL, Melsaether AN, Moy L, Gao Y. Hormonal Effects on Breast Density, Fibroglandular Tissue, and Background Parenchymal Enhancement. Radiographics 2018;38:983-96.
5. Chen JH, Chang YC, Chang D, Wang YT, Nie K, Chang RF, Nalcioglu O, Huang CS, Su MY. Reduction of breast density following tamoxifen treatment evaluated by 3-D MRI: preliminary study. Magn Reson Imaging 2011;29:91-8.
6. Wang J, Azziz A, Fan B, Malkov S, Klifa C, Newitt D, Yitta S, Hylton N, Kerlikowske K, Shepherd JA. Agreement of mammographic measures of volumetric breast density to MRI. PLoS One 2013;8:e81653.
7. Tagliafico A, Bignotti B, Tagliafico G, Astengo D, Martino L, Airaldi S, Signori A, Sormani MP, Houssami N, Calabrese M. Breast density assessment using a 3T MRI system: Comparison among different sequences. PLoS One 2014;9:e99027.
8. Lienart V, Carly B, Kang X, Guzy L, Sajovitz AM, Liebens F. Effect of preventive hormonal therapy on breast density: a systematic qualitative review. ScientificWorldJournal 2014;2014:942386.
9. Tagliafico A, Tagliafico G, Astengo D, Airaldi S, Calabrese M, Houssami N. Comparative estimation of percentage breast tissue density for digital mammography, digital breast tomosynthesis, and magnetic resonance imaging. Breast Cancer Res Treat 2013;138:311-7.
10. Nayeem F, Ju H, Brunder DG, Nagamani M, Anderson KE, Khamapirad T, Lu LJ. Similarity of fibroglandular breast tissue content measured from magnetic resonance and mammographic images and by a mathematical algorithm. Int J Breast Cancer 2014;2014:961679.
11. Lin M, Chan S, Chen JH, Chang D, Nie K, Chen ST, Lin CJ, Shih TC, Nalcioglu O, Su MY. A new bias field correction method combining N3 and FCM for improved segmentation of breast density on MRI. Med Phys 2011;38:5-14.
12. Doran SJ, Hipwell JH, Denholm R, Eiben B, Busana M, Hawkes DJ, Leach MO, Silva ID. Breast MRI segmentation for density estimation: Do different methods give the same results and how much do differences matter? Med Phys 2017;44:4573-92.
13. Tagliafico A, Tagliafico G, Tosto S, Chiesa F, Martinoli C, Derchi LE, Calabrese M. Mammographic density estimation: comparison among BI-RADS categories, a semi-automated software and a fully automated one. Breast 2009;18:35-40.
14. Boston RC, Schnall MD, Englander SA, Landis JR, Moate PJ. Estimation of the content of fat and parenchyma in breast tissue using MRI T1 histograms and phantoms. Magn Reson Imaging 2005;23:591-9.
15. Klifa C, Carballido-Gamio J, Wilmes L, Laprie A, Shepherd J, Gibbs J, Fan B, Noworolski S, Hylton N. Magnetic resonance imaging for secondary assessment of breast density in a high-risk cohort. Magn Reson Imaging 2010;28:8-15.
16. Chang DH, Chen JH, Lin M, Bahri S, Yu HJ, Mehta RS, Nie K, Hsiang DJ, Nalcioglu O, Su MY. Comparison of breast density measured on MR images acquired using fat-

suppressed versus non-fat-suppressed sequences. Med Phys 2011;38:5961-68.
17. Choi YJ, Chen JH, Yu HJ, Li Y, Su MY. Impact of Different Analytic Approaches on the Analysis of the Breast Fibroglandular Tissue Using Diffusion Weighted Imaging. Biomed Res Int 2017;2017:1094354.
18. McDonald ES, Schopp JG, Peacock S, DeMartini WB, Rahbar H, Lehman CD, Partridge SC. Diffusion-weighted MRI: association between patient characteristics and apparent diffusion coefficients of normal breast fibroglandular tissue at 3 T. AJR Am J Roentgenol 2014;202:W496-502.
19. Ledger AE, Scurr ED, Hughes J, Macdonald A, Wallace T, Thomas K, Wilson R, Leach MO, Schmidt MA. Comparison of Dixon sequences for estimation of percent breast fibroglandular tissue. PLoS One 2016;11:e0152152.
20. Sindi R, Sá Dos Reis C, Bennett C, Stevenson G, Sun Z. Quantitative Measurements of Breast Density Using Magnetic Resonance Imaging: A Systematic Review and Meta-Analysis. J Clin Med 2019. doi: 10.3390/jcm8050745.
21. Matsumoto JS, Morris JM, Foley TA, Williamson EE, Leng S, McGee KP, Kuhlmann JL, Nesberg LE, Vrtiska TJ. Three-dimensional physical modeling: applications and experience at Mayo Clinic. Radiographics 2015;35:1989-2006.
22. Sun Z, Lau I, Wong YH, Yeong CH. Personalized three-dimensional printed models in congenital heart disease. J Clin Med 2019. doi: 10.3390/jcm8040522.
23. Perica ER, Sun Z. A Systematic Review of Three-Dimensional Printing in Liver Disease. J Digit Imaging 2018;31:692-701.
24. Sun Z, Liu D. A systematic review of clinical value of three-dimensional printing in renal disease. Quant Imaging Med Surg 2018;8:311-25.
25. Carton AK, Bakic P, Ullberg C, Derand H, Maidment AD. Development of a physical 3D anthropomorphic breast phantom. Med Phys 2011;38:891-6.
26. Burfeindt MJ, Colgan TJ, Mays RO, Shea JD, Behdad N, Van Veen BD, Hagness SC. MRI-Derived 3-D-Printed Breast Phantom for Microwave Breast Imaging Validation. IEEE Antennas Wirel Propag Lett 2012;11:1610-3.
27. Dantuma M, van Dommelen R, Manohar S. Semi-anthropomorphic photoacoustic breast phantom. Biomed Opt Express 2019;10:5921-39.
28. He Y, Liu Y, Dyer BA, Boone JM, Liu S, Chen T, Zheng F, Zhu Y, Sun Y, Rong Y, Qiu J. 3D printed breast phantom for multi-purpose and multi-modality imaging. Quant Imaging Med Surg 2019;9:63-74.
29. He Y, Qin S, Dyer BA, Zhang H, Zhao L, Chen T, Zheng F, Sun Y, Shi L, Rong Y, Qiu J. Characterizing mechanical and medical imaging properties of polyvinyl chloride-based tissue-mimicking materials. J Appl Clin Med Phys 2019;20:176-83.
30. Freed M, de Zwart JA, Loud JT, El Khouli RH, Myers KJ, Greene MH, Duyn JH, Badano A. An anthropomorphic phantom for quantitative evaluation of breast MRI. Med Phys 2011;38:743-53.
31. American College of Radiology. ACR BI-RADS® Atlas: Breast Imaging Reporting and Data System. Reston: American College of Radiology, 2013.
32. Mainiero MB, Lourenco A, Mahoney MC, Newell MS, Bailey L, Barke LD, D'Orsi C, Harvey JA, Hayes MK, Huynh PT, Jokich PM, Lee SJ, Lehman CD, Mankoff DA, Nepute JA, Patel SB, Reynolds HE, Sutherland ML, Haffty BG. ACR Appropriateness Criteria Breast Cancer Screening. J Am Coll Radiol 2016;13:R45-9.
33. Gach HM. T1 and T2 and complex permittivities of mineral oil, silicone oil, and glycerol at 0.35, 1.5, and 3 T. Med Phys 2019;46:1785-92.
34. Niebuhr NI, Johnen W, Echner G, Runz A, Bach M, Stoll M, Giske K, Greilich S, Pfaffenberger A. The ADAM-pelvis phantom-an anthropomorphic, deformable and multimodal phantom for MRgRT. Phys Med Biol 2019;64:04NT05.
35. Niebuhr NI, Johnen W, Güldaglar T, Runz A, Echner G, Mann P, Möhler C, Pfaffenberger A, Jäkel O, Greilich S. Radiological properties of tissue surrogates used in a multimodality deformable pelvic phantom for MR-guided radiotherapy. Med Phys 2016;43:908-16.
36. Rakow-Penner R, Daniel B, Yu H, Sawyer-Glover A, Glover GH. Relaxation times of breast tissue at 1.5 T and 3T measured using IDEAL. J Magn Reson Imaging 2006;23:87-91.

Cite this article as: Sindi R, Wong YH, Yeong CH, Sun Z. Development of patient-specific 3D-printed breast phantom using silicone and peanut oils for magnetic resonance imaging. Quant Imaging Med Surg 2020;10(6):1237-1248. doi: 10.21037/qims-20-251

diagnostics

MDPI

Article

Quantitative Measurement of Breast Density Using Personalized 3D-Printed Breast Model for Magnetic Resonance Imaging

Rooa Sindi [1,2], Yin How Wong [3], Chai Hong Yeong [3] and Zhonghua Sun [1,*]

1 Discipline of Medical Radiation Sciences, School of Molecular and Life Sciences, Curtin University, Perth, WA 6845, Australia; rooa.sindi@postgrad.curtin.edu.au
2 Radio-Diagnostic and Medical Imaging Department, Medical Physics Section, King Fahd Armed Forces Hospital, P.O. Box 9862, Jeddah 21159, Saudi Arabia
3 School of Medicine, Faculty of Health and Medical Sciences, Taylor's University, Subang Jaya 47500, Selangor, Malaysia; YinHow.Wong@taylors.edu.my (Y.H.W.); ChaiHong.Yeong@taylors.edu.my (C.H.Y.)
* Correspondence: z.sun@curtin.edu.au; Tel.: +61-8-9266-7509

Received: 8 September 2020; Accepted: 5 October 2020; Published: 6 October 2020

Abstract: Despite the development and implementation of several MRI techniques for breast density assessments, there is no consensus on the optimal protocol in this regard. This study aimed to determine the most appropriate MRI protocols for the quantitative assessment of breast density using a personalized 3D-printed breast model. The breast model was developed using silicone and peanut oils to simulate the MRI related-characteristics of fibroglandular and adipose breast tissues, and then scanned on a 3T MRI system using non-fat-suppressed and fat-suppressed sequences. Breast volume, fibroglandular tissue volume, and percentage of breast density from these imaging sequences were objectively assessed using Analyze 14.0 software. Finally, the repeated-measures analysis of variance (ANOVA) was performed to examine the differences between the quantitative measurements of breast volume, fibroglandular tissue volume, and percentage of breast density with respect to the corresponding sequences. The volume of fibroglandular tissue and the percentage of breast density were significantly higher in the fat-suppressed sequences than in the non-fat-suppressed sequences ($p < 0.05$); however, the difference in breast volume was not statistically significant ($p = 0.529$). Further, a fat-suppressed T2-weighted with turbo inversion recovery magnitude (TIRM) imaging sequence was superior to the non-fat- and fat-suppressed T1- and T2-weighted sequences for the quantitative measurement of breast density due to its ability to represent the exact breast tissue compositions. This study shows that the fat-suppressed sequences tended to be more useful than the non-fat-suppressed sequences for the quantitative measurements of the volume of fibroglandular tissue and the percentage of breast density.

Keywords: MRI; fibroglandular tissue; breast density; 3D-printed model; fat suppression; TIRM

1. Introduction

Breast density, a measure of dense fibroglandular tissue relative to non-dense fatty tissue, has been determined as an independent risk factor for developing breast cancer [1–4]. Previous studies have reported that the potential risk of breast cancer in women with dense breasts is three- to five-fold higher than in women with fatty breasts [5–7]. Recent developments in breast cancer screening have intensified the need for a standardized imaging protocol and/or measurement method for the evaluation of breast density predominantly for women at an elevated risk of developing breast cancer, such as those with high breast density [4,8–10]. A considerable amount of literature has been published

on the assessment of breast density with several methods and algorithms proposed to segment and/or measure breast density using MRI datasets [11–19]. Nevertheless, research has consistently shown that these methods/algorithms seem to have certain drawbacks, mostly due to the use of a semi-automatic approach or a high-level of dependency on user interaction. Likewise, numerous MR breast-imaging protocols have been applied to the screening and/or the assessment of breast density, ranging from contrast- to non-contrast-enhanced imaging with or without the implementation of fat-suppression techniques [3,4,8–10,20–25]. To date, there has been little consensus on the optimal MR breast-imaging protocol and measurement method for breast density screening and/or assessment, especially in the context of women with dense breast tissues.

The dynamic contrast-enhanced (DCE)-MRI technique has been widely used for the screening of women at high risk of breast cancer and has been included in standard clinical breast MRI protocols [4,8]. Despite its long clinical success, DCE-MRI has certain disadvantages, such as long scanning time, high cost, and potential harm caused by the contrast agent [4,26]. Although contradictory findings have been reported in the literature about the precipitation and accumulation of gadolinium contrast-based agents in the brain, there is no general agreement regarding the risk of repeated gadolinium administration [4,27–29]. Nevertheless, questions have been raised about the safety of prolonged use of DCE-MRI as a primary screening method for the detection of breast cancer and/or the assessment of breast density. On the other hand, the fat-suppression technique has been suggested in breast MRI to improve the visibility of pathology, contrast enhancement, and image quality, thus allowing for better differentiation between dense fibroglandular and non-dense fatty tissues [17,30]. It has been combined with other techniques and/or sequence types due to the difficulty of eliminating the high signal intensity associated with fatty tissues [17,30]. Several methods have been proposed for fat suppression in breast MRI, including chemical shift spectral-selective saturation (CHESS) based on the chemical shift variation between fat and water, inversion recovery (IR) based on variation in T1 relaxation time, hybrid CHESS–inversion recovery methods, and Dixon fat–water separation based on phase variation between fat and water signals at different echo times (TEs) [3,17,20,30–32].

Non-fat-suppressed and fat-suppressed T1-weighted images are frequently used with either 2D spin echo (SE) or 3D gradient echo (GRE) in standard clinical breast MRI protocols [8,17]. Nevertheless, there is no consensus as to which of these sequences/techniques is the most efficient in this regard. The American College of Radiology (ACR) has recommended that the fat-suppressed images with high spatial resolution be used in clinical breast MRI protocols as images acquired with this sequence can eliminate misregistration, which mainly occurs when a patient moves during the acquisition of pre- and post-contrast images [8,17]. However, this recommendation contrasts with that of the European Society of Breast Imaging (EUSOBI), which considers non-fat-suppressed sequences based on the acquisition of subtraction images more useful [17,33]. Despite this, there seems to be some consensus that other breast MRI techniques, including T2-weighted images, DCE, and diffusion-weighted imaging (DWI), tend to benefit from its combination with fat-suppression techniques for several reasons [1,8,17,30]. For instance, turbo inversion recovery magnitude (TIRM), a type of inversion recovery sequence with the advantage of short image acquisition time, has been widely used in the delineation of tumor and/or lymphatic spread and could possibly be combined with fat-suppression technique for the assessment of breast density [4,34]. Patient-specific 3D-printed breast models, derived from a patient's MR imaging data and comparable to the anatomical structures of human tissues, can be a valuable tool for examining different breast MRI protocols, testing the radio frequency coils, and evaluating system performance [35–42]. The aim of this study is to determine the most appropriate MR breast-imaging protocols for the quantitative assessment of breast density using a personalized 3D-printed breast model based on an objective comparison between the non-fat-suppressed and fat-suppressed sequences. We hypothesize that fat-suppressed sequences allow for more accurate assessment of breast density while TIRM with fat-suppressed sequence further enhances its accuracy in quantitative assessment of breast density.

2. Materials and Methods

2.1. Study Subject: A Personalized 3D-Printed Breast Model

A personalized 3D-printed breast model which was developed in our previous study [43] used 3D-printing techniques and tissue-mimicking materials (TMMs) with the intention of simulating the MR-related characteristics of fibroglandular and adipose breast tissues for the quantitative assessment of breast density. The model consisted of two main parts: an outer shell to simulate the breast outline, and an inner shell filled with silicone and peanut oils to mimic the internal breast compositions. The results showed that the silicone and peanut oils successfully resemble the MR-imaging characteristics and T1 relaxation times of fibroglandular and adipose breast tissues, respectively [43]. This combination of findings further supports the hypothesis that such a model could be used to examine different MR breast-imaging protocols in order to determine the optimum for the quantitative assessment of breast density. Figure 1 demonstrates the schematic flowchart of the construction process for developing a personalized 3D-printed breast model.

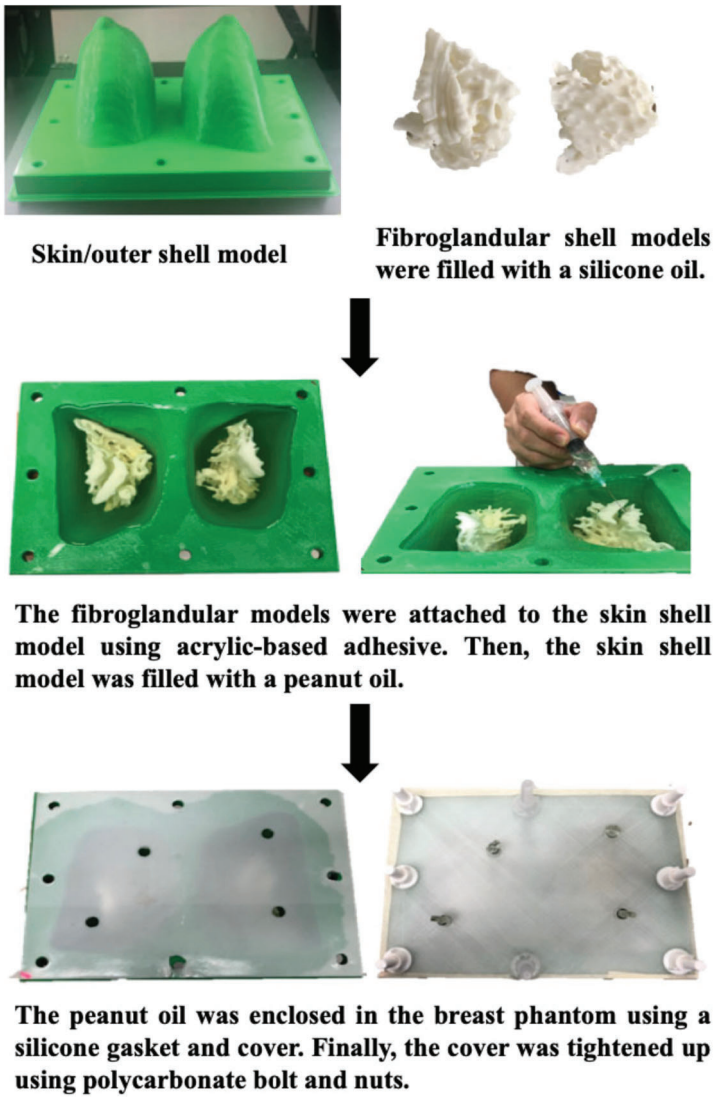

Figure 1. Flow chart demonstrates the construction process of the personalized 3D-printed breast model for MRI. Reprinted with permission under open access from Sindi et al. [43].

2.2. MR Scanning Protocol

The 3D-printed breast model was scanned on a 3T MRI system (MAGNETOM Prisma, Siemens Healthcare, Erlangen, Germany) in a prone position using a dedicated 18-channel breast coil. Different MR imaging sequences were applied to improve the visibility of structure and contrast enhancement, thus allowing for better differentiation between fatty non-glandular and glandular structures. Table 1 displays the image acquisition parameters of the six MR imaging sequences used in this study.

2.3. Quantitative Measurement: Breast Volume, Fibroglandular Tissue Volume, and Percentage of Breast Density

Breast volume and fibroglandular tissue volume were objectively measured with a semi-automated segmentation method using a commercially available biomedical imaging software, Analyze V 14.0 (AnalyzeDirect, Inc., Lexana, KS, USA). Two steps were performed to measure the percentage of breast density from MRI data: breast segmentation and fibroglandular tissue segmentation. The purpose of breast segmentation is to separate the breast's body from the surrounding structure and/or background, while fibroglandular tissue segmentation separates the glandular from the fatty tissue.

To differentiate the breast's body from the background, the breast's boundary was first delineated semi-automatically using an interactive tool based on the threshold signal intensity function by setting seed points on a series of 2D axial slices comprising the entire breast volume. The minimum and maximum threshold limits were then adjusted to define the region of interest. The software spontaneously interpolated between these slices and generated a mask of the whole breast volume. Once the breast's body was segmented out, an automated method incorporating several morphological processing operations and spatial filters were used to segment out the fibroglandular tissue from the surrounding fatty tissue. Upon completion of this segmentation process, the breast volume and fibroglandular tissue volume were measured using a 3D-measurement tool based on the size intensity function. The percentage of breast density was then computed as the ratio of the fibroglandular tissue volume relative to the total breast volume. Finally, the results were analyzed to assess the differences between the measurement of breast volume, fibroglandular tissue volume, and percentage of breast density based on the different MRI sequences.

2.4. Data Synthesis

The acquisition of the different MRI sequences and the implementation of several fat-suppression techniques, as applied in the proposed study, are considered to be technically heterogeneous. To address this complexity and provide more objective comparisons, the six MRI sequence compartments were re-configured into a two-way cross-classification, namely two fat-suppression categories: non-fat-suppression MRI sequences (i.e., MR Seq. 1, 2, and 3) and fat-suppression MRI sequences (i.e., MR Seq. 4, 5, and 6). For the purpose of the analysis, the segmentation processes of both the breast volume and the fibroglandular tissue volume were performed three times, thus extracting three segments from each MRI sequence. Subsequently, the measurements were conducted three times with respect to the volume of the breast, the volume of the fibroglandular tissue, and, thereby, the percentage of the breast density.

Table 1. Image acquisition parameters of the MR breast-imaging sequences using a personalized 3D-printed breast model.

No.	MRI Sequence	Acquisition Type	Orientation, Slice No.	TR (ms)	TE (ms)	TI (ms)	FOV (mm)	Matrix Size	Slice Thickness (mm)	Flip Angle (°)	NSA	Scan Time (min)
1.	Non-fat-suppressed TSE (T2W)	2D	Axial, 33	6080	78		350 × 350	336 × 448	4.0	80	1	1.10
2.	Non-fat-suppressed TSE (T1W)	2D	Axial, 37	709	10		350 × 350	224 × 320	2.9	130	2	2.38
3.	Non-fat-suppressed TSE SPACE (T1W)	3D	Axial, 88	600	3.4		400 × 400	256 × 256	1.6	120	2	2.47
4.	Fat-suppressed TSE SPACE (T1W)	3D	Axial, 88	1500	3.4		400 × 400	256 ×2 56	1.6	120	1	4.58
5.	Fat-suppressed TSE SPACE SPAIR (T1W)	3D	Axial, 88	1500	3.4		400 × 400	256 × 256	1.6	120	1	4.58
6.	Fat-suppressed IR/PFP TIRM (T2W)	2D	Axial, 37	4120	70	230	340 × 340	358 × 448	3.0	80	2	1.51

Abbreviations—TR: repetition time; TE: echo time; TI: inversion time; FOV: field-of-view; NSA: number of signal averages/excitations; 2D: two-dimensional; 3D: three-dimensional; TSE: turbo (fast) spin-echo; T1W: T1-weighted; T2W: T2-weighted; SPACE: sampling perfection with application optimized contrasts using different flip angle evolution; SPAIR: spectral attenuation inversion recovery; IR: inversion recovery; PFP: partial Fourier phase; TIRM: turbo inversion recovery magnitude.

2.5. Statistical Analysis

Statistical analyses were conducted using NCSS V 19.0.5 (NCSS, LLC., Kaysville, UT, USA). The repeated-measures analysis of variance (ANOVA) was performed to examine the difference between the quantitative measurements of breast volume, fibroglandular tissue volume, and percentage of breast density with regard to the non-fat-suppressed and fat-suppressed MRI sequences. This variance model was employed to account for the variation both between sequences (i.e., between subjects) and within repeated measurements (i.e., within subjects). Significance levels were set at the 5% level. Descriptive data and box plots were also produced for all variables, demonstrating the distribution and median of breast volume, fibroglandular tissue volume, and percentage of breast density measured in the non-fat-suppressed and fat-suppressed imaging groups.

3. Results

3.1. Scanning of the Personalized 3D-Printed Breast Model

Figure 2 shows the MR images of the personalized 3D-printed breast model using silicone and peanut oils as surrogates for fibroglandular and fatty breast tissues, respectively, for the various scanning sequences. These oils produced a reasonable level of contrast and MR-related characteristics amongst the T1- and T2-weighted images with and without the implementation of the fat-suppression techniques. Although the most noticeable feature of the personalized 3D-printed breast model was that it was somewhat inhomogeneous, this feature nevertheless mimics the substantial inhomogeneity sometimes encountered in patients' irregular distributions.

The suppression of fat signals in the T1-weighted images with both SPACE and SPAIR acquisitions did not substantially increase the contrast enhancement or visualization between the dense fibroglandular and non-dense fatty structures (Figure 2D,E). A possible explanation for this could be that these types of acquisitions are highly affected by inhomogeneity in the magnetic field, demonstrating inhomogeneous fat suppression in the fatty structures. On the contrary, Figure 2F shows that the fat-suppressed T2-weighted image with TIRM acquisition demonstrated a homogenous high signal intensity in the fibroglandular structure and a low signal intensity in the fatty structure for both the right and left breasts. The suppression of fat signals significantly improved the contrast between the fibroglandular and fatty structures, further enhanced visualization, and provided more anatomical information which may assist in the segmentation and/or quantification of breast density.

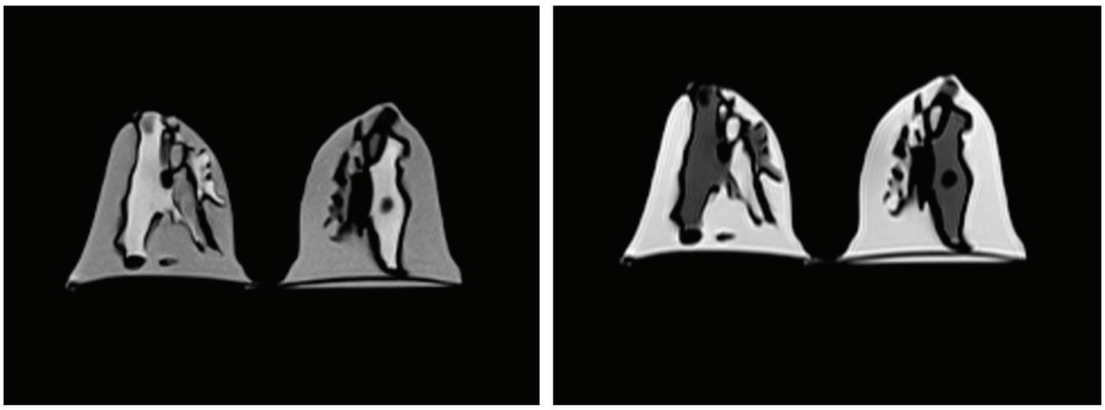

(**A**) (**B**)

Figure 2. *Cont.*

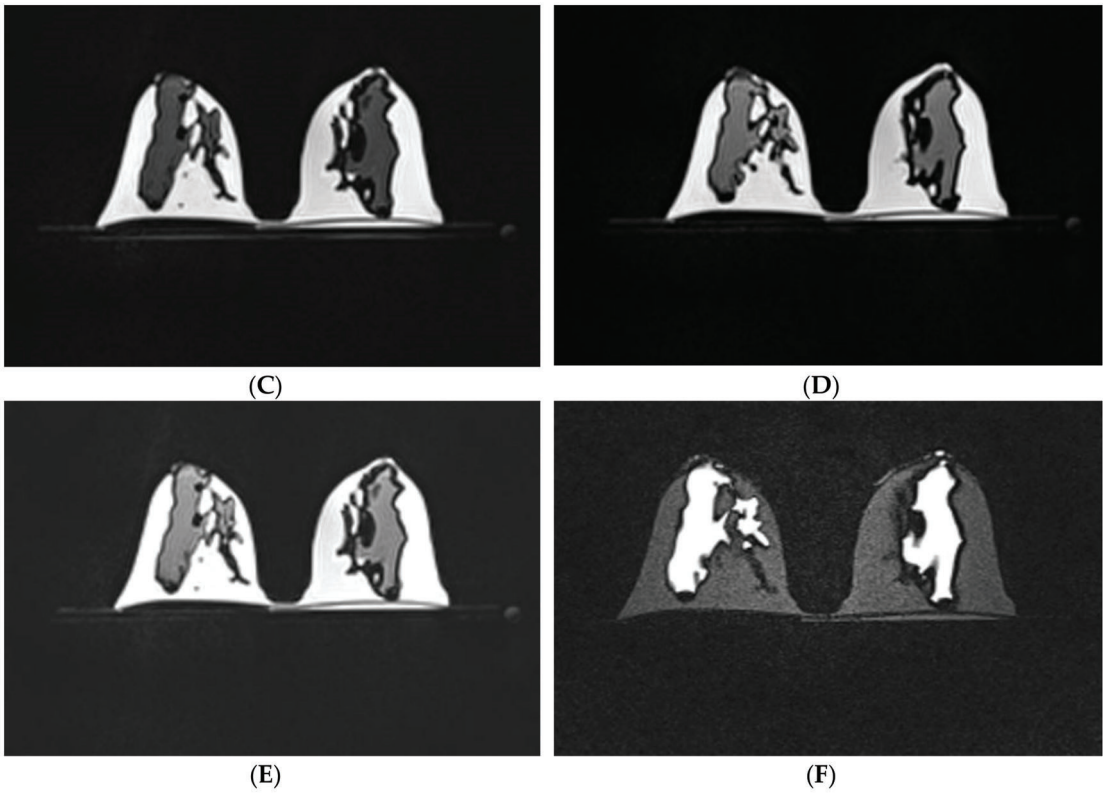

Figure 2. Central axial slice of a personalized 3D-printed breast model for the different MR imaging pulse sequences. (**A**) Non-fat-suppressed TSE (T2W); (**B**) Non-fat-suppressed TSE (T1W); (**C**) Non-fat-suppressed TSE SPACE (T1W); (**D**) Fat-suppressed TSE SPACE (T1W); (**E**) Fat-suppressed TSE SPACE SPAIR (T1W); (**F**) Fat-suppressed IR/PFP TIRM (T2W). For pulse sequences, refer to Table 1.

3.2. Quantitative Measurement of Breast Volume, Fibroglandular Tissue Volume, and Percentage of Breast Density

Table 2 displays the quantitative measurements (mean and standard deviations) of the breast volume, fibroglandular tissue volume, and percentage of breast density for the different MRI sequences. For the SPACE T1-weighted images (i.e., MR Seq. 3 and 4), there was evidence of a difference in breast density between the non-fat-suppressed sequence (7.719 ± 0.366%) and the fat-suppressed sequence (11.698 ± 0.351%). This difference can be explained by the direct relationship between fibroglandular tissue volume and breast density, as shown in Table 2, the volume of fibroglandular tissue measured in the fat-suppressed sequence (i.e., MR Seq. 4) was higher than that in the non-fat-suppressed sequence (i.e., MR Seq. 3): 53.940 ± 1.083 cm^3 and 34.261 ± 1.809 cm^3, respectively.

For the breast density assessment, there was a substantial difference between the non-fat-suppressed sequence (5.401 ± 0.165%) and the fat-suppressed sequence (9.498 ± 0.930%) measured in the T2-weighted images, MR Seq. 1 and MR Seq. 6, respectively. This difference might explain the relatively good improvement in the contrast between the fibroglandular and fatty structures (Figure 2F) owing to the implementation of the fat-suppression technique, which had a major effect on the segmentation process and, therefore, the measurement of breast density.

By contrast, the means of the breast density for the non-fat suppressed (i.e., MR Seq. 2) and the fat-suppressed (i.e., MR Seq. 5) were 7.733 ± 0.365% and 10.467 ± 0.084%, respectively. A comparison of MR Seq. 2 and MR Seq. 5 revealed that the breast volume, fibroglandular tissue volume, and percentage of breast density measured in the fat-suppressed sequence tended to be higher than that measured in the non-fat-suppressed sequence (Table 2).

Table 2. Results of the estimated mean and standard deviation of breast volume, fibroglandular tissue volume, and percentage of breast density for the different MRI sequences using a personalized 3D-printed breast model.

MRI Sequence *	Breast Volume (cm^3)		Fibroglandular Tissue Volume (cm^3)		Breast Density (%)	
	Mean	SD	Mean	SD	Mean	SD
Non-fat-suppression group (MR Sequences 1, 2, and 3)						
MR Seq. 1 (N = 3)	592.291	5.065	31.984	0.735	5.401	0.165
MR Seq. 2 (N = 3)	388.793	4.159	30.067	1.159	7.733	0.365
MR Seq. 3 (N = 3)	443.884	11.913	34.261	1.809	7.719	0.366
Combined (N = 9)	474.989	91.406	32.104	2.144	6.952	1.194
Fat-suppression group (MR Sequences 4, 5, and 6)						
MR Seq. 4 (N = 3)	461.188	4.699	53.940	1.083	11.698	0.351
MR Seq. 5 (N = 3)	462.948	11.882	48.456	1.140	10.467	0.084
MR Seq. 6 (N = 3)	715.784	32.097	67.794	3.623	9.498	0.930
Combined (N = 9)	546.640	128.031	56.730	8.854	10.555	1.077

* For pulse sequences, refer to Table 1.

3.3. Comparison of Measurements Between Non-Fat-Suppression and Fat-Suppression Groups

Table 3 demonstrates the results (mean, standard error, F-ratio, and P-value) of the repeated-measures ANOVA of breast volume, fibroglandular tissue volume, and percentage of breast density with respect to the non-fat-suppression and fat-suppression groups. The box plots of these parameters for the two groups are shown in Figure 3.

Table 3. Results of the repeated-measures ANOVA, including total mean, standard error (SE), F-ratio, probability level (Prob level) of breast volume, fibroglandular tissue volume, and percentage of breast density between two imaging groups: non-fat-suppressed and fat-suppressed MRI pulse sequences.

Breast Density Parameter	Non-Fat-Suppressed (N = 9)		Fat-Suppressed (N = 9)		F-Ratio	Prob Level **
	Mean	SE (4 df *)	Mean	SE (4 df *)		
Breast volume (cm^3)	474.989	73.639	546.640	73.639	0.47	0.5293
Fibroglandular tissue volume (cm^3)	32.104	4.158	56.730	4.158	17.54	0.0138
Breast density (%)	6.952	0.709	10.555	0.709	12.90	0.0229

* The degrees of freedom; ** The significance level of the F-ratio (the probability that the difference between data is significant or not). The significant difference between the quantitative measurements of breast volume, fibroglandular volume, and percentage of breast density based on the non-fat suppressed and the fat-suppressed MRI sequences was determined at the 5% level.

For breast volume, although the mean measured from the non-fat-suppression group (474.989 cm^3) tended to be lower than that from the fat-suppression group (546.640 cm^3), the difference was not statistically significant (p = 0.5293), with an F-ratio of 0.47 and a standard error for both means of 73.639. However, for the fibroglandular tissue volume and the percentage of breast density, the repeated-measures ANOVA showed that the difference between the non-fat-suppression group and the fat-suppression group was statistically significant at the 5% level. The values measured from the non-fat-suppression group were lower than those from the fat-suppression group, as shown in Table 2; Table 3. The mean volume of fibroglandular tissue was 32.104 cm^3 for the non-fat-suppression group and 56.730 cm^3 for the fat-suppression group, which was statistically significant (F = 17.54; p = 0.0138), with a standard error of 4.158. Likewise, there was a significant difference (F = 12.90; p = 0.0229) between the two groups: the mean breast density measured in the non-fat-suppression

group (6.952%) tended to be lower than that of the fat-suppression group (10.555%), with a standard error for both means of 0.709.

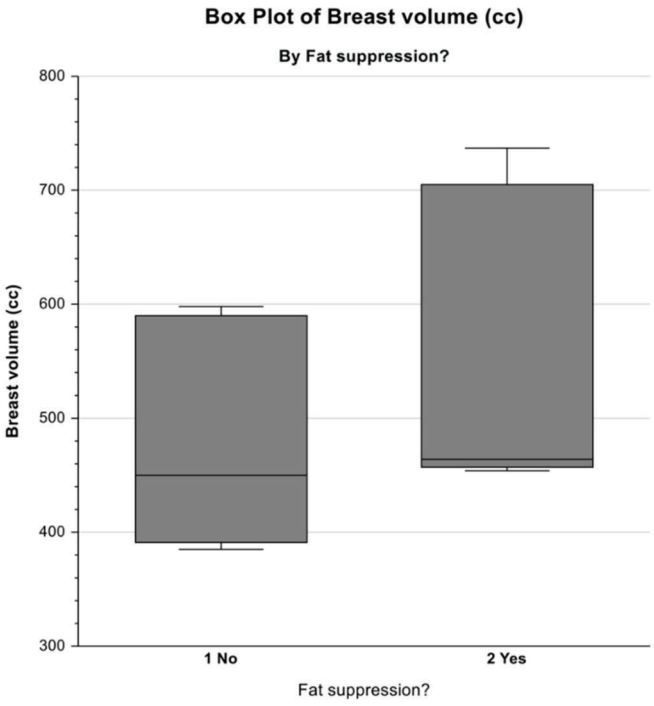

(**A**)

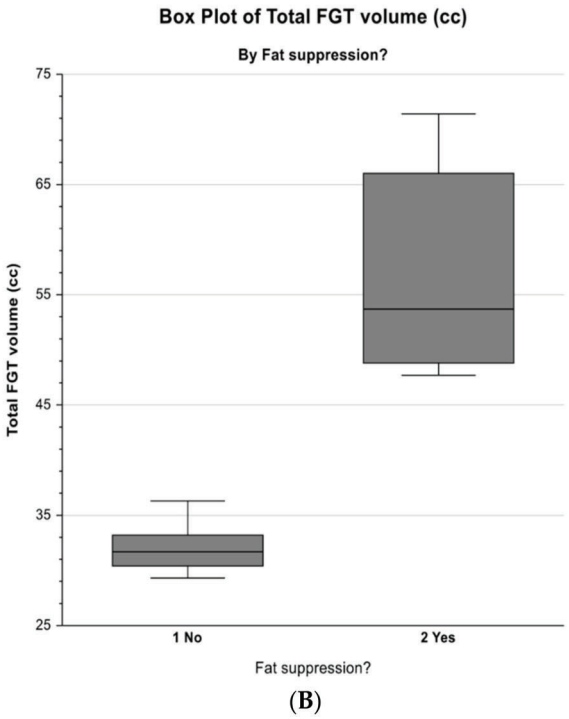

(**B**)

Figure 3. *Cont*.

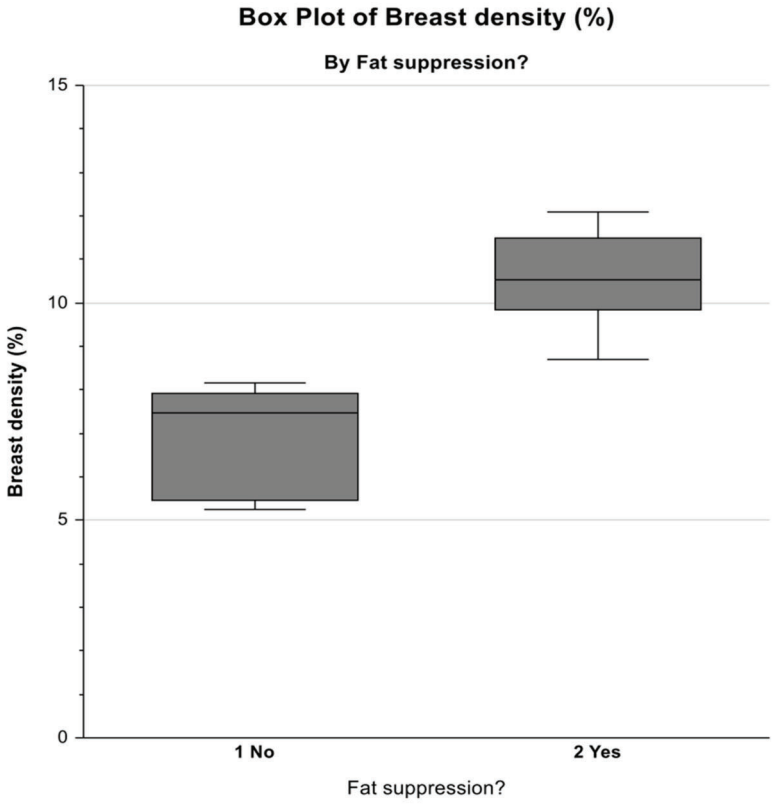

Figure 3. Box plots demonstrate the distribution and median of three main parameters: (**A**) breast volume, (**B**) fibroglandular tissue volume, and (**C**) percentage of breast density measured on the non-fat-suppressed and the fat-suppressed MRI sequences. The six MRI sequences compartments were re-configured into a two-way cross-classification, namely two fat-suppression categories. As shown, "1/No" is the non-fat-suppression, "2/Yes" is the fat-suppression, which are on the *x*-axis, while the three parameters measured with respect to these two corresponding categories are on the *y*-axis.

4. Discussion

Recently, for women with an elevated risk of developing breast cancer, such as those with high breast density, the importance of establishing a standardized MRI protocol and/or measurement method for the assessment of breast density has increased in clinical and research domains. Although fat-suppressed and non-fat-suppressed sequences have frequently been included for both T1- and T2-weighted images in clinical breast MRI protocol, there is no agreement on which of these sequences should be used in this regard [1,8,17,30]. The current study was designed to determine the most appropriate MRI sequence for the quantitative assessment of breast density using a personalized 3D-printed breast model [43] based on an objective comparison between fat-suppressed and non-fat-suppressed sequences. Six MRI sequences were acquired and categorized into fat-suppression and non-fat-suppression categories to examine the difference between the quantitative measurements of breast volume, fibroglandular tissue volume, and percentage of breast density between these two imaging groups.

Comparing the two fat-suppression groups, the repeated-measures ANOVA showed that the differences between the non-fat-suppressed and fat-suppressed MRI sequences (i.e., MR Seq. 1, 2, and 3 and MR Seq. 4, 5, and 6) were statistically significant at the 5% level for both fibroglandular tissue volume and percentage of breast density. On the contrary, the observed difference between these corresponding sequences was not statistically significant with respect to breast volume. The current findings seem to be consistent with other research documenting that the assessment of breast density is considered

to fluctuate with MRI sequences and with the application of fat-suppression techniques [3,16,17]. A comparison of our results with Chang et al. [17], who suggested that breast volumes measured in T1-weighted sequences with and without fat suppression were almost identical for a similar case, is encouraging. Although their results differed from the current study, given that the breast density parameters were analyzed only on the T1-weighted sequences, they are still consistent with our findings, which showed that there was no evidence of a difference in the breast volumes between the non-fat-suppression and the fat-suppression groups (Table 3). A possible explanation for this could be that the measurement of breast volumes based on these two groups was not considerably influenced by the applied imaging techniques and/or segmentation method. Despite the breast volumes measured from the T2-weighted sequences with and without fat suppression being higher than those of the T1-weighted sequences, the difference between the two imaging groups was not significant. This can be attributed to the matrix sizes of the T2-weighted images used with the non-fat-suppressed and fat-suppressed sequences (i.e., MR Seq. 1 and 6), which were 336 × 448 and 358 × 448, respectively.

However, there was a statistically significant difference between fibroglandular tissue volume and percentage of breast density, indicating higher values in the fat-suppressed sequences (MR Seq. 4, 5, and 6) compared to the non-fat-suppressed sequences (MR Seq. 1, 2, and 3), as shown in Tables 2 and 3. This difference can be explained in part by the relatively good contrast enhancement and/or visualization observed between the fibroglandular and the fatty structures resulting from the suppression of fat signals, as was evident in the TIRM with fat-suppressed T2-weighted image (Figure 2F). Although the signal-to-noise ratio and tissue contrast in the non-fat-suppressed images were higher than those in the fat-suppressed images, the results for the fat-suppression group were significantly higher than those for the non-fat-suppression group. Nevertheless, the scanning times for the fat-suppressed sequences were longer than those for the non-fat-suppressed sequences, except for the TIRM, which was 1 min 51 s. As shown in Table 2, breast volume, fibroglandular tissue volume, and percentage of breast density analyzed with TIRM were considerably higher than those of the T1- and T2-weighted sequences with and without fat suppression. Compared to these sequences, the observed increase in breast density parameters from the T2-weighted and TIRM acquisition was probably due to their individual characteristics: the T2-weighted image with fat-suppression technique is known to improve fluid intensity visualization, while TIRM is known to provide more anatomical information [4,44]. Similar findings were obtained by Bu et al. [4], who suggested that the combined DWI and TIRM could be used as an alternative imaging protocol for the screening of women with dense breast tissue. Despite being preliminary findings, our study indicates that TIRM could be incorporated with fat-suppression techniques for the assessment of breast density. Therefore, the fat-suppressed T2-weighted image with TIRM acquisition can be a promising technique for the quantitative assessment of breast density, although further research should be conducted to verify this suggestion.

Overall, the observed differences in breast density measurements between the fat-suppression and non-fat-suppression groups can be attributed to several factors: the segmentation method, image quality, scanning/technical parameters, and tissue contrast achieved by using different MRI pulse sequences. There are, however, other possible reasons; the applied fat-suppression techniques are more susceptible to magnetic field inhomogeneity, especially in the case of the 3T MRI system, where the field heterogeneity can be more protuberant. As shown in Figure 2, the high levels of inhomogeneity in both the fat-suppressed and non-fat-suppressed images might be the major factor—if not the only factor—that can cause such a variation in the segmentation and/or quantification of breast density parameters.

Although this study suggests that the fat-suppressed sequences are more useful than the non-fat-suppressed sequences for the segmentation/measurement of fibroglandular tissue volume and breast density, it is subject to several limitations. First, the assessment of breast density parameters was carried out on a developed 3D-printed breast model using silicone and peanut oils as tissue-equivalent materials and may not reflect the exact distribution of both fibroglandular and fatty structures as seen in human breast tissues. This limitation could be addressed by further research with the use of

more realistic breast models for MRI scanning. Second, the high levels of inhomogeneity in both the fat-suppressed and non-fat-suppressed images could have influenced the segmentation and breast density measurements. This is unavoidable due to the complexity of the MRI scanning sequences. Third, the breast density parameters were segmented and measured using a semi-automated method, which implies that the prospective source of variation between such measurements could be due to a high level of dependency on user interaction. For this reason, multiple segmentations/measurements of the breast density parameters were consistently conducted by the same observer to minimize potential intra-observer variations. However, the applicability of the proposed segmentation and measurement method is relatively high as an interactive 3D tool and would be more useful in the long-term assessment of breast density. Finally, with the implementation of different imaging techniques, acquisition types, and fat-suppression methods, caution must be applied as the findings might not be transferable to clinical practice without further investigation.

For future research, a greater focus on the TIRM with a fat-suppression technique could produce interesting findings on the quantification of breast density, especially for women at high risk of developing breast cancer. Quantitative assessment of breast density parameters in participants' clinical breast MRI datasets, could also be used to investigate and validate this observation.

5. Conclusions

A significant difference was found between the non-fat-suppression and fat-suppression MRI sequences for the quantitative measurements of the volume of fibroglandular tissue and the percentage of breast density. In general, the findings suggest that fat-suppressed sequences are an efficient scanning technique that reflects the exact composition of breast tissues. TIRM with fat-suppressed T2-weighted sequence can be a promising imaging protocol for the segmentation and/or quantification of breast density. Further research is required to verify these findings so that the optimal breast MRI protocols can be developed for clinical application.

Author Contributions: Research conceptualization and methodology: R.S. and Z.S.; data acquisition and analysis: R.S., Y.H.W., C.H.Y.; project administration: Z.S. All authors have read and agreed to the published version of the manuscript.

Funding: This project was funded by the Ministry of Defence, Medical Service Division, Kingdom of Saudi Arabia and Saudi Arabian Cultural Mission (SACM), Australia.

Acknowledgments: We deeply acknowledge the support of Gil Stevenson for his cooperation and assistance in statistical analysis and results interpretation.

Conflicts of Interest: The authors declare no conflict of interest.

References

1. Chen, J.H.; Chang, Y.C.; Chang, D.; Wang, Y.T.; Nie, K.; Chang, R.F.; Nalcioglu, O.; Huang, C.S.; Su, M.Y. Reduction of breast density following tamoxifen treatment evaluated by 3-D MRI: Preliminary study. *Magn. Reson. Imaging* **2011**, *29*, 91–98. [CrossRef] [PubMed]
2. Wang, J.; Azziz, A.; Fan, B.; Malkov, S.; Klifa, C.; Newitt, D.; Yitta, S.; Hylton, N.; Kerlikowske, K.; Shepherd, J.A. Agreement of mammographic measures of volumetric breast density to MRI. *PLoS ONE* **2013**, *8*, e81653. [CrossRef]
3. Tagliafico, A.; Bignotti, B.; Tagliafico, G.; Astengo, D.; Martino, L.; Airaldi, S.; Signori, A.; Sormani, M.P.; Houssami, N.; Calabrese, M. Breast density assessment using a 3T MRI system: Comparison among different sequences. *PLoS ONE* **2014**, *9*, e99027. [CrossRef]
4. Bu, Y.; Xia, J.; Joseph, B.; Zhao, X.; Xu, M.; Yu, Y.; Qi, S.; Shah, K.A.; Wang, S.; Hu, J. Non-contrast MRI for breast screening: Preliminary study on detectability of benign and malignant lesions in women with dense breasts. *Breast Cancer Res. Treat.* **2019**, *177*, 629–639. [CrossRef]
5. Nelson, H.D.; Zakher, B.; Cantor, A.; Fu, R.; Griffin, J.; O'Meara, E.S.; Buist, D.S.; Kerlikowske, K.; Van Ravesteyn, N.T.; Trentham-Dietz, A.; et al. Risk factors for breast cancer for women aged 40 to 49 years: A systematic review and meta-analysis. *Ann. Intern. Med.* **2012**, *156*, 635–648. [CrossRef] [PubMed]

6. McCormack, V.A.; Dos Santos Silva, I. Breast density and parenchymal patterns as markers of breast cancer risk: A meta-analysis. *Cancer Epidem. Biomar.* **2006**, *15*, 1159–1169. [CrossRef] [PubMed]
7. Kerlikowske, K.; Ichikawa, L.; Miglioretti, D.L.; Buist, D.S.; Vacek, P.M.; Smith-Bindman, R.; Yankaskas, B.; Carney, P.A.; Ballard-Barbash, R. Longitudinal measurement of clinical mammographic breast density to improve estimation of breast cancer risk. *J. Natl. Cancer Inst.* **2007**, *99*, 386–395. [CrossRef]
8. Sindi, R.; Sá dos Reis, C.; Bennett, C.; Stevenson, G.; Sun, Z. Quantitative measurements of breast density using magnetic resonance imaging: A systematic review and meta-analysis. *J. Clin. Med.* **2019**, *8*, 745. [CrossRef]
9. Sindi, R.; Sun, Z. Optimal protocols for quantitative assessment of breast density using magnetic resonance imaging. *Australas. Med. J.* **2019**, *12*, 186–188. [CrossRef]
10. Warner, E.; Messersmith, H.; Causer, P.; Eisen, A.; Shumak, R.; Plewes, D. Systematic review: Using magnetic resonance imaging to screen women at high risk for breast cancer. *Ann. Intern. Med.* **2008**, *148*, 671–679. [CrossRef]
11. Nayeem, F.; Ju, H.; Brunder, D.G.; Nagamani, M.; Anderson, K.E.; Khamapirad, T.; Lu, L.J. Similarity of fibroglandular breast tissue content measured from magnetic resonance and mammographic images and by a mathematical algorithm. *Int. J. Breast. Cancer* **2014**, *2014*, 961679. [CrossRef] [PubMed]
12. Lin, M.; Chan, S.; Chen, J.H.; Chang, D.; Nie, K.; Chen, S.T.; Lin, C.J.; Shih, T.C.; Nalcioglu, O.; Su, M.Y. A new bias field correction method combining N3 and FCM for improved segmentation of breast density on MRI. *Med. Phys.* **2011**, *38*, 5–14. [CrossRef] [PubMed]
13. Doran, S.J.; Hipwell, J.H.; Denholm, R.; Eiben, B.; Busana, M.; Hawkes, D.J.; Leach, M.O.; Silva, I.D. Breast MRI segmentation for density estimation: Do different methods give the same results and how much do differences matter? *Med. Phys.* **2017**, *44*, 4573–4592. [CrossRef] [PubMed]
14. Tagliafico, A.; Tagliafico, G.; Tosto, S.; Chiesa, F.; Martinoli, C.; Derchi, L.E.; Calabrese, M. Mammographic density estimation: Comparison among BI-RADS categories, a semi-automated software and a fully automated one. *Breast* **2009**, *18*, 35–40. [CrossRef]
15. Boston, R.C.; Schnall, M.D.; Englander, S.A.; Landis, J.R.; Moate, P.J. Estimation of the content of fat and parenchyma in breast tissue using MRI T1 histograms and phantoms. *Magn. Reson. Imaging* **2005**, *23*, 591–599. [CrossRef]
16. Lu, L.J.; Nishino, T.K.; Johnson, R.F.; Nayeem, F.; Brunder, D.G.; Ju, H.; Leonard, M.H., Jr.; Grady, J.J.; Khamapirad, T. Comparison of breast tissue measurements using magnetic resonance imaging, digital mammography and a mathematical algorithm. *Phys. Med. Biol.* **2012**, *57*, 6903–6927. [CrossRef]
17. Chang, D.H.; Chen, J.H.; Lin, M.; Bahri, S.; Hon, J.Y.; Mehta, R.S.; Nie, K.; Hsiang, D.J.; Nalcioglu, O.; Su, M.Y. Comparison of breast density measured on MR images acquired using fat-suppressed versus nonfat-suppressed sequences. *Med. Phys.* **2011**, *38*, 5961–5968. [CrossRef]
18. Nie, K.; Chang, D.; Chen, J.H.; Hsu, C.C.; Nalcioglu, O.; Su, M.Y. Quantitative analysis of breast parenchymal patterns using 3D fibroglandular tissues segmented based on MRI. *Med. Phys.* **2010**, *37*, 217–226. [CrossRef]
19. Pertuz, S.; McDonald, E.S.; Weinstein, S.P.; Conant, E.F.; Kontos, D. Fully automated quantitative estimation of volumetric breast density from digital breast tomosynthesis images: Preliminary results and comparison with digital mammography and MR imaging. *Radiology* **2016**, *279*, 65–74. [CrossRef]
20. Ledger, A.E.; Scurr, E.D.; Hughes, J.; Macdonald, A.; Wallace, T.; Thomas, K.; Wilson, R.; Leach, M.O.; Schmidt, M.A. Comparison of Dixon sequences for estimation of percent breast fibroglandular tissue. *PLoS ONE* **2016**, *11*, e0152152. [CrossRef]
21. Miyazaki, M.; Wheaton, A.; Kitane, S. Enhanced fat suppression technique for breast imaging. *J. Magn. Reson. Imaging* **2013**, *38*, 981–986. [CrossRef] [PubMed]
22. Kalovidouri, A.; Firmenich, N.; Delattre, B.M.; Picarra, M.; Becker, C.D.; Montet, X.; Botsikas, D. Fat suppression techniques for breast MRI: Dixon versus spectral fat saturation for 3D T1-weighted at 3 T. *Radiol. Med.* **2017**, *122*, 731–742. [CrossRef] [PubMed]
23. Le-Petross, H.; Kundra, V.; Szklaruk, J.; Wei, W.; Hortobagyi, G.N.; Ma, J. Fast three-dimensional dual echo Dixon technique improves fat suppression in breast MRI. *J. Magn. Reson. Imaging* **2010**, *31*, 889–894. [CrossRef] [PubMed]
24. Dogan, B.E.; Ma, J.; Hwang, K.; Liu, P.; Yang, W.T. T1-weighted 3D dynamic contrast-enhanced MRI of the breast using a dual-echo Dixon technique at 3 T. J. *Magn. Reson. Imaging* **2011**, *34*, 842–851. [CrossRef]

25. Clauser, P.; Pinker, K.; Helbich, T.H.; Kapetas, P.; Bernathova, M.; Baltzer, P.A. Fat saturation in dynamic breast MRI at 3 Tesla: Is the Dixon technique superior to spectral fat saturation? A visual grading characteristics study. *Eur. Radiol.* **2014**, *24*, 2213–2219. [CrossRef]
26. An, Y.Y.; Kim, S.H.; Kang, B.J. Differentiation of malignant and benign breast lesions: Added value of the qualitative analysis of breast lesions on diffusion-weighted imaging (DWI) using readout-segmented echo-planar imaging at 3.0 T. *PLoS ONE* **2017**, *12*, e0174681. [CrossRef]
27. Beckett, K.R.; Moriarity, A.K.; Langer, J.M. Safe use of contrast media: What the radiologist needs to know. *Radiographics* **2015**, *35*, 1738–1750. [CrossRef]
28. Kanda, T.; Fukusato, T.; Matsuda, M.; Toyoda, K.; Oba, H.; Kotoku, J.I.; Haruyama, T.; Kitajima, K.; Furui, S. Gadolinium-based contrast agent accumulates in the brain even in subjects without severe renal dysfunction: Evaluation of autopsy brain specimens with inductively coupled plasma mass spectroscopy. *Radiology* **2015**, *276*, 228–232. [CrossRef]
29. Ramalho, M.; Ramalho, J.; Burke, L.M.; Semelka, R.C. Gadolinium retention and toxicity—An update. *Adv. Chronic Kidney Dis.* **2017**, *24*, 138–146. [CrossRef]
30. Del Grande, F.; Santini, F.; Herzka, D.A.; Aro, M.R.; Dean, C.W.; Gold, G.E.; Carrino, J.A. Fat-suppression techniques for 3-T MR imaging of the musculoskeletal system. *Radiographics* **2014**, *34*, 217–233. [CrossRef]
31. McRobbie, D.W.; Moore, E.A.; Graves, M.J.; Prince, M.R. *MRI from Picture to Proton*; Cambridge University Press: Cambridge, UK, 2017.
32. Brown, M.A.; Semelka, R.C.; Dale, B.M. *MRI: Basic Principles and Applications*; John Wiley & Sons Inc.: Hoboken, NJ, USA, 2015.
33. Mann, R.M.; Kuhl, C.K.; Kinkel, K.; Boetes, C. Breast MRI: Guidelines from the European society of breast imaging. *Eur. Radiol.* **2008**, *18*, 1307–1318. [CrossRef]
34. Hauer, M.P.; Uhl, M.; Allmann, K.H.; Laubenberger, J.; Zimmerhackl, L.B.; Langer, M. Comparison of turbo inversion recovery magnitude (TIRM) with T2-weighted turbo spin-echo and T1-weighted spin-echo MR imaging in the early diagnosis of acute osteomyelitis in children. *Pediatr. Radiol.* **1998**, *28*, 846–850. [CrossRef] [PubMed]
35. Freed, M.; Badal, A.; Jennings, R.J.; de Las, H.H.; Myers, K.J.; Badano, A. X-ray properties of an anthropomorphic breast phantom for MRI and x-ray imaging. *Phys. Med. Biol.* **2011**, *56*, 3513–3533. [CrossRef] [PubMed]
36. Carton, A.K.; Bakic, P.; Ullberg, C.; Derand, H.; Maidment, A.D. Development of a physical 3D anthropomorphic breast phantom. *Med. Phys.* **2011**, *38*, 891–896. [CrossRef] [PubMed]
37. Mazzara, G.P.; Briggs, R.W.; Wu, Z.; Steinbach, B.G. Use of a modified polysaccharide gel in developing a realistic breast phantom for MRI. *Magn. Reson. Imaging* **1996**, *14*, 639–648. [CrossRef]
38. Liney, G.P.; Tozer, D.J.; Turnbull, L.W. A simple and realistic tissue-equivalent breast phantom for MRI. *J. Magn. Reson. Imaging* **1999**, *10*, 968–971. [CrossRef]
39. Freed, M.; de Zwart, J.A.; Loud, J.T.; El Khouli, R.H.; Myers, K.J.; Greene, M.H.; Duyn, J.H.; Badano, A. An anthropomorphic phantom for quantitative evaluation of breast MRI. *Med. Phys.* **2011**, *38*, 743–753. [CrossRef]
40. Burfeindt, M.J.; Colgan, T.J.; Mays, R.O.; Shea, J.D.; Behdad, N.; van Veen, B.D.; Hagness, S.C. MRI-derived 3-D-printed breast phantom for microwave breast imaging validation. *IEEE. Antennas. Wirel. Propag. Lett.* **2012**, *11*, 1610–1613. [CrossRef]
41. Dantuma, M.; van Dommelen, R.; Manohar, S. Semi-anthropomorphic photoacoustic breast phantom. *Biomed. Opt. Express.* **2019**, *10*, 5921–5939. [CrossRef]
42. He, Y.; Liu, Y.; Dyer, B.A.; Boone, J.M.; Liu, S.; Chen, T.; Zheng, F.; Zhu, Y.; Sun, Y.; Rong, Y.; et al. 3D printed breast phantom for multi-purpose and multi-modality imaging. *Quant. Imaging Med. Surg.* **2019**, *9*, 63–74. [CrossRef]
43. Sindi, R.; Wong, Y.H.; Yeong, C.H.; Sun, Z. Development of patient-specific 3D-printed breast phantom using silicone and peanut oils for magnetic resonance imaging. *Quant. Imaging Med. Surg.* **2020**, *10*, 1237–1248. [CrossRef] [PubMed]
44. Westra, C.; Dialani, V.; Mehta, T.S.; Eisenberg, R.L. Using T2-weighted sequences to more accurately characterize breast masses seen on MRI. *AJR Am. J. Roentgenol.* **2014**, *202*, 183–190. [CrossRef] [PubMed]

AMJ Australasian Medical Journal [AMJ 2019;12(6):186-188]

Optimal protocols for quantitative assessment of breast density using magnetic resonance imaging

Rooa Sindi, Zhonghua Sun

Discipline of Medical Radiation Sciences, School of Molecular and Life Sciences, Curtin University, Perth, Western Australia, 6845, Australia

Editorial

Please cite this paper as: Sindi R and Sun Z. Optimal protocols for quantitative assessment of breast density using magnetic resonance imaging. AMJ 2019;12(6):186–188. https://doi.org/10.21767/AMJ.2019.3614

Corresponding Author:
Prof Zhonghua Sun
Discipline of Medical Radiation Sciences, School of Molecular and Life Sciences, Curtin University, Perth, WA, 6845, Australia
Email: z.sun@curtin.edu.au

ABSTRACT

Breast density, a measure of dense fibroglandular tissue relative to non-dense fatty tissue, has been confirmed as an independent risk factor of breast cancer. Although some research has been carried out on the quantitative assessment of breast density using breast MRI, there has been no report about the optimal MRI approach in this regard. This editorial highlights key findings reported by a recently published systematic review and met-analysis through analysing the current methods for quantifying breast density using MRI. Cluster analysis was applied to identify the statistical similarities within and between groups based on a Nearest Neighbour/Single Linkage. The analysis found that the non-contrast-enhanced T1-weighted acquisition is one of the most common MR breast-imaging protocols. Also, the fuzzy c-means clustering is the most widespread used algorithm among all breast density segmentation/measurement methods.

Key Words
Breast density, fibroglandular-tissue, magnetic resonance imaging, non-contrast-enhanced T1-weighted, segmentation, fuzzy c-mean clustering

Implications for Practice:

1. What is known about this subject?
Magnetic resonance imaging (MRI) provides excellent details of soft tissue contrast that can be used reliably to differentiate between fibroglandular and fatty tissues through detection of slight changes in density. However, there has been little agreement on what the optimal approach to assess breast density using MRI.

2. What new information is offered in this editorial?
Use of non-contrast-enhanced T1-weighted acquisition and fuzzy c-means clustering algorithm can allow for accurate assessment of breast density. This editorial analyses the current literature by demonstrating the usefulness of using non-contrast-enhanced T1-weighted images and fuzzy c-means clustering algorithm for the quantitative assessment of breast density.

3. What are the implications for research, policy, or practice?
3D printing techniques can be used to design a patient-specific 3D printed breast phantom to develop the optimal MR breast-imaging protocols. An important implication of this is the possibility of quantifying the amount of fibroglandular-tissue, thus simulating the risk factor of breast cancer.

Introduction

Breast density, a measure of dense fibroglandular tissue relative to non-dense fatty tissue, is an independent risk factor for breast cancer.[1-3] This finding confirms the association between breast density and breast cancer as women with dense breasts their likelihood of developing breast cancer is greater than those with fatty breasts.[4,5] Clinically, the assessment of breast density is performed qualitatively using the American College of Radiology (ACR) Breast Imaging-Reporting and Data System (BI-RADS) atlas, according to which density has different classification based on the amount of fibroglandular

tissue.[6] The main limitation of the BI-RADS atlas, however, is the inter- and intra-reader variability, as a result many methods are proposed in the literature regarding the quantification of breast density using MRI data.[7,8] Most of these methods are interpreted as measurements with a semi-automatic thresholding and segmentation approach, to date (and to the best of our knowledge), no consensus has been reached about the optimal approach to quantify breast density. This has been confirmed by our recent systematic review and meta-analysis on the quantitative assessment of breast density using MRI.[9] This editorial attempts to summarize some key findings from the current methods used for the quantitative assessment of breast density using MRI and highlight future research directions.

Quantitative assessment of breast density based on MRI protocols and segmentation/measurement methods

The methodological approach taken in this review is a mixed methodology based on *"metamean"* function in the R system, Version 3.4.1 (http://www.r-project.org/) and cluster analysis using the SPSS Statistics software V 25.0. A total of 38 studies were eventually included in the systematic review and meta-analysis.[1-3,5, 9] A wide range of MR breast-imaging protocols were identified to differentiate between fibroglandular and adipose tissues, with the non-contrast-enhanced T1-weighted either with 2D spin echo or 3D gradient echo being one of the protocols most often used. Regarding breast density segmentation/measurement methods of the studies, 20 studies (51.28%) used FCM clustering algorithm, 7 studies (17.95%) FCM and N3 algorithm, 4 studies (10.26%) in-house software, and one study (2.56%) manual software, whilst two studies did not mention this information. However, because of the heterogeneity nature of the study, the included studies were categorized into different clusters based on their statistical similarities using Euclidean distance and nearest neighbour agglomeration method. Eligibility criteria required individual studies to have independent study sample size, mean, and standard deviation. As a result, only 20 studies fulfilled the inclusion criteria of clustering analysis (Figure 1).[9]

A comparison of the two forest plots of cluster 1 (consisted of 9 studies) and 2 (consisted of 8 studies) reveals that the study means (i.e., cluster 1) are heterogeneous (X^2 = 19.54, P = 0.0066), however, the study variances are not heterogeneous (X^2 = 8.84, P = 0.2641), as shown in Figure 2. On the other hand, the study means (i.e., cluster2) are not heterogeneous (X^2 = 4.77, P = 0.6874), whereas the study variances are mildly heterogeneous (X^2 = 15.54, P = 0.0206) as indicated in Figure 3. Overall, there are two likely causes for the heterogeneity within the breast density studies: the used MR breast-imaging protocol and the applied breast density segmentation/measurement method. The evidence presented thus far supports the idea that optimal approach for the assessment of breast density should be established.

Summary and conclusion

The editorial further confirmed the high level of variation within the breast density studies, a possible explanation for these results may be due to the lack of adequate MR breast-imaging protocols and ideal breast density segmentation or measurement methods. A reasonable approach to tackle this issue could be to develop a patient-specific 3D printed breast phantom with different amounts of breast composition to quantify the volume of fibroglandular-tissue. Further, the 3D printed model can be used to develop optimal MR breast-imaging protocols, therefore, simulating the risk factor of developing breast cancer. 3D printing has been increasingly used in different medical fields ranging from orthopaedic surgery to cardiovascular disease and pre-surgical assessment of tumours.[10-13] Use of 3D printing in breast tissue is limited [14], thus, personalized 3D printed breast models could be a novel approach to overcome current limitations in utilising breast MRI for quantitative assessment of breast density.

References

1. Chen JH, Chang YC, Chang D, et al. Reduction of breast density following tamoxifen treatment evaluated by 3-D MRI: Preliminary study. J Magn Reson Imaging 2011; 29: 91-8.
2. Wang J, Azziz A, Fan B, et al. Agreement of mammographic measures of volumetric breast density to MRI. PloS One 2013; 8: e81653.
3. Tagliafico A, Bignotti B, Tagliafico G, et al. Breast density assessment using a 3T MRI system: Comparison among different sequences. PLoS One 2014; 9: e99027.
4. Lienart V, Carly B, Kang X, et al. Effect of preventive hormonal therapy on breast density: a systematic qualitative review. ~~The~~ Scientific World Journal 2014;
5. Tagliafico A, Tagliafico G, Astengo D, et al. Comparative estimation of percentage breast tissue density for digital mammography, digital breast tomosynthesis, and magnetic resonance imaging. Breast Cancer Res Treat 2013; 138: 311-7.
6. Mainiero MB, Lourenco A, Mahoney MC, et al. ACR appropriateness criteria breast cancer screening. J Am Coll Radiol 2016; 13: 45–49.

7. Lin M, Chan S, Chen J H, et al. A new bias field correction method combining N3 and FCM for improved segmentation of breast density on MRI. Med Phys 2011; 38: 5–14.
8. Doran SJ, Hipwell JH, Denholm R, et al. Breast MRI segmentation for density estimation: Do different methods give the same results and how much do differences matter? Med Phys 2017; 44: 4573–4592.
9. Sindi R, Sá Dos Reis C, Bennett C, Stevenson G, Sun Z. Quantitative Measurements of Breast Density Using Magnetic Resonance Imaging: A Systematic Review and Meta-Analysis. J Clin Med 2019; 8: 745.
10. Matsumoto JS, Morris JM, Foley TA, et al. Three-dimensional physical modeling: applications and experience at Mayo Clinic. Radiographics 2015; 35: 1989-2006.
11. Sun Z, Lau I, Wong YH, Yeong CH. Personalized three-dimensional printed models in congenital heart disease. J Clin Med 2019; 8: 522.
12. Perica E, Sun Z. A systematic review of three-dimensional printing in liver disease. J Digit Imaging 2018; 31: 692-701.
13. Sun Z, Liu D. A systematic review of clinical value of three-dimensional printing in renal disease. Quant Imaging Med Surg 2018; 8: 311-325.
14. He Y, Liu Y, Dyer BA, et al. 3D printed breast phantom for multi-purpose and multi-modality imaging. Quant Imaging Med Surg 2019; 9: 63-74.

PEER REVIEW

Peer reviewed.

CONFLICTS OF INTEREST

The authors declare that they have no competing interests.

FUNDING

None

Figure 1: Scatter plot of the study means versus standard deviations using 6-clusters memberships of the 21 included studies in the subgroup meta-analyses. Legend indicates the number of studies in each cluster, solid fill represents clusters with two or more studies, while open markers represent singleton study. Reprinted with permission under the open access from Sindi et al.[9]

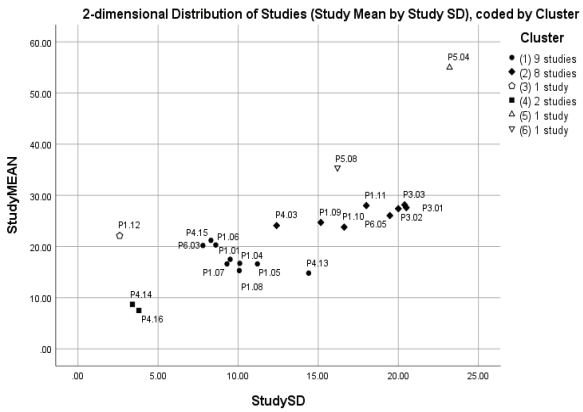

Figure 2: Forest plot of the study means, and 95% confidence limits of the studies in cluster 1 of % breast density. Reprinted with permission under the open access from Sindi et al.[9]

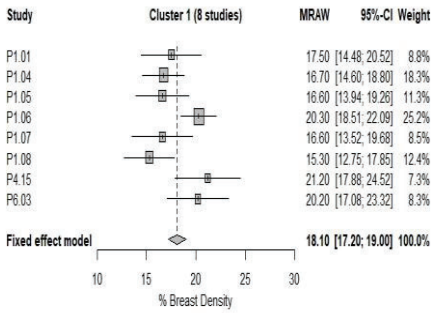

Figure 3: Forest plot of the study means, and 95% confidence limits of the studies in cluster 2 of % breast density. Reprinted with permission under the open access from Sindi et al.[9]

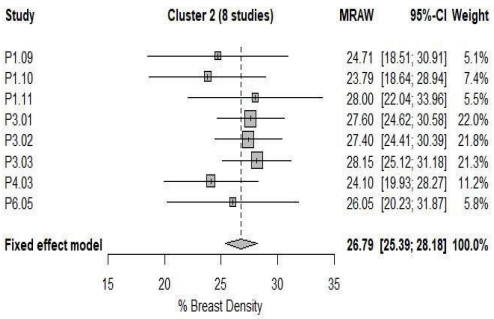

AMJ Australasian Medical Journal [AMJ 2020;13(7):234-238]

Personalized three-dimensional printed breast model for quantitative assessment of breast density using magnetic resonance imaging

Rooa Sindi[1,2], Zhonghua Sun[1]

1. Discipline of Medical Radiation Sciences, School of Molecular and Life Sciences, Curtin University, Perth, Western Australia, 6845, Australia
2. Medical Physics Section, Radio-diagnostic and Medical Imaging Department, King Fahd Armed Forces Hospital, Jeddah, 23311, Kingdom of Saudi Arabia

Editorial

Please cite this paper as: Sindi R and Sun Z. Personalized three-dimensional printed breast model for quantitative assessment of breast density using magnetic resonance imaging. AMJ 2020;13(7):234–238.
https://doi.org/10.35841/1836-1935.13.7.234-238

Corresponding Author:
Prof Zhonghua Sun
Discipline of Medical Radiation Sciences, School of Molecular and Life Sciences, Curtin University, Perth, WA, 6845, Australia
Email: z.sun@curtin.edu.au

ABSTRACT

Three-dimensional (3D) printing has become an increasingly developed technique in the medical field and has been used in many clinical applications. Research has consistently shown that 3D-printed models derived from patient's imaging data can serve as valuable tools for examining different breast-MRI protocols, testing radiofrequency coils, and evaluating system performance. This editorial highlights the utility of personalized 3D-printed breast model for the quantitative breast density assessment using MRI. A personalized 3D-printed breast model was developed and fabricated using silicone and peanut oils to mimic the MR-associated properties of fibroglandular and adipose breast tissues. The silicone and peanut oils' T1 relaxation times were correspondingly determined on a 3T MRI system and linked to the tissue reference values.

Key Words
Magnetic resonance imaging (MRI), breast density, fibroglandular-tissue, three-dimensional printing, model, silicone oil, peanut oil, quantitative, assessment

Implications for Practice:

1. What is known about this subject?

Magnetic resonance imaging (MRI) is widely used as an adjuvant modality for the screening of women at high-risk of developing breast cancer, such as those with high breast density.[1,2] Although some research has been conducted on the use of 3D printing techniques to develop breast phantoms for MRI, there are currently no phantoms available for quantitative breast density assessment based on a realistic morphology of breast structures derived from MR images of human tissues.[3-10]

2. What new information is offered in this editorial?

Personalized 3D-printed breast model using silicone and peanut oils simulates the MR-related characteristics and appearance of fibroglandular and adipose breast tissues, respectively. This editorial summarises our research experience of using 3D printing techniques and tissue mimicking materials (TMMs) to resemble the T1 relaxation times of the corresponding breast tissues.

3. What are the implications for research, policy, or practice?

A personalized 3D-printed breast model can be used to identify the optimal breast MRI protocol and measurement method for the quantitative assessment of breast density, thus estimating the risk of developing of breast cancer.

Introduction

Breast density-an autonomous risk element of breast cancer-is defined as a measure of dense fibroglandular tissue relative to non-dense fatty tissue.[11-13] In line with this risk association, women with dense breasts have shown a greater probability of inducing breast cancer relative to those with fatty breasts.[14,15]

Although some research has been carried out on the development of anthropomorphic breast models for X-ray

imaging, there is still inadequate data available for MR imaging.[3-10] Also, much uncertainty still exists as to whether the most relevant TMMs are able to sufficiently replicate the MR-related characteristics and resemblance of breast structures, especially fibroglandular tissue.[16-19] This has been corroborated by our latest experiment using 3D-printing methods and tissue-equivalent materials to mimic the breast tissue relaxation times for MR imaging.[20] Notwithstanding considerable information about the role of MRI's in quantitative breast density analysis, the optimal imaging protocol and measurement method have not generally been agreed in this repect.[21,22] This editorial summarises some of the experiment's main findings and demonstrates the utility of a personalized 3D-printed breast model for quantitative breast density assessment using MRI.

Personalized 3D-printed breast model using silicone and peanut oils for quantitative breast density assessment

3D-printed models based on patients' imaging data have allowed to learn procedures, educate students, and enhance the individual's perception of complex anatomical structures and pathologies by using such realistic reproductions. In this study, a 3D-printed breast model was developed, with the intention of providing a more precise assessment of breast density based on a realistic morphological breast structures that obtained from MR images of human-tissue. The breast examination was performed on a 1.5T MRI system (MAGNETOM Aera, Siemens, Germany) with a dedicated breast coil. Based on the recommendations from our recent systematic review and meta-analysis, the protocol for breast imaging has been selected as high-resolution, non-contrast-enhanced T1-weighted images, which assist in the distinction between non-glandular fatty tissue and glandular tissue.[21]

Overview and design

The personalized 3D-pinted breast model comprises two main parts: an outer shell, which simulates the texture and form of the skin, and an inner structure, including fibroglandular and fatty tissues, which imitates the breast compositions. Firstly, the 3D skin shell and the cover have been made from polylactic acid (PLA) with the fused deposition modelling (FDM) technology. [20] The outer shell was printed in 0.15 mm layer height, took an average of 40 hours printing time, and had a 3.0 mm average thickness and 12.5 µm resolution (Table 1). Figure 1 shows the personalized 3D-printed breast model of the outer skin layer and sections to be filled with fibroglandular- and adipose-equivalent tissues. Then, the 3D fibroglandular models were constructed as hollow structures and have been made from photopolymer resin with the digital light processing (DLP) technology. [20] They were printed with 10 seconds of curing time per layer, 0.05 mm in layer thickness, took an average of 17 hours printing time for both left- and right-models, and had a 2.0 mm average thickness and 47 µm resolution (Table 1). Figure 2 shows the fabrication of the hollow 3D-printed for both left- and right-fibroglandular models. Finally, the fibroglandular models were submerged in a fat-equivalent medium to replicate the adipose tissue's MR-related properties and T1 relaxation time. The hollow skin and fibroglandular 3D-printed models were scanned on a 3T MRI system (MAGNETOM Prisma, Siemens, Germany) to ensure neither the PLA nor the photopolymer resin produce MR signal.

Results and discussion

The T1 relaxation times of the five designated substances (agarose gel, silicone rubber with/without fish oil, silicone oil, and peanut oil) were determined on the same 3T MRI system, with the objective of simulating the MR-associated properties of the fibroglandular and adipose breast tissues. As shown in Table 2, results indicated that the silicone and peanut oils were found to be closely analogous to the T1 relaxation times and MR-associated properties of the respective tissues, which are 1515.8 ± 105.5 and 405.4 ± 15.1 ms, respectively. Consequently, those substances were selected to fill the hollow 3D-printed models. Figure 3 demonstrates a summary of the fabrication procedure of the personalized 3D-printed breast model. In a brief summary, the hollow 3D-printed fibroglandular models were filled with a silicone oil and then closed using UV-curable resin. Subsequently, the fibroglandular models were fastened inside the skin model using an acrylic-based adhesive. Next, the space between the skin shell and the fibroglandular models was filled with a peanut oil. Thereafter, the breast model was bounded with a self-constructed silicone gasket and cover. Finally, the cover was sealed using polycarbonate bolts and nuts. On completion of the construction process, the personalized 3D-printed breast model was examined on the same 3T MRI system in a prone position using a dedicated 18-channel breast coil. Interestingly, T1- and T2-weighted MR images of the personalized 3D-printed breast model using silicone and peanut oils showed that such model can be utilized as substitutes for the fibroglandular and adipose tissues, respectively. As shown in Figure 4, these selected oils in both T1- and T2-weighted images, yielded a tolerable degree of contrast and MR-associated features. Overall, the T1 relaxation times of the silicone and peanut oils used to imitate the fibroglandular and adipose breast tissues are comparable to their corresponding reference values stated in the literature.

Summary and conclusion

Personalized 3D-printed breast model based on TMMs can be used to determine the optimum MR breast-imaging protocols and measurement methods for the purpose of providing more precise assessments of breast density, thus estimating the risk of breast cancer. The developed model represents a novel approach of utilizing 3D-printing technique by further expanding its applications in the medical domain.

References

1. Mann RM, Balleyguier C, Baltzer PA, et al. Breast MRI: EUSOBI recommendations for women's information. Eur Radiol. 2105;25:3669–3678.
2. Heller SL, Yeong Lin LL, Melsaether AN, et al. Hormonal effects on breast density, fibroglandular tissue, and background parenchymal enhancement. Radiographics. 2018;38:983–996.
3. Carton AK, Bakic P, Ullberg C, et al. Development of a physical 3D anthropomorphic breast phantom. Med Phys. 2011;38:891–6.
4. Mazzara GP, Briggs RW, Wu Z, et al. Use of a modified polysaccharide gel in developing a realistic breast phantom for MRI. Magn Reson Imaging. 1996;14:639–48.
5. Liney GP, Tozer DJ, Turnbull LW. A simple and realistic tissue-equivalent breast phantom for MRI. J Magn Reson Imaging. 1999;10:968–71.
6. Freed M, de Zwart JA, Loud JT, et al. An anthropomorphic phantom for quantitative evaluation of breast MRI. Med Phys. 2011;38:743–53.
7. Burfeindt MJ, Colgan TJ, Mays RO, et al. MRI-derived 3D-printed breast phantom for microwave breast imaging validation. IEEE Antennas Wirel Propag Lett. 2012;11:1610–13.
8. Dantuma M, van Dommelen R, Manohar S. Semi-anthropomorphic photoacoustic breast phantom. Biomed Opt Express. 2019;10:5921–39.
9. He Y, Liu Y, Dyer BA, et al 3D printed breast phantom for multi-purpose and multi-modality imaging. Quant Imaging Med Surg. 2019;9:63–74.
10. He Y, Qin S, Dyer BA, et al. Characterizing mechanical and medical imaging properties of polyvinyl chloride-based tissue-mimicking materials. J Appl Clin Med Phys. 2019;20:176–83.
11. Chen JH, Chang YC, Chang D, et al. Reduction of breast density following tamoxifen treatment evaluated by 3-D MRI: Preliminary study. Magn Reson Imaging. 2011;29:91–98.
12. Wang J, Azziz A, Fan B, et al. Agreement of mammographic measures of volumetric breast density to MRI. PLoS ONE. 2013;8:e81653.
13. Tagliafico A, Bignotti B, Tagliafico G, et al. Breast density assessment using a 3T MRI system: Comparison among different sequences. PLoS ONE. 2014;9:e99027.
14. Lienart V, Carly B, Kang X, et al. Effect of preventive hormonal therapy on breast density: A systematic qualitative review. Sci World J. 2014.
15. Tagliafico A, Tagliafico G, Astengo D, et al. Comparative estimation of percentage breast tissue density for digital mammography, digital breast tomosynthesis, and magnetic resonance imaging. Breast Cancer Res Treat. 2013;138:311–317.
16. Gach HM. T1 and T2 and complex permittivities of mineral oil, silicone oil, and glycerol at 0.35, 1.5, and 3 T. Med Phys. 2019;46:1785–92.
17. Niebuhr NI, Johnen W, Echner G, et al. The ADAM-pelvis phantom-an anthropomorphic, deformable and multimodal phantom for MRgRT. Phys Med Biol. 2019;64:04NT05.
18. Niebuhr NI, Johnen W, Güldaglar T, et al. Radiological properties of tissue surrogates used in a multimodality deformable pelvic phantom for MR-guided radiotherapy. Med Phys. 2016;43:908–16.
19. Rakow-Penner R, Daniel B, Yu H, et al. Relaxation times of breast tissue at 1.5 T and 3T measured using IDEAL. J Magn Reson Imaging. 2006;23:87–91.
20. Sindi R, Wong YH, Yeong CH, et al. Development of patient-specific 3D-printed breast phantom using silicone and peanut oils for magnetic resonance imaging. Quant Imaging Med Surg. 2020;10:1237–1248.
21. Sindi R, Sá Dos Reis C, Bennett C, et al. Quantitative measurements of breast density using magnetic resonance imaging: A systematic review and meta-analysis. J Clin Med. 2019;8:745.
22. Sindi R, Sun Z. Optimal protocols for quantitative assessment of breast density using magnetic resonance imaging. AMJ. 2019;12:186–188.

PEER REVIEW

Peer reviewed.

CONFLICTS OF INTEREST

The authors declare that they have no competing interests.

FUNDING

This study is supported by the Ministry of Defence, Medical Service Division, Kingdom of Saudi Arabia and Saudi Arabian Cultural Mission (SACM), Australia.

Figure 1: 3D-printed breast model of the outer skin layer and compartments to be filled with fibroglandular- and adipose-equivalent tissues. Reprinted with permission under the open access from Sindi et al.[20]

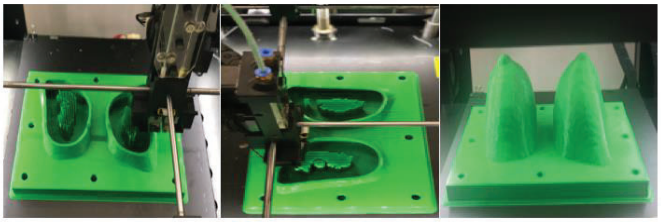

The 3D-printed skin shell and the cover have been made from polylactic acid (PLA) on a Raise3D N2 Plus 3D printer with the FDM technology. The outer shell was printed in 0.15mm layer height, took an average of 40 hours printing time, and had a 3.0mm average thickness and 12.5µm resolution.

Figure 2: 3D-printed models of the internal structures, which are the fibroglandular hollow structures. Reprinted with permission under the open access from Sindi et al.[20]

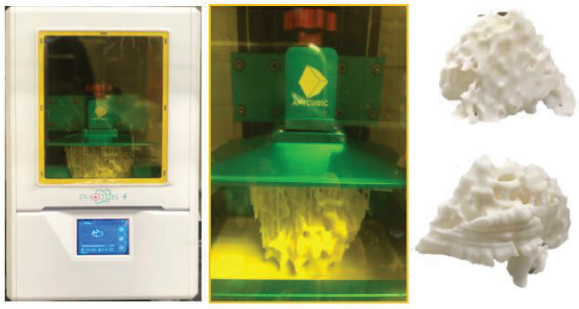

The 3D-printed fibroglandular models were constructed as hollow structures and have been made from photopolymer resin on an Anycubic Photon S 3D DLP UV resin printer with the digital light processing (DLP) technology. They were printed with 10 seconds of curing time per layer, 0.05mm in layer thickness, took an average of 17 hours printing time for both left- and right-models, and had a 2.0mm average thickness and 47µm resolution

Figure 3: Flow chart demonstrates the construction process of the personalized 3D-printed breast model for MRI. Reprinted with permission under the open access from Sindi et al.[20]

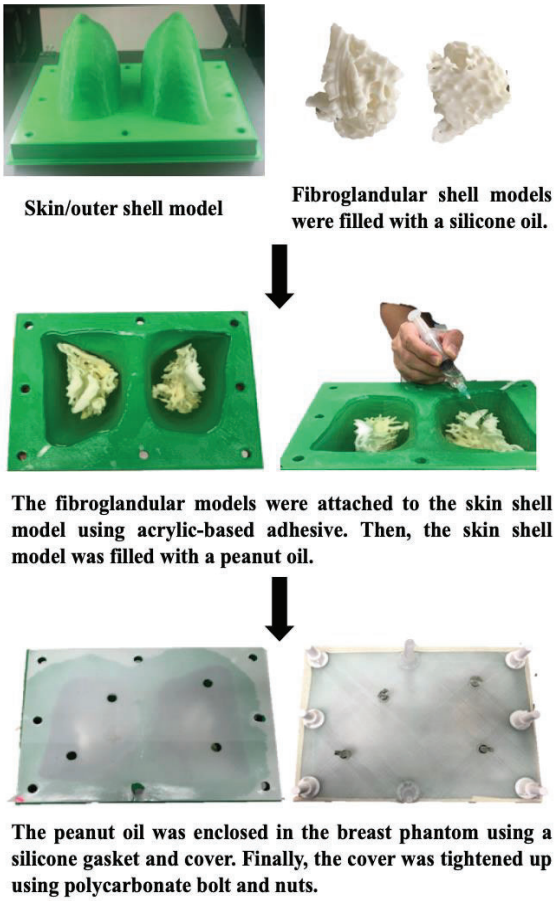

Figure 4: MR images of the personalized 3D-printed breast model. (A): T1-weighted image. (B): T2-weighted image using turbo spin echo (TSE) pulse sequence. Reprinted with permission under the open access from Sindi et al.[20]

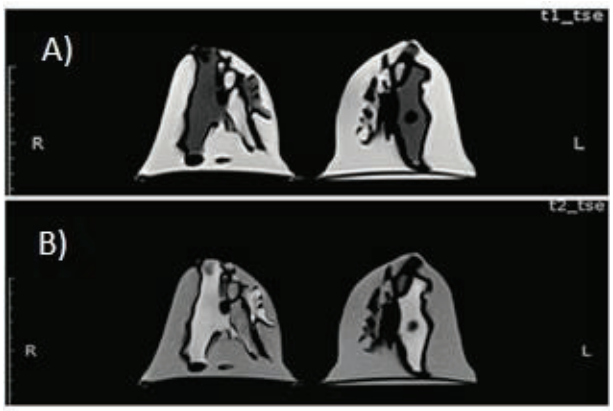

The T1- and T2-weighted MR images of the personalized 3D-printed breast model using silicone and peanut oils as TMMs of the fibroglandular and adipose breast tissues, respectively.

Table 1: 3D-Printing parameters used for the development of the personalized 3D-printed breast model

3D printing parameters	Skin model	Fibroglandular model
Thickness (mm)	3.0	2.0
Layer height (mm)	0.15	0.05
Resolution (µm)	12.5	47
Curing time (sec)	-	10
Printing time (h)	40	17*

(*): For both left and right fibroglandular models.

Table 2: T1 Relaxation times of different materials for tissue surrogates used in the experiment. Reprinted with permission under the open access from Sindi et al.[20]

Phantom Tissue Mimicking Material	T1 (average±SD, ms), 3T Siemens MR Scanner
Fibroglandular shell	No signal
Skin/outer shell	No signal
Silicone rubber	577.2±107.8
Silicone rubber with fish oil	902.1±120.5
Fresh Silicone rubber	638.3±108.5
Silicone oil 50mm^2/s*	1515.8±105.5
Peanut oil (Basso)	405.4±15.1
Peanut Oil (Pressed Purity)	404.1±10.5
Agarose gel 0.5wt%	4015.5±100.2
Agarose gel 1.0wt%	3877.8±130.5
Agarose gel 1.5wt%	3404.8±255.9
Agarose gel 2.0wt%	3572.6±100.4
Agarose gel 2.5wt%	3617.2±101.5

(*): Viscosity unit.